8-2021

In Situ Cosmogenic Backgrounds in the MAJORANA DEMONSTRATOR

Andrew Lopez
University of Tennessee, Knoxville, alopez8@vols.utk.edu

To the Graduate Council:

I am submitting herewith a dissertation written by Andrew Lopez entitled "In Situ Cosmogenic Backgrounds in the MAJORANA DEMONSTRATOR." I have examined the final electronic copy of this dissertation for form and content and recommend that it be accepted in partial fulfillment of the requirements for the degree of Doctor of Philosophy, with a major in Physics.

Yuri V. Efremenko, Major Professor

We have read this dissertation and recommend its acceptance:

Nadia Fomin, Eric D. Lukosi, Lucas Platter, Andrew W. Steiner

Accepted for the Council:

Dixie L. Thompson

Vice Provost and Dean of the Graduate School

(Original signatures are on file with official student records.)

In Situ Cosmogenic Backgrounds of the MAJORANA DEMONSTRATOR

A Dissertation Presented for the

Doctor of Philosophy

Degree

The University of Tennessee, Knoxville

Andrew Michael Lopez

August 2021

Dedicated to my parents

Acknowledgments

I would like to thank my Ph.D. advisor, Dr. Yuri Efremenko for encouraging me to be a better researcher and for always being patient with me. I would also like to thank Dr. Vincent Guiseppe for the guidance and mentoring he provided onsite in South Dakota. Thank you Dr. Ralph Massarcyzk, Dr. Steven Elliott, and the rest of the Los Alamos P-23 Weak Interactions group for hosting me at Los Alamos National Lab for six months. Not only did my analysis skills improve greatly during that short time but working first-hand in a national laboratory environment will be an experience I rely on for the rest of my career. Thank you Dr. Clint Wiseman for patiently showing me the ropes when I first joined the veto group. Additionally I would like to thank all of the members of MAJORANA Collaboration for always being warm and welcoming, showing me how strong a collaboration can be when we work towards a common goal. Finally I would like to thank my family and friends, who never doubted me even when I doubted myself.

Abstract

Neutrino-less double-beta decay is a proposed type of radioactive decay that, if observed, could answer several outstanding physics questions, such as "Is the neutrino its own antiparticle otherwise known as a Majorana particle?", "What is the mass of the neutrino?", and "What is the neutrino mass hierarchy?" As technology and experimental techniques improve, the sensitivity of experiments looking for rare events becomes more dependent on the backgrounds. Some of these backgrounds can be reduced using shielding techniques such as implementing a veto system, selecting radiopure components, and conducting the experiment deep underground. However some amount of cosmogenically induced backgrounds remain as an irreducible background. By understanding how these processes occur within the experimental setup, the effect of these backgrounds on the experimental analysis can be mitigated. The Majorana Demonstrator, located at the Sanford Underground Research Facility in Lead, South Dakota, is currently searching for neutrino-less double-beta decay using two arrays of germanium-76 P-Type Point Contact detectors. In this work, for the first time, actual data from the Majorana Demonstrator is being used to benchmark popular simulation packages to better understand in situ production of radioactive isotopes and provide tools for future low background experiments. The simulation packages FLUKA and GEANT4 are used to estimate the irreducible prompt muon-induced background rate in the Majorana Demonstrator, and the measurement of five muon-induced background signals is conducted. In addition, the University of Tennessee group was responsible for construction, commissioning, maintaining, and data analysis for one of the key Majorana Demonstrator subsystems: The Active Muon Veto System. We will discuss related activities as well.

Table of Contents

List of Tables

List of Figures

List of Abbreviations

1BC One broken Charge-to-Digital converter channel

$\beta\beta(2\nu)$ Two neutrino double beta decay

$\beta\beta(0\nu)$ Neutrinoless double beta decay

Bg Background

CAD Computer Aided Design software

CL Confidence level

CP Charge conjugation parity symmetry

DAQ Data acquisition system

DCR Delayed charge recovery

DEP Double escape peak

DS Data set

EC Electron capture

EnrGe Enriched germanium

ES Excited state

GS Ground state

IT Isomeric transition

LED Light-emitting diode

MH MeiHime particle generator

MJD Majorana Demonstrator

muDT Timestamp difference between muon veto event and germanium detector event

muVeto 1-second muon veto analysis cut

NatGe Natural germanium

NIM Nuclear instrument module

ORCA Object-oriented Real-time Control and Acquisition

PMNS Pontecorvo-Maki-Nakagawa-Sakata

PMT Photomultiplier tube

PPC P-type point contact

QDC Charge-to-digital converter

ROI Region of interest

SE Surviving events

SEP Single escape peak

SFF ShowersFromFile particle generator

SM Standard Model of electroweak interactions

SURF Sanford Underground Research Facility

SW Software

UL Upper limit

UP Underperformance

VME Versa module europa

Chapter 1

Introduction

The MAJORANA DEMONSTRATOR is one of the world's most sensitive $\beta\beta(0\nu)$ decay experiments. The DEMONSTRATOR utilizes an array of natural and enriched germanium detectors which searches for the $\beta\beta(0\nu)$ decay of ^{76}Ge. To be a competitive $\beta\beta(0\nu)$ decay experiment, it is vital that the backgrounds be incredibly low. The primary sources of background in the DEMONSTRATOR are (1) the natural radioactivity of the materials, (2) cosmogenic activation of detectors on the surface, and (3) in situ cosmogenic activation of detectors. This dissertation focuses on the impact of in situ cosmogenic activation. One method the DEMONSTRATOR uses to reduce this impact is to implement an active muon veto system as well as a muVeto analysis cut. This work details software tools developed to optimize the veto system, a simulation used to estimate the veto system efficiency, and a data analysis of in situ cosmogenic backgrounds. This data analysis utilizes a data set with 25.55 $kg \cdot yr$ of enriched germanium exposure, and uses two popular Monte Carlo packages, GEANT4-based MAGE and FLUKA, to benchmark the simulation tools and estimate the total in situ cosmogenic backgrounds in the MAJORANA DEMONSTRATOR. This analysis is the first of its kind for germanium detector arrays.

This dissertation is organized in the following way:

Chapter 2 will provide a brief overview of the relevant physics concepts. The MAJORANA DEMONSTRATOR operational design and current status is discussed in Chapter 3. In Chapters 4 and 5 details about the active veto system are given, along with a description

of the software tool developed to monitor the status of the system. Chapter 6 will describe the search muon-induced signatures to be found in the MAJORANA data. Chapter 7 gives an introduction to the Monte Carlo packages used in this work. Chapters 8 and 9 describe two auxiliary simulation studies performed. One to quantify the muon tagging efficiency of the veto system and another to estimate the effect of the MAJORANA shielding on ambient neutrons. Chapters 10 & 11 discuss the simulations and analysis performed to estimate the irreducible muon-induced background signals in the MAJORANA DEMONSTRATOR. Chapter 12 will describe the TALYS simulations performed in order to estimate the excited state production rate of key signature isotopes using both the MAGE and FLUKA simulation results. Chapter 13 details the comparison of the simulation and data analysis results. Finally, Chapter 14 will briefly discuss the results of these studies.

Chapter 2

Physics

The study of neutrinos has been a hot topic in the scientific community. Neutrinos were first postulated in 1930 by Wolfgang Pauli. At the time, beta decay was thought to be the emission of a single electron from a nucleus. Therefore it was expected that the beta decay of a specific isotope should have a distinct, well-defined energy. As the beta particles were measured to occupy a continuous energy spectrum, Pauli postulated the existence of a new particle which could explain the spectrum. In a letter to the scientific community [29], Pauli writes: "I have hit upon a desperate remedy to save the 'exchange theorem' of statistics and the energy theorem. Namely [there is] the possibility that there could exist in the nuclei electrically neutral particles that I wish to call neutrons ... The continuous β-spectrum would then become understandable by the assumption that in β decay a neutron is emitted together with the electron, in such a way that the sum of the energies of neutron and electron is constant". Pauli also states that this postulated particle must have "something like about 10 times the penetrating capacity of a γ ray". This "neutron" later becomes known as a neutrino. It was not until 1956 that neutrinos were first detected in what is now called the Cowan-Reines neutrino experiment [29].

2.1 Properties of Neutrinos

Since their discovery, much has been uncovered about neutrinos. Three types or flavors of neutrino have been discovered, the electron-neutrino, ν_{e} , muon-neutrino, ν_{μ} , and the

tau-neutrino, ν_τ. In the Standard Model of Electroweak Interactions, or SM for short, there is no explanation of how neutrinos can be massive particles, and no explanation as to whether neutrinos are Dirac particles or Majorana particles [24]. Dirac particles can be described by the Dirac Equation, a relativistic wave equation. This wave equation can be used to predict the behavior of a Dirac particle, and directly implies the existence of a corresponding antiparticle. The electron, muon, and tauon are all Dirac particles with observed antiparticles. It is possible that neutrinos are Majorana particles rather than Dirac particles. A Majorana particle has the unique property of being its own antiparticle [24].

2.1.1 Neutrino Oscillations

It has been confirmed that at least two types of neutrino are massive from observation of neutrino oscillations [24]. Multiple experiments with solar, atmospheric, reactor and accelerator neutrinos have provided evidence that as a neutrino of any flavor travels, there is a non-zero probability that it will transition into a different flavor of neutrino, this is called a neutrino oscillation. Neutrino oscillation can only occur if (1) not all neutrinos are massless, and (2) there is a non-zero mixing of the neutrino flavors.

The simplest explanation of neutrino oscillation is an analogue to the explanation of quark oscillation. This is an extension of the SM that assumes neutrinos are Dirac particles and there are only three light neutrinos, ν_1, ν_2, and ν_3. In this model, along with the knowledge that the neutrinos oscillate, the three neutrino flavors (ν_e , ν_μ , ν_τ) can be understood as the weak eigenstates of the three neutrino mass eigenstates, $|\nu_1\rangle$, $|\nu_2\rangle$, and $|\nu_3\rangle$ with eigenvalues m_1, m_2, and m_3 respectively. For example, the electron neutrino state can be written as: $\nu_e = U_{e1}\,|\nu_1\rangle + U_{e2}\,|\nu_2\rangle + U_{e3}\,|\nu_3\rangle$, where U_{e1} , U_{e2} , U_{e3} are mixing elements of a 3x3 unitary matrix known as the Pontecorvo-Maki-Nakagawa-Sakata (PMNS) matrix, or the neutrino mixing matrix [24]. This matrix is analogous to the Cabibbo-Kobayashi-Maskawa matrix, i.e. the quark mixing matrix. If all three neutrinos are massless, then flavor oscillation cannot occur. The PMNS matrix is characterized by seven fundamental parameters:

i) 3 angles $(\theta_{12}, \theta_{23}, \theta_{13})$

ii) 3 neutrino masses $m_1,\ m_2,\ m_3$

iii) 1 CP (charge conjugation parity symmetry) violation phase.

If the neutrinos are instead Majorana particles then the PMNS matrix will have two additional CP violation phases. Various neutrino oscillation experiments such as Super-Kamiokande [50], KamLAND [35], T2K [3], Daya Bay [11], and Double Chooz [34] have been able to determine the 3-neutrino oscillation parameters, θ_{12}, θ_{23} , θ_{13} , $|\Delta m^2_{21}|$, $|\Delta m^2_{31}|$, $|\Delta m^2_{32}|$ with high precision [62]. However as neutrino oscillation experiments are only sensitive to difference of masses squared, $|\Delta m^2_{ij}|$ [24], they are unable to determine (1) the absolute mass scale of the neutrinos or (2) the mass hierarchy of the neutrinos which can be described as the normal ordering ($m_3 > m_2 > m_1$) or the inverted ordering ($m_2 > m_1 > m_3$). Additionally, neutrino oscillation has not been observed to violate CP symmetry, so these experiments are unable to measure a non-zero CP violation phase [24]. Therefore neutrino oscillation experiments cannot provide evidence of neutrinos being Dirac particles (1 CP violation phase) or Majorana particles (3 CP violation phases) [62].

2.1.2 Neutrino Mass Mechanism

In the SM, fermions are given mass through the Higgs mechanism via a Yukawa coupling [62]. For leptons, this coupling can be expressed by the Lagrangian

$$-\mathcal{L}_{\text{Yukawa,lepton}} = Y^{\ell}_{ij}\bar{L}_{Li}\phi E_{Rj} + \text{h.c. [62]} \tag{2.1}$$

After spontaneous symmetry breaking this term leads to charged lepton masses

$$m^{\ell}_{ij} = Y^{\ell}_{ij}\frac{\nu}{\sqrt{2}} \text{ [62]}, \tag{2.2}$$

where ν is the vacuum expectation value of the Higgs field. However, all neutrinos in the SM have been observed to be solely left-handed. No Yukawa interaction can be built with only left handed neutrinos. Therefore, in the Standard model, all neutrinos are massless. In principle, a neutrino mass term could be generated with only left handed neutrinos, but these

mechanisms are forbidden in the SM, as they violate total lepton symmetry by two units [62]. One must go beyond the Standard Model to explain the neutrino mass mechanism.

If the Standard Model is extended by the addition of m number of sterile neutrinos, ν_{si} (with $i = 1, ..., m$), a Lagrangian that leads to new mass terms can be constructed.

$$-\mathcal{L}_{M_\nu} = M_{Dij}\bar{\nu}_{Lj} + \frac{1}{2}M_{Nij}\bar{\nu}_{si}\nu^c_{sj} + \text{h.c. [62]}, \tag{2.3}$$

where M_D is a complex matrix of dimension m×3 and M_N is a symmetric m×m matrix. The first term generates a mass term,

$$M_{Dij} = Y^\nu_{ij}\frac{\nu}{\sqrt{2}} \text{ [62]}, \tag{2.4}$$

after spontaneous electroweak symmetry breaking from Yukawa interactions. This first term is called the Dirac mass term due to the similarity to the SM charged fermion mass term.

Equation 2.3 can be rewritten as:

$$-\mathcal{L}_{M_\nu} = \frac{1}{2}\begin{pmatrix}\overline{\tilde{\nu}^c_L} & \overline{\tilde{\nu}_s}\end{pmatrix}\begin{pmatrix}0 & M_D^T \\ M_D & M_N\end{pmatrix}\begin{pmatrix}\tilde{\nu}_L \\ \tilde{\nu}^c_s\end{pmatrix} + \text{h.c. [62]} \tag{2.5}$$

This Lagrangian can be expressed in terms of the mass eigenstates as:

$$-\mathcal{L}_{M_\nu} = \frac{1}{2}\sum_{k=1}^{3+m} m_k\bar{\nu}_{Mk}\nu_{Mk} \text{ [62]}, \tag{2.6}$$

where $\nu_{Mk} = \nu_{mass,k} + \nu^c_{mass,k}$. These states are called Majorana neutrinos as they obey the Majorana condition $\nu_M = \nu^c_M$, which implies that the neutrino and antineutrino states are the same. If $M_N = 0$, then only the Dirac mass terms are allowed and equation 2.5 describes the SM extension of the 3 known neutrinos with the addition of m sterile neutrinos, where all neutrinos are Dirac particles. If the mass eigenvalues of M_N are much higher than the scale of electroweak symmetry breaking, i.e. $M_N >> M_D$, then we see the light neutrinos have mass: $\nu_{light} \approx -\frac{M_D^2}{M_N}$, and the heavy neutrinos have mass: $\nu_{heavy} \approx M_N$ [62]. This mass mechanism is known as the See-Saw Type 1 mechanism, as if one mass is large, then the other must be small. If the mass M_N is on the order of Grand Unified Theory scale $M_N \approx 10^5 - 10^{12}$

GeV, then the heavy neutrinos would be undetectable with current technology, and the light neutrinos mass would be on the order of 1 eV, which is comparable to current upper limits [14].

2.2 Double-Beta decay

Double beta decay ($\beta\beta(2\nu)$) is a second-order weak process in which two neutrons in a nucleus simultaneously decay into two protons: $(\mathrm{A}, \mathrm{Z}) \rightarrow (\mathrm{A}, \mathrm{Z}+2) + 2\mathrm{e}^- + 2\nu$. This process is also called two neutrino double beta decay. Double beta decay can also occur in reverse, with two protons being converted into two neutrons. Double beta decay can occur if single beta decay is suppressed by energy convervation. No known conservation law forbids double beta decay if it is energetically allowed. Double beta decay was first detected in 1987 and has been actively studied by the scientific community [38]. Currently, data on the rate of this process exists for more than a dozen isotopes with lifetimes ranging from $7 \cdot 10^{18} - 2 \cdot 10^{24}$ years [21]. The study of double beta decay makes it possible to test existing nuclear matrix element calculations and gives deep insights into nuclear physics.

2.2.1 Neutrino-less Double-Beta Decay

Another form of double beta decay, called neutrinoless double beta decay ($\beta\beta(0\nu)$): $(\mathrm{A}, \mathrm{Z}) \rightarrow (\mathrm{A}, \mathrm{Z}+2) + 2\mathrm{e}^-$, is hypothetically possible but has not yet been detected [22] [25]. Neutrinoless double beta decay violates lepton number conservation through annihilation of the neutrinos, this is only possible if the neutrino is a Majorana particle (i.e. its own antiparticle). If the neutrino is a Majorana particle and has non-zero mass, this process will exist and its rate will be sensitive to the neutrino mass [62].

The simplest $\beta\beta(0\nu)$ decay mechanism is the light Majorana neutrino exchange, although theorists are investigating other potential mechanisms. Figure 2.1 shows the Feynman Diagram for the $\beta\beta(0\nu)$ light neutrino exchange.

If light Majorana neutrino exchange is the dominant mechanism for $\beta\beta(0\nu)$ decays, then the rate of $\beta\beta(0\nu)$ decay is given by the equation:

$$(T^{0\nu}_{1/2})^{-1} \;=\; G_{0\nu}(Q_{\beta\beta}, Z)|M^{0\nu}|^2 < m_{\beta\beta} >^2 \;\; [36]\; [53], \tag{2.7}$$

where $G_{0\nu}$ is the phase space factor, $M^{0\nu}$ is the nuclear matrix element, and $< m_{\beta\beta} >^2$ is the so-called effective majorana mass. The effective majorana mass can be obtained by

$$< m_{\beta\beta} >^2 = \; |\sum_{i=1}^{3} U^2_{ei} m_i|^2 \; [36]\; [53], \tag{2.8}$$

where m_i are the three Majorana neutrino mass eigenstates, and U_{ei} are the elements of the PMNS mixing matrix with the two additional Majorana CP violating phases [53]. The phase space factor $G_{0\nu}$ has been calculated for a variety of $\beta\beta(0\nu)$ isotopes and is known to high precision. The nuclear matrix element $M^{0\nu}$, cannot be measured experimentally and must be calculated. The nuclear matrix element calculation relies on sophisticated nuclear many-body theories and is subject to uncertainty. A variety of nuclear models have been used to perform this calculation. Currently, these models show a factor of $\sim 2-3$ spread in nuclear matrix element values for a particular $\beta\beta(0\nu)$ isotope. Figure 2.2, adopted from [44], shows a comparison of nuclear matrix elements for eleven different $\beta\beta(0\nu)$ isotopes.

There are uncertainties in the values for the neutrino mixing parameters and neutrino mass eigenstate differences which results in an ambiguous correlation between the effective majorana mass and the mass of the lightest neutrino, see Figure 2.3 from [43]. The aim of the next generation of $\beta\beta(0\nu)$ decay experiments is to search most, if not all, of the inverted ordering phase space.

Neutrinoless double beta decay has an unambiguous signature. The sum of the energy of two electrons is equal to the energy of the double beta transition and the width is determined only by detector resolution. The sensitivity of a $\beta\beta(0\nu)$ experiment is limited by the Poisson statistics in the region of interest (ROI). The one-sigma sensitivity in the presence of background B, for an experiment with isotope mass of M, and observation time t can be expressed as:

$$T^{0\nu}_{1/2} = \ln 2 \frac{\epsilon \alpha x N_A}{A} \sqrt{\frac{Mt}{\sigma_E B}} \text{ [36] [53]}, \tag{2.9}$$

where ϵ is the efficiency of the experiment at detecting the decay, α is the isotopic abundance of the target, N_A is Avogadro's number, x is the number of atoms per molecule that can undergo double beta decay, A is the molecular mass of the target, and σ_E is the energy resolution in the ROI. For $\beta\beta(0\nu)$ experiments, availability of enriched target material, decay detection efficiency, detector energy resolution, and amount of background are of paramount importance.

2.3 Status of the Field

There is an extensive worldwide program searching for $\beta\beta(0\nu)$ decay. It has been ongoing for about three decades and has produced many exciting results with various $\beta\beta(0\nu)$ isotopes. Table 2.1 represents the most sensitive results from currently running $\beta\beta(0\nu)$ decay experiments. The corresponding limits on the effective majorana mass are shown as well. The spread in the effective majorana mass limits is primarily due to the uncertainties in the nuclear matrix elements.

The best limits on the effective majorana mass have been obtained by experiments with very different approaches. So far, ^{76}Ge experiments have benefited from extremely good energy resolution and ^{136}Xe experiments have benefited from a large fiducial mass of isotope. Both types of experiments tried to achieve low background levels, the importance of which is illustrated in the $\beta\beta(0\nu)$ decay detection sensitivity plot (Figure 2.4). In the future, the most sensitive experiments should incorporate three components in their design: large mass of isotope, excellent energy resolution, and negligibly small background at the region of interest. As shown in Figure 2.4 even a few background events in the ROI can dramatically limit sensitivity of an experiment to the value of neutrino mass.

To date, the best limit on the effective majorana mass, if normalized to the mass of the target isotope, has been achieved by ^{76}Ge experiments. This reflects the fact that

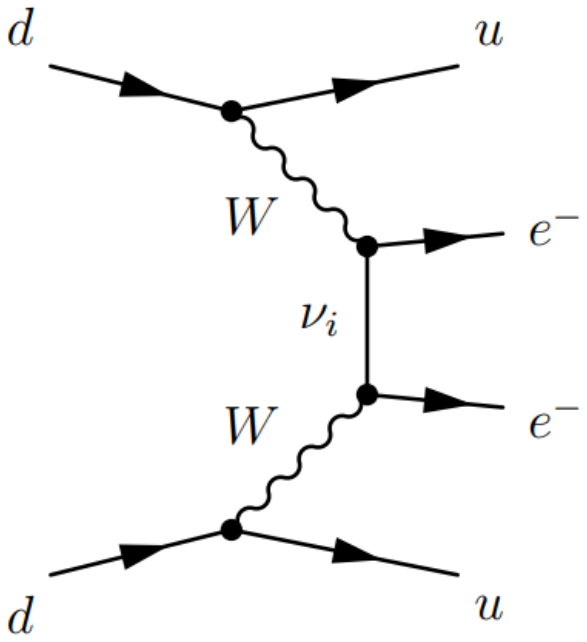

Figure 2.1: Feynman diagram of $\beta\beta(0\nu)$ decay through light neutrino exchange [25].

Table 2.1: The half life ($T^{0\nu}_{1/2}$) lower limit and effective majorana mass ($m_{\beta\beta}$) upper limit results from the most sensitive $\beta\beta(0\nu)$ decay experiments.

Isotope	$T^{0\nu}_{1/2}$ [years]	$m_{\beta\beta}$ [meV]	Experiment
^{137}Xe	$> 1.07 \cdot 10^{26}$	$< (61 - 165)$	KamLAND-ZEN [2018] [41]
^{137}Xe	$> 3.5 \cdot 10^{25}$	$< (93 - 286)$	EXO-200 [2019] [19]
^{76}Ge	$> 1.8 \cdot 10^{26}$	$< (79 - 180)$	GERDA [2020] [13]
^{76}Ge	$> 2.7 \cdot 10^{25}$	$< (200 - 433)$	MAJORANA [2019] [15]
^{130}Te	$> 1.5 \cdot 10^{25}$	$< (140 - 400)$	CUORE [2020] [28]

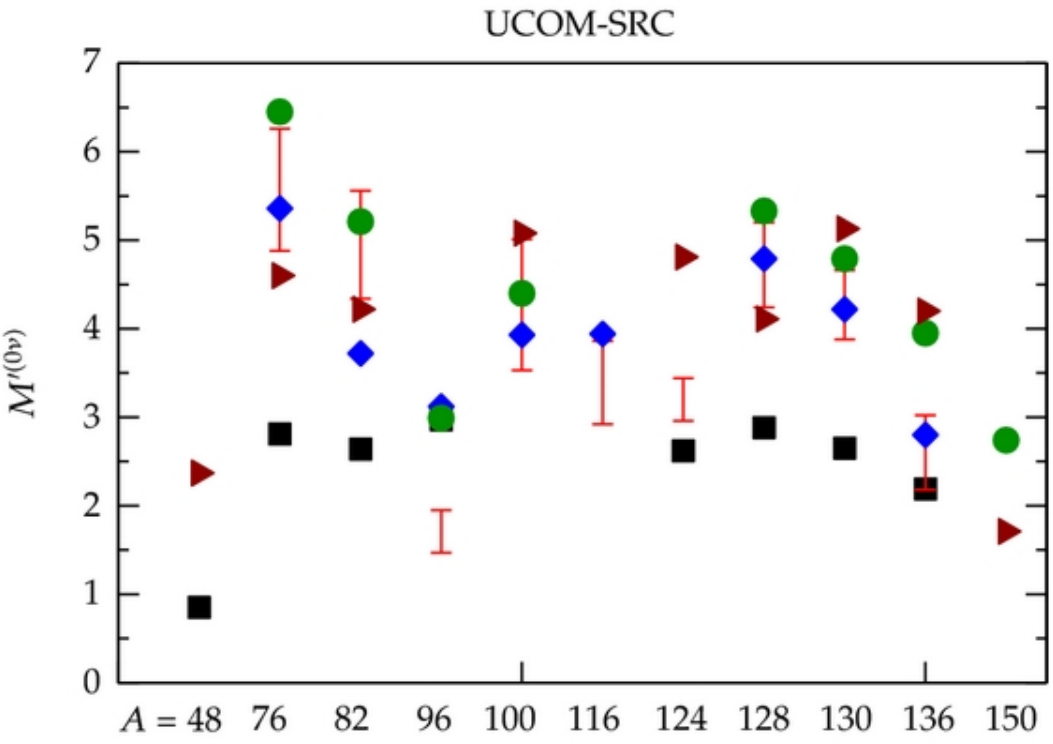

Figure 2.2: Comparison of nuclear matrix element evaluations for multiple $\beta\beta(0\nu)$ isotopes using various nuclear models [44].

the germanium detector technology has the best energy resolution of all other $\beta\beta(0\nu)$ materials. This fantastic energy resolution allows the experiment to focus on a narrow region of interest which is favorable when attempting to reduce backgrounds. First generation germanium $\beta\beta(0\nu)$ experiments: IGEX [1] and Heidelberg-Moscow [51] have a total isotope mass of a few kilograms and use "off the shelf" components for detector infrastructure and shielding. Therefore, we can expect future ^{76}Ge experiments to have a significant improvement in sensitivity with a larger amount of isotope and a dedicated approach to selecting low background components for detector infrastructure and shielding. There are two major germanium-based $\beta\beta(0\nu)$ experiments taking data now: the German led GERDA experiment [13] and the USA led MAJORANA DEMONSTRATOR [15]. Both experiments deployed $\sim 30-40$ kilograms of isotope mass, but they have very different approaches to shielding. GERDA is using naked germanium detectors submerged in cryogen to protect from ambient background. The MAJORANA DEMONSTRATOR is using a closely spaced array of germanium detectors inside a cryostat built out of low background copper. The MAJORANA cryostat is then surrounded by conventional solid shielding materials. Both experiments are in a friendly competition to achieve the lowest background and best energy resolution. They are presently on the path to combine their efforts into a single germanium-based $\beta\beta(0\nu)$ experiment: LEGEND-200 [8].

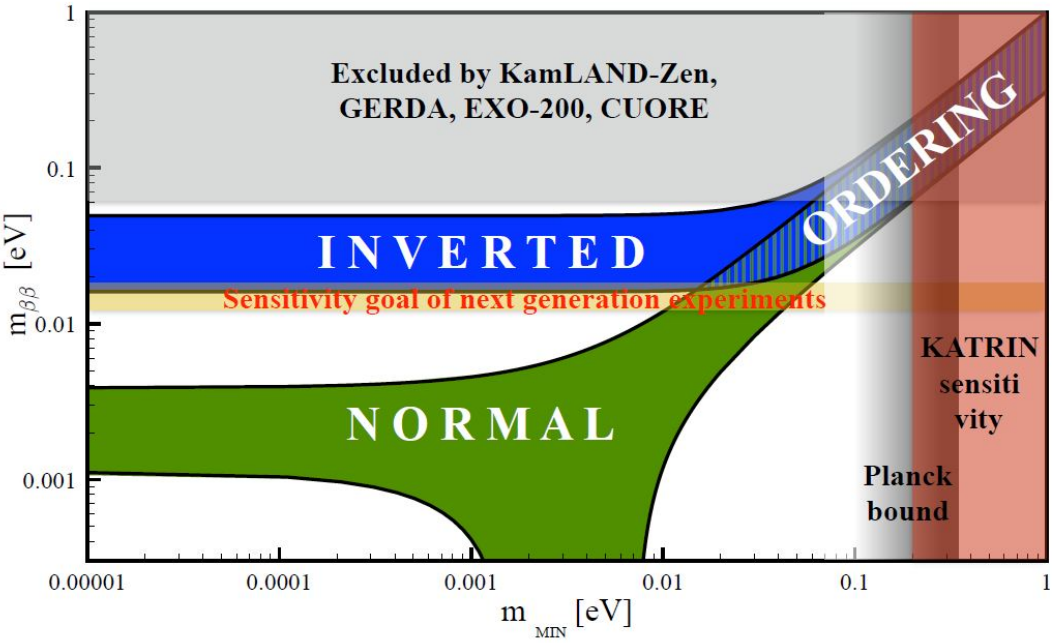

Figure 2.3: Correlation between lightest neutrino mass and the effective majorana mass measurable in $\beta\beta(0\nu)$ decay experiments, assuming SM extension of three sterile neutrinos [43].

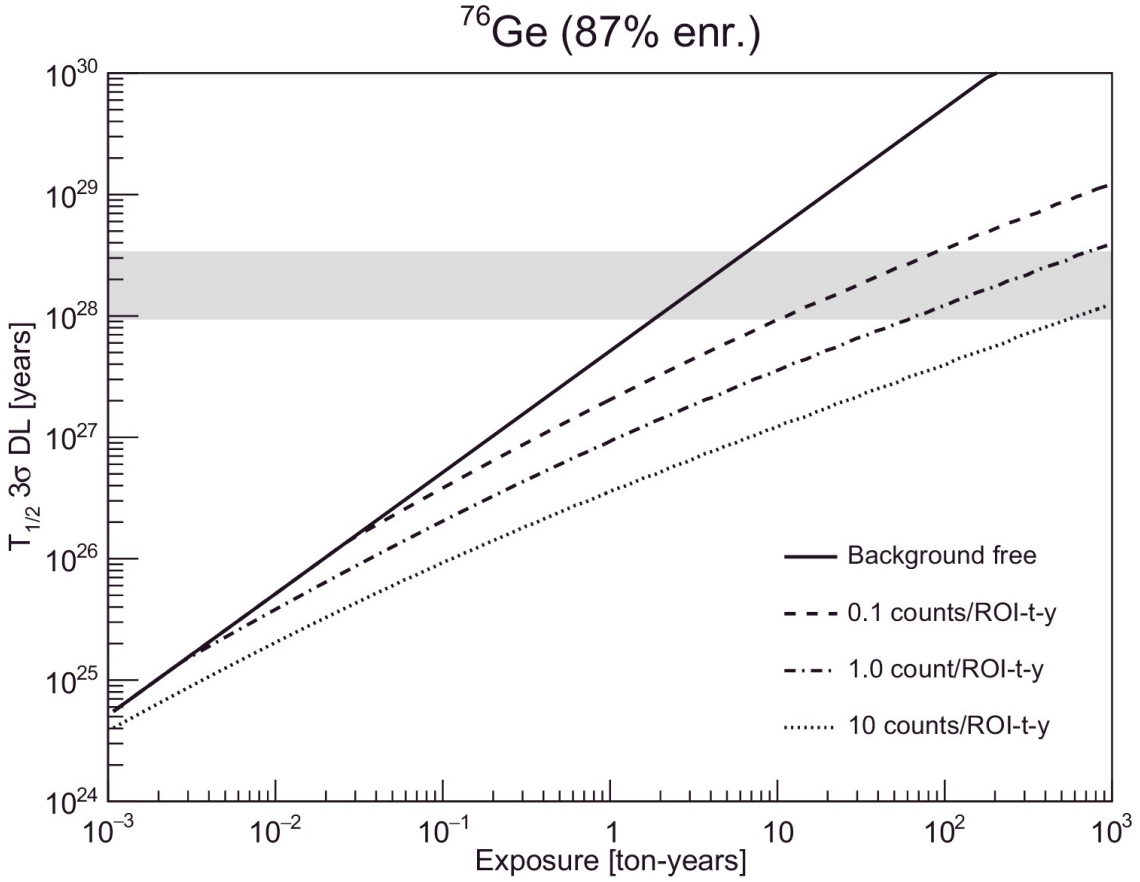

Figure 2.4: Sensitivity of ^{76}Ge $\beta\beta(0\nu)$ experiments in the presense of various amounts of backgrounds [47]. The gray area is a target sensitivity to cover the inverted ordering of the neutrino mass hierarchy.

Chapter 3

Majorana Demonstrator Overview

The Majorana Demonstrator is one of the world's most sensitive $\beta\beta(0\nu)$ decay experiments. The Demonstrator is an extremely low background array of natural and enriched germanium detectors which searches for the $\beta\beta(0\nu)$ decay of ^{76}Ge. The experiment is currently operating on the 4850' level of the Sanford Underground Research Facility (SURF) in Lead, SD. This location is a former gold mine which has been converted into one of the world's premier underground research facilities.

Figure 3.1 shows an illustration of the Demonstrator experiment.

The Majorana Demonstrator aims to achieve four specific goals [4] [42]:

1. Search for $\beta\beta(0\nu)$ decays in ^{76}Ge using state-of-the-art technologies.

2. Achieve an unprecedentedly low background rate at or below 2 c/(FWHM $\cdot$ tonne $\cdot$ y) in a 2.5 keV FWHM (full-width half-maximum) at the surrounding the 2039 Q-value for ^{76}Ge $\beta\beta(0\nu)$ decay.

3. Demonstrate the feasibility of scaling the technology to a tonne-scale germanium experiment.

4. Perform searches for physics beyond the Standard Model.

The first three goals recognize that measuring $\beta\beta(0\nu)$ decay is a meaningful objective. To date, numerous $\beta\beta(0\nu)$ experiments have predicted $\beta\beta(0\nu)$ lifetimes of greater than $10^{23} - 10^{25}$ years, using a variety of different isotopes. As the scientific community continues

to search for $\beta\beta(0\nu)$ decay, experiments continue to get larger and more expensive making the $\beta\beta(0\nu)$ detector isotope selection an extremely important decision. The first goal represents the collaboration's aim to produce a competitive $\beta\beta(0\nu)$ measurement and demonstrate the significant advantages ^{76}Ge detectors have over other isotopes in $\beta\beta(0\nu)$ searches. Additionally, the Heidelberg-Moscow $\beta\beta(0\nu)$ experiment found evidence of a $\beta\beta(0\nu)$ decay, predicting a half-life ($T^{0\nu}_{\beta\beta}$) of $1.5 \cdot 10^{25}$ years [51]. The DEMONSTRATOR currently predicts a lower limit on the half-life ($T^{0\nu}_{\beta\beta}$) of $2.7 \cdot 10^{25}$ years (90% CL), which does not support this claim [15].

The second goal was based on the sensitivity requirements of a tonne-scale ^{76}Ge $\beta\beta(0\nu)$ experiment. Tonne-scale ^{76}Ge $\beta\beta(0\nu)$ experiments aim to achieve a sensitivity to $\beta\beta(0\nu)$ half life greater than 10^{27} years and achieve a sensitivity to the effective Majorana mass that will fully encompass the inverted ordering neutrino mass predictions. A background level less than 2 c/(FWHM $\cdot$ tonne $\cdot$ y) in the DEMONSTRATOR would scale to a background level of less than 1 c/(FWHM $\cdot$ tonne $\cdot$ y) in such a tonne-scale experiment. The third goal considers the difficulty of producing a similar style ^{76}Ge $\beta\beta(0\nu)$ experiment on the tonne scale. These difficulties include demonstrating low background is achievable, demonstrating that fielding modular arrays of germanium detectors is viable and expandable, and demonstrating that data acquisition can be expanded to the tonne-scale. The DEMONSTRATOR has an advantage in that each individual germanium detector has a high $\beta\beta(0\nu)$ detection efficiency which does not diminish when additional detectors or modules are installed.

The fourth goal recognizes that the low-noise, high energy resolution germanium detectors fielded in the low background environment allows for additional campaigns to investigate physics processes outside of the Standard Model. These campaigns include studies of bosonic dark matter electric couplings, solar axion electric couplings, Pauli exclusion principle violating transitions, electron decay, fractionally charged lightly ionizing particles, and tri-nucleon decay [7] [16] [18]. These "Beyond Standard Model" analyses are outside the scope of this work.

3.1 Detector Design

3.1.1 Modules

The germanium detectors are separated into two modules. Each module contains seven strings of detectors with each string holding $3-5$ detectors. The seven strings are then secured in a cryostat. Each cryostat is custom built out of electroformed copper that has been formed and machined underground. Electroforming copper and machining it underground reduces the amount of cosmogenically induced radioactivity in the copper components, primarily the cryostats and the string hardware components.

Figure 3.2 shows the cryostat and strings of one module. This cryostat, complete with thermosyphon and liquid nitrogen dewar, constitutes one module. Each module acts independently of the other. The modular design of the cryostats can be easily expanded to the tonne scale. The modules, once inserted, will be enclosed by several layers of shielding.

3.1.2 Shielding

The Demonstrator uses several types of shielding to reduce the amount of background in the detector arrays [4]. The Demonstrator operates deep underground with approximately 4850' of rock directly overhead. The rock greatly reduces the amount of cosmic rays which reach the detectors. The remaining shield layers completely encompass the sensitive parts of the experiment, creating a cube of shielding with the detector modules in the center. The outermost layer of the Demonstrator shield is 12" of passive polyethylene, two inches of which is borated, that is designed to stop ambient neutrons in the lab. Next is an active muon veto system made out of scintillating plastic. The veto system is the topic of Chapter 4. The layers of shielding encompassed by the veto system are inside a radon enclosure that is constantly being purged with nitrogen gas. The thickest layer of shielding comes next in the form of lead bricks. The last two layers of shield are comprised of copper sheets. The copper sheets have very low radioactivity which means that this layer of shielding will release very few photons, and therefore contribute little to the background. These copper layers are made from ultra-pure electroformed copper. The copper was electroformed and machined

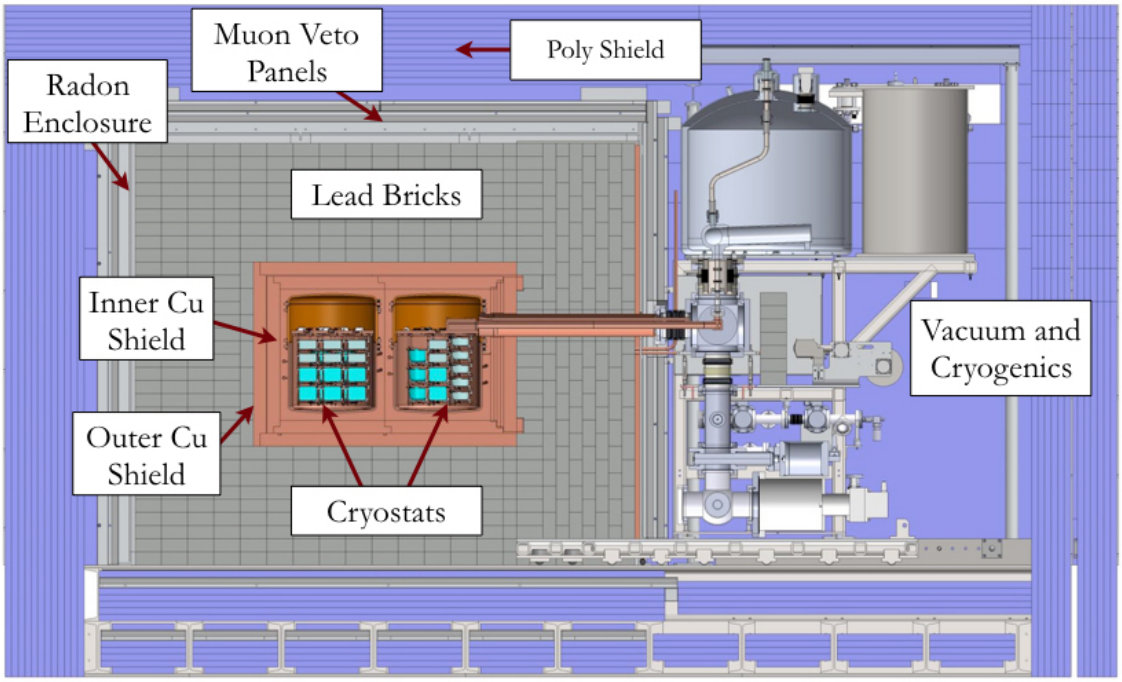

Figure 3.1: Illustration of the cross section of the MAJORANA DEMONSTRATOR.

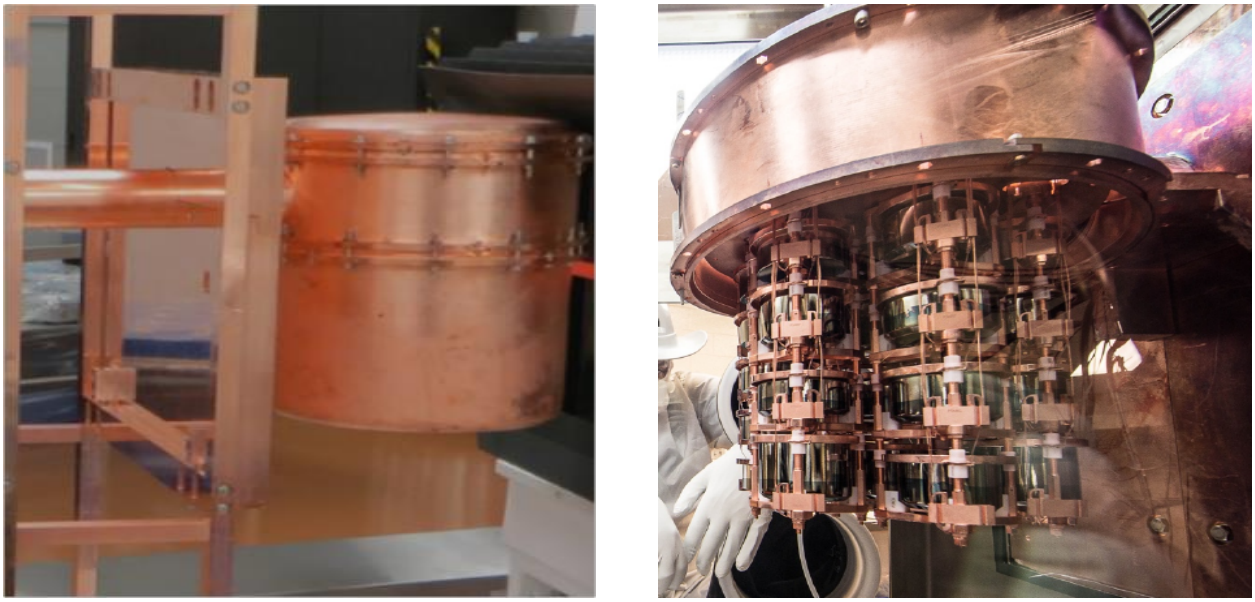

Figure 3.2: Cryostat of one module during insertion into the shield (left) and during detector string installation (right).

on the 4850' level of the Sanford Underground Research Facility and has not returned to the surface after being processed.

The detector modules fit into the center of these shielding layers. The shield was designed to accomodate the removal or insertion of the individual detector modules with minimal impact on the shield configuration.

3.1.3 Detector Technology

The DEMONSTRATOR is using 44 kg of P-Type Point Contact (PPC) cylindrical germanium detectors. 29 kg of detectors are built out of 87 percent isotropically enriched ^{76}Ge and the remaining 15 kg are built out of natural germanium. On each crystal there is a small area implanted with boron, this spot is the p+ point contact. The rest of the surface is passivated and acts as the n+ contact. An electric field is applied across the detector (n+ contact held at positive bias voltage) in order to collect the electron-hole pairs produce in the crystal by charged particles.

Figure 3.3 shows a photograph of a PPC germanium crystal used in the DEMONSTRATOR. There are several advantages to choosing this element and this detector technology. Enriched ^{76}Ge crystals can act as both source and detector of $\beta\beta(0\nu)$ decays, and are commercially available. The PPC germanium detectors have fantastic energy resolution compared to other $\beta\beta(0\nu)$ detector technologies. The MAJORANA collaboration achieved the best energy resolution, at the $Q_{\beta\beta}$ value, of all $\beta\beta(0\nu)$ experiments [15]. Energy resolution determines how well the detector can distinguish the $\beta\beta(0\nu)$ signal (a 2039 keV energy deposition) from background events with similar, but not equal energies. Energy resolution was measured to be 2.53 ± 0.08 keV at the ^{76}Ge $Q_{\beta\beta}$ value of 2039 keV. PPC detectors have small signal contacts which results in low electronics noise. Also the PPC geometry creates a weighting potential across each detector. This weighting potential is strong near the point contact and a relatively low elsewhere in the detector. When energy is deposited in a detector crystal, the weighting potential will force the charge to move towards the point contact. The time it takes the charge to move to the point contact is called the charge drift time. For single-site events, the energy deposited in the detector crystal during an event will occur in only one point-like location. For multi-site events, a charge is deposited at multiple locations within the

detector. It is very likely that the multi-site depositions will have different charge drift times, and the charges will reach the point contact at slightly different times. This leads multi-site events to produce a signal with a current pulse that is degraded in amplitude with respect to the current pulse of a single-site event of the same energy. By utilizing pulse shape analysis techniques these multi-site events (γ-induced background events) can be distinguished from single-site events ($\beta\beta(0\nu)$ events) and removed from the $\beta\beta(0\nu)$ analysis.

3.2 Background

Understanding and minimizing background sources is a vital part of rare event experiments. The MAJORANA collaboration identified five categories of background events. The categories are:

1. Backgrounds as a result of the natural radioactivity of the materials.
2. Backgrounds as a result of cosmogenic activation of the germanium detectors.
3. In situ muon-induced backgrounds.
4. External, environmental background sources.
5. Neutrino-induced backgrounds.

These categories will be the topic in this section.

Figure 3.4 shows the MAJORANA DEMONSTRATOR background estimate based on extensive assay and simulation programs conducted by the MAJORANA Collaboration.

The natural radioactivity is the largest contributing category in the background model, and was a driving factor during the material selection and shielding design of the experiment. The most efficient way of reducing these background events is to only use materials with very low natural radioactivity. The collaboration conducted a large assay campaign to measure the radioactivity of each material used in the experiment [5]. Once the design was finalized, the collaboration constructed a lab space on the 4850' level of SURF to purify copper for use in the experiment. In this lab, commercial copper was dissolved and reformed through

a process called electroforming to remove radio-chemical impurities. This ultra-clean radio-pure copper was used create the components nearest to the detectors, such as the cryostats and detector unit frames.

Another source of background are cosmogenic particles which interact with the detectors. These cosmogenic particles, such as muons, can interact with the detector and create radioactive isotopes. These background events are split into two different types: (1) long-lived radioactive isotopes induced by cosmogenic particles, referred to as "cosmogenic activation", and (2) short-lived radioactive isotopes induced by cosmogenic particles, referred to as "in situ muon-induced backgrounds". The physics involved with both type of cosmogenically-induced background are similar, however from a background mitigation perspective it is easier to treat each type separately.

First the background due to cosmogenic activation of detectors on the surface will be addressed. While the detectors were on the surface for fabrication or transportation, long-lived and short-lived radionuclides were produce in the crystals. This is due to the high cosmogenic flux and low efficiency cosmogenic shielding. After fabrication and testing, the detectors were transported underground as soon as possible to mitigate any further cosmogenic activation. Once underground the detectors were stored in additional shielding while the collaboration continued preparing for the construction of the DEMONSTRATOR. There is no way to remove radioactive isotopes from a detector once the isotope is created, it can only decay naturally. The short-lived radionuclides will quickly decay away (in a matter of weeks at most), and will generally be gone before the detectors begin taking data. Therefore the short-lived radionuclides produced on the surface will not produce many, if any, background signals in the data. The long-lived radionuclides produced on the surface will remain in the detectors. These long-lived nuclides remain in the detectors for a matter of months or years, decaying away randomly. The collaboration does not have the luxury of waiting until these long-lived nuclides can fully decay, so the detectors are installed and these radioactive isotopes produce background signals at random times. The collaboration, cognizant of these long-lived isotopes, reduced the amount of cosmogenic activation in the detectors by choosing ground transportation over air transportation when applicable, and minimizing the time detectors spent above ground. The collaboration carefully tracked the

time spent above ground for each detector. These tracking logs allow an accurate estimate of the cosmogenic activation background contribution.

Next the in situ muon-induced backgrounds will be addressed. The cosmogenic activation previously discussed will continue to occur even after the detectors are stored underground. However, the cosmogenic flux in the lab is considerably smaller than on the surface, with muons being the only cosmogenic particle able to penetrate through the rock into the lab space. At the surface of SURF, the muon flux was measured to be $(1.149 \pm 0.017) \cdot 10^{-2} \mu/\mathrm{s/cm^2/sr}$ [45]. At the 4850 foot level of SURF, the muon flux was measured to be $(5.31 \pm 0.17) \cdot 10^{-9} \mu/\mathrm{s/cm^2}$ [6]. For that reason, the cosmogenic activation backgrounds produced while the detectors are underground are called muon-induced backgrounds. Specifically, the in situ muon-induced backgrounds refer to cosmogenic activation background events that occur while the detectors are taking data. The cosmogenic activation will again create long-lived and short-lived radioactive isotopes in the detectors. The long-lived radionuclides will decay over a period of months or years, however as the rate of cosmogenic activation is low, relatively few long-lived radionuclides are produced when compared with the surface cosmogenic activation. Furthermore, as the DEMONSTRATOR will only be taking data for ~ 10 years, these in situ long-lived radionuclides are expected to have a very small contribution to the background. Instead the short-lived radionuclides are expected to have a non-negligible contribution to the background. When a short-lived radionuclide is produced, it begins to decay over a period of seconds, days, or weeks. It is reasonable to assume that after many half-lives have passed, the detectors will still be taking data. The short-lived radionuclides will continuously be created and decay away, with each decay contributing to the background. In order to mitigate this background contribution, the collaboration included an active muon veto system in the experiment. The active muon veto system is used to identify when a cosmogenic muon passes through the experiment. With this capability, the collaboration developed an analysis cut, the muVeto cut, to remove the majority of background signals produced by the muon-induced short-lived radionuclides. From simulations, the collaboration determined that the majority ($> 90\%$) of these muon-induced background signals occur within one second of a muon event. The collaboration

then uses simulations to estimate the remaining contribution to the background. These in situ muon-induced background events are the primary study of this thesis work.

The lab environment also contains sources of background. Specifically, radon and photons in the lab space, or (α,n) interactions in the surrounding rock can produce backgrounds in the detectors. Portions of the DEMONSTRATOR shield, such as the radon enclosure purged with nitrogen, was designed with these background sources in mind.

Solar and atmospheric neutrinos can also be a source of background. However neutrinos have very small interaction cross sections with matter. They can easily pass through the rock into the lab space and create a background signal. By the same token, the probability of a neutrino inducing a background signal is small and can be estimated.

3.3 Analysis Cuts

After the data acquisition system (DAQ) records the raw data from the detectors, the detector output is combined into a data event which contains all detector signals within a four μs coincidence time window. Various analysis cuts are then applied to the MAJORANA data events in an effort to reduce $\beta\beta(0\nu)$ background events.

The two primary analysis cuts used in this work are the 1-second muVeto cut and the Granularity cut. The muVeto cut was developed to remove $\beta\beta(0\nu)$ background events induced by cosmogenic muons. This is achieved by rejecting all detector events which occur up to one second after a muon veto event. The collaboration determined, using simulations, that a threshold value of one second was optimal to reject muon-induced background events while minimizing loss of exposure. The muon event tagging process is described in Chapter 4. The muVeto cut threshold of one second is supported by the simulation results discussed in Chapter 8.

The Granularity cut, rejects all events with detector granularity/multiplicity greater than 1. The PPC germanium crystals double as both a detector and a source of $\beta\beta(0\nu)$ signals. As mentioned previously, a $\beta\beta(0\nu)$ signal will appear as a single-site event in the detector. A consequence of this is that a single $\beta\beta(0\nu)$ decay cannot appear in more than detector. Given that the $\beta\beta(0\nu)$ decay is an incredible rare interaction, if it occurs in nature at all, it

is unlikely that two $\beta\beta(0\nu)$ decays would occur in two different detectors within a few μs. In order to reduce the risk of identifying a false positive $\beta\beta(0\nu)$ signal, any data event which contains a signal in more than one detector (detector granularity greater than 1) is rejected. This Granularity cut makes it simple to differentiate potential $\beta\beta(0\nu)$ candidates from other physics events.

Other analysis cuts used in the $\beta\beta(0\nu)$ analysis include:

LNFill cut: Approximately every 36 hours the liquid nitrogen dewars of the modules are automatically refilled. During this time, $\sim$ 30 minutes, the fill process can create microphonic noise in the module that is being filled. Therefore all detector events in this time period are discarded. The liquid nitrogen fills in Module 1 and Module 2 do not occur at the same time, instead the fill times are tracked separately for each module.

AvsE cut: A pulse shape analysis cut that was developed to reject multi-site events in a detector. By comparing the maximum amplitude of the current pulse (A) with the energy (E), multi-site events can be differentiated from single-site events and rejected. This cut was tuned using ^{208}Tl in the thorium decay chain. The ^{208}Tl can create both a single-site event and a multi-site event. When the 2614.5 keV gamma from ^{208}Tl interacts with a nucleus of the detector, an electron positron pair can be created. When this happens it can be that the annihilation photons from the electron positron pair both escape leaving a peak (Double Escape Peak/DEP) with energy degraded by exactly two times the electron mass, E_{DEP} = 1592.5 keV. These double escape peak events are single-site events, like $\beta\beta(0\nu)$ events. If only one annihilation photon escapes, a peak (Single Escape Peak/SEP) with energy degraded by one electron mass will be seen, E_{SEP} = 2103.5 keV. The AvsE cut was tuned to accept 90% of ^{208}Tl single-site events and 10% of ^{208}Tl multi-site events to match Monte Carlo simulations [15].

Delayed Charge Recovery (DCR) cut: The Delayed Charge Recovery (DCR) analysis cut was developed to identify and reject events along the passivated surface, which

in turn would remove the majority of the α particles events which contribute to the $\beta\beta(0\nu)$ background [15].

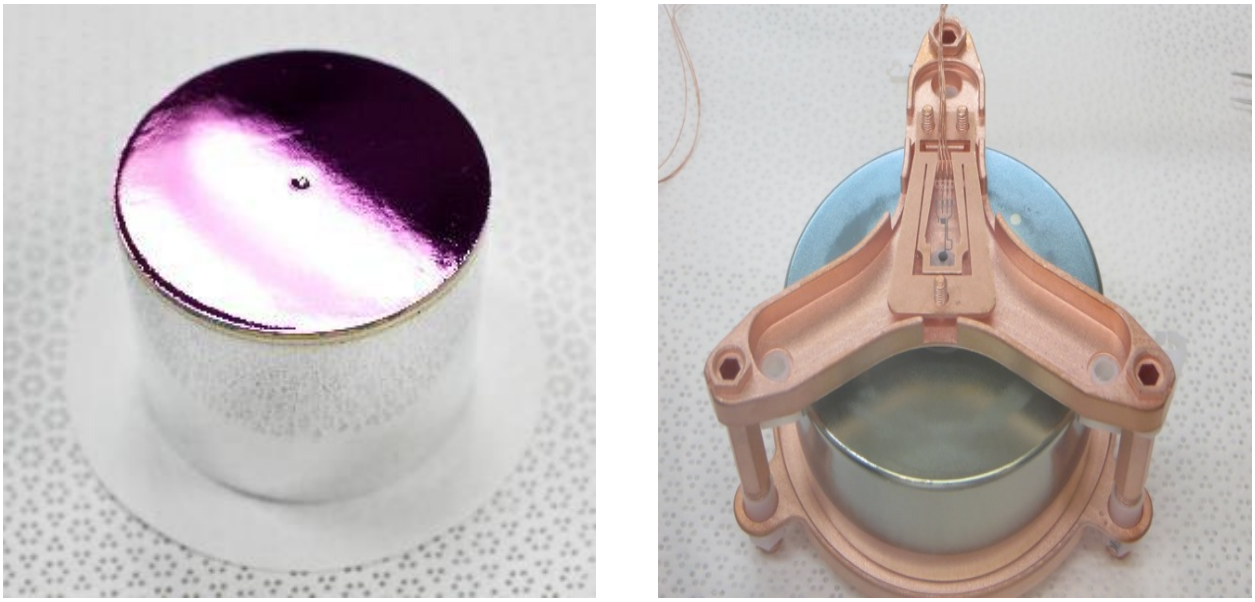

Figure 3.3: Image of a MAJORANA high purity germanium PPC crystal (left) and a MAJORANA detector unit with attached electronics front end board (right).

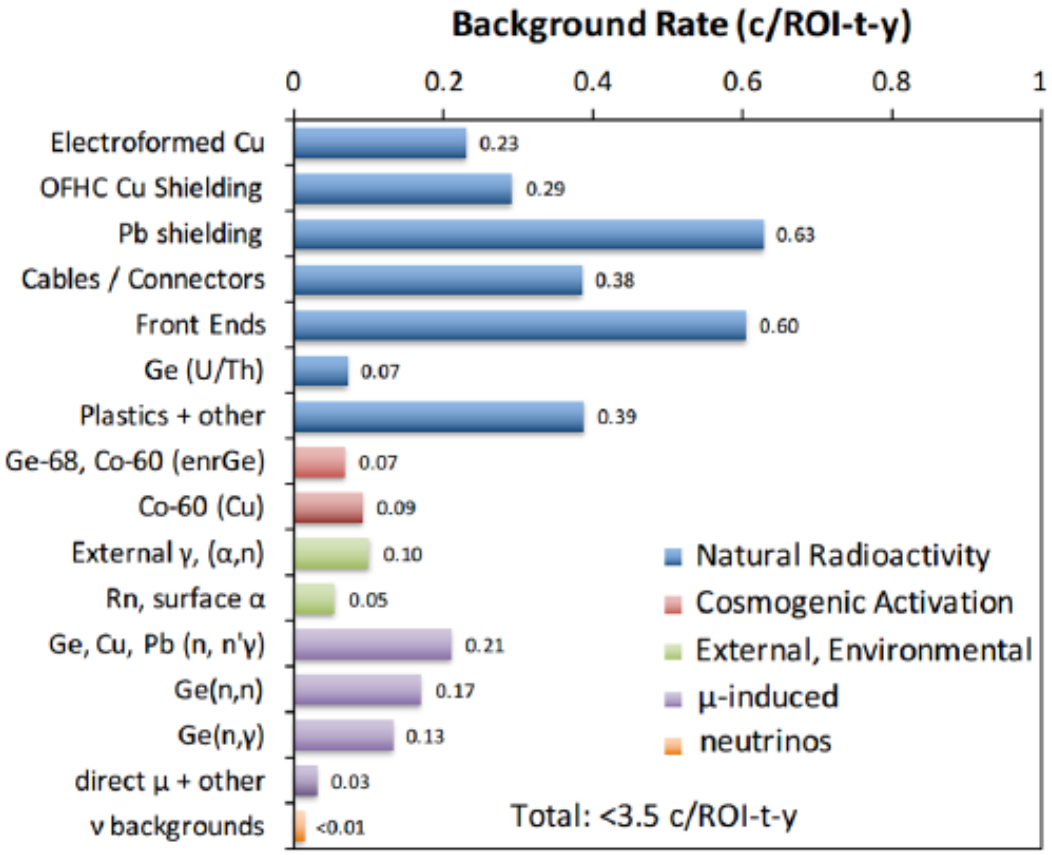

Figure 3.4: MAJORANA DEMONSTRATOR Background estimate, from background model [33].

Chapter 4

Majorana Veto System

The active muon veto system is designed to identify muons as they pass near the Majorana detectors. This information will then be used to remove detector events that are likely caused by these cosmic muons and would appear as a background to the $\beta\beta(0\nu)$ search.

4.1 Physical Design

The veto system is a segmented 32-panel array that closely surrounds the lead shield and radon enclosure of the Majorana Demonstrator creating a rectangular prism with area 37 square meters [6]. Figure 4.1 shows the veto panels after installation. The prism consists of four panels on the north, south, east, west, and top faces with 12 panels on the bottom face. These panels create two layers of scintillating plastic. The dual layer nature of the veto system can be used to extract directional information about the muons that pass through. The segmented nature of the system also makes removal of panels simple, so that detector modules can be inserted or removed with minimal impact to the muon detection efficiency as the other veto panels can continue operating.

Each panel is a 1" thick EJ-204B scintillator sheet that is completely encapsulated by aluminum cladding. Wavelength shifting fibers are embedded in the scintillator and connect to an attached 1.27 centimeter photomultiplier tube (PMT). This allows the light from each panel to be read out individually. Additionally each panel has an embedded LED which is

used to test individual panel performance. Figure 4.2 shows a veto panel without aluminum cladding.

The MAJORANA active veto system was designed, fabricated, and tested at the Univeristy of Tennessee Knoxville.

4.2 Hardware Trigger and Electronics

The veto system data acquisition system (DAQ) implements both Versa Module Europa (VME) and Nuclear Instrument Module (NIM) electronic modules. Figure 4.3 depicts the layout of the veto electronics system. Raw signals from the PMT's are split into two paths at amplifiers. One path goes to a Charge-to-Digital Converter (QDC) for digitization. The other path goes through logic units to determine if a given event will "trigger" the system and be recorded to a data file. If an event is triggered, then all 32 panel QDC values are read out simultaneously, assigned a timestamp from the scaler card, and recorded in a data file. Two sets of logic have been used to determine whether a veto event is recorded. Prior to the MAJORANA Data Set 1 (DS1), the criteria was "At least one panel in each discriminator bank has a signal amplitude above the hardware trigger threshold." This condition is highly efficient for through going muons and was employed in the MAJORANA muon flux measurement [6]. Since DS1, the criteria has been "Any two panels have signal amplitudes above the hardware trigger threshold." This condition is still highly efficient for through going muons and is also more sensitive to rare trajectories. The hardware trigger threshold was determined separately for each panel after fabrication. Over the lifetime of the MAJORANA DEMONSTRATOR the veto system has been used in various configurations, including a period of time when a QDC channel was broken and could not be used. Table 4.1 shows the history of the veto system since DS0.

4.3 Veto Panel Signals

The energy information from the PMT's is recorded by the two QDC cards with 16 channels each. A channel will read out a nonzero value, called the QDC pedestal, when the channel

Figure 4.1: Veto Panels in place on MJD

Figure 4.2: Fabricated veto panel without aluminum cladding.

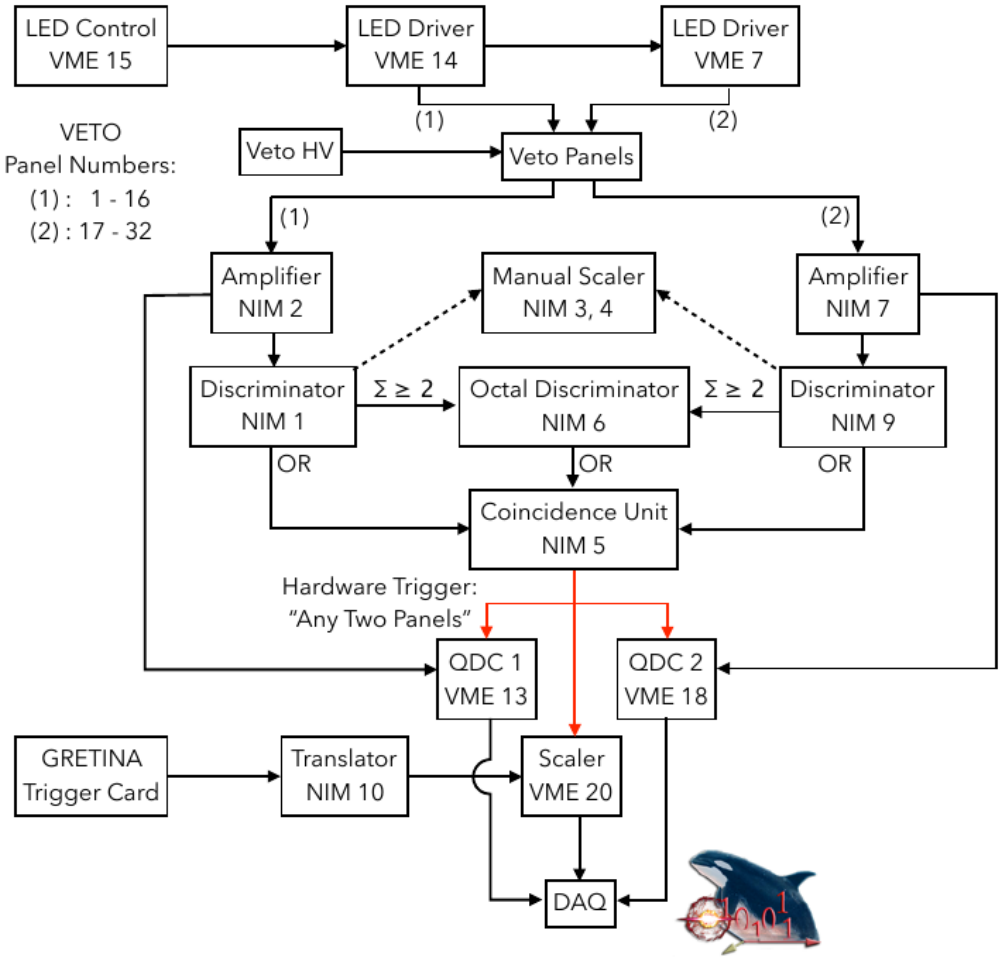

Figure 4.3: Block diagram of the veto electronics system to the data acquisition system (DAQ) controlled by ORCA application.

received no meaningful input, i.e. events in other panels triggered the readout of the system. These pedestals can fluctuate due to changes in the veto system and need to be routinely checked. There are multiple features visible in the raw QDC spectra as shown in Figure 4.4. The QDC pedestal appears as a large spike near the lowest bin, followed by a low energy tail from environmental gammas. At higher energies are the muon peak and the gaussian LED peak. The muon peak is generally obscured by LED signals until they are identified and isolated. This procedure will be described later.

All pedestal signals must be removed in order to properly analyze the veto signals. This is accomplished by selecting a veto panel software trigger threshold (SW threshold). The numerical value of these thresholds is the panel pedestal QDC value plus 35. These veto SW thresholds are calculated for each panel automatically during data processing. With the SW thresholds in hand, any veto panel signal with QDC value greater than the panel SW threshold is considered to be a true scintillation signal. The true scintillation signals are utilized to identify muon-induced scintillations in the veto panels. They are further used in this work to identify and analyze muon-induced detector events. Another useful quantity is the panel multiplicity of each veto event. The veto multiplicity is a count of how many panels register a signal above the SW threshold in a given event.

4.4 LED Signals and Tagging

Included in the veto electronics are a dual timer card and two 16 channel input/output register cards. These three cards are used in combination to pulse all 32 embedded LEDs simultaneously at a frequency designated by the collaboration. These LED signals will be used to perform several run-level error checks of the veto system, these error checks are described in detail in Chapter 5. In order to perform these checks, the veto events must be separated into two categories:

1. Events caused by embedded LEDs inducing scintillation (LED events).

2. Events caused by external particles inducing scintillation (physics events).

Table 4.1:
Veto configurations used during data taking at SURF. The south and east panels are removed when performing upgrades in or near the detector modules, e.g. installation of detector Module 2 or installation of the inner copper shield.

Start Date	Start Run #	Data Set	# of panels	Description
July 10, 2015	3057	DS0	31	1 Broken QDC Channel (1BC)
Oct. 13, 2015	∼8229	DS0	27	No South Panels & 1BC
Oct. 22, 2015	∼8419	DS0	23	No South or East Panels & 1BC
Jan. 22, 2016	9846	DS1	31	1BC
July 22, 2016	∼15892	DS1	27	No East Panels & 1BC
Aug. 9, 2016	16313	DS3	31	1BC
Feb. 21, 2017	∼23240	DS5ab	32	All 32 Panels
Dec. 10, 2019	∼58005	DS7	28	No East Panels
Dec. 12, 2019	58066	DS7	32	All 32 Panels
Feb. 26, 2020	∼61117	DS7	28	No South Panels
March 5, 2020	61166	DS7	32	All 32 Panels
Aug. 24, 2020	66674	DS7	28	No East Panels
Aug. 27, 2020	66786	DS7	24	No South or East Panels
Aug. 28, 2020	66811	DS7	32	All 32 Panels

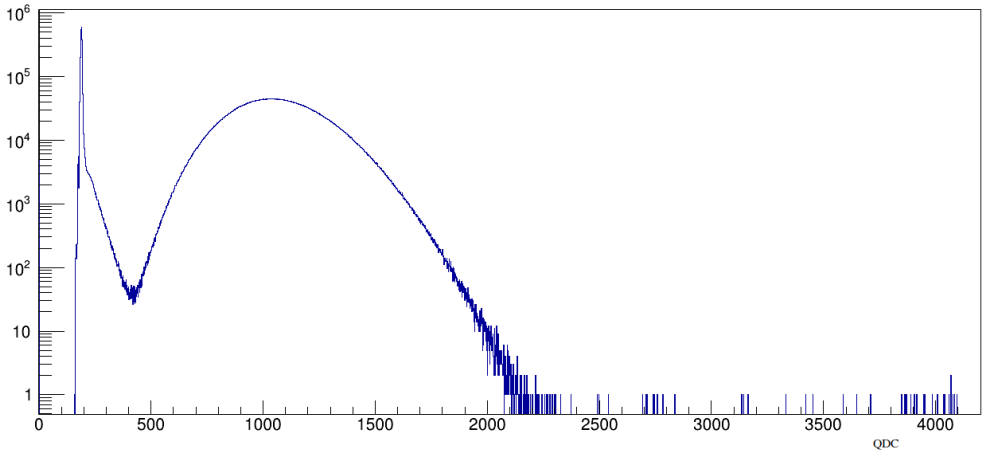

Figure 4.4: Raw QDC spectra of panel 10, one of the bottom panels. Taken from 180.7 days of data. Shown clearly in the spectra are the low energy pedestal, the low energy tail from gammas, and the high energy LED peak. The muon events are obscured by the LED peak.

Since all 32 LEDs are pulsed simultaneously, categorizing the veto events is simple. During data processing, any veto event that fulfills the criteria "veto panel multiplicity greater than LED threshold" is tagged as an LED event. In reality, this criteria is slightly more complicated than described. Since the veto system sometimes operates in a configuration without all 32 panels operating, a variable LED threshold is used. To determine the LED threshold of a particular run, the number of operating veto panels is counted. The LED threshold is then defined as "the number of operating panels minus 5". If less than 10 panels are operating then no events will be tagged as LEDs, also several errors would be thrown. This scenario is unlikely and would indicate a problem with the veto system. The LED pulses are incredibly stable (see Figure 4.5), which allows them to be used to quantify the performance of the veto system as a whole, as well as help identify other potential data errors.

4.5 Muon Tagging

The most important function of the veto system is to tag muon events. Based on previous muon simulations, the collaboration selected a muon veto cut (muVeto cut) of 1 second. This cut is used to identify detector events that fall within 1 second of a muon-tagged veto event, and remove them from further analysis. In order to apply this cut, the veto physics events caused by muons are separated from veto physics events caused by other particles (e.g. photons). Cosmogenic muons that penetrate to the veto system will generally be of higher energy than photons produced near the veto system. This energy difference manifests as a difference in the energy depositions in the panels (i.e. QDC spectra) with muons depositing more energy than photons. Criteria for identifying muon events also utilizes their characteristic large energy deposition. For each panel a high-energy muon threshold is selected based on the QDC spectra. This threshold falls inbetween the QDC photon peak and QDC muon peak, maximizing the amount of photons cut while minimizing the amount of muons cut by the threshold. These thresholds are stable and remain appropriate unless a change in the veto electronics occurs (e.g. QDC card is replaced). A similar muon threshold selection process was tested in a surface lab with great results [27]. This procedure has been

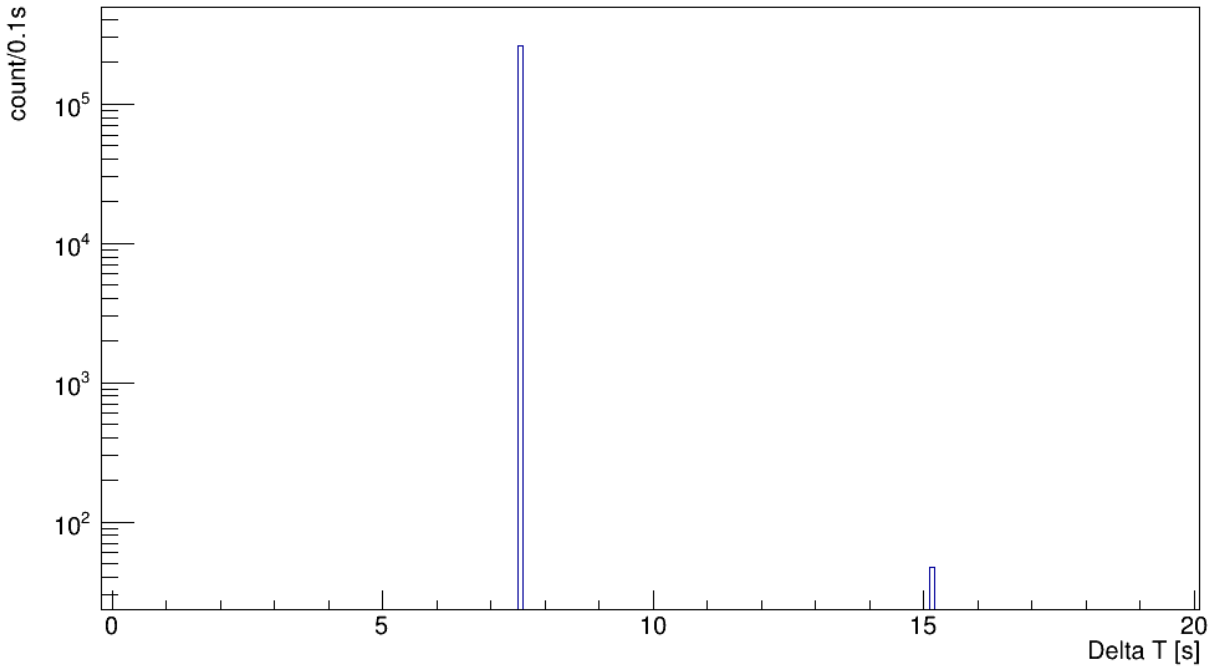

Figure 4.5: Delta T between LED tagged events in Data Set 3. LED period expected to be $\sim$7.55 seconds.

repeated in a surface lab for all veto panels to verify the value of the muon threshold. Figure 4.6 shows the results of a muon tag with a low energy muon threshold and a high energy muon threshold.

Muons are expected to pass through the DEMONSTRATOR with very little deflection. Therefore, with two layers of panels on each side, a passing muon should deposit energy in at least two panels. Any veto event that fulfills the following two criteria is tagged as a muon event:

1. Not an LED event.

   Each panel has an embedded LED which we pulse regularly to check if the panel/PMT is operating properly. We identify these events as "non-physics" by the fact that all 32 LEDs should generate light at the same time. We use a "veto panel multiplicity greater than or equal to the maximum panel multiplicity minus 5" to identify and ignore veto LED events. When all 32 veto panels are installed and operating the maximum possible multiplicity is 32, events recognized as 'non-LED events' have less than 27 veto multiplicity, and events recognized as 'LEDs events' have at least 27 veto multiplicity. The primary configuration of the veto system includes all 32 panels operating. At various points throughout the experiment other veto system configurations, with less than 32 panels operating, have been used (See Chapter 8).

2. At least two panels record QDC value greater than the high-energy muon threshold.

   Muons tend to deposit more energy in our panels than gammas. We leverage this information, along with the configuration of our panels to confidently distinguish muon events from gamma events by defining a high energy muon threshold for each panel [27]. Given that the veto configuration consists of 32 panels in a cube shape, with two panels per layer, a penetrating particle like a muon is expected to pass through approximately four panels. The conservative criteria "At least two panels receive high energy deposits (QDC above muon threshold)" is used to identify muon events and ignore gamma events.

In Chapter 8, the efficiency of this muon tag criteria is investigated using a MAGE simulation [26], and the 1-second muVeto cut is verified to be appropriate and effective.

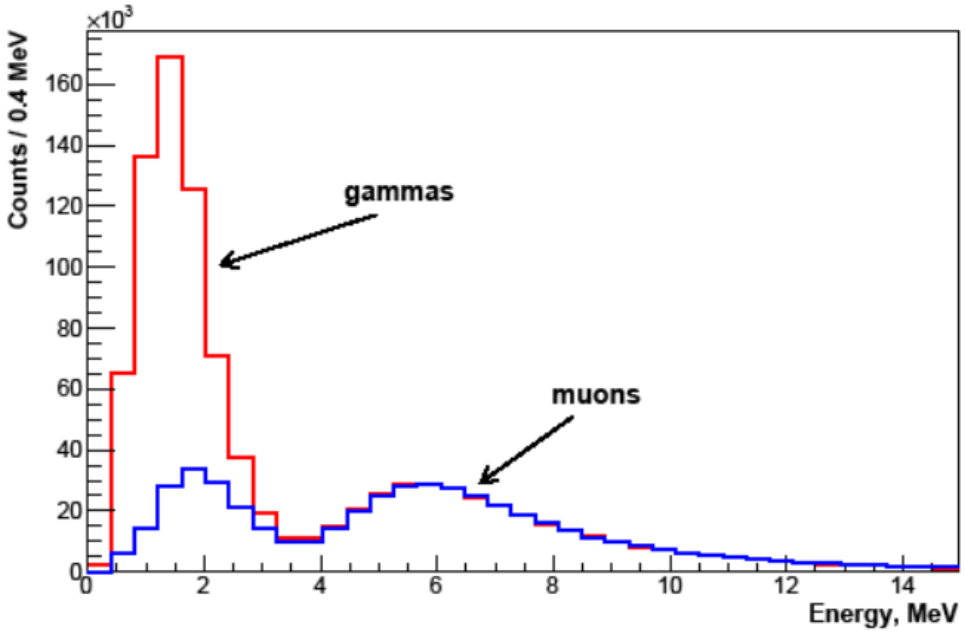

Figure 4.6: Self-triggering spectra of veto panel. Red spectrum represents events that exceed "low energy muon threshold". Blue spectrum represents events that exceed "high energy muon threshold". Some gamma events remain in the blue spectrum due to random coincidence. Figure from [27].

Chapter 5

Veto Performance

As as active system, the MAJORANA muon veto system must be operating and functioning properly to be of any use. A software application, called auto-veto, was developed by myself and a collaborator in order to test for a variety of veto system and veto data errors. The auto-veto program performs a few different veto related tasks:

1. Perform LED event tagging.
2. Perform muon event tagging.
3. Organize veto data into a data structure for separate recording.
4. Perform error checks, and report the system status to the collaboration.

These tasks contribute to all MAJORANA data analyses, either by contributing to the MAJORANA data cleaning and run selection processes, contributing to the muVeto analysis cut, or through identifying muon-induced detector events for analysis as in this work. These tasks are performed as part of the standard data processing suite for each run. This chapter will focus primarily on task 4, the error checks. The LED event tagging and muon event tagging procedures are discussed in Chapter 4.

5.1 Error Checks

The MAJORANA veto system has been built and reliably operating 24/7 for eight years, without external interference. Therefore, extensive strategies have been developed to monitor all parameters of the system. These strategies have been implemented via the "Error Check" portion of the auto-veto software application. This portion of auto-veto is used to scrutinize all data coming from the veto system. Currently, there are 27 implemented error checks. There are two types of veto errors: errors in the raw data and errors indicating the system is underperforming. Tables 5.1, 5.2, 5.3, and 5.4 describe the error checks that are currently implemented. These errors are separated into one of three categories:

1. Actionable: Impacts veto system efficiency. Requires action from collaborator to fix.

2. Minor: Can potentially impact veto system efficiency. Either can be fixed automatically with analysis techniques or cannot be fixed by any means. Requires no action from collaborator.

3. Diagnostic: Does not impact veto system efficiency. Used by veto experts to diagnose error causes. Requires no action from collaborator.

Three examples will be discussed to illustrate the purpose of these categories.
Example 1 Actionable: "LED frequency very low/high, corrupted, or LED's off". The panels see fewer LEDs than expected, potentially zero. This requires veto experts to check the LED peaks in QDC spectra, and potentially have an onsite collaborator investigate the electronic LED control cards (Dual Timer card/16 channel I/O Register cards).
Example 2 Minor: "Bad Timestamp: FFFF FFFF FFFF FFFF". The corruption of a scaler timestamp makes it impossible to properly apply the muon cut, as the timestamp of the muon is unknown. However, auto-veto will recognize that the timestamp is corrupted and estimate the true value using either the SBC timestamp or the nearest detector event timestamps. An error has occurred, but the timestamp of the veto event has been recovered.
Example 3 Diagnostic: "Unknown Card is Present". This error would be thrown if the DAQ software fails to recognize one of the cards (scaler card or QDC card) and therefore fail to

interpret the data. This run would have many errors thrown, however the presence of this error tells the veto expert to first investigate the raw data.

Table 5.1:
Veto errors ($\#1 - \#7$) checked with auto-veto program. Error Types: Data or Underperformance (UP). Categories: Actionable, Minor, or Diagnostic.

Error #	Name	Description	Error Type	Category
1	Missing channels ($<$ 32 veto datas in event)	At least 1 panel has not returned a QDC value	Data	Minor
2	Extra Channels ($>$ 32 veto datas in event)	More than 32 QDC values have been recorded	Data	Minor
3	Scaler only (no QDC data)	No data from QDC cards has been recorded	Data	Minor
4	Bad Timestamp: FFFF FFFF FFFF FFFF	Scaler timestamp for a veto event has been corrupted	Data	Minor
5	QDCIndex - ScalerIndex $\neq$ 1 or 2	QDC card data packet was not received sequentially with Scaler card data packet	Data	Minor
6	Duplicate channels (channel shows up multiple times)	Multiple values recorded for one panel	Data	Minor
7	HW Count Mismatch (SEC - QEC $\neq$ 1 or 2)	Scaler and QDC card Event Count values do not match	Data	Minor

Table 5.2:
Veto errors (#8−#14) checked with auto-veto program. Error Types: Data or Underperformance (UP). Categories: Actionable, Minor, or Diagnostic.

Error #	Name	Description	Error Type	Category
8	MJTRun run number doesn't match input file	Run # of veto data doesn't match run # of detector data	Data	Minor
9	MJTVetoData cast failed (missing QDC data)	Missing data from QDC card	Data	Minor
10	Indexes of QDC1 and Scaler differ by more than 2	QDC card 1 data packet does not arrive sequentially after the Scaler card data packet	Data	Minor
11	Indexes of QDC2 and Scaler differ by more than 2	QDC card 2 data packet does not arrive sequentially after the Scaler packet	Data	Minor
12	Indexes of either QDC1 or QDC2 PRECEDE the scaler index	QDC card data packet arrives before Scaler card data packet	Data	Minor
13	Indexes of either QDC1 or QDC2 EQUAL the scaler index	Arrival order of QDC card data packet and Scaler card data packet is unknown	Data	Minor
14	Unknown Card is present	Data packet comes from unrecognized veto card	Data	Diagnostic

Table 5.3:
Veto errors (#15 − #21) checked with auto-veto program. Error Types: Data or Underperformance (UP). Categories: Actionable, Minor, or Diagnostic.

Error #	Name	Description	Error Type	Category
15	Scaler and SBC Timestamp Desynch	Recorded Scaler card and SBC timestamps differ by > 1 second	Data	Minor
16	Scaler Event Count reset	Scaler card event count spontaneously reset to zero during run	Data	Minor
17	Scaler Event Count increment by $> +1$	Scaler card event count increased without recording a data packet	Data	Minor
18	QDC1 Event Count reset	QDC card 1 event count spontaneously reset to zero during run	Data	Minor
19	QDC1 Event Count increment by $> +1$	QDC card 1 event count increased without recording a data packet	Data	Minor
20	QDC2 Event Count reset	QDC card 2 event count spontaneously reset to zero during run	Data	Minor
21	QDC2 Event Count increment $> +1$	QDC card 2 event count increased without recording a data packet	Data	Minor

Table 5.4:
Veto errors (#22 – #27) checked with auto-veto program. Error Types: Data or Underperformance (UP). Categories: Actionable, Minor, or Diagnostic.

Error #	Name	Description	Error Type	Category
22	Buffer Flush	Scaler and QDC card buffers emptied at start of run. These veto events cannot be correlated with detector events.	Data	Diagnostic
23	LED frequency very low/high, corrupted, or LED's off	LED frequency is much higher or lower than expected	UP	Actionable
24	QDC threshold not found	QDC pedestal of at least 1 panel could not be found	UP	Diagnostic
25	Low # of LEDs seen in panel.	At least one panel tagged fewer LEDs than expected	UP	Diagnostic
26	Failure to sync veto and Ge data	Veto and Detector Timestamp sync failed	UP	Diagnostic
27	Panel Hit Count = 0	At least one panel recorded no scintillations	UP	Actionable

5.2 Error Rates

The 27 errors checked are intended to be a robust selection, giving the collaboration enough information to quickly identify an issue and develop a solution. Some of these errors have not occurred in any recorded veto runs. Only six errors (Errors 1, 4, 15, 22, 23, 26) have a strong impact on the ability to apply a muon cut to the detector data. These errors will be the focus of this section. Errors 25 (Low # of LEDs seen in panel) and 27 (Panel Hit Count = 0) will have an effect on the muon tag efficiency of the veto system, however, these errors are generally thrown during known veto panel outages. Table 5.5 shows the error rates during Data Sets 0, 3, and 6. The error rate of Error 23 (LED frequency very low/high, corrupted, or LED's off) is expected to be zero. However, the non-zero error rate shown does not indicate a problem with the panels, instead it indicates a problem with the system configuration. After certain operations in the lab, the LEDs must be reactivated manually. On occasion the LEDs have not been reactived properly and the LEDs remained off after data taking resumed. At these times, the auto-veto program has alerted the collaboration and the LEDs are reactivated a short time later.

Implementation of these error checks has led to numerous improvements of the veto system. Investigation of the relatively common timestamp corruption (Error 4) during DS0 led the collaboration to move the veto electronics into a separate VME computer bus, resulting in the reduction of the error rate for all runs after DS0. Similarly, investigation of the scaler and SBC timestamp desynch (Error 15) led to changes in the DAQ during DS5 which reduced the error rate to ~ 0 for DS6 and onward. This error was vital to identify as a desynch greatly impacts the veto timestamp and muVeto cut efficiency. However, these desynchs can be identified and are corrected in post processing.

Table 5.5:
Error rates of important veto errors.

		2149 DS0 runs (Livetime = 45.9 days)	733 DS3 runs (Livetime = 29.9 days)	4870 DS6 runs (Livetime = 180.7 days)
Error #	Name	% of events effected	% of events effected	% of events effected
1	Missing Channels	0.10	0.02	0.02
4	Bad Timestamp	4.13	0.00	$\sim$ 0.00
15	Scaler and SBC Timestamp Desynch	0.00	$\sim$ 0.55% of runs	$\sim$ 0.53% of runs
22	Buffer flush	0.05	0.01	0.01
23	LED frequency low/high, corrupted, or LED's off	4.75	22.5	0.64
26	Failure to sync veto and Ge data	0.00	0.00	0.00
Other	All other veto errors	$\leq$ 0.1	$\leq$ 0.02	$\leq$ 0.2

5.3 Veto Run Quality

The veto run quality is also graded during error checking. The grading system uses two grades:

1. "Gold": Veto system performing as expected.

2. "Silver": Evidence suggests the veto system is performing suboptimally.

The grade of a veto run is determined by two factors: (1) the veto and detector data synchronization and (2) the efficiency of tagging LED events. The logic is that if the veto system is properly recording (and tagging) all of the LED events, then the system is very likely also recording all physics events properly. Also if the veto and detector data are synced properly then the muon veto cut can be applied properly. The data synchronization criterion is simple to confirm as that is an error check. Measuring the LED tag efficiency is slightly more difficult. For each run, the number of LEDs tagged ($\mathrm{LED_{seen}}$) and the time difference between the LEDs (LEDDT) are recorded. The LEDDT is then used to measure the LED period. The measured LED period and the duration of the run are used to estimate the number of LEDs that should be detected by the veto system in the run ($\mathrm{LED_{expected}}$). The efficiency of the LED tag is then calculated by comparing $\mathrm{LED_{seen}}$ with $\mathrm{LED_{expected}}$. After analyzing known good veto runs and known bad veto runs it was determined that a run should be demoted to "Silver" if the system detects less than 99 percent of LEDs in a long (greater than 1000 seconds) run, or the system detects less than 95 percent of LEDs in a short (less than 1000 seconds) run. The criteria for a "Gold" veto run are:

1. LED tagging efficiency greater than 99% (greater than 95% if run duration less than 1000 seconds)

2. Veto-Detector data synchronization completed without errors.

This grade clearly communicates to the collaboration the status of the veto system.

Chapter 6

Data Analysis

This chapter summarizes the search for specific muon-induced background signals in the MAJORANA DEMONSTRATOR data. The measurement of these signals will give are valuable points of comparison that can be used to draw insightful conclusions from simulations of muon-induced backgrounds. This analysis was performed as a blind analysis, where the analysis code and methodology were tested on an open set of data and reviewed by an internal committee before being used on a blind set of data. The open analysis results as well as the combined open and blind analysis results are shown.

6.1 Data Preparation

In this analysis, we searched for data signatures that are induced by cosmic muons that pass through the system. The first task was to use the veto system to tag muons in the veto data. With the muon event data tagged and stored it becomes possible to scan the germanium detector data for specific energy depositions that are coincident with, and therefore likely induced by, cosmic muons. This section will discuss how muons are being tagged and which information is being stored.

6.1.1 Muon Tagging

The muon tagging software used in this analysis is a modified version of the muon tagging software used during standard MAJORANA data production described in Chapter 4. The modified tagger gives us the ability to test various muon tag criteria without effecting data production. First, the software trigger Charge-to-Digital Conversion (QDC) value threshold is located for each QDC channel (veto panel). This process is identical to the process used in the standard data production, where the QDC pedestal in each channel is identified and a small value is added to create the software trigger threshold. The software trigger threshold is our criteria for differentiating physics events caused by scintillation from pedestal events in the recorded data. Once the scintillation events were identified, we applied criteria to separate the muon events from other types of events. The muon criteria are the same criteria applied during standard data production.

1. **Not an LED event.**

   Each panel has an embedded LED which we pulse regularly to check if the panel/PMT is operating properly. We identify these events as "non-physics" by the fact that all 32 LEDs should generate light at the same time. However, at certain times not all 32 veto panels were active (See Chapter 8). Therefore we use a "veto panel multiplicity greater than or equal to the maximum panel multiplicity minus 5" to identify and ignore veto LED events.

2. **At least two panels record QDC value greater than the high-energy muon threshold.**

   Muons tend to deposit more energy in our panels than gammas. We leverage this information, along with the configuration of our panels to confidently distinguish muon events from gamma events by defining a high energy muon threshold for each panel [27]. Given that the veto configuration consists of 32 panels in a cube shape, with 2 panels per layer, a penetrating particle like a muon is expected to pass through approximately four panels. The conservative criteria "At least two panels receive high energy deposits (QDC above muon threshold)" is used to identify muon events and ignore gamma events. Figure 6.1 shows the raw QDC of physics events (i.e. non-LED

events) in a single panel. The low QDC gamma peak can be clearly distinguished from high QDC muons after a certain QDC threshold, ∼500 QDC in this panel.

As a muon passes through a veto panel it will induce scintillation. Based on the veto system design, a muon that passes directly through the experiment will pass through four panels and cause scintillation. A muon can also create a shower of particles as it moves through the various materials in the experiment. These particles can also cause scintillation as they pass through a veto panel. Therefore, a single muon is expected to have a veto multiplicity of four, however higher multiplicities are possible. It is unlikely that a muon will create a shower large enough to span the experiment and cause scintillation in all 32 panels. The muon panels were measured to have greater than 99% muon tagging efficiency during fabrication and testing [27]. Additionally, MaGe simulations [26] were used to determine the overall muon tagging efficiency of the veto system. These simulations are discussed in Chapter 8. When all 32 panels are installed and operating properly the muon tagging efficiency is 96.71%. Multiple veto panel configurations were used over the selected data set, with the muon tagging efficiency ranging from 95.90%, when eight specific panels were uninstalled for shield improvements, to 96.71%, when all 32 panels were operational. Once the muon events were tagged the relevant data, such as run number, timestamp, timestamp uncertainty, and muon panel multiplicity were saved to a data file. This file was then used to determine which detector events were in coincidence with a muon. Figure 6.2 shows the panel multiplicity of veto events tagged as muons and events tagged as LEDs.

Each muon tagged in the data also has an associated timestamp uncertainty due to the fact that the veto system and germanium detectors use different data acquisition systems and must be synced at the start of each data run. This timestamp uncertainty comes directly from the veto-germanium detector synchronization, however if a run has one of several veto errors then the uncertainty is expanded in a specific way depending on the error. The time windows selected in this analysis were expanded to include this uncertainty. For example, suppose the signature time window of dS after a muon is chosen. If the muon has a timestamp T with uncertainty dT, then the time window used for events near this muon (for this signature)

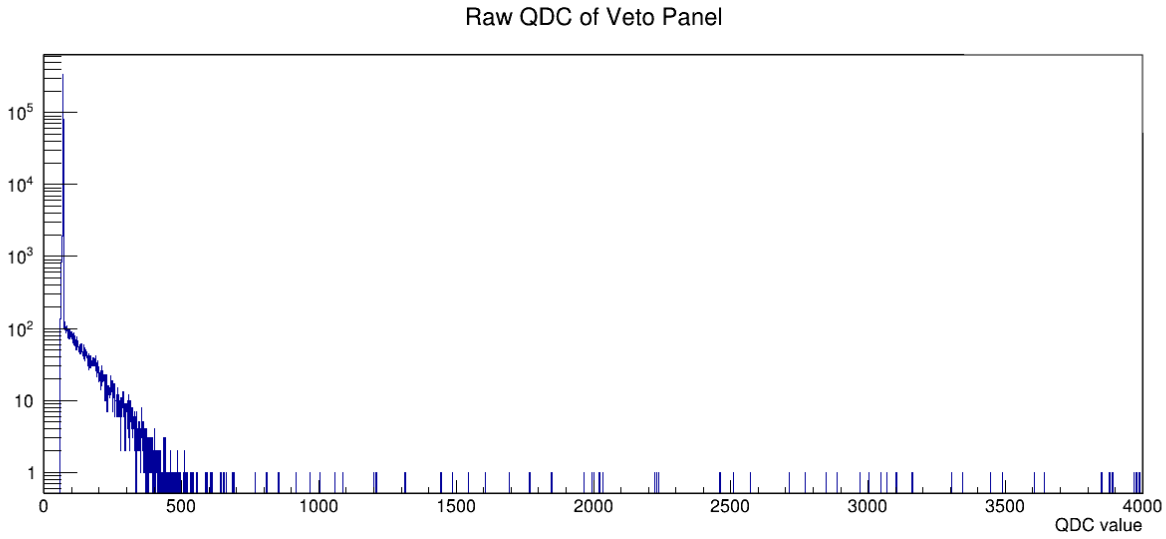

Figure 6.1: Raw QDC of veto panel #29. The pedestal is visible near 60 QDC, and the gamma peak can be seen from $62-500$ QDC. The muon QDC threshold was determined for each veto panel by identifying where the gamma tail terminates. The muon threshold here is 500. Data from DS3.

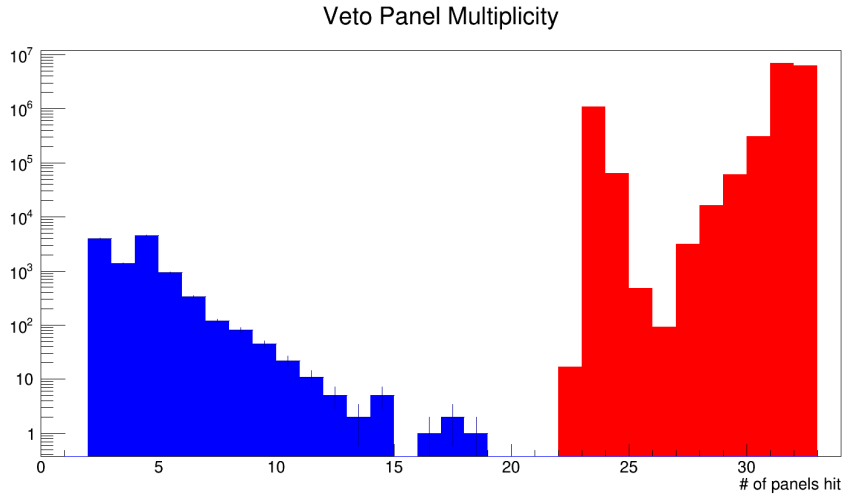

Figure 6.2: Veto panel multiplicity of all 11450 events tagged as muons (blue) and all events tagged as LEDs (red). Data from DS0, DS1, DS2, DS3, DS5, DS6a open.

will be:

$$\text{Data Time Window} = [\text{T} - |\text{dT}|,\ \text{T} + |\text{dT}| + \text{dS}] \tag{6.1}$$

The veto timestamp uncertainty was calculated during MAJORANA DEMONSTRATOR data auto-production. Figure 6.3 shows the timestamp uncertainty, measured in seconds, for each muon tagged in the open data set.

Veto LED Tag

The veto LED tag used in this analysis, and by the collaboration, makes the primary assumption that a muon passing through the laboratory will not trigger most of the veto panels (generally more than 27 panels). It has been speculated that a muon will create a particle shower large enough to trigger all of the veto panels while passing through the lab. An investigation was performed of the DS3 LED tagged events and muon tagged events to search for evidence of such a muon shower.

Electronic LED driver cards are used to pulse all 32 LEDs in the veto panels at the same time. The LED driver card allows the user to set an LED frequency. The LEDs should therefore trigger with a very specific, and stable period. We argue that any LED event that has a timestamp difference from the previous LED equal to the LED period is clearly a true LED and cannot be a shower muon event. The data acquisition system for the veto system is not perfect, occasionally an LED will be missed. In these cases the next LED will record a timestamp difference equal to twice the LED period. Therefore it is likely that LED timestamp difference values that are a low (less than four) multiple of the LED period are likely also true LED events. It is incredibly unlikely that shower muon would occur precisely when an LED is expected. Figure 4.5 shows the timestamp differences for all LED tagged in events in DS3. For the duration of DS3, the LED period was set to 7.55 seconds. All LED tagged events of DS3 have timestamp difference values which are clear multiples of the LED period, with no outlier events. This indicates that all of the LED tagged events are true LEDs, and is evidence that no shower muon events with veto multiplicity greater than the maximum multiplicity minus five occur in DS3. Data Set 3 has an average livetime of ~ 29

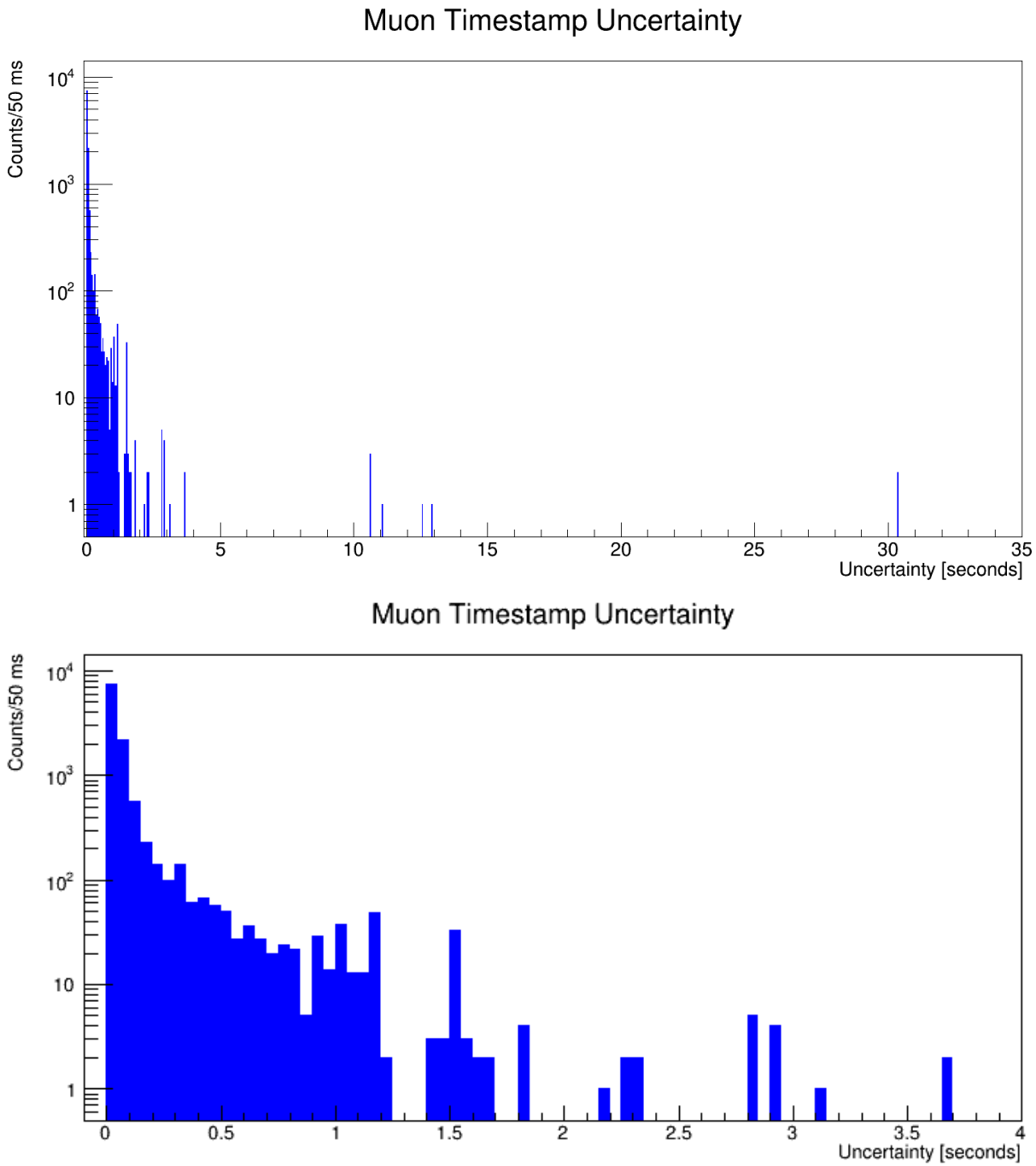

Figure 6.3: Muon timestamp uncertainty for each of the 11450 muons tagged in the dataset. X-axis is in seconds. The lower plot is an expansion of the upper plot. Data from DS0, DS1, DS2, DS3, DS5, and DS6a open.

days [37], therefore the frequency of shower muon events should be small, if they occur at all.

When the veto system is triggered, data from all 32 veto panels is read out simultaneously. The panels that did not scintillate, i.e. were not hit, read out a low QDC value called the pedestal. On average the LED amplitude is larger than a muon amplitude. Therefore the summed QDC spectrum of muon events (low/medium multiplicity) is expected to be distinct from the summed QDC spectrum of LED events (high multiplicity and amplitude). DS3 was investigated and a clear distinction between LED tagged events and muon tagged events was found. Figure 6.4 shows the summed QDC events of DS3. There are three muon events which have a summed QDC value around the LED spectrum tail. Upon further investigation these three events appear to be medium multiplicity shower muon events that were correctly identified as muons. Each of these events has a $16-17$ veto panel multiplicity (triggers many panels), many of which, 14 panels each, have a high energy QDC value (QDC value above muon threshold). The high QDC value found in these events is likely caused by a combination of the muon causing ~ 4 panels to scintillate and the particle shower created by the muon causing the other ~ 10 panels to scintillate. Each event is preceded by and followed by a true LED event (LED time difference = 7.55 seconds) so it is unlikely that these events are LEDs.

6.1.2 Muon Acceptance

In the open data set, 11450 events were tagged as muon events but not all were used in this analysis. This analysis requires access to all data in a time window T, immediately following a muon event. As the time window selected for each signature is small compared to the standard duration of a run, it follows that the majority of muons will have the entire time window available for analysis. Only the muons that appear near the end of a run need to be investigated to ensure that the full time window is accessible. There are a variety of reasons that the time window may be inaccessible, however all originate due to a signature time window that spans two sequential data runs. These reasons include:

1. The last portion of the time window may be in a run that is blind.

2. The last portion of the time window may be in a run that is a Calibration run or a non-standard run not used for physics analysis.

3. The last portion of the time window may be in a run that did not pass the run selection/data quality checks.

4. At the start of a run the timestamps may have been reset, making it difficult to accurately select the last portion of the time window. This typically occurs after the weekly germanium detector threshold measurement.

5. A signature time window spans 3 sequential runs, due to a run having an incredible short duration.

To account for these cases, any muon which did not have access to the largest signature time window (240 seconds) was rejected from the analysis of all signatures. The exposure was corrected to account for this window rejection. In the open data set used in this analysis, 401 muons (3.50%) did not have access to the full 240 second time window and were not used in the analysis resulting in a loss of 1.836 kg $\cdot$ d of natural germanium exposure and a loss of 6.557 kg $\cdot$ d of enriched germanium exposure. The remaining 11049 muons were used to perform the open signature search. In the blind data set used in this analysis, 11 muons (0.10%) did not have access to the full 240 second time window and were not used in the analysis resulting in a loss of 0.105 kg $\cdot$ d of natural germanium exposure and a loss of 0.275 kg $\cdot$ d of enriched germanium exposure. The remaining 11289 muons were used to perform the blind signature search.

6.1.3 Veto-Germanium Timing Offset

The veto system and the germanium detectors used two different data acquisition systems and therefore different clocks. These clocks were synchronized at the start of each run by using physical events. After synchronization the time difference between the muon veto event and the detector events (muDT) was calculated by comparing the muon and detector timestamps. When considering detector events coincident with a muon (within 1 second of a muon-tagged veto signal) we expect a peak near muDT = 0, with a width proportional

to the germanium detector drift times, that decays exponentially. The events in this peak would consist of prompt events caused directly by muons interacting in both germanium detectors and veto panels, whereas the tail would consist of delayed events caused by muon-interaction products (e.g. secondary gammas and neutrons). In the data, we found that there is a no peak at muDT = 0, and instead there was a clear peak at muDT = $\sim$52 μs see Figure 6.5. This peak represents a 52 μs offset between the germanium and veto data acquisition systems. We identified the peak at muDT = 52 μs to be prompt muon events. The signatures in this analysis are delayed events and so will not be found in the prompt muDT peak. Any candidate event with muDT value greater than or equal to 52 μsand less than 54 μs was removed as a prompt event. Additionally, since no coincident germanium-veto events will have a muDT value less than this [52,54) μs window, the signature time windows will be extended by 54 μs to account for this timing offset.

6.2 Data Set

This analysis used the same data sets and channel selection information as the MAJORANA $\beta\beta(0\nu)$ 26 kg $\cdot$ yr analysis [15] with the exclusion of DS4 and several additional runs. For the duration of DS4 there was an additional clock (the Module 2 clock) which had to be synced with both the veto clock and the Module 1 clock to accurately determine the muon timestamp. Rather than include more uncertainty due to this additional clock sync we decided to exclude DS4 which contains a total exposure of 176.703 kg $\cdot$ d. An additional run selection cut, the Veto Status cut, of "Veto Status equal to Gold" was applied. The Veto Status tag was developed by the veto group to indicate clearly if the veto system was under-performing (less than 99% LED tagging efficiency) during the run. One possible consequence of veto system under-performance is true LEDs being tagged incorrectly as muons. This is apparent in runs 4463, 5741, and 6961. Significantly more muons were tagged in these runs (4463, 5741, and 6961) than expected (when compared to other runs in the data set), at 138, 50, and 384 muon events respectively. Many of the tagged muons in these runs have veto multiplicity $12 - 17$. Further investigation shows that multiple panels in these runs were

under performing. These panels failed to identify at least 10 LED events. This is a strong indication that the events with multiplicity $12 - 17$ are actually LED events.

In the open data analysis, 726 runs were removed by the Veto Status cut: 383 from DS0, 71 from DS1, 4 from DS2, 171 from DS3, 80 from DS5a, 16 from DS5b, and 1 from DS6a. These removed runs result in the loss of 282.890 kg $\cdot$ d of enriched germanium exposure and 94.350 kg $\cdot$ d of natural germanium exposure.

For analysis of the blind runs 18 runs were removed by the Veto Status cut: 4 from DS1, and 8 from DS2. These removed runs result in the loss of 5.207 kg $\cdot$ d of enriched germanium exposure and 0.509 kg $\cdot$ d of natural germanium exposure.

The exposure was calculated using the MAJORANA collaboration exposure calculation [37] and then applying exposure corrections. Only good germanium detectors were used to identify signatures, these were selected using an analysis tag called "isGood". Two standard MAJORANA DEMONSTRATOR data cleaning cuts (AvsE and DCR) were not in this analysis. The efficiency of these cuts has not been evaluated at the low energy range ($\sim$200 keV) of this analysis. Additionally, both the AvsE and DCR cuts are only intended for events with energy greater than 500 keV [17] [57]. Neither the 1-second muVeto cut nor the LNFill cut were applied in this analysis so a correction was included for these cuts [37]. Additionally the exposure lost due to our Veto Status cut and our Muon Acceptance cut were included as a correction. Table 6.1 summarizes the corrected exposure of each data set for natural and enriched detectors used in this analysis.

6.3 Signatures

Five signals from four isotopes have been selected for this study. One ^{71}Ge de-excitation, one ^{75}Ge de-excitation, two ^{69}Ge de-excitations, and one ^{77}Ge de-excitation. These signatures were chosen because they fulfill two criteria:

1. These isotopes have among the highest production rates in germanium, according to muon MAGE/FLUKA simulations (Chapters 10 and 11).

2. These isotopes have clear energy signatures with short half-lives.

Table 6.1: Data set information and corrected exposure [37]. The natural and enriched detectors are considered separately. The label "(o)" indicates open data and the label "(b)" indicates blind data.

Data Set	Start Date	End Date	Exposure(total)	Exposure(^{enr}Ge)	Exposure(^{nat}Ge)
DS0(o)	6/26/15 2335	10/7/15 8183	492.898 ± 10.900 kg·d	358.834 ± 6.959 kg·d	134.064 ± 3.941 kg·d
DS1(o)	12/24/15	5/24/16	708.117 ± 11.161 kg·d	646.286 ± 9.693 kg·d	61.832 ± 1.468 kg·d
DS1(b)	12/24/15 8722	5/24/16 14502	202.706 ± 3.099 kg·d	185.836 ± 2.71 kg·d	16.870 ± 0.389 kg·d
DS2(o)	5/24/16	8/05/16	115.145 ± 1.802 kg·d	104.630 ± 1.554 kg·d	10.515 ± 0.248 kg·d
DS2(b)	5/24/16 14503	8/05/16 15892	372.176 ± 5.723 kg·d	338.943 ± 4.953 kg·d	33.233 ± 0.770 kg·d
DS3(o)	8/05/16 15893	10/12/16 18589	346.949 ± 7.291 kg·d	283.850 ± 5.410 kg·d	63.098 ± 1.881 kg·d
DS4(o)	10/03/16 60000623	10/12/16 60002394	176.703 ± 3.174 kg·d	102.858 ± 1.473 kg·d	73.845 ± 1.701 kg·d
DS5a+5b	10/13/16 18623	03/17/17 23958	2874.986 ± 50.355 kg·d	1919.387 ± 28.181 kg·d	955.599 ± 22.174 kg·d
DS5c(o)	03/17/17	05/11/17	267.582 ± 4.524 kg·d	179.225 ± 2.539 kg·d	88.357 ± 1.985 kg·d
DS5c(b)	03/17/17 23959	05/11/17 25671	834.268 ± 14.051 kg·d	560.859 ± 7.924 kg·d	273.409 ± 6.127 kg·d
DS6a(o)	05/11/17	04/18/18	1928.278 ± 31.715 kg·d	1400.698 ± 19.943 kg·d	527.581 ± 11.772 kg·d
DS6a(b)	05/11/17 25672	04/18/18 37088	4567.950 ± 74.593 kg·d	3353.517 ± 47.623 kg·d	1214.433 ± 26.970 kg·d
DS0-DS5b(o)			12.908 ± 0.232 kg·yr	9.352 ± 0.146 kg·yr	3.556 ± 0.086 kg·yr
DS0-DS6a(o)			18.920 ± 0.331 kg·yr	13.678 ± 0.207 kg·yr	5.243 ± 0.124 kg·yr
DS0,1,2,3,5,6a(o)			18.437 ± 0.322 kg·yr	13.396 ± 0.203 kg·yr	5.041 ± 0.119 kg·yr
DS0,1,2,3,5,6a(b)			16.364 ± 0.267 kg·yr	12.154 ± 0.173 kg·yr	4.211 ± 0.094 kg·yr
DS0,1,2,3,5,6a(total)			34.801 ± 0.589 kg·yr	25.550 ± 0.376 kg·yr	9.251 ± 0.213 kg·yr

The five signatures are:

- 198.354 keV level two-step Isomeric Transition (IT) decay ($t_{1/2} \sim 20.4$ ms) of ^{71}Ge ($E_\gamma = 198.394$ keV)
- 139.69 keV level IT decay ($t_{1/2} = 47.7$ s) of ^{75}Ge ($E_\gamma = 139.68$ keV)
- 86.76 keV level de-excitation ($t_{1/2} = 5$ μs) of ^{69}Ge ($E_\gamma = 86.78$ keV) (Not used In final analysis)
- 397.94 keV level de-excitation ($t_{1/2}$= 2.81 μs) of ^{69}Ge ($E_\gamma = 397.94$ keV). (Not used in final analysis)
- 159.71 keV level de-excitation ($t_{1/2}$= 53.7 s) of ^{77}Ge ($E_\gamma = 159.66$ keV)

6.4 Random Coincidence Background

An important background to this analysis are the random coincident events that mimic one of the selected signatures. The open data set used in the signature search was also used to measure the random coincidence background rate for each signature. To measure the background rate, six 240 second time windows were investigated. The six background windows start at $t_{\text{local}} = [200\text{s}, 440\text{s}, 680\text{s}, 920\text{s}, 1160\text{s}, 1400\text{s}]$, where $t_{\text{local}} = 0$ is the start of the run. Multiple windows were chosen to increase the statistics of the random coincidence background measurement. These windows are investigated for each run in the data set if the run contains the entire window, i.e. the $t_{\text{local}} = [1400\text{s}, 1640\text{s}]$ window is only searched in run "A", if run "A" has a duration longer than 1640 seconds. All detector events that occur in a time window were isolated and studied. For each signature, the number of events in each time window that also fell in the signature energy window ($E_\gamma \pm 5$ keV) and survived the analysis cuts were counted. These detector events were then used to calculate a signature-specific random coincidence background rate for each of the six time windows. Each window has similar total exposure and similar random coincidence background rate measurements. The signature-specific background rate used in this analysis is the average of the six signature background rates, weighted by window exposure. All of the combined time windows studied

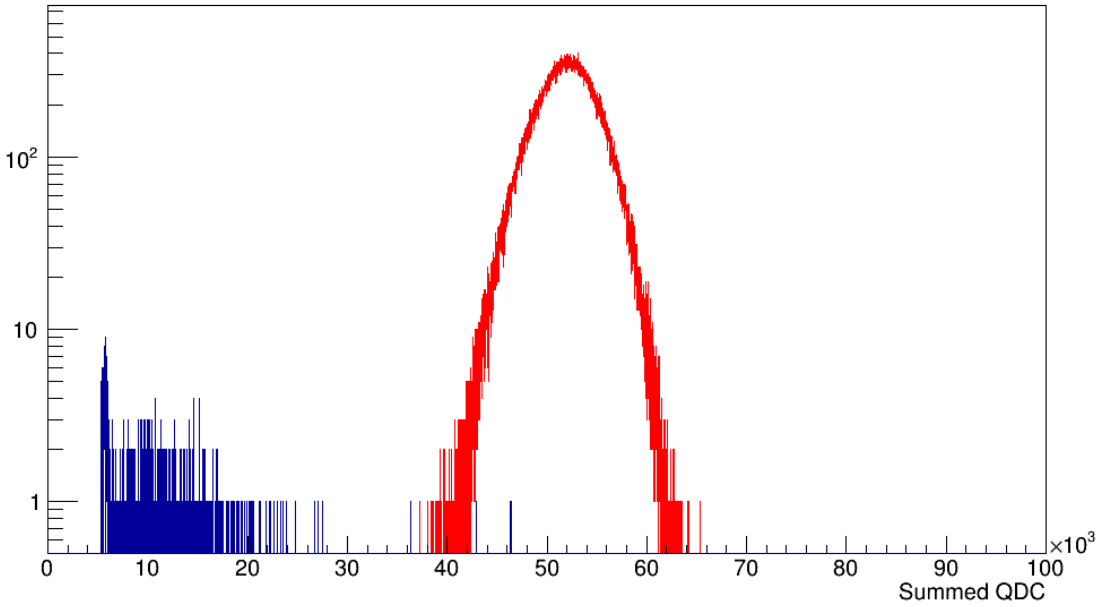

Figure 6.4: Summed QDC value of LED tagged events (red) and muon tagged events (blue) in Data Set 3.

Table 6.2: Random coincidence background rates of the selected signatures. Comparison of DS0, DS12356 measurements in this work along side total MAJORANA event rate at these energies [15].

Signature	Energy [keV]	Bg Rate [c/kg/day/keV] DS0 NatGe	DS0 EnrGe	DS12356 NatGe	DS12356 EnrGe	MJD DS0-6a NatGe+EnrGe
^{71m1}Ge	198.394	$0.160^{+0.028}_{-0.028}$	$0.125^{+0.015}_{-0.015}$	$0.021^{+0.004}_{-0.004}$	$0.015^{+0.002}_{-0.002}$	~ 0.015
^{75m1}Ge	139.68	$0.180^{+0.029}_{-0.029}$	$0.139^{+0.016}_{-0.016}$	$0.029^{+0.004}_{-0.004}$	$0.018^{+0.002}_{-0.002}$	~ 0.015
^{77m1}Ge	159.71	$0.170^{+0.029}_{-0.029}$	$0.137^{+0.016}_{-0.016}$	$0.021^{+0.004}_{-0.004}$	$0.019^{+0.002}_{-0.002}$	~ 0.015

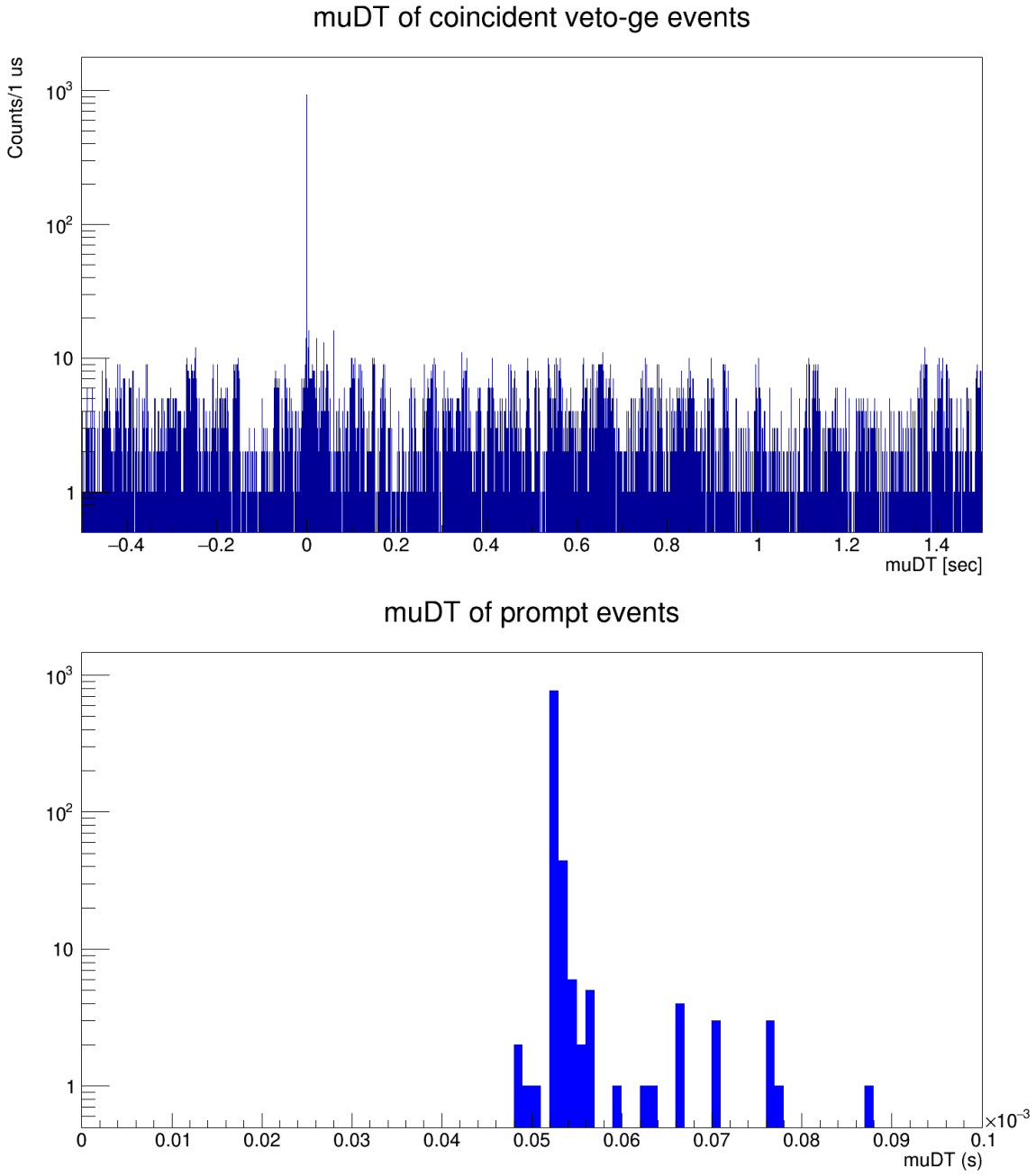

Figure 6.5: Time Spectra of coincident Ge events with peak at [52,54) μs. Data from DS0,1,2,3,5,6a open. The lower plot is an expansion of the peak shown in the upper plot.

correspond to an exposure of 982.48 kg · d natural germanium, and 2461.84 kg · d enriched germanium. Major shielding was added to the DEMONSTRATOR between DS0 and DS1. For this reason the background rates in DS0 and in DS12356 were calculated separately to account for the higher background in DS0. Table 6.2 shows the random coincidence background rates for all three signatures used in the final analysis along with the MAJORANA event rate [15]. The expected background counts of the signatures are calculated later in the document (The "Backgrounds" section of each signature).

6.4.1 Background Comparison

As a cross-check, the random coincidence background rate was measured for each signature using only the blind data. Table 6.3 shows the relevant rates in both the open and blind data.

The same processing code was used for both measurements.

The blind Bg rates differ, sometimes significantly, from the open Bg rates. This difference is very likely due to the different composition of the open and blind data sets. The blind data set is $\sim 70\%$ DS6a, while the open data set is $\sim 29\%$ DS6a. Additionally, $\sim 10\%$ of the blind data set is from before DS3 (DS1 and DS2), while $\sim 25\%$ of the open data set is from before DS3 (DS0, DS1, and DS2). The later data sets (DS5c, DS6a) have more shielding installed than the earlier data sets (DS0, DS1), so it is reasonable to see this difference in random coincidence background rate. When the background rates are compared data set to data set, i.e. DS6a open compared to DS6a blind, there is agreement within one standard deviation. The signature-specific expected Bg for the blind data set was calculated using the blind Bg rate.

6.5 ^{71}Ge

As a muon passes through matter it is likely to produce protons, electrons, neutrons, and gammas, or interact inelastically with detectors, if it interacts at all. The direct signal in the detectors from a muon passage is easily rejected by its magnitude and distribution as well as timing coincidence with the veto detectors. Activation of the germanium detectors

by cosmic particles can create long-lived isotopes that mimic our $\beta\beta(0\nu)$ signal upon decay. These long-lived isotopes cannot be vetoed.

6.5.1 ^{71}Ge Decay Signature

Interactions caused by neutrons are the primary production mechanism for the isotope ^{71}Ge in the DEMONSTRATOR. ^{71}Ge can be produced via the reactions $^{70}\mathrm{Ge}(\mathrm{n},\gamma)^{71}\mathrm{Ge}$, $^{72}\mathrm{Ge}(\gamma,\mathrm{n})^{71}\mathrm{Ge}$, $^{72}\mathrm{Ge}(\mathrm{n},2\mathrm{n})^{71}\mathrm{Ge}$, and $^{72}\mathrm{Ge}(\mu,\mathrm{n})^{71}\mathrm{Ge}$. These reactions can occur in both the natural germanium detectors and in the enriched germanium detectors. The energetic de-excitation of ^{71}Ge can lead to the ground state or to a meta-stable state $^{71\mathrm{m}}$Ge. The meta-stable (198.354 keV) state will undergo an IT decay ($t_{1/2} = 20.40$ ms) via a middle state of 174.956 keV ($t_{1/2} = 79$ ns) to the ground state, emitting two gammas of 23.438 keV ($t_{1/2} = 20.40$ ms) and 174.956 keV ($t_{1/2} = 79$ ns) respectively. Both gamma emissions have half-lives which are short enough to maintain correlation with a muon passing through our veto system. Since the 174.956 keV transition is so short-lived, we will search for a combined signal of 198.394 keV [10]. Figure 6.6 shows the energy level scheme ^{71}Ge up to our 198.354 keV level of interest.

6.5.2 Event Selection

At our signature energy of 198.394 keV, our energy resolution is ~ 1 keV [46]. The energy window of plus/minus 5 keV was chosen as a conservative value.
The time window 204.0 ms was chosen for the high probability to observe the signature. The time window was extended by 54 μs to account for the veto-Ge timing offset.

The possible total deposition energy is 198.394 (174.956 plus 23.438) keV. We select a candidate event of energy within 5 keV of that energy, following a muon event within 204.0 ms plus 54 μs (10 times of 20.40 ms), if the timestamp falls between [52,54) μs it will be removed as a prompt background (see Section 6.1.3).

Table 6.3: Random coincidence background rates of the selected signatures. Comparison of DS12356 open and DS125c6a blind measurements in this work.

Signature	Energy [keV]	Bg Rate [c/kg/day/keV]			
		DS12356 open		DS125c6a blind	
		NatGe	EnrGe	NatGe	EnrGe
^{71m1}Ge	198.394	$0.021^{+0.004}_{-0.004}$	$0.015^{+0.002}_{-0.002}$	$0.014^{+0.003}_{-0.003}$	$0.015^{+0.002}_{-0.002}$
^{75m1}Ge	139.68	$0.029^{+0.004}_{-0.004}$	$0.018^{+0.002}_{-0.002}$	$0.016^{+0.003}_{-0.003}$	$0.015^{+0.002}_{-0.002}$
^{77m1}Ge	159.71	$0.021^{+0.004}_{-0.004}$	$0.019^{+0.002}_{-0.002}$	$0.014^{+0.003}_{-0.003}$	$0.015^{+0.002}_{-0.002}$

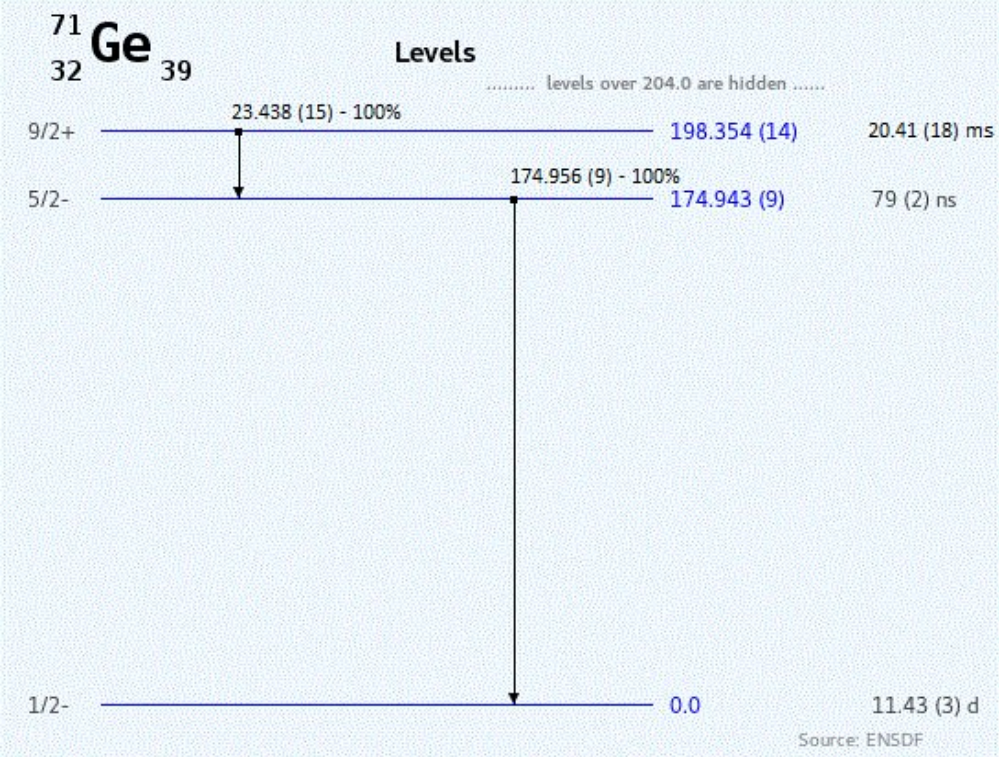

Figure 6.6: Energy level scheme for ^{71}Ge including gamma energies. Figure generated on [49].

6.5.3 Backgrounds

^{71}Ge can also be produced through the electron capture (EC) decay of ^{71}As with a half-life of $t_{1/2} = 65.28$ h [10]. ^{71}As in this case can be produced by proton interactions with ^{70}Ge and ^{72}Ge. Due to the long half-life of the decay, the relatively small abundance of ^{70}Ge and ^{72}Ge, and the short signature time window this background is not significant.

One potential background is the de-excitation of ^{75m}As to the ground state ^{75}As (E_γ =198.6 keV). ^{75m}As can be created in the detectors through beta (β) decay of ^{75}Ge ($t_{1/2}$ = 82.78 m) and ^{75m}Ge ($t_{1/2}$ = 47.7 s). The ^{75m}Ge β-decay has a very small branching ratio (0.03%), so backgrounds from this energy level can be ignored. We estimate the amount of ^{75}Ge isotopes produced in this data set using results of a MaGe simulation of muons on the Demonstrator (See Table 6.5 for MaGe isotopic production rate). From the simulation, we expect to see 26 counts in the natural detectors and 68 counts in the enriched detectors. The probability of seeing the immediate ^{75}Ge β-decay in our signature time window is as follows:

$$\epsilon_{\Delta T_{\text{immediate}}} = \int_0^{0.204} \text{dte}^{-t\times\ln 2/4966.8} \Big/ \int_0^{\text{inf}} \text{dte}^{-t\times\ln 2/4966.8} = 0.0033\% \tag{6.2}$$

where the half-life of the ^{75}Ge β-decay is 82.78 min = 4966.8s.

It is also possible for the ^{75}Ge isotope to survive until the next muon appears and then undergo β-decay. We expect the full detector array to see one muon every four hours. The (maximum) probability of seeing the ^{75}Ge β-decay in our time window after surviving until the next muon is as follows:

$$\epsilon_{\Delta T_{\text{delayed}}} = \int_{14400}^{14400.204} \text{dte}^{-t\times\ln 2/4966.8} \Big/ \int_0^{\text{inf}} \text{dte}^{-t\times\ln 2/4966.8} = 3.816\cdot 10^{-4}\% \tag{6.3}$$

where the half-life of the ^{75}Ge β-decay is 82.78 min (4966.8 seconds).

The expected background due to ^{75}Ge β-decays is then calculated using the largest of these probabilities.

$$^{75}\text{Ge } \beta - \text{decay background} = (26 + 68 \text{ events}) \times 0.0033\% = 0.003102 \text{ events} \tag{6.4}$$

Therefore this background is not significant.

Another potential background is the de-excitation of the 192.19 keV ^{75m2}Ge to the ground state [55]. This de-excitation occurs in two steps:

- 192.19 keV ^{75m2}Ge $\rightarrow$ 139.69 keV ^{75m1}Ge. The half-life of this de-excitation is 216 ns.
- 139.69 keV ^{75m1}Ge $\rightarrow$ ground state ^{75}Ge. The half-life of this de-excitation is 47.7 s.

The 192.19 keV state described will only be a background if both de-excitations occur within a single data event. The efficiency of seeing both de-excitations within 20 μs can be calculated since the time window of a data event is $\sim$ 20 μs. $\epsilon_{\Delta T1}$ will describe the probability that the 192.19 keV ^{75m2}Ge $\rightarrow$ 139.69 keV ^{75m1}Ge state transition occurs within 20 μs. $\epsilon_{\Delta T2}$ will describe the probability that the 139.69 keV ^{75m1}Ge $\rightarrow$ ground state ^{75}Ge transition occurs within 20 μs.

$$\epsilon_{\Delta T1} = \int_0^{20000.0\text{ns}} \text{dte}^{-\text{t}\times\ln 2/216\text{ns}} \Big/ \int_0^{\text{inf}} \text{dte}^{-\text{t}\times\ln 2/216\text{ns}} > 99.999999\% \tag{6.5}$$

where the half-life is $\sim$ 216 ns.

$$\epsilon_{\Delta T2} = \int_0^{0.00002\text{s}} \text{dte}^{-\text{t}\times\ln 2/47.7\text{s}} \Big/ \int_0^{\text{inf}} \text{dte}^{-\text{t}\times\ln 2/47.7\text{s}} = 2.90628 \cdot 10^{-5}\% \tag{6.6}$$

where the half-life is $\sim$ 47.7 s. So the total efficiency of seeing both de-excitations within a 20 μs window is

$$\epsilon_{\Delta T1} \times \epsilon_{\Delta T2} = 100\% \times 2.90628 \cdot 10^{-5}\% = 2.90628 \cdot 10^{-5}\% \tag{6.7}$$

So this background is not significant.

Another important source of background is the random coincidence background. This occurs when a detector event within the signature energy window and within the signature time window is found, but the event was not induced by a muon. These event are indistinguishable from true muon-induced events and are the prominent source of background in this study. As discussed in Section 6.4, the random coincidence background rate was measured throughout the open data sets. Those background rates are used to estimate the

expected background value for each signature in the analysis. The expected background (Bg_{Exp}) was calculated as follows:

$$Bg_{Exp} = \Sigma_{DS}\,[(\text{Bg Rate})_{DS} \times (\text{Signature Search Exposure})_{DS}] \times \text{Size of Energy Window} \tag{6.8}$$

and

$$(\text{Signature Search Exposure})_{DS} = (\text{Effective Mass})_{DS} \times (\text{Combined Search Window Livetime}) \tag{6.9}$$

The effective mass is used to accurately represent the exposure of the combined signature search windows in this analysis. The effective mass values were calculated using the total candidate search livetime (livetime combined of muon search windows) and the active mass in each data set [30][31][60][32][58][59].

The random coincidence background for the 198.394 keV ^{71}Ge signature in the open data is estimated to be:

$$\text{NatGe} : 0.096 \pm 0.012 \text{ Events} \tag{6.10}$$

$$\text{EnrGe} : 0.204 \pm 0.018 \text{ Events} \tag{6.11}$$

The random coincidence background for the 198.354 keV ^{71}Ge signature in the blind data is estimated to be:

$$\text{NatGe} : 0.034 \pm 0.007 \text{ Events} \tag{6.12}$$

$$\text{EnrGe} : 0.086 \pm 0.012 \text{ Events} \tag{6.13}$$

6.5.4 Efficiency

We simulated 10^6 ^{71m}Ge isotopes throughout the natural and enriched detectors using MaGe. An energy cut of E $\in$ (198.394 $\pm$ 5 keV) was applied and 672,721 detector depositions survived.

However each germanium detector has a "dead layer" which is not included in this result. The dead layer refers to two small outer regions of a detector in which energy deposits behave differently. The two regions are a truly dead layer, in which energy deposits do not give rise to detector signals, and a partially dead layer, sometimes called a transition layer, in which energy deposits give rise to energy degraded signals [61]. To estimate the effect of a dead layer on the signature detection efficiency, a 1 mm truly dead layer was applied to the detectors. The thickness value of 1 mm was taken from the dead layer measurement of a Majorana detector (MALBEK) [61]. In this measurement the total dead layer thickness (truly dead layer and transition layer) was found to be 0.933 $\pm$ 0.018 mm. After the 1 mm truly dead layer was applied, 622,718 detector depositions survive the energy cut. We find that we are overestimating the energy cut efficiency as each detector has a non-zero dead layer, and the result of the 0 mm dead layer simulation is an upper limit. The uncertainty of the energy cut efficiency $\delta_{\epsilon_{\mathrm{E}}}$ is calculated using the percent difference of the 0 mm dead layer and 1 mm dead layer results.

The efficiency of the energy cut is

$$\text{Percent Uncertainty}: \ \delta_{\epsilon_{\mathrm{E}}} = |(622718 - 672721)|/(0.5 \times (672721 + 622718)) = 7.72\% \tag{6.14}$$

$$\epsilon_{\mathrm{E}}\delta_{\epsilon_{\mathrm{E}}} = 672721/10^6\delta_{\epsilon_{\mathrm{E}}} = 0.672721^{+0.0000}_{-0.0519} \tag{6.15}$$

Before discussing the efficiency of the time (ΔT) cut first let's consider the likelihood of seeing both gamma depositions (23.438 keV and 174.956 keV) within the same event. The time window of a data (detector) event is $\sim$20 μs. The efficiency of the 174.956 keV

deposition occurring within 2 μs of the 23.438 keV deposition is

$$\epsilon_{\Delta T_{decay}} = \int_0^{2000.0} dt e^{-t \times \ln 2/79} \Big/ \int_0^{inf} dt e^{-t \times \ln 2/79} = 0.99999997\% \tag{6.16}$$

where the half-life is $\sim$ 79 ns. Therefore, we are confident that both depositions will be seen together in a single 20 μs data event, if they are seen at all.

The efficiency of the ΔT cut is

$$\epsilon_{\Delta T} = \int_{0.002}^{204.0} dt e^{-t \times \ln 2/20.4} \Big/ \int_0^{inf} dt e^{-t \times \ln 2/20.4} = 0.999 \tag{6.17}$$

where the half-life is 20.40 ms, and the lower bound of 2 μs represents the 2 μs of prompt events being removed by the [52,54) μs time cut.

Therefore, the total efficiency is

$$\epsilon_{\text{Total}} = \epsilon_{71m1} = \epsilon_E \delta_{\epsilon_E} \epsilon_{\Delta T} = 0.672721 \delta_{\epsilon_E} \times 0.999 = 0.672048^{+0.00034}_{-0.05188} \tag{6.18}$$

6.5.5 Candidate Events

See Table 6.4 for details about the ^{71}Ge events and Table 6.5 for candidate events of all signatures.

In the open analysis, there are five detector events that exhibit the 198.354 keV two-step ^{71}Ge (E_γ = 198.394 keV) signature. The distribution of events is as follows:

DS0 - 0 events (0 Natural/0 Enriched)

DS1 - 1 events (0 Natural/1 Enriched)

DS2 - 0 events

DS3 - 0 events

DS5 - 3 events (2 Natural/1 Enriched)

DS6 - 1 events (1 Natural/0 Enriched)

Total: 5 events ($3\pm\sqrt{3}$ Natural/$2\pm\sqrt{2}$ Enriched)

Fifteen additional events were found within the [52,54) μs prompt window and were removed from consideration.

Figure 6.7 shows the open candidate event waveforms.

In the blind analysis, there are five detector events that exhibit the 198.354 keV two-step ^{71}Ge (E_γ = 198.394 keV) signature. The distribution of events is as follows:

DS1 - 0 events (0 natural/ 0 enriched)

DS2 - 1 events (0 natural/ 1 enriched)

DS5c - 1 events (1 natural/ 0 enriched)

DS6a - 3 events (0 natural/ 3 enriched)

Total: 5 events ($1\pm\sqrt{1}$ natural/ $4\pm\sqrt{4}$ enriched)

Figure 6.8 shows the energy spectrum and Time Since Muon (muDT) of the open and blind candidate events.

6.5.6 Discussion

The open analysis contains 13.396±0.203 kg · yr of enriched germanium exposure and 5.041± 0.119 kg · yr of natural germanium exposure. The blind analysis contains 12.154 ± 0.173 kg · yr of enriched germanium exposure and 4.211 ± 0.094 kg · yr of natural germanium exposure.

The production rate of the 198.354 keV ^{71}Ge excited state is calculated using the candidate events, the expected background event count, exposure, the total signature efficiency and the uncertainty for each quantity (Eq. 6.18). The open analysis uses the candidate events, expected background, and exposure from the open data set. The open and blind analysis uses the candidate events, expected backgrounds, and exposure for the open and blind data sets, combined by addition.

The expected background count in the open data set is 0.096±0.012 counts in natural detectors, and 0.204 ± 0.018 counts in enriched detectors. The expected background count in the blind data set is 0.034 ± 0.007 counts in natural detectors, and 0.086 ± 0.012 counts in enriched detectors.

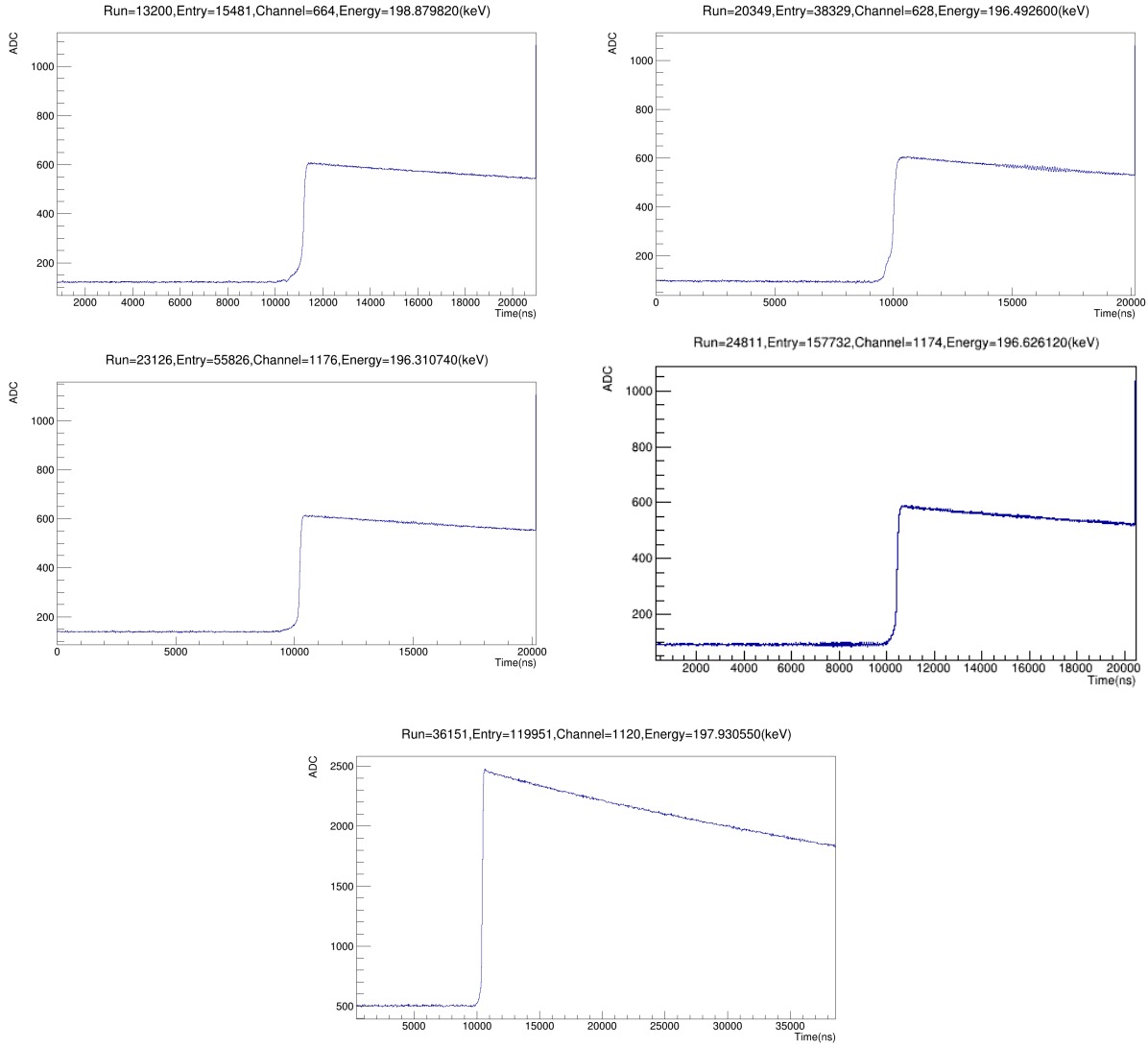

Figure 6.7: Waveforms of each ^{71}Ge candidate event in the open data set.

Table 6.4: Candidate events of ^{71}Ge-like signature.

DS	Run	Event #	Detector	muonMultiplicity	Energy (keV)	muDT (s)	Material
1	13200	15481	C1P3D4	4	198.87982	0.044529	EnrGe
5	20349	38329	C1P4D2	4	196.49260	0.0034570	NatGe
5	23126	55826	C2P3D1	4	196.31074	0.0147028	EnrGe
5	24811	157732	C2P2D1	2	196.62612	0.0025212	NatGe
6	36151	119951	C2P4D4	4	197.93055	7.090e-05	NatGe
0	4263	43135	C1P1D1	4	199.76604	0.000052	NatGe
0	4898	30205	C1P1D4	4	198.52081	0.000052	EnrGe
0	5571	18553	C1P5D1	4	198.738400	0.000052	NatGe
1	10629	26866	C1P2D2	4	197.562998	0.000052	EnrGe
1	11453	7635	C1P6D3	5	198.142351	0.000053	EnrGe
5	20903	110929	C1P2D3	3	198.649054	0.000052	EnrGe
5	21263	92516	C1P3D2	4	200.489815	0.000053	EnrGe
5	21788	91344	C1P4D2	4	199.995975	0.000052	NatGe
5	24811	157732	C2P2D1	4	196.626129	0.000052	NatGe
6	28080	109858	C1P3D4	4	199.781500	0.000052	EnrGe
6	29234	6700	C1P3D3	4	200.284260	0.000052	EnrGe
6	30247	77709	C2P5D4	4	202.601717	0.000052	EnrGe
6	33719	53690	C2P7D4	3	203.128133	0.000052	NatGe
6	35028	109167	C2P2D3	5	194.378991	0.000053	NatGe
6	36070	121002	C1P7D4	4	201.104260	0.000053	EnrGe

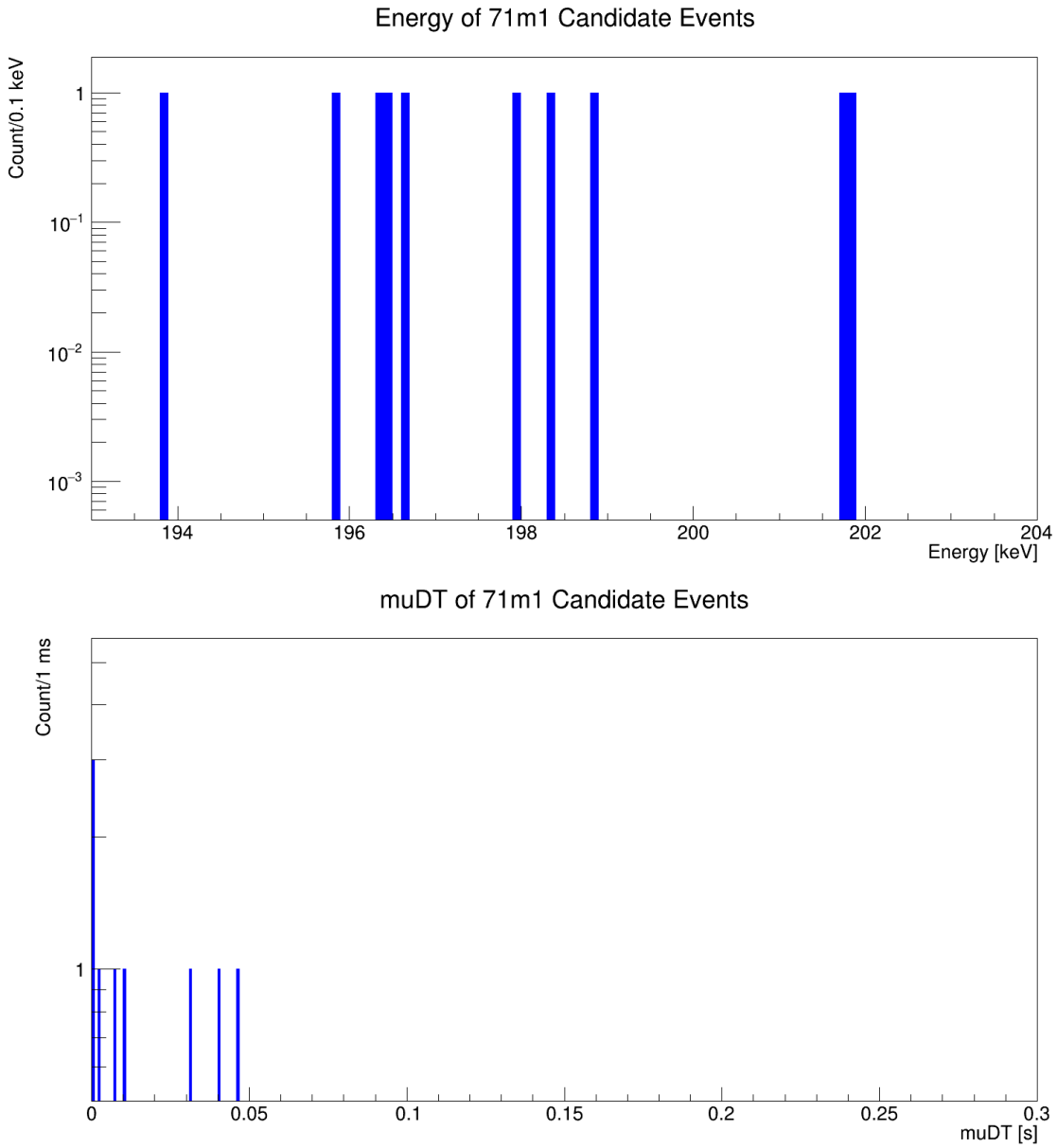

Figure 6.8: Open and blind analysis: Energy spectrum and Time Since Muon (muDT) for all ^{71}Ge candidate events, open and blind.

Table 6.5: Event statistics, upper limits, and production rates of ^{71}Ge-like, ^{75}Ge-like, ^{77}Ge-like, and ^{69}Ge-like events for DS0-DS3, DS5, DS6a. The upper limits (UL) are the calculated using the Feldman-Cousins method with a 68.27% confidence level.

	Open		Open and Blind	
	NatGe	EnrGe	NatGe	EnrGe
^{71m1}**Ge** (198.394 keV γ)				
Candidate Events	$3^{+1.732}_{-1.732}$	$2^{+1.414}_{-1.414}$	$4^{+2.732}_{-2.732}$	$6^{+3.414}_{-3.414}$
Expected Bg Events	$0.096^{+0.012}_{-0.012}$	$0.204^{+0.018}_{-0.018}$	$0.130^{+0.019}_{-0.019}$	$0.290^{+0.030}_{-0.030}$
Exp. rate [c/(kg·yr)]	$0.857^{+0.516}_{-0.516}$	$0.199^{+0.158}_{-0.158}$	$0.622^{+0.442}_{-0.442}$	$0.333^{+0.201}_{-0.201}$
Signal Count UL	5.205	4.045	6.645	8.985
Rate UL [c/(kg·yr)]	$1.537^{+0.124}_{-0.124}$	$0.449^{+0.035}_{-0.035}$	$1.069^{+0.086}_{-0.086}$	$0.523^{+0.041}_{-0.041}$
^{75m1}**Ge** (139.68 keV γ)				
Candidate Events	$59^{+7.681}_{-7.681}$	$131^{+11.446}_{-11.446}$	$104^{+14.389}_{-14.389}$	$213^{+20.501}_{-20.501}$
Expected Bg Events	$67.465^{+8.105}_{-8.105}$	$117.410^{+10.561}_{-10.561}$	$98.991^{+14.335}_{-14.335}$	$189.857^{+20.443}_{-20.443}$
Exp. rate [c/(kg·yr)]	$-1.851^{+2.756}_{-2.756}$	$1.118^{+1.570}_{-1.570}$	$0.597^{+2.663}_{-2.663}$	$0.998^{+1.467}_{-1.467}$
Signal Count UL	2.455	25.420	15.830	38.465
Rate UL [c/(kg·yr)]	$0.537^{+0.035}_{-0.035}$	$2.091^{+0.131}_{-0.131}$	$1.886^{+0.123}_{-0.123}$	$1.659^{+0.104}_{-0.104}$
^{69m1}**Ge** (86.78 keV γ)				
Exp. rate [c/(kg·yr)]	Not Implemented			
^{69m2}**Ge** (397.94 keV γ)				
Exp. rate [c/(kg·yr)]	Not Implemented			
^{77m1}**Ge** (159.66 keV γ)				
Candidate Events	$47^{+6.856}_{-6.856}$	$137^{+11.705}_{-11.705}$	$81^{+12.687}_{-12.687}$	$202^{+19.767}_{-19.767}$
Expected Bg Events	$53.644^{+7.123}_{-7.123}$	$120.815^{+10.772}_{-10.772}$	$81.644^{+13.019}_{-13.019}$	$193.941^{+20.733}_{-20.733}$
Exp. rate [c/(kg·yr)]	$-8.590^{+14.084}_{-14.084}$	$7.874^{+9.476}_{-9.476}$	$-0.454^{+13.813}_{-13.813}$	$2.056^{+8.523}_{-8.523}$
Signal Count UL	2.650	28.510	9.180	22.885
Rate UL [c/(kg·yr)]	$3.426^{+0.220}_{-0.220}$	$13.870^{+0.853}_{-0.853}$	$6.467^{+0.413}_{-0.413}$	$5.837^{+0.359}_{-0.359}$

$$\begin{aligned}\text{Open Rate}_{\text{Nat}} &= \text{Candidates}/\epsilon_{71\text{m}1}/\text{Exp}_{\text{NatGe}} - \text{Background}/\epsilon_{71\text{m}1}/\text{Exp}_{\text{NatGe}} \\ &= (0.886 \pm 0.5163) - (0.028 \pm 0.004) \\ &= 0.857^{+0.5163}_{-0.5163}\ \text{c/kg} \cdot \text{yr} \end{aligned} \tag{6.19}$$

$$\begin{aligned}\text{Open Rate}_{\text{Enr}} &= \text{Candidates}/\epsilon_{71\text{m}1}/\text{Exp}_{\text{EnrGe}} - \text{Background}/\epsilon_{71\text{m}1}/\text{Exp}_{\text{EnrGe}} \\ &= (0.222 \pm 0.158) - (0.023 \pm 0.003) \\ &= 0.199^{+0.1581}_{-0.1581}\ \text{c/kg} \cdot \text{yr} \end{aligned} \tag{6.20}$$

$$\begin{aligned}\text{(Open and Blind) Rate}_{\text{Nat}} &= \text{Candidates}/\epsilon_{71\text{m}1}/\text{Exp}_{\text{NatGe}} - \text{Background}/\epsilon_{71\text{m}1}/\text{Exp}_{\text{NatGe}} \\ &= (0.643 \pm 0.442) - (0.021 \pm 0.004) \\ &= 0.622^{+0.442}_{-0.442}\ \text{c/kg} \cdot \text{yr} \end{aligned} \tag{6.21}$$

$$\begin{aligned}\text{(Open and Blind) Rate}_{\text{Enr}} &= \text{Candidates}/\epsilon_{71\text{m}1}/\text{Exp}_{\text{EnrGe}} - \text{Background}/\epsilon_{71\text{m}1}/\text{Exp}_{\text{EnrGe}} \\ &= (0.349 \pm 0.201) - (0.017 \pm 0.002) \\ &= 0.333^{+0.201}_{-0.201}\ \text{c/kg} \cdot \text{yr} \end{aligned} \tag{6.22}$$

The Feldman-Cousins method [39] was used to determine the upper limit. For the open analysis, the 68.27% signal count upper limit is 5.205 counts in the natural detectors, and 4.045 counts in the enriched detectors. For the open and blind analysis, the 68.27% signal count upper limit is 6.645 counts in the natural detectors, and 8.985 counts in the enriched detectors. The corresponding 68.27% upper limit production rates were calculated.

$$\text{Open FC 68.27\% UL Rate}_{\text{Nat}} = 1.536 \pm 0.124 \text{ c/kg} \cdot \text{yr} \tag{6.23}$$

$$\text{Open FC 68.27\% UL Rate}_{\text{Enr}} = 0.449 \pm 0.035 \text{ c/kg} \cdot \text{yr} \tag{6.24}$$

$$\text{(Open and Blind) FC 68.27\% UL Rate}_{\text{Nat}} = 1.069 \pm 0.086 \text{ c/kg} \cdot \text{yr} \tag{6.25}$$

$$\text{(Open and Blind) FC 68.27\% UL Rate}_{\text{Enr}} = 0.523 \pm 0.041 \text{ c/kg} \cdot \text{yr} \tag{6.26}$$

All production rates are recorded in Table 6.5.

6.6 ^{75}Ge

6.6.1 ^{75}Ge Decay Signatures

Secondary neutrons can also produce ^{75}Ge in our detectors, primarily created through the reactions $^{74}\text{Ge}(\text{n},\gamma)^{75}\text{Ge}$, $^{76}\text{Ge}(\gamma,\text{n})^{75}\text{Ge}$, $^{76}\text{Ge}(\text{n},2\text{n})^{75}\text{Ge}$, and $^{76}\text{Ge}(\mu,\text{n})^{75}\text{Ge}$. The energetic de-excitation of ^{75}Ge can lead to the ground state or to a meta-stable state $^{75\text{m}}$Ge. The meta-stable (139.69 keV) state will undergo an IT decay ($t_{1/2} = 47.7$ s) to the ground state, emitting a gamma of 139.68 keV. The IT decay can also emit two gammas of 77.86 keV and 61.92 keV instead of one gamma of 139.68 keV, however the relative intensity of the two-gamma decay is sufficiently low to be considered negligible [55]. This IT decay has a half-life which is short enough to maintain correlation with a muon passing through our veto system.

The meta-stable state can also β-decay to ^{75}As, however the branching ratio (0.03%) shows that this pattern is not very significant. [55]

Figure 6.9 shows the energy level scheme ^{75}Ge up to our 139.69 keV level of interest.

6.6.2 Event Selection

At our signature energy of 139.68 keV, our energy resolution is ~ 0.8 keV [46]. The energy window of plus/minus 5 keV was chosen as a conservative value.
The time window 240.0 s was chosen for the high probability of observing the signature while having a small impact on the muon rejection rate discussed in Section 6.1.2. The time window was extended by 54 μs to account for the veto-Ge timing offset.

The possible gamma energy is 139.68 keV. We select a candidate event of energy within 5 keV of the gamma energy, following a muon event within 240.0 s plus 54 μs ($\sim$5 times of 47.7 s). If the timestamp falls between [52,54) μs it will be removed as a prompt background (see Section 6.1.3).

6.6.3 Backgrounds

One potential background of the 139.68 keV signature is the β-decay of ^{75m}Ge to ^{75}As, however as discussed in 6.6.1 the branching ratio is not large enough for this background to be significant. Another potential background of the 139.68 keV signature is electron capture on ^{57}Co ($E_\gamma = 136.47356$ keV, $t_{1/2} = 271.74$ days). The requirement of coincidence with a muon suppresses this background.

Another important source of background is the random coincidence background. This occurs when a detector event within the signature energy window and within the signature time window is found, but the event was not induced by a muon. These event are indistinguishable from true muon-induced events and are the prominent source of background in this study. As discussed in Section 6.4, the random coincidence background rate was measured throughout the open data sets. Those background rates are used to estimate the expected background value for each signature in the analysis. The expected background

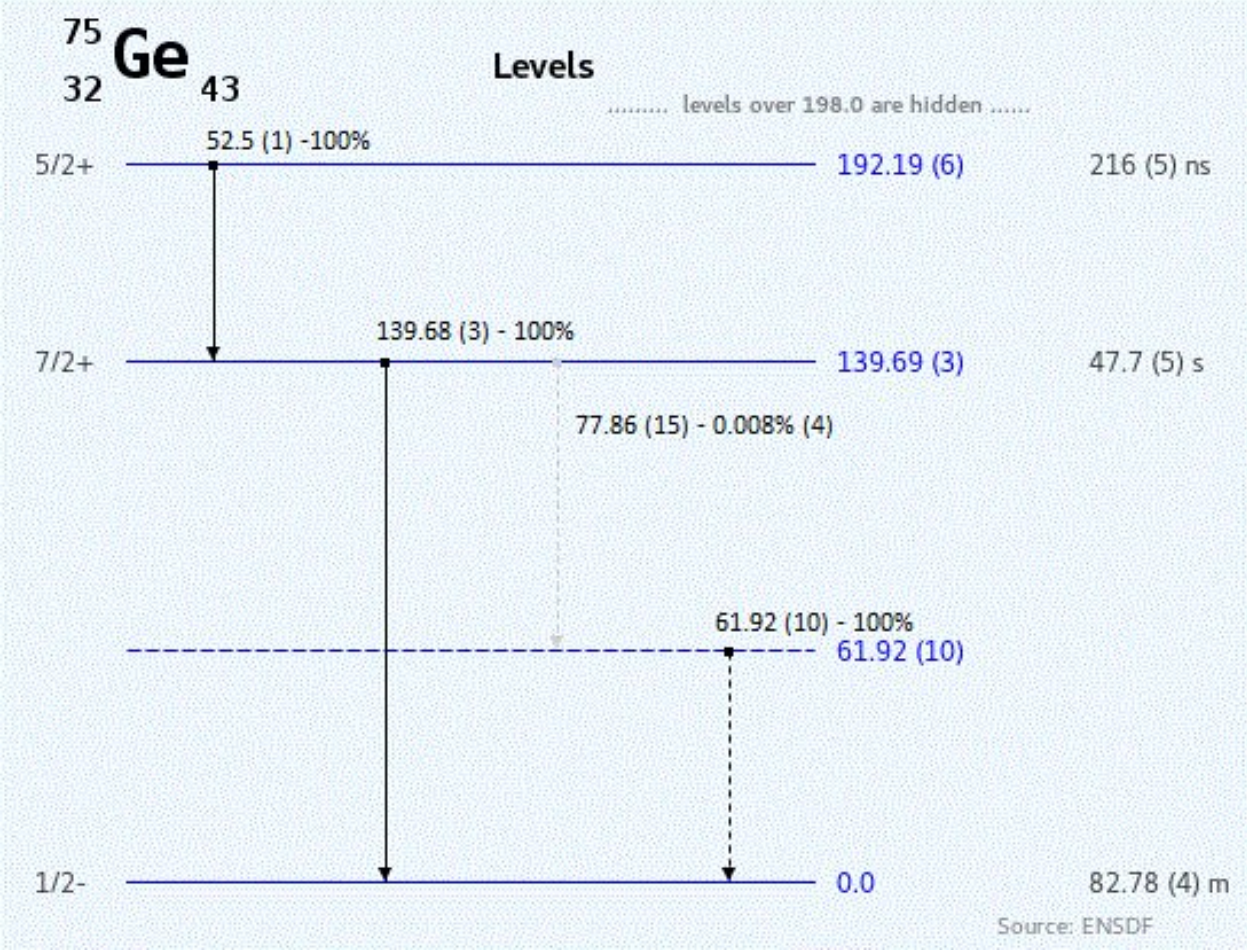

Figure 6.9: Energy level scheme for ^{75}Ge including gamma energies. Figure generated on [49].

(Bg_{Exp}) was calculated as follows:

$$\begin{aligned} Bg_{Exp} \;=\; \Sigma_{DS}\,[(\text{Bg Rate})_{DS} \;\times\; (\text{Signature Search Exposure})_{DS}]\times \\ \text{Size of Energy Window} \end{aligned} \tag{6.27}$$

and

$$\begin{aligned} (\text{Signature Search Exposure})_{DS} = \;\; (\text{Effective Mass})_{DS} \;\times \\ (\text{Combined Search Window Livetime}) \end{aligned} \tag{6.28}$$

The effective mass is used to accurately represent the exposure of the combined signature search windows in this analysis. The effective mass values were calculated using the total candidate search livetime (livetime combined of muon search windows) and the active mass in each data set [30][31][60][32][58][59].

The random coincidence background for the 139.68 keV ^{75}Ge signature in the open data is estimated to be:

$$\text{NatGe} : 67.465 \pm 8.105 \text{ Events} \tag{6.29}$$

$$\text{EnrGe} : 117.410 \pm 10.561 \text{ Events} \tag{6.30}$$

The random coincidence background for the 139.68 keV ^{75}Ge signature in the blind data is estimated to be:

$$\text{NatGe} : 31.526 \pm 6.230 \text{ Events} \tag{6.31}$$

$$\text{EnrGe} : 72.447 \pm 9.882 \text{ Events} \tag{6.32}$$

6.6.4 Efficiency

As discussed in Section 6.5.3 it is unlikely that both de-excitations (192.19 keV ^{75}Ge $\rightarrow$ 139.69 keV ^{75}Ge $\rightarrow$ ground state ^{75}Ge) will occur in a single data event, therefore there is

little worry that 139.69 keV ^{75}Ge signals will be masked by 192.19 keV ^{75}Ge decays to the ground state.

We simulated 10^6 ^{75}Ge isotopes (E = 139.69 keV) throughout the natural and enriched detectors using MaGe. An energy cut of E $\in$ (139.68 $\pm$ 5 keV) was applied and 936,006 detector depositions survived.

However each germanium detector has a "dead layer" which is not included in this result. The dead layer refers to two small outer regions of a detector in which energy deposits behave differently. The two regions are a truly dead layer, in which energy deposits do not give rise to detector signals, and a partially dead layer, sometimes called a transition layer, in which energy deposits give rise to energy degraded signals [61]. To estimate the effect of a dead layer on the signature detection efficiency, a 1 mm truly dead layer was applied to the detectors. The thickness value of 1 mm was taken from the dead layer measurement of a Majorana detector (MALBEK) [61]. In this measurement the total dead layer thickness (truly dead layer and transition layer) was found to be 0.933 $\pm$ 0.018 mm. After the 1 mm truly dead layer was applied, 880,783 detector depositions survive the energy cut. We find that we are overestimating the energy cut efficiency as each detector has a non-zero dead layer, and the result of the 0 mm dead layer simulation is an upper limit. The uncertainty of the energy cut efficiency $\delta_{\epsilon_{\mathrm{E}}}$ is calculated using the percent difference of the 0 mm dead layer and 1 mm dead layer results.

The efficiency of the energy cut is

$$\text{Percent Uncertainty}: \ \delta_{\epsilon_{\mathrm{E}}} = |(936006 - 880783)|/(0.5 \times (936006 + 880783)) = 6.08\% \tag{6.33}$$

$$\epsilon_{\mathrm{E}}\delta_{\epsilon_{\mathrm{E}}} = 936006/10^6\delta_{\epsilon_{\mathrm{E}}} = 0.936006^{+0.057}_{-0.057} \tag{6.34}$$

The efficiency of the ΔT cut is

$$\epsilon_{\Delta\mathrm{T}} = \int_{2\mu\mathrm{s}}^{240\mathrm{s}} \mathrm{dte}^{-\mathrm{t}\times\ln 2/47.7} \Big/ \int_{0}^{\mathrm{inf}} \mathrm{dte}^{-\mathrm{t}\times\ln 2/47.7} = 0.9694 \tag{6.35}$$

where the half-life is ~ 47.7 s, and the lower bound of 2 μs represents the 2 μs of prompt events being removed by the [52,54) μs time cut.

Therefore, the total efficiency is

$$\epsilon_{\text{Total}} = \epsilon_{75\text{m1}} = \epsilon_{\text{E}}\delta_{\epsilon_{\text{E}}}\epsilon_{\Delta\text{T1}} = 0.936006\delta_{\epsilon_{\text{E}}} \times 0.9694 = 0.90736^{+0.055}_{-0.055} \tag{6.36}$$

6.6.5 Candidate Events

See Table 6.5 for total candidate events. In the open analysis, there are 190 detector events that exhibit the 139.69 keV level ^{75}Ge (E_γ = 139.68 keV) signature. The distribution of events is as follows:

DS0 - 53 events (12 natural/41 enriched)

DS1 - 20 events (4 natural/16 enriched)

DS2 - 4 events (2 natural/2 enriched)

DS3 - 10 events (3 natural/7 enriched)

DS5 - 64 events (25 natural/39 enriched)

DS6 - 39 events (13 natural/26 enriched)

Total: 190 events ($59\pm\sqrt{41}$ natural/$131\pm\sqrt{96}$ enriched)

Fifteen additional events were found within the [52,54) μs prompt window and were removed from consideration.

In the blind analysis, there are 127 detector events that exhibit the 139.69 keV level ^{75}Ge (E_γ = 139.68 keV) signature. The distribution of events is as follows:

DS1 - 5 events (0 natural/ 5 enriched)

DS2 - 11 events (2 natural/ 9 enriched)

DS5c - 31 events (15 natural/ 16 enriched)

DS6a - 80 events (28 natural/ 52 enriched)

Total: 127 events ($45\pm\sqrt{45}$ natural/ $82\pm\sqrt{82}$ enriched)

Figures 6.10 – 6.12 and Figures 6.13 – 6.15 show the energy spectra and Time Since Muon (muDT) of the open and blind candidate events in natural germanium and enriched germanium respectively.

6.6.6 Discussion

The open analysis contains 13.396±0.203 kg · yr of enriched germanium exposure and 5.041± 0.119 kg · yr of natural germanium exposure. The blind analysis contains 12.154 ± 0.173 kg · yr of enriched germanium exposure and 4.211 ± 0.094 kg · yr of natural germanium exposure.

The production rate of the 139.69 keV ^{75}Ge excited state is calculated using the candidate events, the expected background count, exposure, the total signature efficiency (Eq. 6.36), and the uncertainty for each quantity. The open analysis uses the candidate events, expected background, and exposure from the open data set. The open and blind analysis uses the candidate events, expected backgrounds, and exposure for the open and blind data sets, combined by addition.

The expected background count in the open data set is 67.465 ± 8.105 counts in natural detectors, and 117.410 ± 10.561 counts in enriched detectors. The expected background count in the blind data set is 31.526 ± 6.230 counts in natural detectors, and 72.447 ± 9.882 counts in enriched detectors.

$$\begin{aligned}\text{Open Rate}_{\text{Nat}} &= \text{Candidate}/\epsilon_{75\text{m1}}/\text{Exp}_{\text{NatGe}} - \text{Background}/\epsilon_{75\text{m1}}/\text{Exp}_{\text{NatGe}} \\ &= (12.900 \pm 1.878) - (14.751 \pm 2.016) \\ &= -1.851^{+2.756}_{-2.756}\ \text{cts/kg} \cdot \text{yr} \end{aligned} \tag{6.37}$$

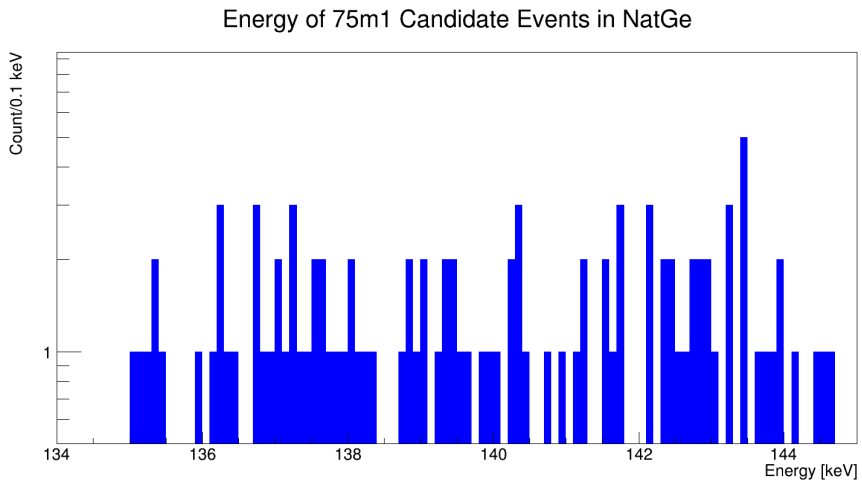

Figure 6.10: Open and blind analysis: Energy spectrum for all ^{75}Ge candidate events, open and blind, in natural germanium.

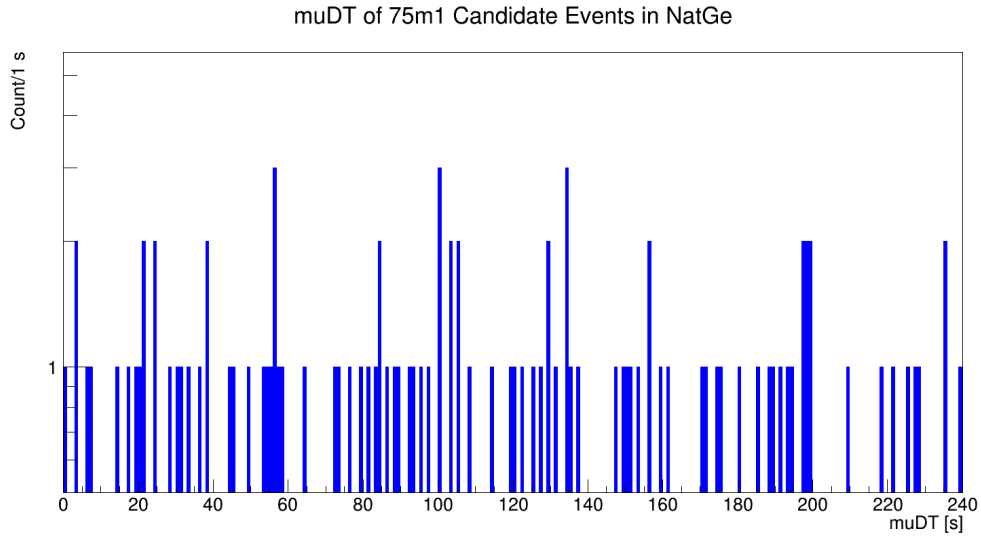

Figure 6.11: Open and blind analysis: Time Since Muon for all ^{75}Ge candidate events, open and blind, in natural germanium.

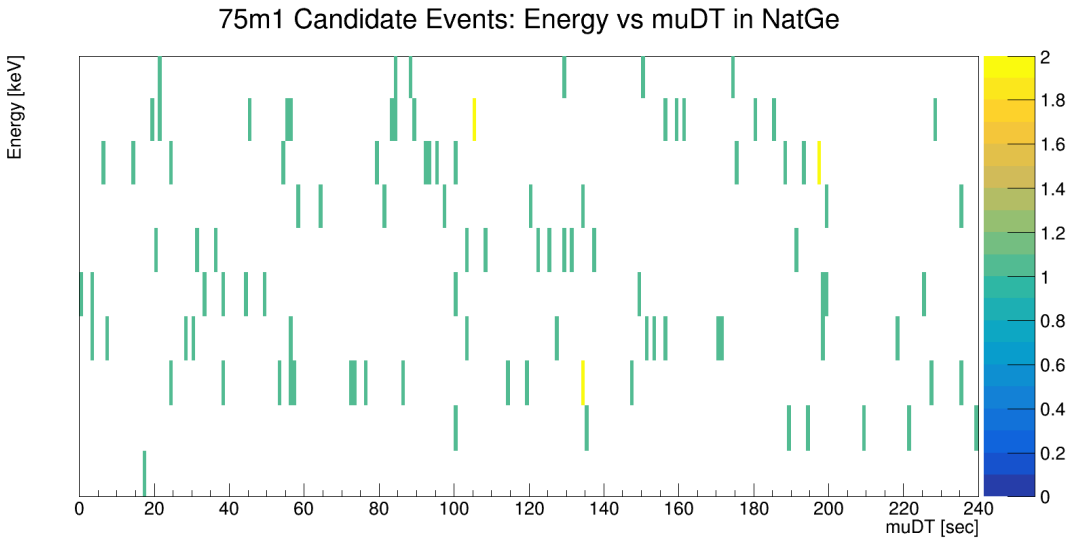

Figure 6.12: Open and blind analysis: Energy vs Time Since Muon for all ^{75}Ge candidate events, open and blind, in natural germanium.

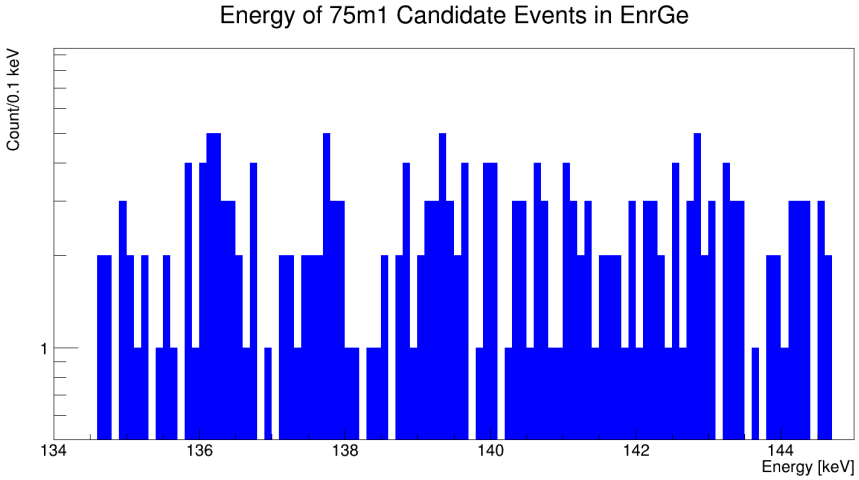

Figure 6.13: Open and blind analysis: Energy spectrum for all ^{75}Ge candidate events, open and blind, in enriched germanium.

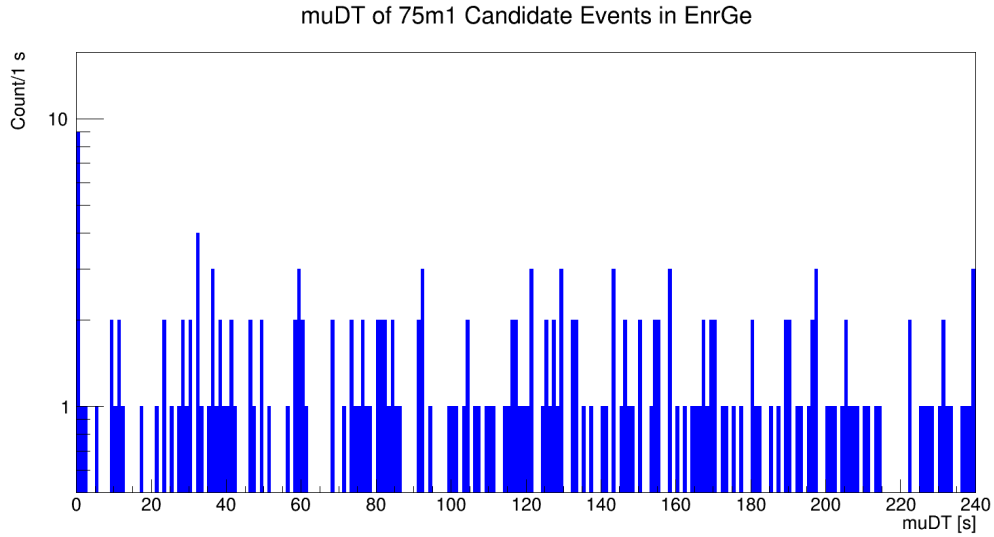

Figure 6.14: Open and blind analysis: Time Since Muon for all ^{75}Ge candidate events, open and blind, in enriched germanium.

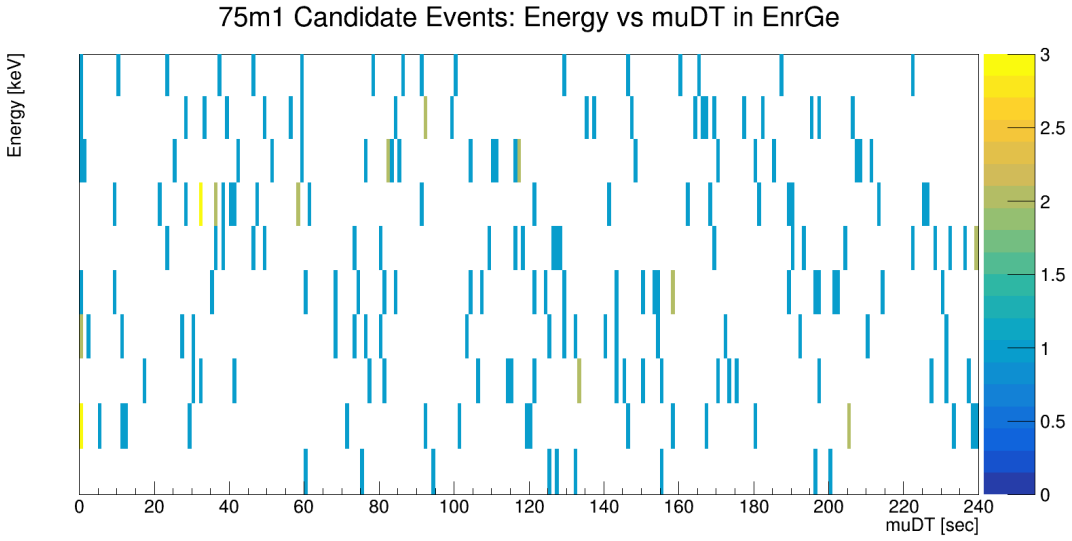

Figure 6.15: Open and blind analysis: Energy vs Time Since Muon for all ^{75}Ge candidate events, open and blind, in enriched germanium.

$$\begin{aligned}\text{Open Rate}_{\text{Enr}} &= \text{Candidate}/\epsilon_{75\text{m1}}/\text{Exp}_{\text{EnrGe}} - \text{Background}/\epsilon_{75\text{m1}}/\text{Exp}_{\text{EnrGe}} \\ &= (10.777 \pm 1.159) - (9.659 \pm 1.059) \\ &= 1.118^{+1.570}_{-1.570}\ \text{cts/kg} \cdot \text{yr}\end{aligned} \tag{6.38}$$

$$\begin{aligned}\text{(Open and Blind) Rate}_{\text{Nat}} &= \text{Candidate}/\epsilon_{75\text{m1}}/\text{Exp}_{\text{NatGe}} - \text{Background}/\epsilon_{75\text{m1}}/\text{Exp}_{\text{NatGe}} \\ &= (12.390 \pm 1.894) - (11.793 \pm 1.872) \\ &= 0.597^{+2.663}_{-2.663}\ \text{cts/kg} \cdot \text{yr}\end{aligned} \tag{6.39}$$

$$\begin{aligned}\text{(Open and Blind) Rate}_{\text{Enr}} &= \text{Candidate}/\epsilon_{75\text{m1}}/\text{Exp}_{\text{EnrGe}} - \text{Background}/\epsilon_{75\text{m1}}/\text{Exp}_{\text{EnrGe}} \\ &= (9.188 \pm 1.055) - (8.190 \pm 1.020) \\ &= 0.998^{+1.467}_{-1.467}\ \text{cts/kg} \cdot \text{yr}\end{aligned} \tag{6.40}$$

The Feldman-Cousins method [39] was used to determine the upper limit. For the open analysis, the 68.27% signal count upper limit is 2.455 counts in the natural detectors, and 25.420 counts in the enriched detectors. For the open and blind analysis, the 68.27% signal count upper limit is 15.83 counts in the natural detectors, and 38.465 counts in the enriched detectors. The corresponding 68.27% upper limit production rates are calculated.

$$\text{Open FC 68.27\% UL Rate}_{\text{Nat}} = 0.537 \pm 0.035\ \text{cts/kg} \cdot \text{yr} \tag{6.41}$$

$$\text{Open FC 68.27\% UL Rate}_{\text{Enr}} = 2.091 \pm 0.131 \text{ cts/kg} \cdot \text{yr} \tag{6.42}$$

$$\text{(Open and Blind) FC 68.27\% UL Rate}_{\text{Nat}} = 1.886 \pm 0.123 \text{ cts/kg} \cdot \text{yr} \tag{6.43}$$

$$\text{(Open and Blind) FC 68.27\% UL Rate}_{\text{Enr}} = 1.659 \pm 0.104 \text{ cts/kg} \cdot \text{yr} \tag{6.44}$$

All production rates are recorded in Table 6.5.

6.7 ^{69}Ge

6.7.1 ^{69}Ge Decay Signatures

Secondary protons and neutrons contribute to the production of ^{69}Ge in our detectors through the reactions ^{70}Ge(p, d)^{69}Ge, ^{70}Ge(γ, n)^{69}Ge, ^{70}Ge(n, 2n)^{69}Ge, ^{70}Ge(μ, n)^{69}Ge, and through decays of ^{69}As produced in our detectors through ^{70}Ge(p,2nγ)^{69}As. The energetic de-excitation of ^{69}Ge can lead to the ground state or the meta-stable states 86.76 keV ^{69m1}Ge and 397.94 keV ^{69m2}Ge. The 86.76 keV ^{69m1}Ge state will decay directly to the ground state with a half-life of 5.1 μs. Similarly, the 397.94 keV ^{69m2}Ge state will also decay directly to the ground state with a half-life of 2.81 μs [56]. Both de-excitations have half-lives short enough to maintain correlation with a muon passing through our system.

Figure 6.16 shows the energy level scheme ^{69}Ge up to our 397.946 keV level of interest.

There has been some discussion on the effectiveness of this signature as applied in this work. As the half-lives of the de-excitations are on the order of μs some of these signature events are invisible to this analysis. For example, since detector energy depositions are built into 20 μs events then it is possible that the ^{69}Ge isotope can be produced through an

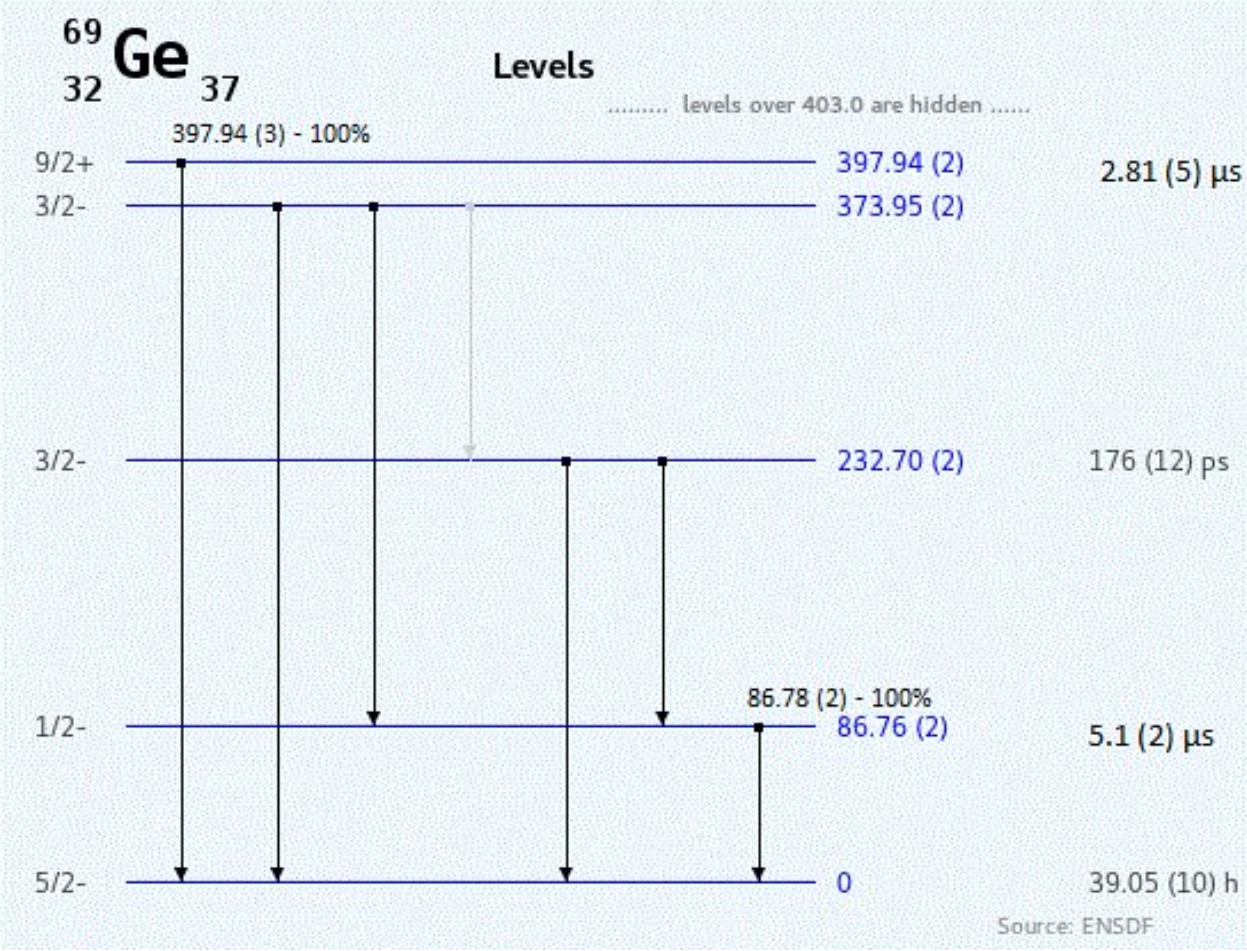

Figure 6.16: Energy level scheme for ^{69}Ge including relevant gamma energies. Figure generated on [49].

interaction such as ^{70}Ge(p,d)^{69}Ge, and decay within the same detector event. Such an event would have a detector energy outside of the signature energy window and would therefore not be identified as a candidate event in this analysis. Instead a different signature might look for the bi-product of the interaction first (d in this example) and then the isotope decay. This kind of signature might be more appropriate for this isotope.

6.7.2 Event Selection

At our signature energies of 86.78 keV and 397.94 keV, our energy resolution is $\sim$ 0.7 keV and $\sim$ 1 keV respectively [46]. The energy window of plus/minus 5 keV was chosen as a conservative value.

The time windows 51 μs and 29 μs were chosen for the high probability of observing the signature. The time window was extended by 54 μs to account for the veto-Ge timing offset.

The possible gamma energies are 86.78 keV and 397.94 keV. We select a candidate event of energy within 5 keV of either gamma energy, following a muon event within 51 μs plus 54 μs (10 times of 5.1 μs) for the 86.78 keV gamma or 29 μs plus 54 μs ($\sim$10 times of 2.81 μs) for the 397.94 keV gamma. If the timestamp falls between [52,54) μs it will be removed as a prompt background (see Section 6.1.3).

6.7.3 Backgrounds

One potential background of the 86.78 keV signature is the IT decay of ^{68m}Cu from the surrounding copper ($E_\gamma = 84.6$ keV, $t_{1/2} = 3.75$ min).

The probability of seeing the ^{68m}Cu decay in our signature time window is as follows:

$$\epsilon_{\Delta T} = \int_0^{0.000051} \mathrm{dt} e^{-t \times \ln 2/225} \Big/ \int_0^{\inf} \mathrm{dt} e^{-t \times \ln 2/225} = 1.57 \cdot 10^{-5}\% \tag{6.45}$$

where the half-life of the ^{68m}Cu decay is 3.75 minutes (225 seconds). So this background is not significant.

The effective mass is used to accurately represent the exposure of the combined signature search windows in this analysis. The effective mass values were calculated using the total

candidate search livetime (livetime combined of muon search windows) and the active mass in each data set [30][31][60][32][58][59].

The isotopes ^{87}Mo, ^{79}Kr, ^{116}Rh, and ^{153}Er are all potential backgrounds for the 397.94 keV signature, however it is unlikely that they would be found in our detector modules.

6.7.4 Efficiency

First the efficiency of the 86.76 keV ^{69}Ge signature. We simulated 10^6 ^{69}Ge isotopes (E = 86.76 keV) throughout the natural and enriched detectors using MaGe. An energy cut of E $\in$ (86.78 $\pm$ 5 keV) was applied and 981,053 detector depositions survived.

The efficiency of the energy cut is

$$\epsilon_{\mathrm{E1}} = 981053/10^6 = 98.1053\% \tag{6.46}$$

The efficiency of the ΔT1 cut is

$$\epsilon_{\Delta \mathrm{T1}} = \int_2^{51} \mathrm{dte}^{-\mathrm{t}\times\ln 2/5.1} \Big/ \int_0^{\mathrm{inf}} \mathrm{dte}^{-\mathrm{t}\times\ln 2/5.1} = 76.1013\% \tag{6.47}$$

where the half-life is 5.1 μs, and the lower bound of 2 μs represents the 2 μs of prompt events being removed by the [52,54) μs time cut.

Therefore, the total efficiency is about

$$\epsilon_{\mathrm{Total}} = \epsilon_{\mathrm{69m1}} = \epsilon_{\mathrm{E1}}\epsilon_{\Delta \mathrm{T1}} = 98.1053\% \times 76.1013\% = 74.6594\% \tag{6.48}$$

Second the efficiency of the 397.94 keV ^{69}Ge signature. We simulated 10^6 ^{69}Ge isotopes (E = 397.94 keV) throughout the natural and enriched detectors using MaGe. An energy cut of E $\in$ (397.94 $\pm$ 5 keV) was applied and 356,912 detector depositions survived.

The efficiency of the energy cut is

$$\epsilon_{\mathrm{E2}} = 356912/10^6 = 35.6912\% \tag{6.49}$$

The efficiency of the ΔT2 cut is

$$\epsilon_{\Delta T2} = \int_{2}^{29} \mathrm{dt} e^{-t \times \ln 2/2.81} \Big/ \int_{0}^{\mathrm{inf}} \mathrm{dt} e^{-t \times \ln 2/2.81} = 60.98\% \tag{6.50}$$

where the half-life is 2.81 μs, and the lower bound of 2 μs represents the 2 μs of prompt events being removed by the [52,54) μs time cut.

Therefore, the total efficiency is about

$$\epsilon_{\mathrm{Total}} = \epsilon_{69\mathrm{m2}} = \epsilon_{\mathrm{E2}} \epsilon_{\Delta T2} = 35.6912\% \times 60.98\% = 21.7645\% \tag{6.51}$$

However, the half-lives of both ^{69}Ge signatures are nearly the same magnitude as the MAJORANA DEMONSTRATOR data event window (20 μs). This indicates it is possible for an excited state of ^{69}Ge to be produced and decay within a single data event. Such events would be invisible to this analysis. An additional simulation was used to estimate the percentage of "invisible" ^{69}Ge signatures. We simulated 10^7 gammas on a cube of ^{70}Ge. ^{69}Ge was produced by 78,255 of these gammas. In total, 21 $^{69\mathrm{m1}}$Ge and 4 $^{69\mathrm{m2}}$Ge isotopes were produced. The signals were built into 20 μs detector events and an energy cut of E $\in$ (86.76 $\pm$ 5 keV) was applied and 11 detector events survived, however only 3 were true $^{69\mathrm{m1}}$Ge de-excitations. A separate energy cut of E $\in$ (397.94 $\pm$ 5 keV) was applied and 4 detector events survived, however none of these were true $^{69\mathrm{m2}}$Ge de-excitations. This is strong evidence to suggest that both of these ^{69}Ge signatures are invisible to this analysis technique.

The ^{69}Ge signatures will not be implemented in this analysis due to low detection efficiency.

6.7.5 Discussion

The ^{69}Ge signatures are not implemented in this analysis due to low detection efficiency.

All production rates are recorded in Table 6.5.

6.8 ^{77}Ge

6.8.1 ^{77}Ge Decay Signatures

Secondary neutrons can also produce ^{77}Ge in our detectors, primarily created through the reaction ^{76}Ge(n, γ)^{77}Ge. The energetic de-excitation of ^{77}Ge can lead to the ground state or to a meta-stable state ^{77m}Ge. The meta-stable (159.71 keV) state will undergo an IT decay ($t_{1/2} = 53.7$) s to the ground state 19% of the time, emitting a gamma of 159.66 keV. The other 81% of the time, the meta stable state will β-decay directly to ^{77}As $t_{1/2} = 53.7$ s. The IT decay has a half-life which is short enough to maintain correlation with a muon passing through our veto system.

Figure 6.17 shows the energy level scheme ^{77}Ge up to our 159.71 keV level of interest.

6.8.2 Event Selection

At our signature energy of 159.66 keV, our energy resolution is $\sim$ 0.8 keV [46]. The energy window of plus/minus 5 keV was chosen as a conservative value.
The time window 240.0 s was chosen for the high probability of observing the signature while having a small impact on the muon rejection rate discussed in Section 6.1.2. The time window was extended by 54 μs to account for the veto-Ge timing offset.

The possible gamma energy is 159.66 keV. We select a candidate event of energy within 5 keV of the gamma energy, following a muon event within 240.0 s plus 54 μs ($\sim$4.5 times of 53.7 s). If the timestamp falls between [52,54) μs it will be removed as a prompt background (see Section 6.1.3).

6.8.3 Backgrounds

One potential background of the 159.71 keV signature is the IT decay of ^{77m}Se ($E_\gamma = 162.0$ keV ($t_{1/2} = 17.36$ s), which itself is produced by the β-decay of ^{77}As ($t_{1/2} = 38.83$ h). The requirement of coincidence with a muon suppresses this background. Two other

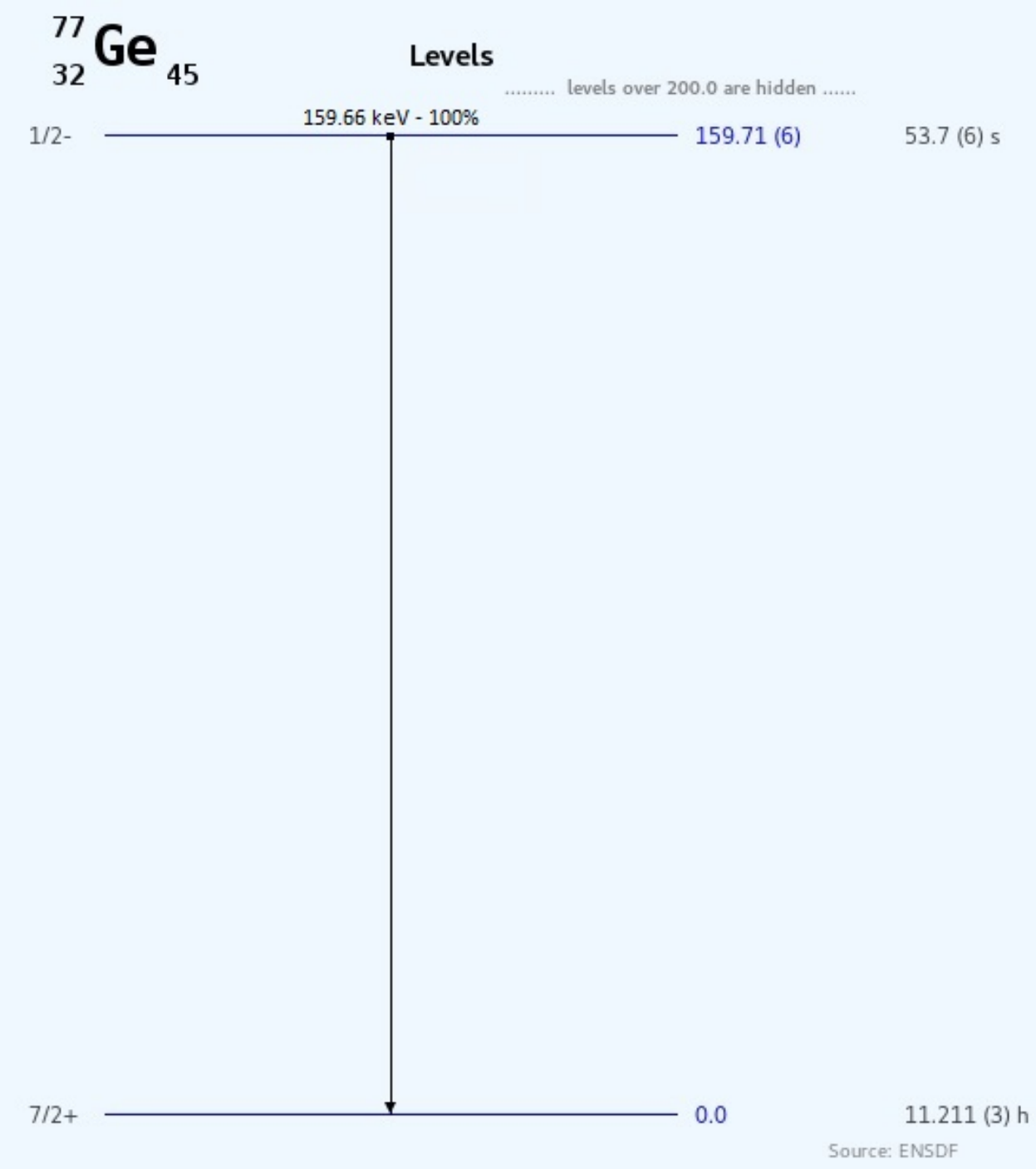

Figure 6.17: Energy level scheme for ^{77}Ge including gamma energies. Figure generated on [49].

potential backgrounds of the 159.71 keV signature are the β-decay of ^{227}Rn ($E_\gamma = 162.14$ keV ($t_{1/2} = 22.5$ s), and the alpha decay of ^{209}Rn ($E_\gamma = 154.195$ keV ($t_{1/2} = 28.5$ min). The nitrogen shield purge, along with the requirement of coincidence with a muon, suppresses these backgrounds.

Another important source of background is the random coincidence background. This occurs when a detector event within the signature energy window and within the signature time window is found, but the event was not induced by a muon. These event are indistinguishable from true muon-induced events and are the prominent source of background in this study. As discussed in Section 6.4, the random coincidence background rate was measured throughout the open data sets. Those background rates are used to estimate the expected background value for each signature in the analysis. The expected background (Bg_{Exp}) was calculated as follows:

$$\begin{aligned} Bg_{Exp} \;=\; & \Sigma_{DS}\,[(\text{Bg Rate})_{DS} \;\times\; (\text{Signature Search Exposure})_{DS}]\times \\ & \text{Size of Energy Window} \end{aligned} \tag{6.52}$$

and

$$\begin{aligned} (\text{Signature Search Exposure})_{DS} = \; & (\text{Effective Mass})_{DS} \;\times \\ & (\text{Combined Search Window Livetime}) \end{aligned} \tag{6.53}$$

The effective mass is used to accurately represent the exposure of the combined signature search windows in this analysis. The effective mass values were calculated using the number of muons and the active mass in each data set [30][31][60][32][58][59].

The random coincidence background for the 159.71 keV ^{77}Ge signature in the open data is estimated to be:

$$\text{NatGe} : 53.644 \pm 7.123 \text{ Events} \tag{6.54}$$

$$\text{EnrGe} : 120.815 \pm 10.772 \text{ Events} \tag{6.55}$$

The random coincidence background for the 159.71 keV ^{77}Ge signature in the blind data is estimated to be:

$$\text{NatGe} : 28.000 \pm 5.896 \text{ Events} \tag{6.56}$$

$$\text{EnrGe} : 73.126 \pm 9.961 \text{ Events} \tag{6.57}$$

6.8.4 Efficiency

First the efficiency of the 159.71 keV ^{77}Ge signature. We simulated 10^6 ^{77}Ge isotopes (E = 159.71 keV) throughout the natural and enriched detectors using MaGe. An energy cut of E $\in$ (159.71 $\pm$ 5 keV) was applied and 160,691 detector depositions survived.

However each germanium detector has a "dead layer" which is not included in this result. The dead layer refers to two small outer regions of a detector in which energy deposits behave differently. The two regions are a truly dead layer, in which energy deposits do not give rise to detector signals, and a partially dead layer, sometimes called a transition layer, in which energy deposits give rise to energy degraded signals [61]. To estimate the effect of a dead layer on the signature detection efficiency, a 1 mm truly dead layer was applied to the detectors. The thickness value of 1 mm was taken from the dead layer measurement of a Majorana detector (MALBEK) [61]. In this measurement the total dead layer thickness (truly dead layer and transition layer) was found to be 0.933 $\pm$ 0.018 mm. After the 1 mm truly dead layer was applied, 151,387 detector depositions survive the energy cut. We find that we are overestimating the energy cut efficiency as each detector has a non-zero dead layer, and the result of the 0 mm dead layer simulation is an upper limit. The uncertainty of the energy cut efficiency δ_{ϵ_E} is calculated using the percent difference of the 0 mm dead layer and 1 mm dead layer results.

The efficiency of the energy cut is

$$\text{Percent Uncertainty}: \ \delta_{\epsilon_{\mathrm{E}}} = |(160691 - 151387)|/(0.5 \times (160691 + 151387)) = 5.96\% \tag{6.58}$$

$$\epsilon_{\mathrm{E}}\delta_{\epsilon_{\mathrm{E}}} = 160691/10^6\delta_{\epsilon_{\mathrm{E}}} = 0.160691^{+0.009}_{-0.009} \tag{6.59}$$

The different branching ratios between $^{77\mathrm{m}}$Ge IT decay and β-decay are encapsulated in this MaGe simulation, and so do not need to be considered separately.

The efficiency of the ΔT cut is

$$\epsilon_{\Delta\mathrm{T}} = \int_{2\mu\mathrm{s}}^{240} \mathrm{dte}^{-\mathrm{t}\times\ln 2/53.7} \Big/ \int_{0}^{\mathrm{inf}} \mathrm{dte}^{-\mathrm{t}\times\ln 2/53.7} = 0.9549 \tag{6.60}$$

where the half-life is $\sim$ 53.7 s, and the lower bound of 2 μs represents the 2 μs of prompt events being removed by the [52,54) μs time cut.

Therefore, the total efficiency is about

$$\epsilon_{\mathrm{Total}} = \epsilon_{77\mathrm{m1}} = \epsilon_{\mathrm{E}}\delta_{\epsilon_{\mathrm{E}}}\epsilon_{\Delta\mathrm{T}} = 0.160691\delta_{\epsilon_{\mathrm{E}}} \times 0.9549 = 0.15344^{+0.009}_{-0.009} \tag{6.61}$$

6.8.5 Candidate Events

See Table 6.5 for total candidate events.

In the open analysis, there are 178 detector events that exhibit the 159.71 keV level ^{77}Ge (E_γ = 159.66 keV) signature. The distribution of events is as follows:

DS0 - 67 events (20 natural/ 47 enriched)

DS1 - 19 events (3 natural/ 16 enriched)

DS2 - 0 events

DS3 - 9 events (0 natural/ 9 enriched)

DS5 - 66 events (16 natural/ 50 enriched)

DS6 - 23 events (8 natural/ 15 enriched)

Total: 184 events ($47\pm\sqrt{47}$ natural/ $137\pm\sqrt{131}$ enriched)

22 additional events were found within the [52,54) μs prompt window and were removed from consideration.

In the blind analysis, there are 99 detector events that exhibit the 159.71 keV level ^{77}Ge (E_γ = 159.66 keV) signature. The distribution of events is as follows:

DS1 - 7 events (2 natural/ 5 enriched)

DS2 - 7 events (0 natural/ 7 enriched)

DS5c - 28 events (13 natural/ 15 enriched)

DS6a - 57 events (19 natural/ 38 enriched)

Total: 99 events ($34\pm\sqrt{34}$ natural/ $65\pm\sqrt{65}$ enriched)

Figures 6.18 – 6.20 and Figures 6.21 – 6.23 show the energy spectra and Time Since Muon (muDT) of the open and blind candidate events in natural germanium and enriched germanium respectively.

6.8.6 Discussion

The open analysis contains 13.396 ± 0.203 kg $\cdot$ yr of enriched germanium exposure and 5.041 ± 0.119 kg $\cdot$ yr of natural germanium exposure. The blind analysis contains 12.154 ± 0.173 kg $\cdot$ yr of enriched germanium exposure and 4.211 ± 0.094 kg $\cdot$ yr of natural germanium exposure.

The production rate of the 159.71 keV ^{77}Ge excited state is calculated using the candidate events, the expected background count, exposure, the total signature efficiency (Eq. 6.61), and the uncertainty for each quantity. The open analysis uses the candidate events, expected background, and exposure from the open data set. The open and blind analysis uses the candidate events, expected backgrounds, and exposure for the open and blind data sets, combined by addition.

The expected background count in the open data set is 53.644 ± 7.123 counts in natural detectors, and 120.815 ± 10.772 counts in enriched detectors. The expected background

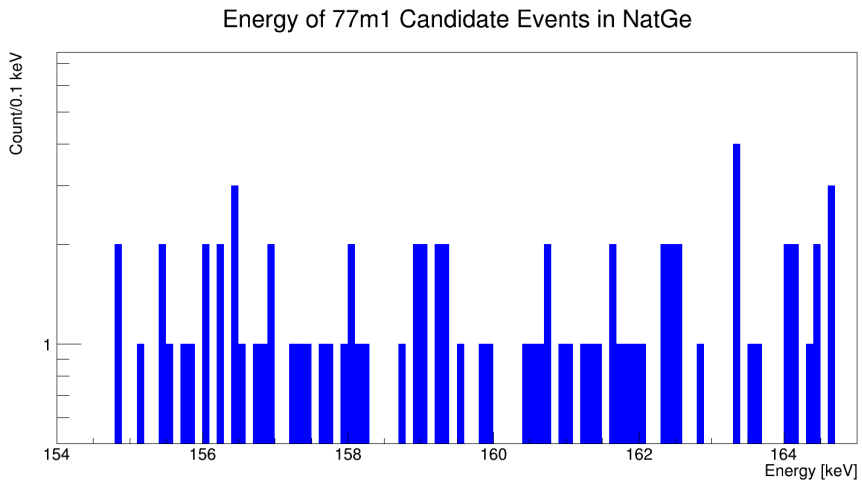

Figure 6.18: Open and blind analysis: Energy spectrum for all ^{77}Ge candidate events, open and blind, in natural germanium.

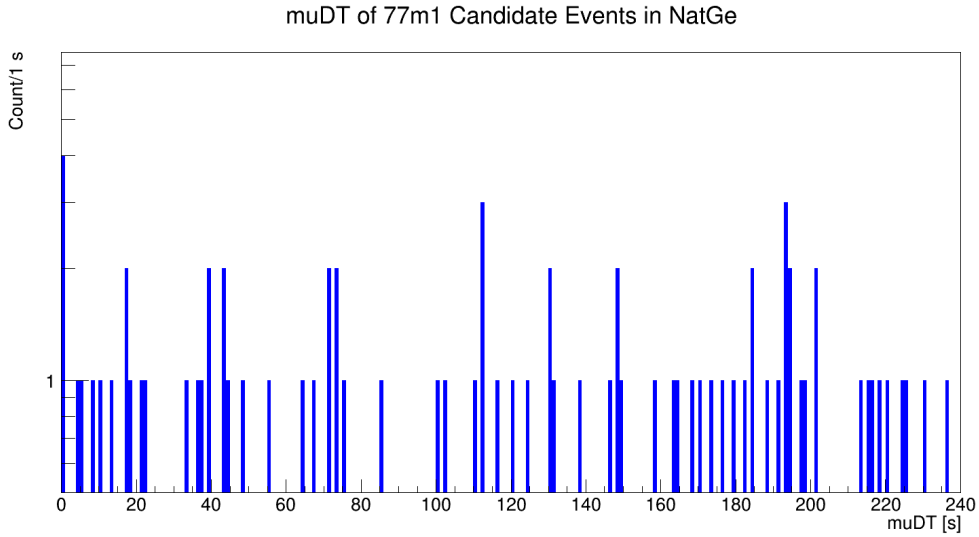

Figure 6.19: Open and blind analysis: Time Since Muon for all ^{77}Ge candidate events, open and blind, in natural germanium.

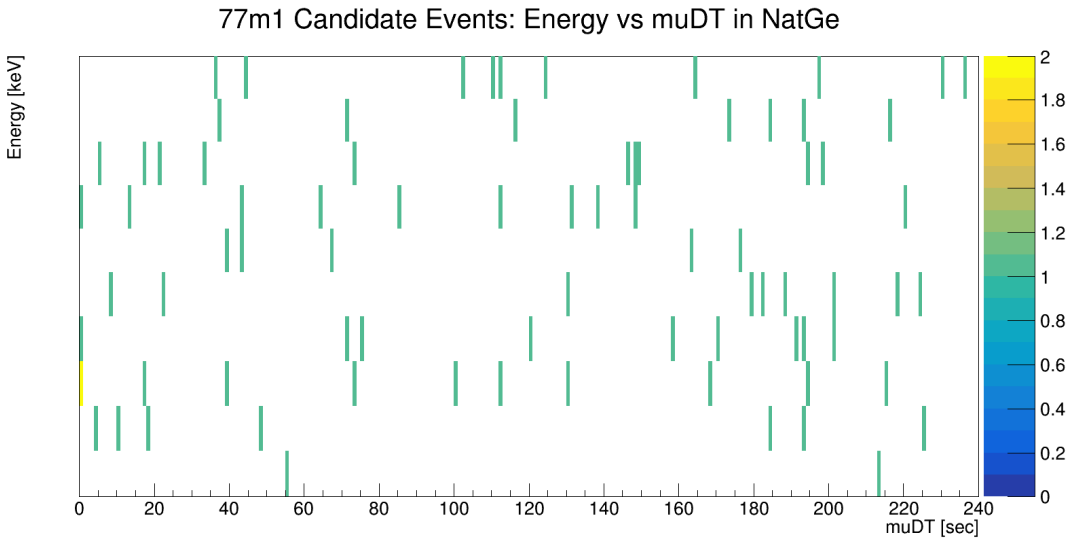

Figure 6.20: Open and blind analysis: Energy vs Time Since Muon for all ^{77}Ge candidate events, open and blind, in natural germanium.

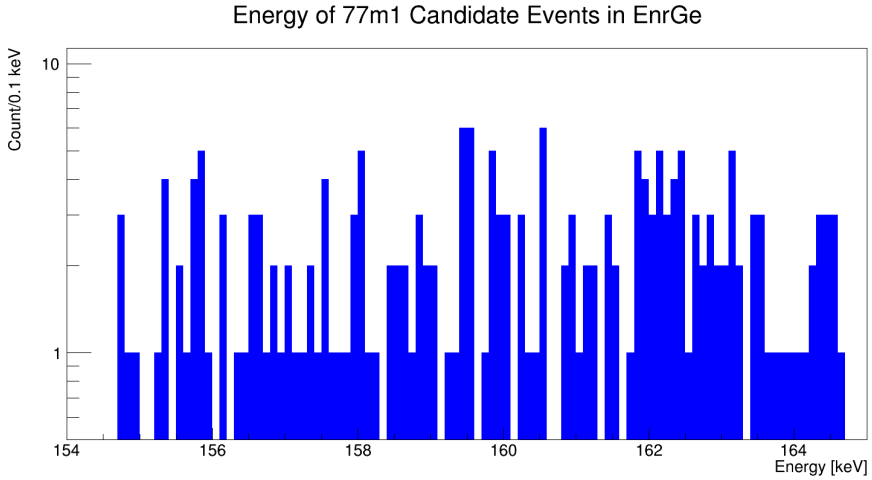

Figure 6.21: Open and blind analysis: Energy spectrum for all ^{77}Ge candidate events, open and blind, in enriched germanium.

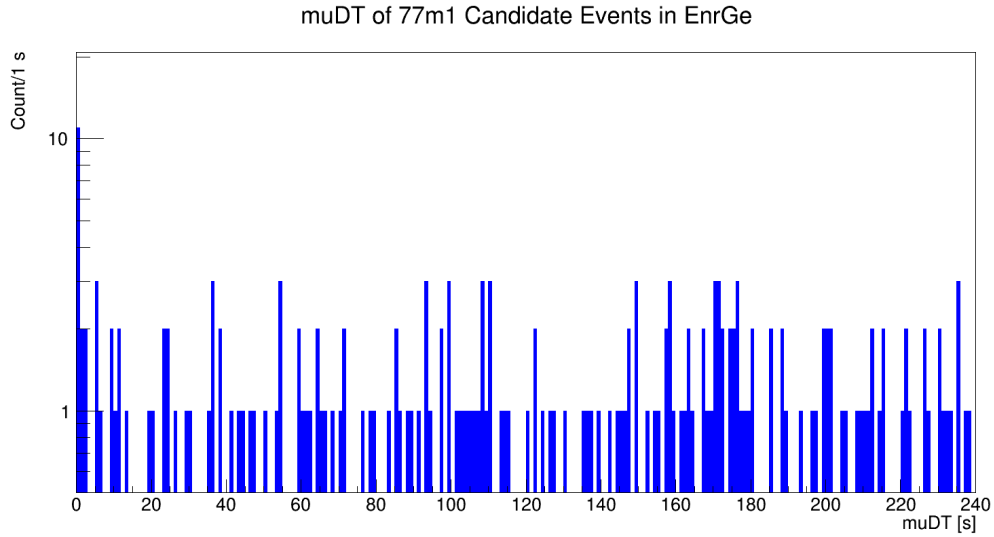

Figure 6.22: Open and blind analysis: Time Since Muon for all ^{77}Ge candidate events, open and blind in enriched germanium.

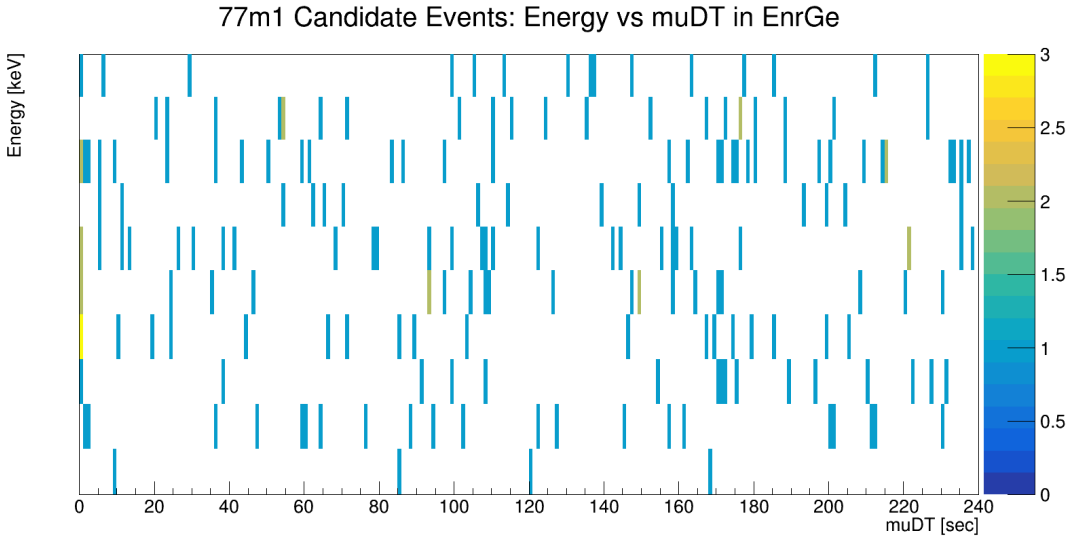

Figure 6.23: Open and blind analysis: Energy vs Time Since Muon for all ^{77}Ge candidate events, open and blind, in enriched germanium.

count in the blind data set is 28.000 ± 5.896 counts in natural detectors, and 73.126 ± 9.961 counts in enriched detectors.

$$\begin{aligned}\text{Open Rate}_{\text{Nat}} &= \text{Candidate}/\epsilon_{77\text{m1}}/\text{Exp}_{\text{NatGe}} - \text{Background}/\epsilon_{77\text{m1}}/\text{Exp}_{\text{NatGe}} \\ &= (60.769 \pm 9.683) - (69.360 \pm 10.228) \\ &= -8.590^{+14.084}_{-14.084}\ \text{cts/kg} \cdot \text{yr} \end{aligned} \tag{6.62}$$

$$\begin{aligned}\text{Open Rate}_{\text{Enr}} &= \text{Candidate}/\epsilon_{77\text{m1}}/\text{Exp}_{\text{EnrGe}} - \text{Background}/\epsilon_{77\text{m1}}/\text{Exp}_{\text{NatGe}} \\ &= (66.651 \pm 7.017) - (58.777 \pm 6.367)\ \text{cts/kg} \cdot \text{yr} \\ &= 7.874^{+9.476}_{-9.476}\ \text{cts/kg} \cdot \text{yr} \end{aligned} \tag{6.63}$$

$$\begin{aligned}\text{(Open and Blind) Rate}_{\text{Nat}} &= \text{Candidate}/\epsilon_{77\text{m1}}/\text{Exp}_{\text{NatGe}} - \text{Background}/\epsilon_{77\text{m1}}/\text{Exp}_{\text{NatGe}} \\ &= (57.062 \pm 9.653) - (57.516 \pm 9.881) \\ &= -0.454^{+13.813}_{-13.813}\ \text{cts/kg} \cdot \text{yr} \end{aligned} \tag{6.64}$$

$$\begin{aligned}\text{(Open and Blind) Rate}_{\text{Enr}} &= \text{Candidate}/\epsilon_{77\text{m1}}/\text{Exp}_{\text{EnrGe}} - \text{Background}/\epsilon_{77\text{m1}}/\text{Exp}_{\text{NatGe}} \\ &= (51.526 \pm 5.953) - (49.470 \pm 6.099)\ \text{cts/kg} \cdot \text{yr} \\ &= 2.056^{+8.523}_{-8.523}\ \text{cts/kg} \cdot \text{yr} \end{aligned} \tag{6.65}$$

The Feldman-Cousins method [39] was used to determine the upper limit. For the open analysis, the 68.27% signal count upper limit is 2.650 counts in the natural detectors, and

28.510 counts in the enriched detectors. For the open and blind analysis, the 68.27% signal count upper limit is 9.180 counts in the natural detectors, and 22.885 counts in the enriched detectors. The corresponding 68.27% upper limit production rates are calculated.

$$\text{Open FC 68.27\% UL Rate}_{\text{Nat}} = 3.426 \pm 0.220 \text{ cts/kg} \cdot \text{yr} \tag{6.66}$$

$$\text{Open FC 68.27\% UL Rate}_{\text{Enr}} = 13.870 \pm 0.853 \text{ cts/kg} \cdot \text{yr} \tag{6.67}$$

$$\text{(Open and Blind) FC 68.27\% UL Rate}_{\text{Nat}} = 6.467 \pm 0.413 \text{ cts/kg} \cdot \text{yr} \tag{6.68}$$

$$\text{(Open and Blind) FC 68.27\% UL Rate}_{\text{Enr}} = 5.837 \pm 0.359 \text{ cts/kg} \cdot \text{yr} \tag{6.69}$$

All production rates are recorded in Table 6.5.

6.9 Conclusion

For this data analysis five de-excitation signatures were investigated. Three of the signatures were found to be viable using the analysis technique described. Analysis code was developed to search for and identify these energy signatures immediately following muon events in the veto data. The excited state production rates of these three isotopes were measured and are shown in Table 6.5.

The three excited state production rates can also be used to as a point of comparison for the muon on MAJORANA DEMONSTRATOR simulations performed in Chapters 10 and 11.

This comparison is described in Chapter 13.

Chapter 7

Simulation Overview

Two Monte Carlo simulation packages were used in this work, GEANT4 with the MAGE framework and FLUKA, as well as TALYS. MAGE and FLUKA are used in this work to perform simulations of muons and neutrons on to the DEMONSTRATOR and study the induced background in detectors. TALYS is used in this work to estimate the excited state production rate of specific signature isotopes from the ground state production rates calculated in the MAGE and FLUKA simulation analyses.

7.1 MaGe and Geant4

The GEANT4 particle transport code is a C++ based simulation toolkit that was developed, and is currently maintained by the GEANT4 collaboration, an international collaboration formed by individuals from a variety of universities, institutes, and high-energy Physics experiments. Throughout this work two different versions of GEANT4 were used, Geant4.10.4.p02 and Geant4.10.5 [12].

The MAGE code is a C++ based GEANT4 application framework for low-background germanium experiments. MAGE was developed jointly by the MAJORANA and GERDA collaborations [26].

7.1.1 General

The GEANT4 toolkit is commonly used for many differently applications, from smaller studies of irradiation of cube satelites to full-scale detector simulations of accelerator experiments. At its core, GEANT4 is an object-oriented package that handles the communication between various software components of the simulation, such as particle generation, particle tracking, detector response, and data storing [12]. GEANT4 is open source, allowing individuals to develop C++ classes that suit their unique needs. This makes GEANT4 highly flexible. Once a user has installed the GEANT4 toolkit they then design the simulation using these C++ classes and compile it into an executable. The users have control over every part of their simulation from the particle generation, to the physics list. Changing small details in a simulation generally requires recompiling the executable, which makes version control (of the specific simulation) difficult and makes it tricky to properly compare results between colleagues.

The MAGE framework was developed in order to standardize simulation results within the MAJORANA and GERDA collaborations and limit the reproduction of work between the collaborations [26]. Instead of compiling each different simulation into different executables, MAGE allows the user to compile a single executable and select the simulation details at run-time via a macro. Many different experimental geometries, particle generators, data output schemes, and physics lists which the collaborators require are included in the MaGe code.

7.1.2 Particle Generator

For the MAGE muon simulations discussed in this work (Chapters 8 and 10), the MAJORANA particle generator ShowersFromFile was used. This generator was developed by the MAJORANA collaboration to utilize measurements taken onsite in future simulations while minimizing computation time. The ShowersFromFile generator draws primary particles from a source data file at random and places them at the ceiling of the DEMONSTRATOR cavern space with a corresponding momentum and direction. This source data file is the result of a MAGE simulation performed by a collaborator, wherein cosmic ray muons with a wide

range of energies were propagated from the surface through the rock to the MAJORANA detector room. Topological surveys and muon flux measurements at the surface were used to generate the source data file with proper normalization. This generator allows the user to choose to generator muons or muon showers. For the simulations in this work only muons were generated as primaries. The energy spectrum for the primary muons is shown in Figure 7.1.

7.1.3 Geometry

The MAJORANA DEMONSTRATOR geometry used in the MAGE simulations is a comprehensive geometry that has been developed over many years. This geometry, called the complete geometry, closely matches the final configuration of DEMONSTRATOR with with all components installed; the data taking configuration when the commissioning phase of the experiment was completed. Components were coded based on engineering and CAD drawings used during construction and commissioning phases of the experiment. Particular attention was paid to the components that are inside the lead shield, as they are expected to have the largest impact. In addition to the shielding, detectors, and cryostats, smaller components such as signal cables and support screws are also included. Figures 7.2, 7.3, and 7.4 show renderings of the detector units, the strings inside a single module, and the shielding respectively, as programmed in the MAGE geometry. Also included in MAGE are options to modify specific parts of the geometry without modifying the MAGE source code. These options are included to allow collaborators to more accurately simulate specific data taking periods of the commissioning phase. For example, a single module can be removed to represent the experimental geometry in earlier data sets, when only one detector array was installed and operating.

7.2 FLUKA

The FLUKA particle transport code is a FORTRAN-based Monte Carlo simulation package that was developed, and is currently maintained jointly by the European Laboratory for

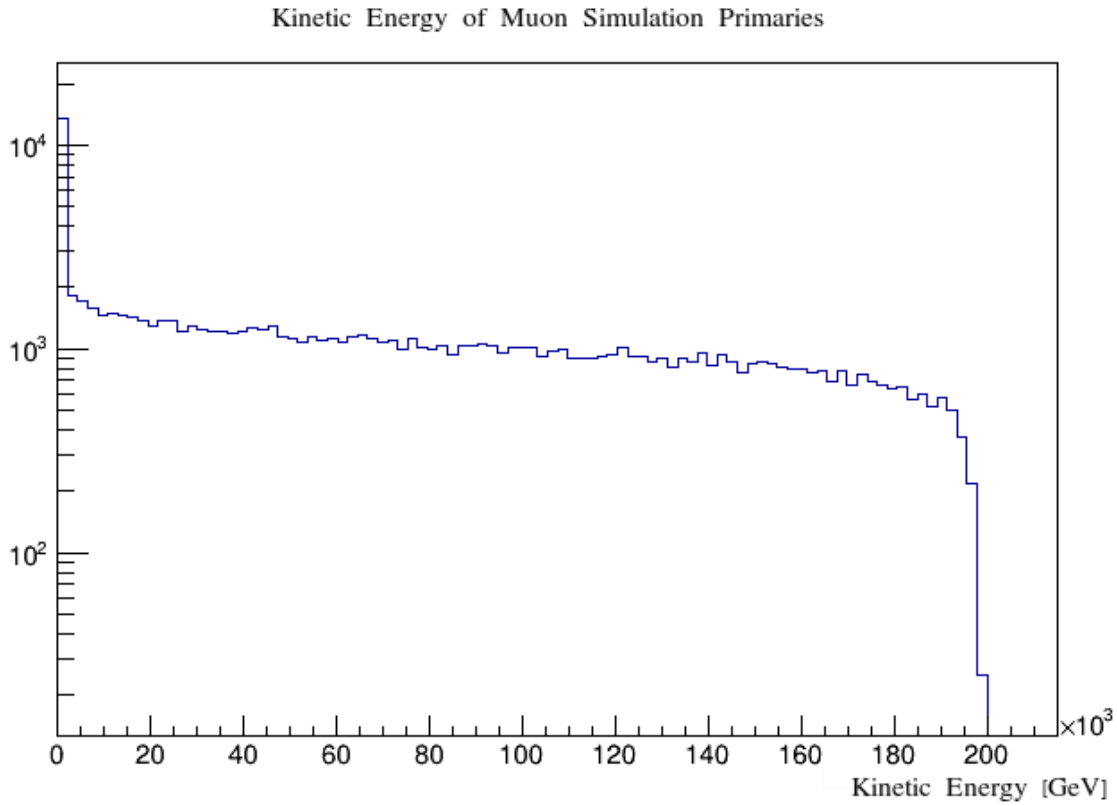

Figure 7.1: The muon kinetic energy spectrum used in the ShowersFromFile generator (MaGe and FLUKA versions).

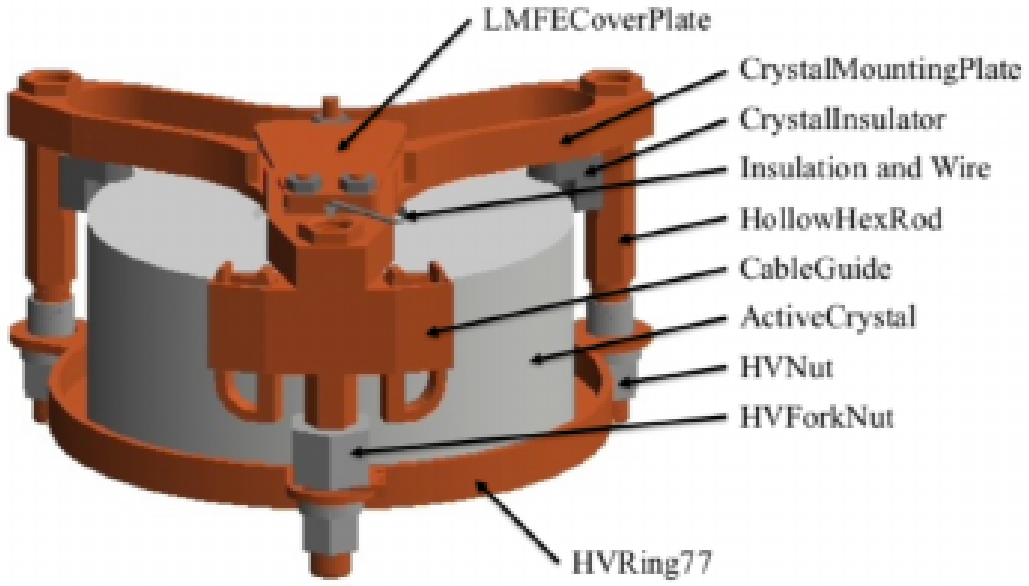

Figure 7.2: Rendering of an individual MaGe Majorana Demonstrator detector unit

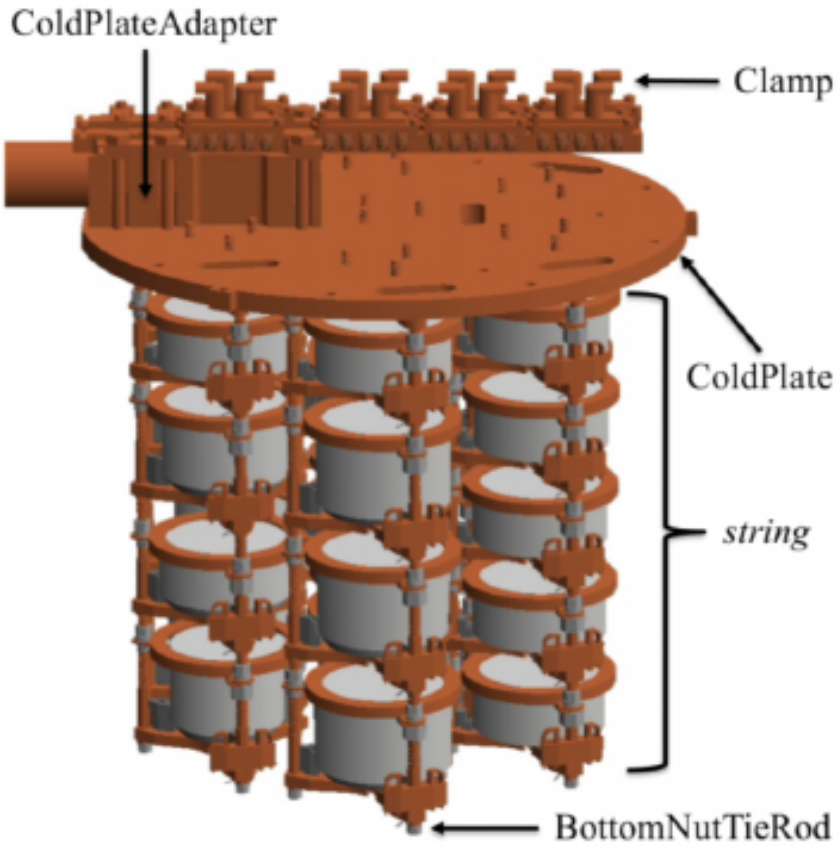

Figure 7.3: Rendering of a MaGe Majorana Demonstrator module with outer casing removed.

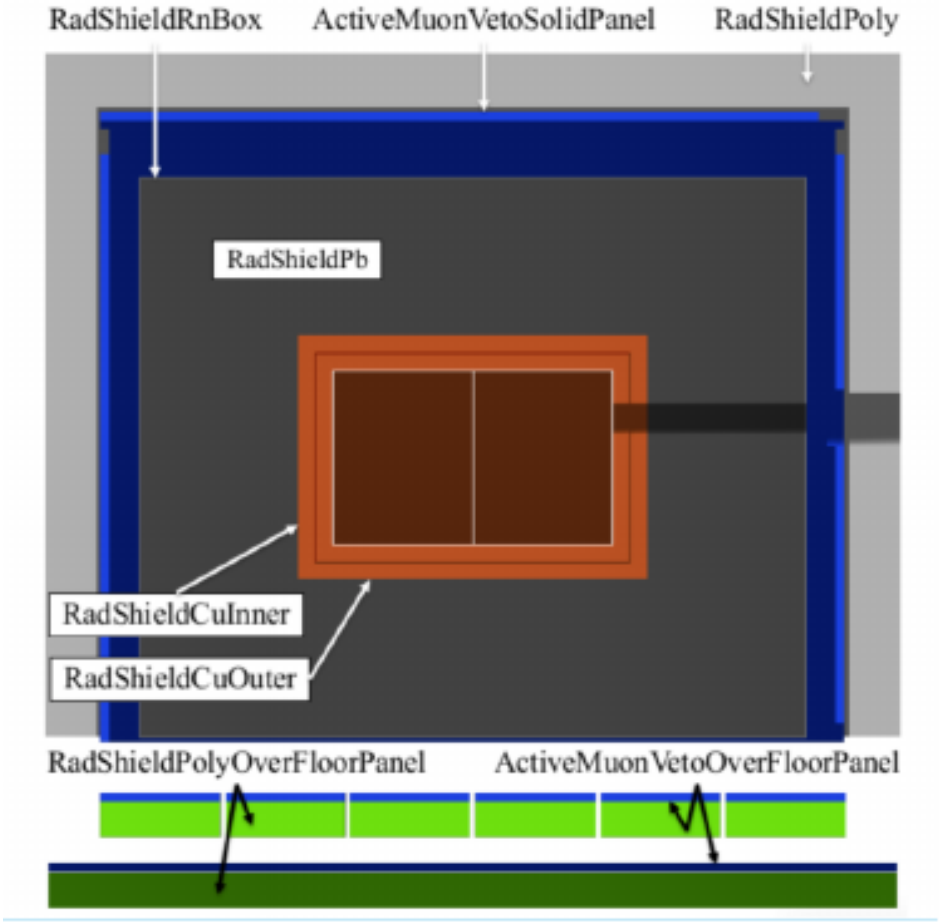

Figure 7.4: Rendering of the MaGe Majorana Demonstrator shielding

Particle Physics (CERN) and the Italian National Institute for Nuclear Physics (INFN) [40]. FLUKA version fluka2011.2x.6 was used in this work.

7.2.1 General

The FLUKA particle transport code can be used in for a variety of applications, such as accelerator physics, including target design and shielding activation, neutrino physics, radiotherapy, cosmic rays, calorimetry, and dosimetry. The FLUKA source code is not open to individuals outside of the development team which allows strict version control, with older versions of FLUKA becoming locked after a set period of time. Therefore all users use essentially the same FLUKA executable, with the simulation details being described in a separate input file. Since FLUKA is not open source, users are slightly limited in their control, however many commonly used functions are included as FLUKA "Cards" or as FORTRAN user routines the user can modify [40].

As an example, cards can be used to define a relatively simple particle generator such as a beam or isotropic point source of monoenergetic particles, however if the user requires a particle generator with a more unique qualities then a FORTRAN user routine, source.f, is available for editing and can be activated via a card.

FLUKA development is ongoing. One missing feature which effects this work is that isomer production of nuclei during radioactive decay is not currently implemented. The current implementation allows isomer patching, which simply splits nuclei evenly between the ground state and isomer. For the FLUKA simulations in this work isomer patching is turned on, however simulated isomer production rates are ignored and instead TALYS simulations are used to estimate isomer production rates.

7.2.2 Particle Generator

For the FLUKA muon simulations discussed in this work (11), two particle generators were used. The MAJORANA ShowersFromFile generator, and the MAJORANA MeiHime generator. The ShowersFromFile generator is the same generator used in the MAGE simulations, adapted to work with the FORTRAN-based FLUKA. A FLUKA source user routine was

modified to fulfill this task. The MeiHime generator is also available in the MaGe framework. The MeiHime generator is based on the paper "Muon-Induced Background Study for Underground Laboratories" by D.-M. Mei and A. Hime [54]. Of interest are the model for a fit of muon depth-intensity-relation measurements and the muon energy spectrum. Mei and Hime use the model to calculate the total muon intensity arriving below the surface at a specific vertical depth, with the assumption that the surface is flat.

$$\mathrm{I_{th}(h,\theta) = (I_1 \cdot e^{-hsec(\theta)/\lambda_1} + I_2 \cdot e^{-hsec(\theta)/\lambda_2})sec(\theta)} \tag{7.1}$$

where $\mathrm{I_1}$, $\mathrm{I_2}$, λ_1, and λ_2 are free parameters determined using experimental data, h is the vertical depth, and θ is the azimuthal angle of the muon from vertical.

The energy spectrum of through going muons at our depth of $\mathrm{h_0}$ = 4.3 km.w.e. can be written as

$$\mathrm{dN/dE_\mu(\theta) = Ae^{-b(h_0/cos(\theta))(\gamma_\mu - 1)} \cdot (E_\mu + \epsilon_\mu(1 - e^{-b(h_0/cos(\theta)}))^{-\gamma_\mu}} \tag{7.2}$$

where A is the normalization constant, $\mathrm{E_\mu}$ is the muon energy at depth $\mathrm{h_0/cos(\theta)}$, and (b, γ_μ, ϵ_μ) are free parameters determined using experimental data.

The MeiHime generator creates primaries by sampling randomly from the intensity distribution at h = 4.3 km.w.e. to determine the muon azimuthal angle, and then sampling randomly from the associated energy spectrum to determine the muon energy. A random radial angle is chosen uniformly from $[0, 2\pi]$. The particle is then randomly placed on the x-y plane on the ceiling of the detector room.

In this work, when using either generator only muons were generated as primaries.

An additional particle generator was used to estimate the effect of the Majorana shielding on ambient neutrons. For this neutron generator neutrons were placed randomly on the surface of a cube that surrounds the Demonstrator. Each neutron was then given a random momentum inward toward the detectors. The neutron energy spectrum measured at the China Jinping Underground Laboratory [48], shown in Figure 7.5, was used to determine the energy of the neutron. The results of this neutron simulation are discussed in Chapter 9.

7.2.3 Geometry

The MAJORANA DEMONSTRATOR geometry used in the FLUKA muon simulations is a simplified version of the complete MAGE geometry. The collaboration had not used FLUKA for any large simulation campaigns, so I had to completely rebuild the geometry in FORTRAN to be compatible with FLUKA. All major components, such as the detectors, the cryostats, and the shielding, were included , however the smaller components are not in the FLUKA geometry. See Figure 7.6 for a visualization of the FLUKA geometry. Missing components include detector cables (high-voltage and signal), detector support components (string tie rods, detector Low-Mass Front End, support screws and bolts), liquid nitrogen dewars, electronic boxes, the vacuum systems, and the calibration tracks. These missing components fall into two categories. They are either (1) far away from the detectors, thus any muon interactions are unlikely to be a substantial contribution to the background (e.g. LN dewars), or (2) close to the detectors, but small enough that muon interactions are unlikely to be a substantial contribution to the background (e.g. signal cables).

An additional MAJORANA DEMONSTRATOR geometry was used in the FLUKA ambient neutron simulations. This additional geometry, called the prototype geometry, closely matches the shield configuration of the Prototype data set, the first data taking configuration used by the DEMONSTRATOR. The prototype geometry is equivalent to the complete FLUKA geometry with the 12" polyethylene shield, the inner copper shield, and the crossarm shielding components missing. The prototype FLUKA geometry is shown in Figure 7.7.

7.3 Geometry Comparison

Since different versions of the MAJORANA DEMONSTRATOR geometry are being used by MAGE and FLUKA an additional MAGE simulation was run to investigate the effective difference between these geometries. This comparison was done using Geant4.10.4.p02. A separate MAGE geometry (Slim) was built by removing components that are missing the FLUKA geometry from the complete MAGE geometry (Full). Using the ShowersFromFile generator, 10.02 years worth of statistics were gathered for the Full and Slim geometry. For each geometry, the detector depositions were gathered into 20 μs events (to mimic the

Majorana Demonstrator data) and two analysis cuts (1-second muon veto cut and granularity greater than 1 cut) were applied. The events that survive both cuts are used to estimate the irreducible muon-induced background rate. This process is described in greater detail during Chapter 10. Figure 7.8 shows the muon-induced background rate for both geometries. Over the entire energy spectrum there is a $\sim$ 8% difference. Over the 400 keV background window [1950 keV, 2350 keV] there is a $\sim$ 16% difference. Since the Full geometry and Slim geometry results are within one standard deviation of each other, the missing components in the Slim geometry do not contribute substantially to the muon-induced background and can be ignored.

7.4 TALYS

TALYS is a software package specifically designed to model nuclear reactions [52].

TALYS has been developed jointly at NRG Petten, the Netherlands, CEA-Bruyeres-le-Chatel, France; University of Brussels, Belgium; and International Atomic Energy Agency, Vienna.

The TALYS code is used to simulate one of seven primary particles onto a target nucleus. The possible primary particles are: neutrons, protons, deuterons, tritons, ^{3}He, alphas, or gammas. The target nucleus can have an atomic number that ranges from 3 (Lithium) to 124 (Unbiquadium). The target nucleus can have a mass number (A) from 5 to 339, with the extra condition that the combination of atomic number and mass number must be present in the TALYS mass database. Additionally, TALYS allows the user to select naturally occurring compounds, e.g. natural germanium consists of ^{70}Ge, ^{72}Ge, ^{73}Ge, ^{74}Ge and ^{76}Ge, or define a new composition with file that defines the isotope abundance.

TALYS version 1.95 was used in this work.

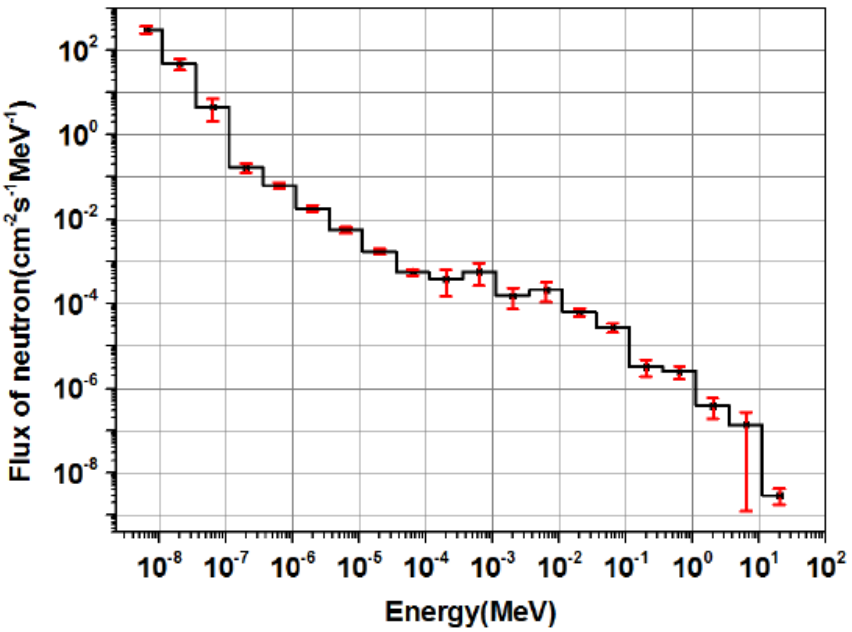

Figure 7.5: Energy spectrum of neutrons measured at China Jinping Underground Laboratory [48].

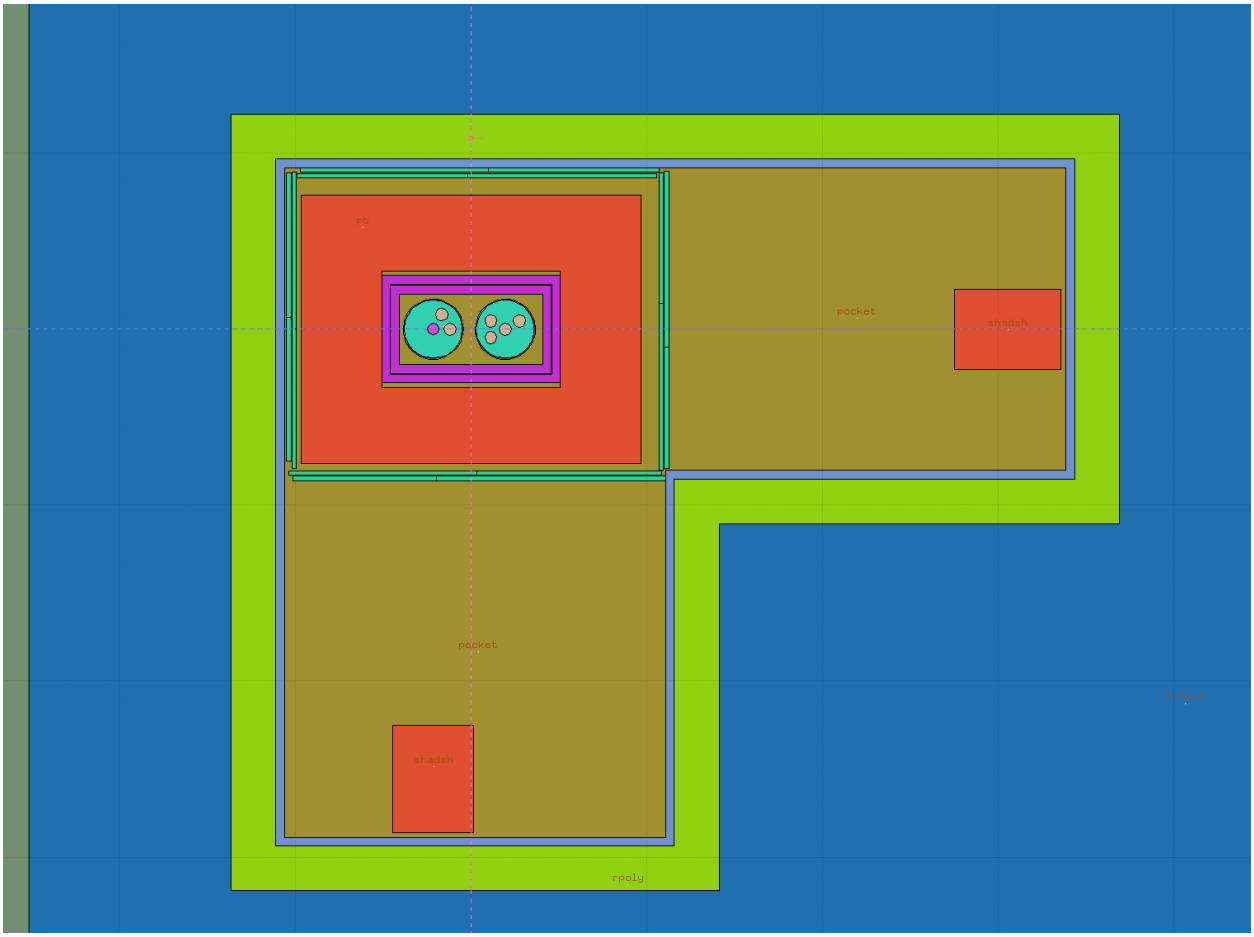

Figure 7.6: Bird's-Eye complete FLUKA geometry visualization. Note: Not all components are visible from this angle, specifically seven strings and both cryostat crossarms.

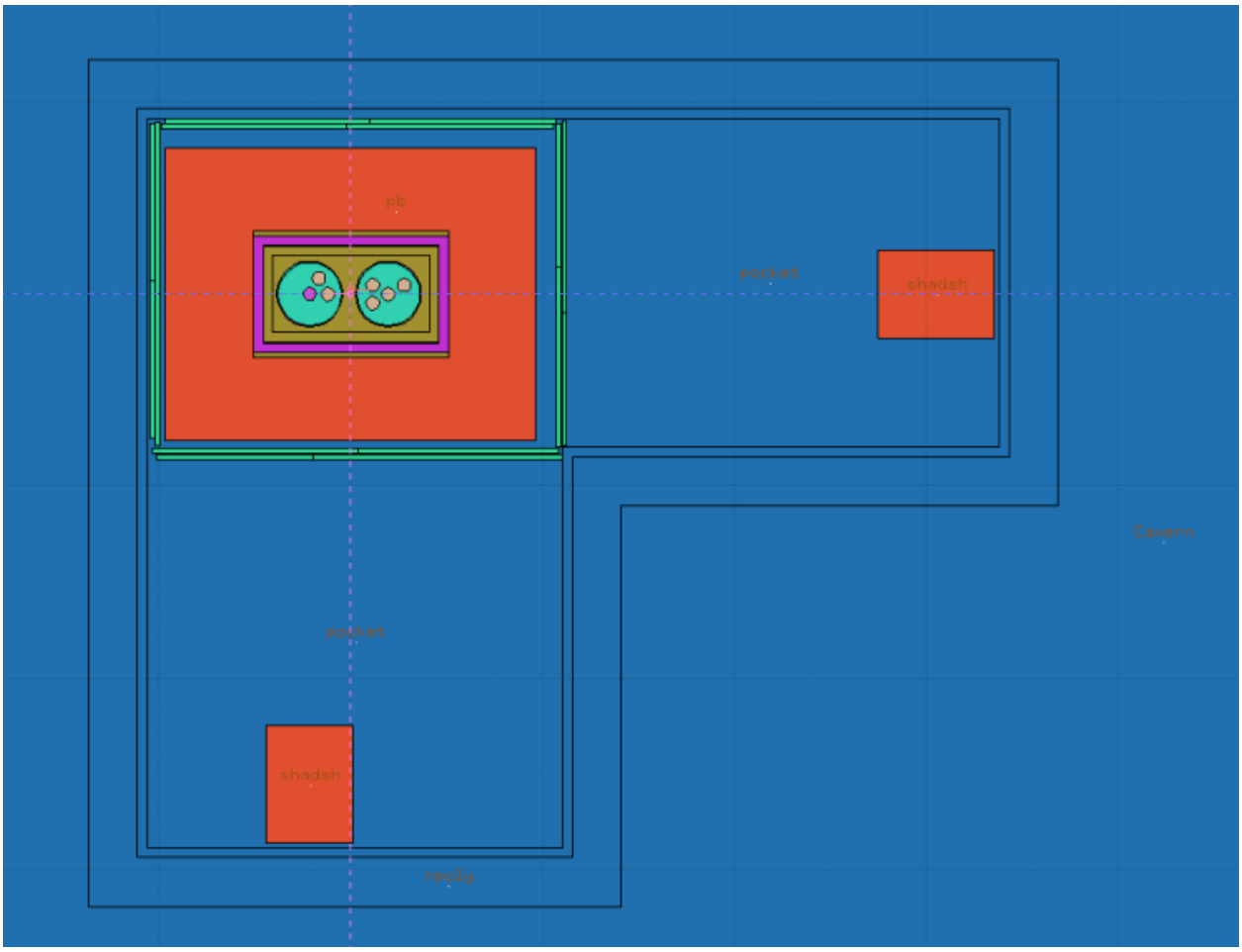

Figure 7.7: Bird's-Eye prototype FLUKA geometry visualization. Note: Not all components are visible from this angle, specifically seven strings and both cryostat crossarms.

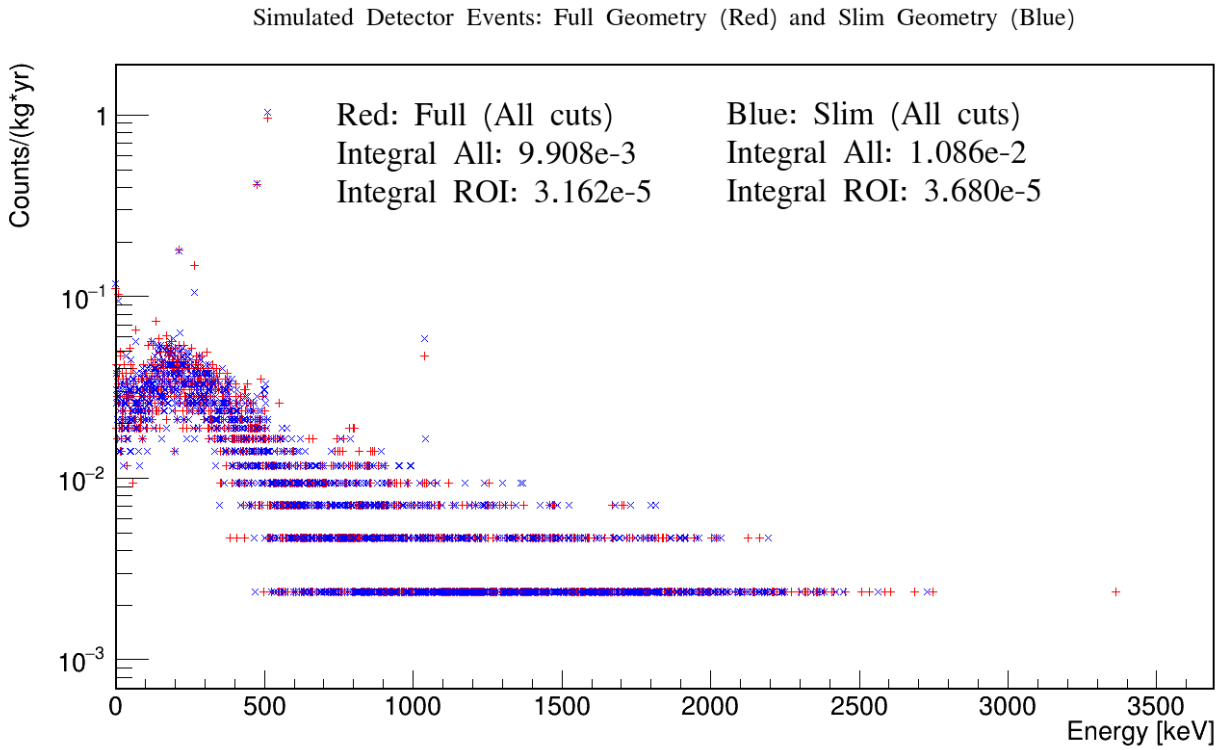

Figure 7.8: Histogram of simulated irreducible muon-induced background energy signals in germanium detectors. Red: MaGe simulation using Full geometry. Blue: MaGe simulation using Slim geometry. Integral All gives the spectra integral over the entire energy range [0 keV, 4000 keV]. Integral ROI gives the spectra integral over the energy range [1950 keV, 2350 keV], which contains the $\beta\beta(0\nu)$ Q-value.

Chapter 8

Veto Efficiency Simulation

Recall that the purpose of the veto system is to identify when a muon passes through the system so that most muon-induced backgrounds can be properly removed from the $\beta\beta(0\nu)$ and other analyses. During R&D of the veto system, the individual veto panels were found to have very high muon detection efficiency (>99%) [27]. Given the high efficiency of the individual panels, along with the fact that the MAJORANA veto system completely surrounds the lead shielding, one can assume that the muon detection efficiency of the completed 32-panel veto system is also high. However, the complete 32-panel configuration is not the only veto panel configuration used in the MAJORANA DEMONSTRATOR. At various points during the commissioning and operating phases of the experiment it was both practical and necessary to temporarily operate the veto system with less than 32 panels.

This chapter will cover a MAGE-based simulation analysis which estimates the muon-tagging efficiency of the veto system in its 32-panel configuration, as well as a few other significant configurations that have been used in the DEMONSTRATOR. It is possible for a muon to enter the lab space, pass through the corner of a veto panel, and exit the lab space without ever coming near the germanium detectors. The collaboration is not concerned about these cases, as these muon are very unlikely to induce backgrounds in the detectors. The collaboration is only interested in identifying muons that create backgrounds in the detectors that impact the $\beta\beta(0\nu)$ analysis. To that end, this simulation analysis focuses on muons that pass through the veto system and induce backgrounds events, which will not be removed by the muVeto cut, in a detector. The veto system efficiency estimated in this

chapter is the 'Efficiency of tagging muons which pass through a veto panel into the lead shielding and create a background signal'.

The MaGe simulation used for this analysis is also used in Chapter 10 to estimate the irreducible muon-induced background rate of the Majorana Demonstrator. Primary muons were generated using the ShowersFromFile generator described in Chapter 7. The full Demonstrator geometry was implemented. The simulation generated 199,600 primary muons onto the standard Majorana geometry with the complete shielding configuration. This corresponds to 1.86 years worth of statistics, approximately 26.28 $\text{kg} \cdot \text{yr}$ natural germanium exposure and 54.07 $\text{kg} \cdot \text{yr}$ enriched germanium exposure. MaGe was compiled with Geant4 version, Geant4.10.5.

8.1 The Veto Signature for Simulated Muons

With the MaGe simulation output it is easy to determine when a simulated muon passes through a specific veto panel. It is more difficult to determine whether the veto system in the lab would correctly recognize this particle as a muon. All muon tagging criteria used in the lab must be applied to the simulation output to make this determination.

For the veto system to tag an event as a muon, the following three requirements must be met:

1. Particle passes through a veto panel (i.e. a veto panel must receive a signal).
2. Event is not LED
3. At least two panels have a QDC value greater than 500.

Requirement 1 is interpreted as "A muon must pass through a veto panel, into the lead shielding, and induce a signal in the germanium detectors", as these are the events the system was designed to veto. Applying Requirement 2 to the simulation output is trivial since only muons were simulated. In order to apply Requirement 3, the threshold of 500 QDC must be translated into units of the simulation (MeV). A direct conversion from QDC to MeV was not available. On average a high energy muon will deposit 2 MeV per gram

of material. This corresponds to at least 5 MeV of deposited energy in each panel. This fact was combined with the average muon QDC value for the top four horizontal panels across 2250 runs. This translates the conservative threshold of 500 QDC into $\approx$ 1.73 MeV. As the energy deposited by each simulated particle is readily available, applying the correct threshold becomes possible.

So the simulation muon tag used in the efficiency study can be written as:

1. Muon passes through veto panel into lead shielding and induces a signal in a germanium detector.

2. At least two panels in the chosen veto configuration have an event energy deposition greater than 1.73 MeV.

Again, the lab requirement 'Event is not an LED' is not included here as it is trivial. The maximum number of muons a configuration can detect with the simulation tag is:

> Number of muons that pass through a veto panel into the lead shielding, and induce a signal in a germanium detector.

8.1.1 MaGe: muVeto Cut (Ge events)

The MaGe simulation uses only muons as a source making it trivial to identify the muon-induced detector events. However, many muon-induced backgrounds are removed from the $\beta\beta(0\nu)$ analysis by the muVeto analysis cut. This cut is simple to reproduce in the simulation. Each muon simulated begins at timestamp, t = 0. The muVeto cut is then applied by removing all simulated detector events with a timestamp less than one second. Additionally, this simulation provided an independent check of the muVeto cut. In Section 8.3.3 the timestamps of all muon-induced backgrounds are investigated and 'one second' is confirmed to be the most appropriate length for the muVeto cut.

8.1.2 Summary

MJD Data LED Tag:

A veto event is an LED if the panel multiplicity is greater than the maximum panel

multiplicity in the run minus five.

MJD Data Muon Tag:

A veto event is a muon if (1) the event is not an LED and (2) at least two panels have a QDC value greater than 500.

Simulation Muon Tag:

A simulation event is identified as a muon if (1) the primary muon passes through the lead shield, (2) the primary muon creates signal in the germanium detectors, and (3) at least two panels in geometry have an energy deposition greater than 1.73 MeV.

8.2 Veto System Configurations

Table 4.1 shows the veto configurations that have been used during the DEMONSTRATOR data taking period. For this analysis, all configurations used during data taking were investigated along with a few additional configurations of interest. Each veto configuration fulfills a specific purpose. A detailed description of the veto system configurations and their use are described below:

vetoAll: Default configuration. All 32 veto panels are installed and operating. This configuration is used whenever possible.

vetoEastOff: Configuration used when work on east module is being done. The four eastern veto panels are removed to allow access to the east detector module.

vetoSouthOff: Configuration used when work on south module is being done. The four southern veto panels are removed to allow access to the south detector module.

vetoESOff: Configuration used when work was being done to install inner copper shielding. The four eastern and four southern veto panels are removed to allow complete access to the internal cavity

HorizPanel: Configuration used to measure muon flux at Davis Campus [6]. Only four top and twelve bottom panels operating. While this configuration was in use, testing was being performed on a prototype detector module (i.e. before DS0). No detector

data that uses this veto configuration is used in this work or in most MAJORANA analyses.

BrokeQDC15: Configuration used for a portion of DS3. One of the QDC card channels was broken, making one panel inoperable.

P0Off, P1Off, P6Off: Panels 0, 1, 6 have shown sub-optimal LED detection performance. In these cases, LED amplitude is very close to pedestal resulting in undetected LEDs. The LED amplitude of a panel is expected to drop slowly over time as LED starts to die. These configurations are simulated as a precaution to understand the effect these panels have on the muon tagging efficiency of the system.

P01Off, P06Off, P16Off, P016Off: Various configurations of panels 0, 1, & 6 being turned off. P016Off assumes all three panels are dead.

Table 8.1 summarizes the veto configurations investigated in this analysis.

8.3 Results

The results of the study will be divided into (1) how effective the veto system is at identifying muon events, and (2) how effective the veto system is at rejecting muon-induced detector signals.

8.3.1 Results: Muon Tagging

The maximum number of muons that a configuration can detect is: "Total number of muons that pass through lead shield AND result in a detector signal".

Table 8.2 shows how many muons, which pass through the lead shielding and create a signal in the detectors, are identified as muons by each geometry, using the same simulation muon tag described in Sections 8.1 and 8.1.2.

Table 8.1: Veto configurations investigated for this analysis. Note: Panel numbers below are zero-indexed (i.e. Panel 0 ≡ Panel #1).

Name	# of panels	Description
vetoAll	32	All 32 Panels
vetoEastOff	28	No East Panels
vetoSouthOff	28	No South Panels
vetoESOff	24	No East/South Panels
HorizPanel	16	Top & Bottom Panels only
BrokeQDC15	31	Panel 15 off
P0Off	31	Panel 0 turned off
P1Off	31	Panel 1 turned off
P6Off	31	Panel 6 turned off
P01Off	30	Panels 0 & 1 turned off
P06Off	30	Panels 0 & 6 turned off
P16Off	30	Panels 1 & 6 turned off
P016Off	29	Panels 0, 1, & 6 turned off

Table 8.2: Results (Muons tagged by veto system). Using Muon tag: Edep > 1.73 MeV & muThreshold Panel Multiplicity > 2.

Configuration	# of μ that pass through Pb & create signal in Ge	# of μ identified by geometry	%
All 32 panels	15196	14696	96.71
EastOff	15196	14678	96.59
SouthOff	15196	14678	96.59
East & South Off	15196	14573	95.90
HorizPanel	15196	14193	93.40
BrokeQDC15	15196	14694	96.70
P0Off	15196	14691	96.68
P1Off	15196	14695	96.70
P6Off	15196	14694	96.70
P01Off	15196	14690	96.67
P06Off	15196	14689	96.66
P16Off	15196	14691	96.68
P016Off	15196	14686	96.64

The simulation shows that 96.7% of muons that induce backgrounds in the detectors will be identified by the 32-panel veto system configuration. This is confirmation that the veto system will work as intended. If a side panel, such as Panel 0, Panel 1, or Panel 6 should fail, there will be almost no impact on overall muon detection efficiency of the veto system. As expected, if panels are removed from the East or South walls to perform work, the muon detection efficiency of the veto system is slightly reduced. A decrease in efficiency is expected but unavoidable. This study provides the first estimates of the veto system muon detection efficiency for the collaboration.

8.3.2 Results: Muon-Induced Background Rejection

While it is important to consider whether muons can be correctly identified by the veto system, it is also important to determine whether the muon-induced detector depositions can be accurately rejected.

Following from Table 8.2, Table 8.3 details how many detector events which occur can be recognized as muon-induced for each geometry, and the effect of the muVeto and Granularity cuts. Detector energy deposits have been built into events with 20 μs time windows by detector channel.

In total, 192,418 detector events were induced by the simulated muons. The 1-second muVeto cut is only applied when the veto system tags a muon event. Therefore some of the detector events with timestamp less than 1 second will survive because the incident muon was not tagged by the veto system configuration. Column three contains the maximum number of detector events which can be rejected by the muVeto cut, i.e. detector events which were induced by a muon that was correctly tagged by the veto system configuration. Column five shows the effect of the 1-second muVeto cut on the detector events identified as muon-induced. Regardless of the veto configuration, the muVeto cut rejects 97.12% of these muon-induced background events (See Table 8.3 Columns 3, 5, and 6). The other 2.88%, along with the detector events not recognized as muon-induced, are not rejected by the muVeto cut and remain in the $\beta\beta(0\nu)$ analysis. However, there is an additional analysis cut, the Granularity greater than 1 cut, which will reject a portion of the remaining events. Column

seven shows the total number of detector events, out of all 192,418 events, that remain as $\beta\beta(0\nu)$ backgrounds after applying the muVeto and Granularity cuts. The Granularity cut does a remarkable job at removing muon-induced background events. Consider the 32-panel configuration, the Granularity cut rejected $\sim 80\%$ (16,135 out of 20,229) of the muon-induced detector events that survived the muVeto cut. These results show that in any of these veto system configurations, the collaboration can expect the 1-second muVeto and Granularity cuts to remove $\sim 97.8\%$ of all muon-induced backgrounds.

8.3.3 Results: Potential muVeto Cut Improvements

Currently the muVeto cut rejects all detector events that occur within one second of a muon event. This cut has been shown in this work to have an efficiency of 97.12% for all veto configurations.

Figure 8.1 shows the timestamps of all muon-induced detector events in the MaGe simulation. Out of all 192,418 detector events, 186,977 events (97.17%) occur within the first second. A similar simulation result, performed by the collaboration, was a primary factor in choosing a duration of 1-second for the muVeto analysis cut.

It is possible to increase the efficiency of the muVeto cut by increasing the cut threshold to a value above one second. Such an improvement will come at the cost of detector livetime, therefore any change must be considered carefully. Here the question of whether to improve the muVeto cut by increasing the threshold value above one second is considered. As a best case scenario, only the 32-panel configuration will be considered.

For the 32-panel configuration, out of the 192,418 muon-induced detector events in the simulation only 4094 events survive the muVeto and Granularity cuts and remain as a background in the $\beta\beta(0\nu)$ analysis.

Figure 8.2 shows the timestamps of the surviving events. For readability the time axis only extends to 20,000 seconds. These surviving events are evenly spread out in time with no apparent peaks.

Recall that this muon simulation represents 1.87 years of livetime. Now consider an aggressive change to the muVeto cut, from one second to 100 seconds. Extending the muVeto cut to 100 seconds would remove 62 of the 4094 surviving $\beta\beta(0\nu)$ backgrounds, a 1.51%

Table 8.3: Results (Detector/Ge event rejection). Detector/Ge depositions built into 20 μs "events" by channel. Using Muon tag: Energy Deposition $>$ 1.73 MeV & muon Multiplicity $>$ 2. Using the 1-second muVeto cut. Using Granularity cut. Events that survive all cuts are labeled SE.

Configuration	# of Ge events	# tagged as μ-induced	%	# cut by muVeto	% (of Col. 3)	# of SE	%
All 32 panels	192418	177292	92.14	172189	97.12	4094	2.13
EastOff	192418	177191	92.09	172089	97.12	4097	2.13
SouthOff	192418	177292	92.14	172189	97.12	4094	2.13
East & SouthOff	192418	177186	92.08	172084	97.12	4099	2.13
HorizPanel	192418	177014	91.99	171912	97.12	4119	2.18
BrokeQDC15	192418	177292	92.14	172189	97.12	4094	2.13
P0Off	192418	177292	92.14	172189	97.12	4094	2.13
P1Off	192418	177292	92.14	172189	97.12	4094	2.13
P6Off	192418	177237	92.11	172136	97.12	4095	2.13
P01Off	192418	177292	92.14	172189	97.12	4094	2.13
P06Off	192418	177237	92.11	172136	97.12	4095	2.13
P16Off	192418	177237	92.11	172136	97.12	4095	2.13
P016Off	192418	177237	92.11	172136	97.12	4095	2.13

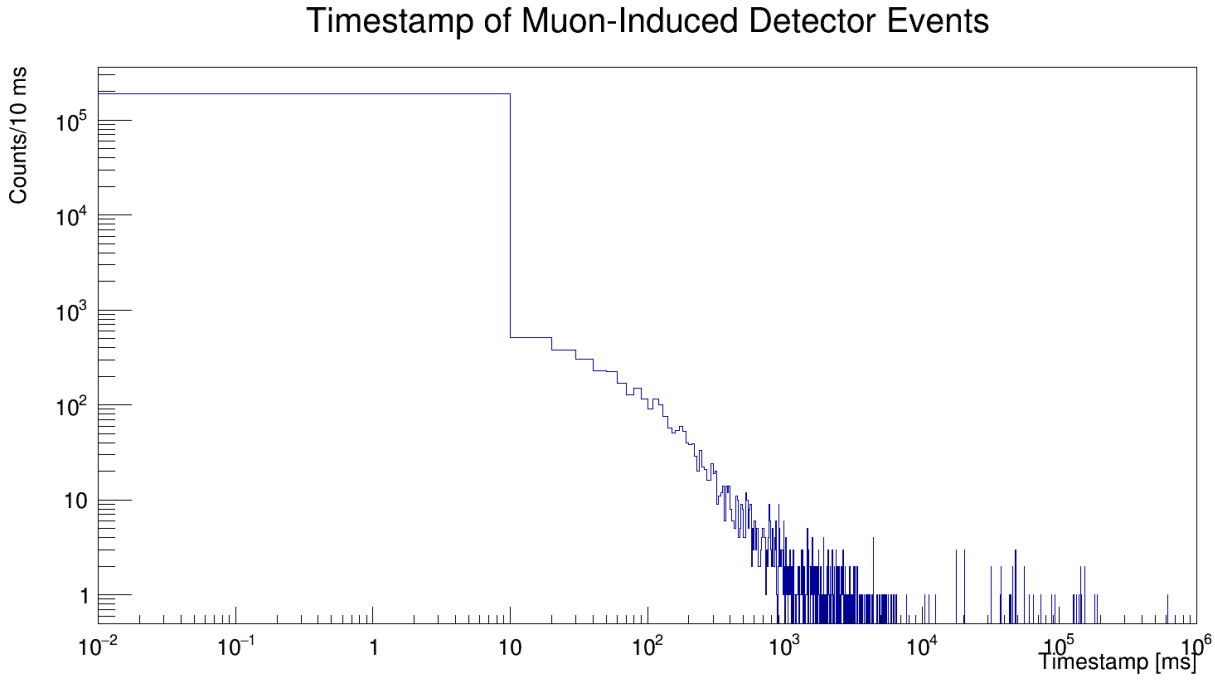

Figure 8.1: Timestamp of all muon-induced detector events.

decrease in amount of background events. This extension would also remove $\sim$ 17 days of detector livetime, a 2.49% reduction in livetime. The improvement to the background in this case is minor and the impact of the reduced livetime is expensive. These results support a one second threshold as the ideal muVeto cut timing threshold.

8.4 Conclusion

This simulation study shows that with all 32 panels installed and operating, and with the assumption that the electronics/DAQ are operating correctly, the veto system muon tagging efficiency is $\sim$ 96.7%. It also shows that for the two other most frequent configurations (EastOff & SouthOff) the muon tagging efficiency is $\sim$ 96.6%.

With all 32 panels installed and operating, and with the assumption that the electronics/DAQ are operating correctly, the muVeto and Granularity analysis cuts are estimated to remove 97.87% of all muon-induced detector events. The remaining 2.13% of detector events will contribute to the background in the $\beta\beta(0\nu)$ analysis. This 2.13% is the combination of the inefficiency of the muVeto and Granularity cuts, and the inefficiency of the muon tagging for each geometry. These results also show that the granularity cut is very good at removing cosmogenic backgrounds. The other analysis cuts used in the $\beta\beta(0\nu)$ analysis might reduce this 2.13% background further however no study of the other cuts' effect on these cosmogenic backgrounds has been performed.

This study also supports the use of the 1-second muVeto cut, as a larger time cut (100-second muVeto cut) was shown to be unfavorable.

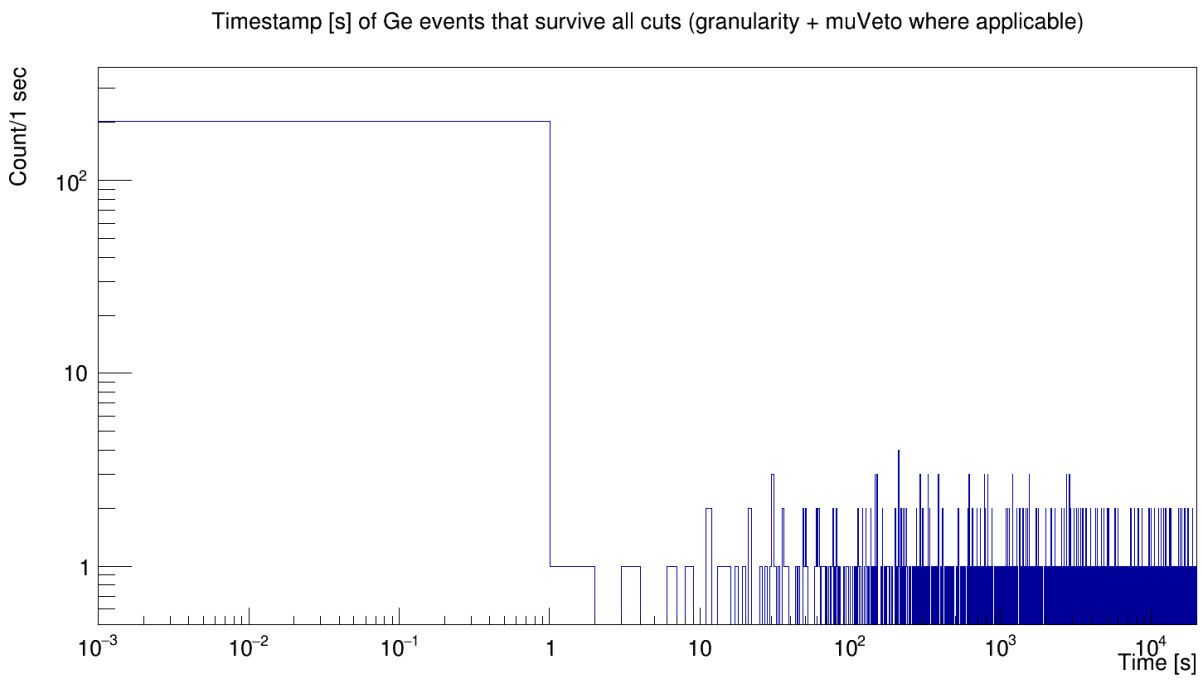

Figure 8.2: Timestamp of all events that survive muVeto and Granularity cuts in the 32-Panel veto configuration.

Chapter 9

Environmental Neutron Simulations

The passive polyethylene layers of the MAJORANA shield were designed to stop ambient neutrons in the lab. Several collaborators were performing an analysis that included the MAJORANA prototype module data. Since this initial data-taking configuration (prototype geometry) had significantly less polyethylene than the final as-built shield configuration (complete geometry), they were concerned about backgrounds from ambient neutrons. The collaboration asked me to perform simulations of ambient neutrons on to the Prototype geometry and the complete MAJORANA geometry to compare the effect of these neutrons. Polyethylene is a commonly used neutron shield material. The polystyrene veto panels, being similar in composition to the polyethylene sheets, are also effective of stopping ambient neutrons. The FLUKA complete geometry has three layers of poly-like material: 10" of polyethylene, 2" of borated polyethylene, and 2" of polystyrene veto panels. The FLUKA prototype geometry only has one layer of poly-like material: 2" of polystyrene veto panels. The prototype geometry has no outer layers of polyethylene.

A FLUKA simulation was used to compare the neutron-stopping capability of the final as-built shield configuration (compete geometry) with the initial data-taking configuration (prototype geometry).

There are three benefits to this comparison:

1. Quantify how many ambient neutrons are expected to reach the detectors in the prototype geometry configuration.

2. Quantify how many ambient neutrons are expected to reach the detectors in the complete geometry configuration.

3. Estimate the effect of the additional shielding on ambient neutrons.

The first benefit allows the collaborators who are using prototype data to better understand the backgrounds. While the prototype data will not be used for the $\beta\beta(0\nu)$ analysis, other analyses performed by the collaboration can benefit from using the prototype data. This result will help collaborators estimate the ambient neutron background and determine whether the prototype data can be used in their analyses.

The second benefit reinforces the collaboration's stance that, in the complete geometry configuration, ambient neutrons are an insigificant source of background to the $\beta\beta(0\nu)$ signature.

The third benefit allows the collaboration to re-evaluate the shield design. Collaborators can use this result to help determine whether the additional shielding is worth the extra time, space, and monetary investment.

9.0.1 Simulation Properties

The simulation was performed using FLUKA version fluka2011.2x.6. Both the complete FLUKA geometry and the prototype FLUKA geometry were used. For each geometry, 350 million primary neutrons were generated using the neutron generator described in 7.2.2. The ambient neutron flux was measured to be $(1.7 \pm 0.1 \pm 0.1 \cdot 10^{-6})$ cm^{-2}s^{-1} in the Davis Campus of the Sanford Underground Research Facility [23]. This corresponds to a simulated livetime of 5.05 years in each geometry.

9.0.2 Results

Of the 350 million neutrons simulated in the prototype geometry, 132,000 transmitted through the shielding into a cryostat. This translates to a transmission probability of 0.0377%, or an ambient neutron rate inside the cryostats of 2.98 neutrons per hour.

Of the 350 million neutrons simulated in the complete geometry, zero transmitted through the shielding into a cryostat. Furthermore, the simulation results showed that no neutron

penetrated through the veto panel layer. These results show that the three shield layers of poly-like material are very effective at shielding the detectors from ambient neutrons.

This study shows that the as-built final shielding configuration does a fantastic job of stopping ambient neutrons. Furthermore the additional polyethylene shielding makes a noticeable improvement when compared to the prototype shielding. As expected the low neutron penetration rate shows that the ambient neutrons are an insignificant source of background for the MAJORANA DEMONSTRATOR when compared to the other background sources.

Chapter 10

MaGe Muon simulation

A MaGe simulation was performed in order to estimate the irreducible muon-induced background rate of the Majorana Demonstrator after analysis cuts. Primary muons were generated using the ShowersFromFile generator described in Chapter 7. The full Demonstrator geometry was implemented. The simulation generated 1.86 years worth of statistics, approximately 26.28 kg · yr natural germanium exposure and 54.07 kg · yr enriched germanium exposure. MaGe was compiled with Geant4 version, Geant4.10.5.

10.1 Event Builder

The Majorana Data Aquisition (DAQ) system has limitations, such as detector signal collection speed, data travel and write speeds, which are not present in the MaGe simulation. In order to get an accurate background estimate, the simulation data was built into detector events that mimic the event builder used in the DAQ.

When an energy deposition is made in a germanium detector, the DAQ records the timestamp of the initial deposition and polls all of the active detectors. All detectors then report to the DAQ the amount of energy deposited in them and also provide a signal waveform. Based on the characterization of the Majorana detectors, a 20 μs window is chosen to ensure that all of the energy has drifted through the bulk to the detector contact and has been readout by the electronics.

In the simulation processing, when a deposition is made in a detector the timestamp is recorded and a 20 μs time window is created. During this time window the energy depositions of each detector are summed individually. This "event" is then recorded to a data file with details such as timestamp, number of detectors hit, and amount of energy deposited in each detector. This is done for all detector depositions in the simulation.

10.2 Analysis Cuts

These 20 μs events provide an estimate for the total amount of muon-induced background in the experiment. However, various data analysis cuts have been developed to remove events that are likely background from the $\beta\beta(0\nu)$ candidate events. For this work two analysis cuts have been implemented, the "1-second muon veto" (muVeto, for short) cut and the "granularity greater than 1" (Granularity, for short) cut.

Based on previous MaGe based muon simulations, the collaboration has estimated that the majority of muon-induced backgrounds deposit in the detectors within one second. This is supported by simulations detailed in Chapter 8. Therefore, the muVeto cut was developed and implemented into the data analysis procedures. The muVeto cut is simple, if a detector event occurs within one second (plus timestamp uncertainties) of a event tagged by the veto system as a muon, then the detector event is removed from the $\beta\beta(0\nu)$ analysis candidate events. The muVeto cut is applied in the same way to the simulated detector events. The veto system efficiency has been studied in this work (see Chapter 8). These results show that 97.17% of all muon-induced detector events occur within one second, the 1-second muVeto cut has a muon-induced background rejection efficiency of 97.12%, and the 1-second muVeto and Granularity cuts have a combined muon-induced background rejection efficiency of 97.8%.

Additionally as $\beta\beta(0\nu)$ is a highly localized process, i.e. the electrons will not travel far before being absorbed, then if $\beta\beta(0\nu)$ occurs within a detector only that detector should fire. Therefore, a simple but important analysis cut is the Granularity cut, which removes any detector event in which more than one detector fires from the $\beta\beta(0\nu)$ analysis candidate events. The Granularity cut is applied in the same way to the simulated detector events.

10.3 Simulated Muon-Induced Background Events

The muon-induced event rate can be calculated after processing the simulation data. First consider all possible muon-induced events (Energy $\in$ [0 keV, 14000 keV]). The MaGe simulation predicts a total muon-induced event rate of 2696.62 $\pm$ 10.13 c/kg $\cdot$ yr in the natural detectors and a total muon-induced event rate of 2116.77 $\pm$ 6.26 c/kg $\cdot$ yr in the enriched detectors. After applying the muVeto and Granularity analysis cuts, MaGe predicts an irreducible muon-induced background rate of 59.17 $\pm$ 1.50 c/kg $\cdot$ yr in the natural detectors, and 43.20 $\pm$ 0.89 c/kg $\cdot$ yr in the enriched detectors. These events will survive the analysis cuts and remain as a background to Majorana analyses.

Of particular interest to the $\beta\beta(0\nu)$ analysis is the amount of muon-induced background within a 400 keV window [1950 keV, 2350 keV] surrounding the $\beta\beta(0\nu)$ Q-value of 2039 keV. In this energy region, MaGe predicts the muon-induced event rate is 32.08 $\pm$ 1.10 c/kg $\cdot$ yr in the natural detectors and 25.76 $\pm$ 0.69 c/kg $\cdot$ yr in the enriched detectors without any analysis cuts. After applying the muVeto and Granularity analysis cuts, MaGe predicts an irreducible muon-induced background rate of 0.08 $\pm$ 0.05 c/kg $\cdot$ yr in the natural germanium detectors and 0.26 $\pm$ 0.07 c/kg $\cdot$ yr in the enriched germanium detectors. These events will remains as a background to the Majorana $\beta\beta(0\nu)$ analysis. Table 13.2 shows the MaGe muon-induced background along with the FLUKA rates discussed in Chapter 11.

Figures 10.1 and 10.2 show the energy spectra of the muon-induced background signals before and after analysis cuts for the natural germanium detectors and enriched germanium detectors respectively. As expected, the muVeto and Granularity cuts greatly reduce the amount of background signals in the natural and enriched detectors.

The MaGe simulation data also contains information about the physical processes that created each detector event. This data can be used to identify which particles and materials create the most muon-induced backgrounds in the Majorana Demonstrator. This information will be a helpful reference when a collaboration is designing a new experiment. Table 10.1 shows the processes that occur in the Majorana Demonstrator to create the majority of muon-induced background events in the [1950 keV, 2350 keV] window. In the Majorana Demonstrator, the primary source of muon-induced backgrounds near

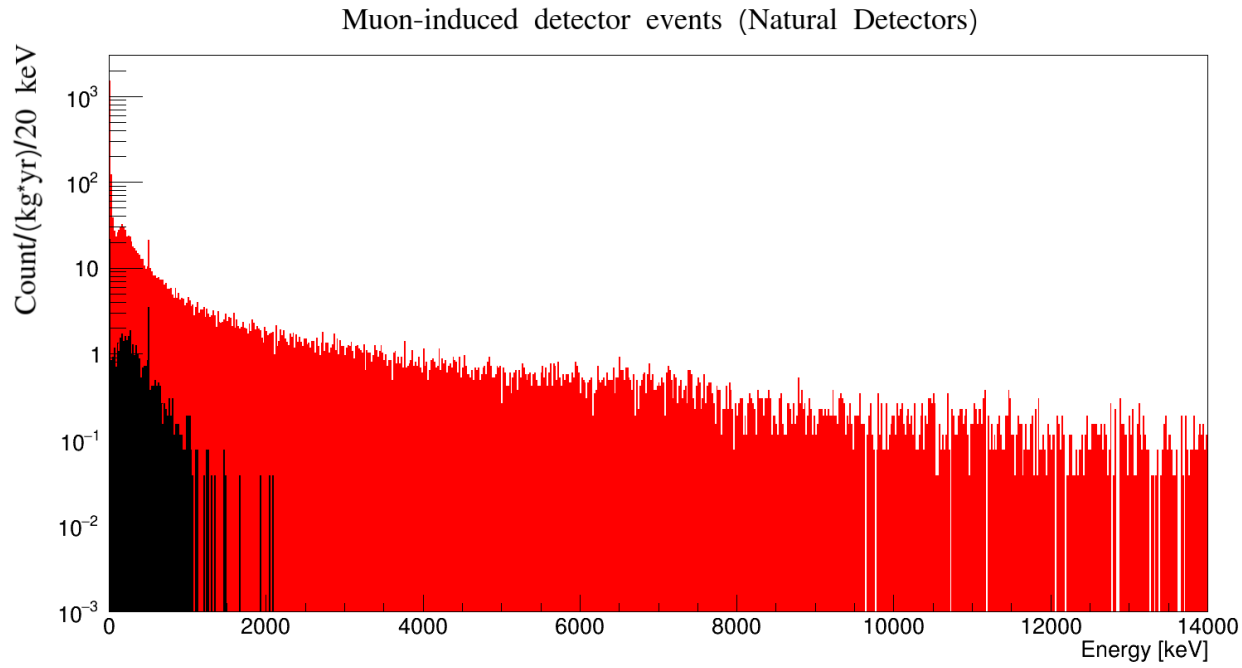

Figure 10.1: Energy Spectra of muon-induced natural germanium detector events simulated with MaGe. Red: No analysis cuts. Black: muVeto and Granularity cut.

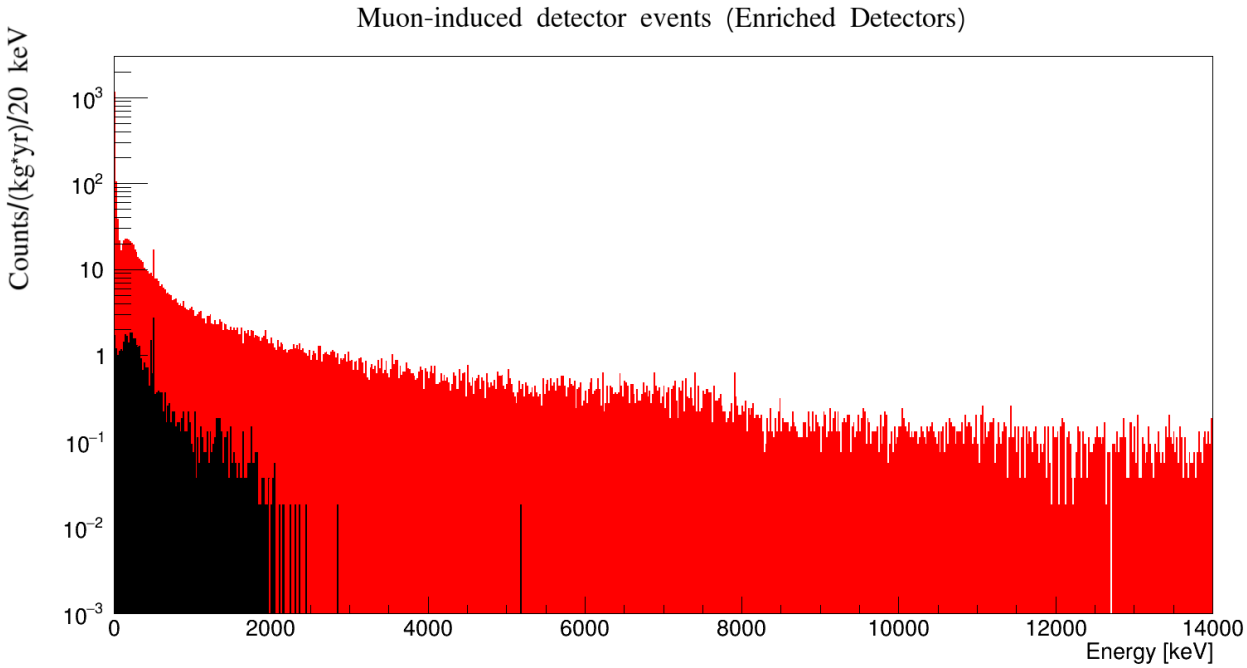

Figure 10.2: Energy Spectra of muon-induced enriched germanium detector events simulated with MaGe. Red: No analysis cuts. Black: muVeto and Granularity cut.

the $\beta\beta(0\nu)$ Q-value are depositions from gammas. In the region of interest, gammas create 53.46% of backgrounds in the natural detectors and 44.49% of backgrounds in the enriched detectors. These gammas can be created in any layer of the DEMONSTRATOR shield by a passing muon. The remaining major source of background in this energy region are from the creation and decay of ^{75}Ge and ^{77}Ge. Combined, both isotopes create 42.45% of the background in the natural detectors and 50.29% of the background in the enriched detectors. These isotopes are being created inside the detectors by neutron and gamma interactions. Since the $\beta\beta(0\nu)$ detector is made of germanium, the ^{75}Ge and ^{77}Ge background sources cannot be completely eliminated.

10.4 Production Rates of Data Analysis Isotopes

The MAGE simulation data will be compared with the data analysis results in Chapter 13. The production rates of the first excited states of ^{71}Ge, ^{75}Ge, and ^{77}Ge will be used in the comparison.

Table 12.4 shows the estimated amount of excited state isotopes produced in the MAGE simulations. The method used to perform this estimate is described in Chapter 12.

10.4.1 ^{71}Ge

In the natural germanium detectors, 519 isotopes of ground state (GS) ^{71}Ge were produced. In the enriched germanium detectors, 7 isotopes of ground state ^{71}Ge were produced. The ground state production rates are then calculated using the simulation exposure. The ground state ^{71}Ge production rate in natural germanium is 19.75 $\pm$ 0.87 c/kg $\cdot$ yr, and the rate in the enriched germanium is 0.13 $\pm$ 0.05 c/kg $\cdot$ yr. Using the Feldman-Cousins method [39], the 68.7% production rate upper limit is calculated to be 20.62 $\pm$ 0.89 c/kg $\cdot$ yr in natural germanium and 0.19 $\pm$ 0.06 c/kg $\cdot$ yr in enriched germanium. From the TALYS simulations of Chapter 12, the estimated amount of ^{71m}Ge isotopes in the MAGE simulation is 0.0 isotopes in the natural germanium and 0.0 isotopes in the enriched germanium. This corresponds to a production rate of 0.00 $\pm$ 0.04 c/kg $\cdot$ yr in the natural germanium and a production rate of 0.00 $\pm$ 0.02 c/kg $\cdot$ yr in the enriched germanium. As before, the 68.7% ^{71m}Ge production

rate upper limit is calculated to be 0.05 ± 0.04 c/kg · yr in the natural germanium and 0.02 ± 0.02 c/kg · yr in the enriched germanium.

The ground state isotope count and the excited state estimate can be found in Table 12.4. The excited state production rates and production rate upper limits can be found in Table 13.1 along with the FLUKA excited state production rates and upper limits (Chapter 11).

10.4.2 ^{75}Ge

In the natural germanium detectors, 410 isotopes of ground state ^{75}Ge were produced. In the enriched germanium detectors, 386 isotopes of ground state ^{75}Ge were produced. The ground state production rates are then calculated using the simulation exposure. The ground state ^{75}Ge production rate in natural germanium is 15.60 ± 0.77 c/kg · yr, and the rate in the enriched germanium is 7.14 ± 0.36 c/kg · yr. Using the Feldman-Cousins method [39], the 68.7% production rate upper limit is calculated to be 16.37 ± 0.79 c/kg · yr in natural germanium and 7.50 ± 0.37 c/kg · yr in enriched germanium. From the TALYS simulations of Chapter 12, the estimated amount of ^{75m}Ge isotopes in the MaGe simulation is 77.9 isotopes in the natural germanium and 101.2 isotopes in the enriched germanium. This corresponds to a production rate of 2.96 ± 0.34 c/kg · yr in the natural germanium and a production rate of 1.87 ± 0.19 c/kg · yr in the enriched germanium. As before, the 68.7% ^{75m}Ge production rate upper limit is calculated to be 3.30 ± 0.35 c/kg · yr in the natural germanium and 2.06 ± 0.20 c/kg · yr in the enriched germanium.

The ground state isotope count and the excited state estimate can be found in Table 12.4. The excited state production rates and production rate upper limits can be found in Table 13.1 along with the FLUKA excited state production rates and upper limits (Chapter 11).

10.4.3 ^{77}Ge

In the natural germanium detectors, 41 isotopes of ground state ^{77}Ge were produced. In the enriched germanium detectors, 635 isotopes of ground state ^{77}Ge were produced. The

ground state production rates are then calculated using the simulation exposure. The ground state ^{77}Ge production rate in natural germanium is 1.56 $\pm$ 0.24 c/kg $\cdot$ yr, and the rate in the enriched germanium is 11.74 $\pm$ 0.47 c/kg $\cdot$ yr. Using the Feldman-Cousins method [39], the 68.7% production rate upper limit is calculated to be 1.80 $\pm$ 0.26 c/kg $\cdot$ yr in natural germanium and 12.21 $\pm$ 0.48 c/kg $\cdot$ yr in enriched germanium. From the TALYS simulations of Chapter 12, the estimated amount of ^{77m}Ge isotopes in the MaGe simulation is 24.3 isotopes in the natural germanium and 375.7 isotopes in the enriched germanium. This corresponds to a production rate of 0.93 $\pm$ 0.19 c/kg $\cdot$ yr in the natural germanium and a production rate of 6.95 $\pm$ 0.36 c/kg $\cdot$ yr in the enriched germanium. As before, the 68.7% ^{77m}Ge production rate upper limit is calculated to be 1.11 $\pm$ 0.21 c/kg $\cdot$ yr in the natural germanium and 7.31 $\pm$ 0.37 c/kg $\cdot$ yr in the enriched germanium.

The ground state isotope count and the excited state estimate can be found in Table 12.4. The excited state production rates and production rate upper limits can be found in Table 13.1 along with the FLUKA excited state production rates and upper limits (Chapter 11).

Table 10.1: Particle Interactions in the MAJORANA DEMONSTRATOR that create the majority of muon-induced backgrounds in the [1950 keV,2350 keV] energy region.

Geant4 Process	Source Particle	% of ROI Bg: NatGe	% of ROI Bg: EnrGe
phot/compt	gamma	53.46	44.49
eIoni	^{75}Ge	33.00	15.00
msc	^{77}Ge	0.00	10.88
compt	^{77}Ge	0.00	23.38
ionIoni	^{75}Ge	3.95	1.03
eIoni	^{77}Ge	5.50	0.00
Total		95.91	94.78

Chapter 11

FLUKA Muon simulations

Two FLUKA simulation were performed in order to estimate the irreducible muon-induced background rate of the MAJORANA DEMONSTRATOR after analysis cuts. One simulation generated primary muons using the ShowersFromFile generator, the other generated primary muons using the MeiHime generator. Both muon generators are described in Chapter 7. Each simulation gathered fifty years worth of statistics (706.73 kg $\cdot$ yr of natural germanium exposure and 1454.11 kg $\cdot$ yr of Enriched germanium exposure). A slightly less detailed version of the MAGE DEMONSTRATOR geometry was used in these simulation, however both detector modules and all shielding were still included. FLUKA version fluka2011.2x.6 was used to perform these simulation.

11.1 Event Builder

As discussed in Chapter 10 the simulation data has to be processed with an event builder to properly mimic the MAJORANA Data Aquisition (DAQ) system. An event builder, identical in effect to the MAGE event builder, was created to handle the FLUKA output.

In the simulation processing, when a deposition is made in a detector the timestamp is recorded and a 20 μs time window is created. During this time window the energy depositions of each detector are summed individually. This "event" is then recorded to a data file with details such as timestamp, number of detectors hit, and amount of energy deposited in each detector. This is done for all detector depositions in the simulation.

11.2 Analysis Cuts

As in the MaGe simulation analysis, two analysis cuts have been implemented, the "1-second muon veto" (muVeto, for short) cut and the "granularity greater than 1" (Granularity, for short) cut.

The muVeto cut is simple but effective, if a detector event occurs within one second (plus timestamp uncertainties) of a event tagged by the veto system as a muon, then the detector event is removed from the $\beta\beta(0\nu)$ analysis candidate events.

The Granularity cut removes any 20 μs detector event in which more than one detector produces a signal. Such an event cannot be from a $\beta\beta(0\nu)$ decay.

11.3 Simulated Muon-Induced Background Events

The muon-induced event rate can be calculated after processing the simulation data. For each FLUKA simulation, two energy ranges are considered: The [0, 14000 keV] energy window, which contains all possible detector depositions, and the region of interest [1950 keV, 2350 keV], which is a 400 keV window surrounding the $\beta\beta(0\nu)$ Q-value of 2039 keV.

11.3.1 ShowersFromFile Simulation

First consider all possible muon-induced events (Energy $\in$ [0 keV, 14000 keV]). The FLUKA ShowersFromFile simulation predicts a total muon-induced event rate of 615.45 $\pm$ 0.93 c/kg $\cdot$ yr in the natural detectors and a total muon-induced event rate of 544.65 $\pm$ 0.61 c/kg $\cdot$ yr in the enriched detectors. After applying the muVeto and Granularity analysis cuts, FLUKA SFF predicts an irreducible muon-induced background rate of 12.62 $\pm$ 0.13 c/kg $\cdot$ yr in the natural detectors, and 13.91 $\pm$ 0.10 c/kg $\cdot$ yr in the enriched detectors. These events will survive the analysis cuts and remain as a background to Majorana analyses.

Now consider the region of interest (Energy $\in$ [1950 keV, 2350 keV]). In this energy region, FLUKA SFF predicts the muon-induced event rate is 2.40 $\pm$ 0.06 c/kg $\cdot$ yr in the natural detectors and 2.09 $\pm$ 0.04 c/kg $\cdot$ yr in the enriched detectors without any analysis cuts. After applying the muVeto and Granularity analysis cuts, FLUKA SFF predicts an

irreducible muon-induced background rate of 0.07 ± 0.01 c/kg · yr in the natural germanium detectors and 0.04 ± 0.01 c/kg · yr in the enriched germanium detectors. These events will remains as a background to the MAJORANA $\beta\beta(0\nu)$ analysis. Table 13.2 shows the FLUKA SFF muon-induced background along with the FLUKA MH rates and the MAGE rates discussed in Chapter 10.

Figures 11.1 and 11.2 show the energy spectra of the muon-induced background signals before and after analysis cuts for the natural germanium detectors and enriched germanium detectors respectively. As expected, the muVeto and Granularity cuts greatly reduce the amount of background signals in the natural and enriched detectors.

11.3.2 MeiHime Simulation

First consider all possible muon-induced events (Energy ∈ [0 keV, 14000 keV]). The FLUKA MeiHime simulation predicts a total muon-induced event rate of 244.38 ± 0.59 c/kg · yr in the natural detectors and a total muon-induced event rate of 214.93 ± 0.38 c/kg · yr in the enriched detectors. After applying the muVeto and Granularity analysis cuts, FLUKA MH predicts an irreducible muon-induced background rate of 3.91 ± 0.07 c/kg · yr in the natural detectors, and 4.23 ± 0.05 c/kg · yr in the enriched detectors. These events will survive the analysis cuts and remain as a background to MAJORANA analyses.

Now consider the region of interest (Energy ∈ [1950 keV, 2350 keV]). In this energy region, FLUKA MH predicts the muon-induced event rate is 1.24 ± 0.04 c/kg · yr in the natural detectors and 0.74 ± 0.02 c/kg · yr in the enriched detectors without any analysis cuts. After applying the muVeto and Granularity analysis cuts, FLUKA MH predicts an irreducible muon-induced background rate of 0.05 ± 0.01 c/kg · yr in the natural germanium detectors and 0.015 ± 0.003 c/kg · yr in the enriched germanium detectors. These events will remains as a background to the MAJORANA $\beta\beta(0\nu)$ analysis. Table 13.2 shows the FLUKA MH muon-induced background along with the FLUKA SFF rates and the MAGE rates discussed in Chapter 10.

Figures 11.3 and 11.4 show the energy spectra of the muon-induced background signals before and after analysis cuts for the natural germanium detectors and enriched germanium

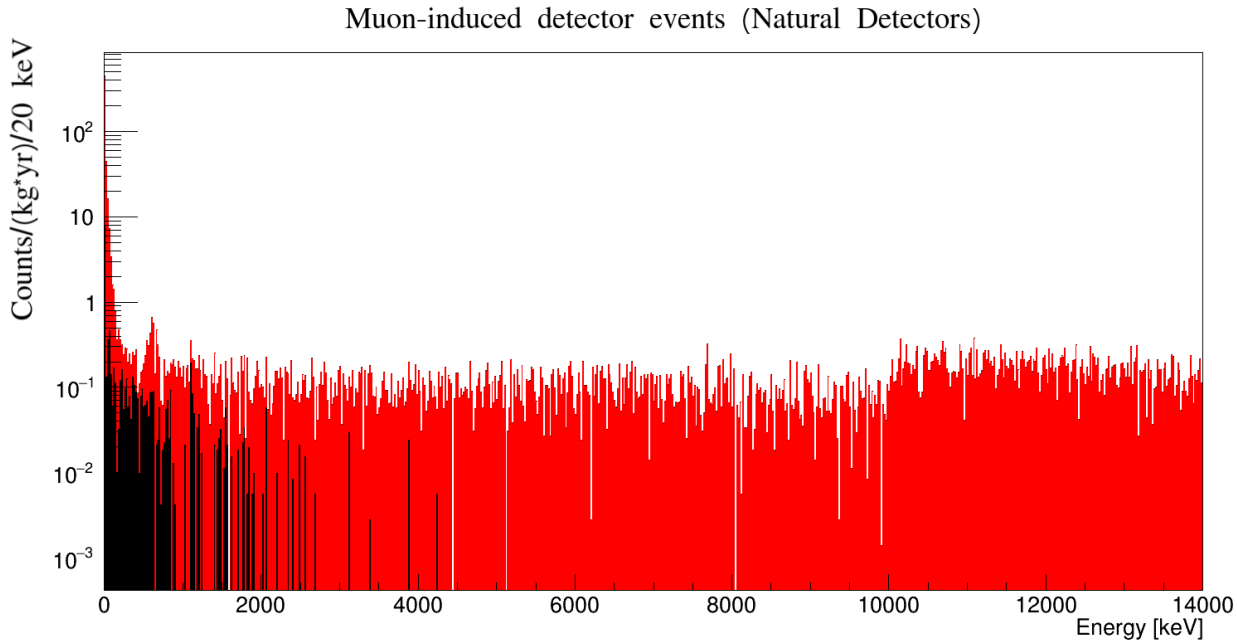

Figure 11.1: Energy Spectra of muon-induced natural germanium detector events simulated with FLUKA using the ShowersFromFile generator. Red: No analysis cuts. Black: muVeto and Granularity cuts.

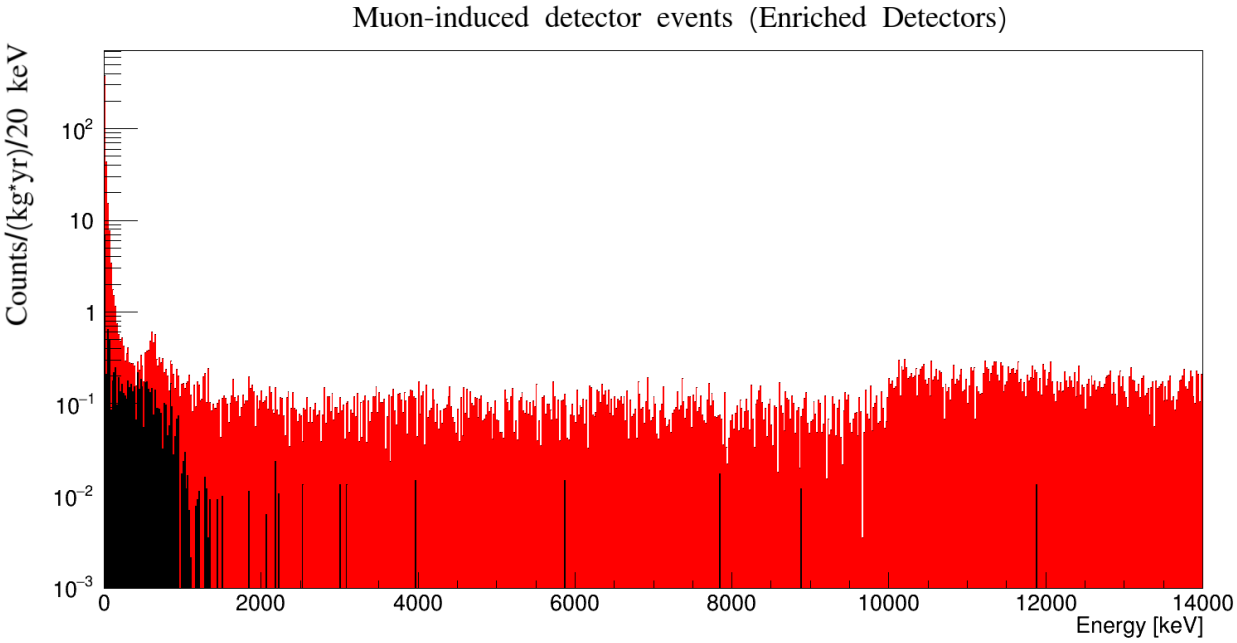

Figure 11.2: Energy Spectra of muon-induced enriched germanium detector events simulated with FLUKA using the ShowersFromFile generator. Red: No analysis cuts. Black: muVeto and Granularity cuts.

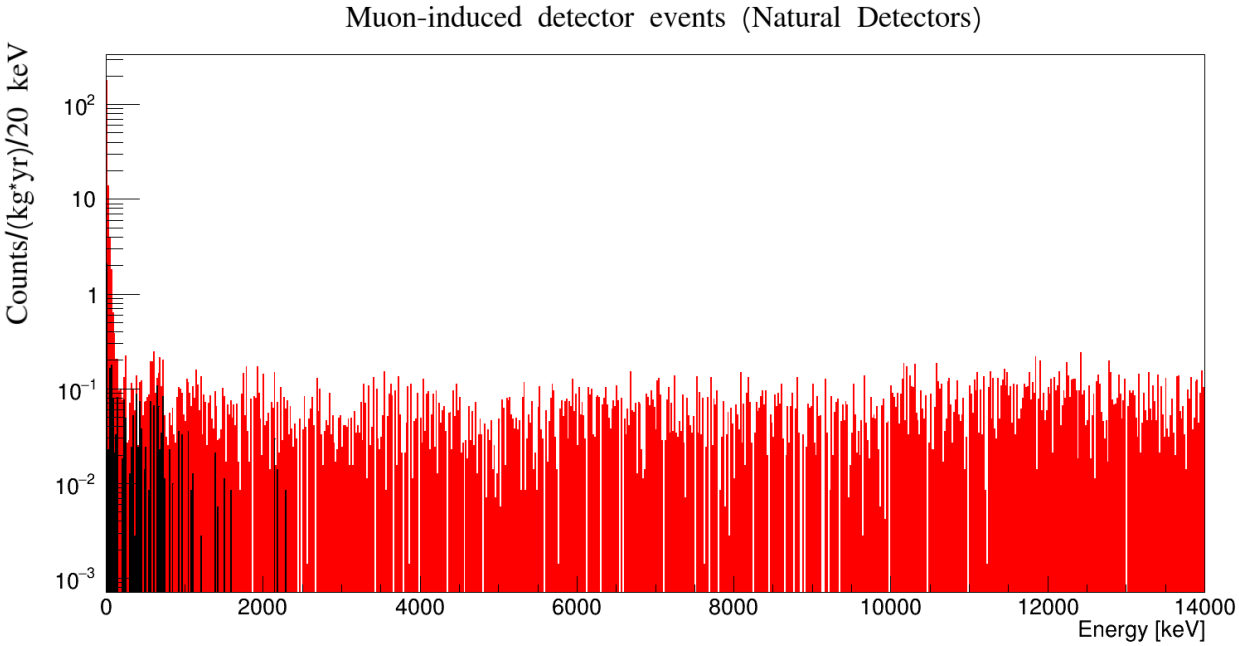

Figure 11.3: Energy Spectra of muon-induced natural germanium detector events simulated with FLUKA using the MeiHime generator. Red: No analysis cuts. Black: muVeto and Granularity cuts.

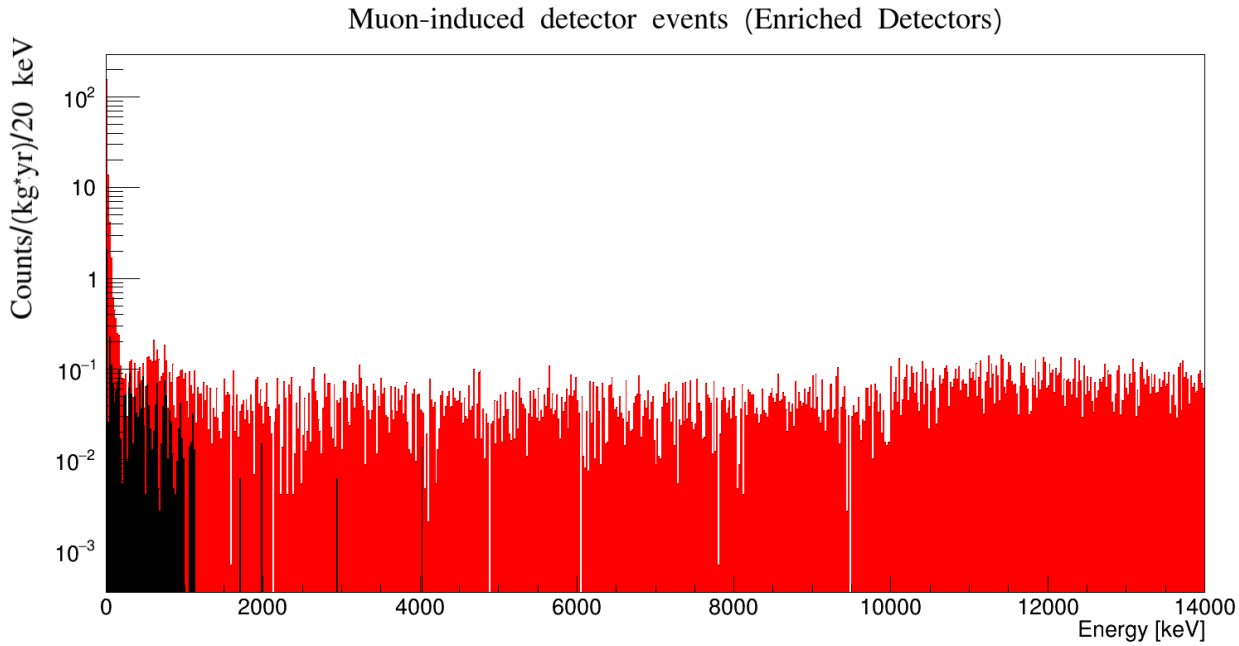

Figure 11.4: Energy Spectra of muon-induced enriched germanium detector events simulated with FLUKA using the MeiHime generator. Red: No analysis cuts. Black: muVeto and Granularity cuts.

detectors respectively. As expected, the muVeto and Granularity cuts greatly reduce the amount of background signals in the natural and enriched detectors.

11.4 Production Rates of Data Analysis Isotopes

The FLUKA simulation data will be compared with the data analysis results discussed in Chapter 13. The production rates of the first excited states of ^{71}Ge, ^{75}Ge, and ^{77}Ge will be used in the comparison.

As FLUKA does not accurately simulate nuclei excitation, the ^{71m}Ge, ^{75m}Ge, and ^{77m}Ge production rate must be estimated. TALYS simulations will be used in conjunction with the ^{71}Ge, ^{75}Ge, and ^{77}Ge ground state production extracted from the FLUKA simulations to perform this estimate.

The estimated ^{71m}Ge, ^{75m}Ge, and ^{77m}Ge counts is shown in Table 12.4. The details of this estimate is described in Chapter 12.

These estimates are then used to calculate a production rate for ^{71}Ge, ^{75}Ge, and ^{77}Ge.

11.4.1 ShowersFromFile Production Rates

First the production rates of the FLUKA ShowersFromFile simulations will be discussed.

^{71}Ge

In the natural germanium detectors, 734 isotopes of ground state (GS) ^{71}Ge were produced. In the enriched germanium detectors, 1312 isotopes of ground state ^{71}Ge were produced. The ground state production rates are then calculated using the simulation exposure. The ground state ^{71}Ge production rate in natural germanium is 1.04 ± 0.04 c/kg $\cdot$ yr, and the rate in the enriched germanium is 0.90 ± 0.02 c/kg $\cdot$ yr. Using the Feldman-Cousins method [39], the 68.7% production rate upper limit is calculated to be 1.08 ± 0.04 c/kg $\cdot$ yr in natural germanium and 0.93 ± 0.03 c/kg $\cdot$ yr in enriched germanium.

From the TALYS simulations of Chapter 12, the estimated amount of ^{71m}Ge isotopes in the MaGe simulation is 0.0 isotopes in the natural germanium and 0.0 isotopes in the enriched germanium. This corresponds to a production rate of 0.0000 ± 0.0014 c/kg $\cdot$ yr in

the natural germanium and a production rate of 0.0000 ± 0.0007 c/kg · yr in the enriched germanium. As before, the 68.7% ^{71m}Ge production rate upper limit is calculated to be 0.0018 ± 0.0016 c/kg · yr in the natural germanium and 0.0009 ± 0.0008 c/kg · yr in the enriched germanium.

The ground state isotope count and the excited state estimate can be found in Table 12.4. The excited state production rates and production rate upper limits can be found in Table 13.1 along with the MaGe excited state production rates and upper limits (Chapter 10).

^{75}Ge

In the natural germanium detectors, 415 isotopes of ground state ^{75}Ge were produced. In the enriched germanium detectors, 1403 isotopes of ground state ^{75}Ge were produced. The ground state production rates are then calculated using the simulation exposure. The ground state ^{75}Ge production rate in natural germanium is 0.59 ± 0.03 c/kg · yr, and the rate in the enriched germanium is 0.97 ± 0.03 c/kg · yr. Using the Feldman-Cousins method [39], the 68.7% production rate upper limit is calculated to be 0.62 ± 0.03 c/kg · yr in natural germanium and 0.99 ± 0.03 c/kg · yr in enriched germanium.

From the TALYS simulations of Chapter 12, the estimated amount of ^{75m}Ge isotopes in the MaGe simulation is 79.5 isotopes in the natural germanium and 367.2 isotopes in the enriched germanium. This corresponds to a production rate of 0.112 ± 0.013 c/kg · yr in the natural germanium and a production rate of 0.253 ± 0.013 c/kg · yr in the enriched germanium. As before, the 68.7% ^{75m}Ge production rate upper limit is calculated to be 0.125 ± 0.013 c/kg · yr in the natural germanium and 0.266 ± 0.014 c/kg · yr in the enriched germanium.

The ground state isotope count and the excited state estimate can be found in Table 12.4. The excited state production rates and production rate upper limits can be found in Table 13.1 along with the MaGe excited state production rates and upper limits (Chapter 10).

^{77}Ge

In the natural germanium detectors, 18 isotopes of ground state ^{77}Ge were produced. In the enriched germanium detectors, 53 isotopes of ground state ^{77}Ge were produced. The ground state production rates are then calculated using the simulation exposure. The ground state ^{77}Ge production rate in natural germanium is 0.026 $\pm$ 0.006 c/kg $\cdot$ yr, and the rate in the enriched germanium is 0.036 $\pm$ 0.005 c/kg $\cdot$ yr. Using the Feldman-Cousins method [39], the 68.7% production rate upper limit is calculated to be 0.032 $\pm$ 0.007 c/kg $\cdot$ yr in natural germanium and 0.042 $\pm$ 0.005 c/kg $\cdot$ yr in enriched germanium.

From the TALYS simulations of Chapter 12, the estimated amount of ^{77m}Ge isotopes in the MaGe simulation is 10.6 isotopes in the natural germanium and 30.8 isotopes in the enriched germanium. This corresponds to a production rate of 0.015 $\pm$ 0.005 c/kg $\cdot$ yr in the natural germanium and a production rate of 0.021 $\pm$ 0.004 c/kg $\cdot$ yr in the enriched germanium. As before, the 68.7% ^{77m}Ge production rate upper limit is calculated to be 0.021 $\pm$ 0.005 c/kg $\cdot$ yr in the natural germanium and 0.025 $\pm$ 0.004 c/kg $\cdot$ yr in the enriched germanium.

The ground state isotope count and the excited state estimate can be found in Table 12.4. The excited state production rates and production rate upper limits can be found in Table 13.1 along with the MaGe excited state production rates and upper limits (Chapter 10).

11.4.2 MeiHime Production Rates

Now the production rates of the FLUKA MeiHime simulations will be discussed.

^{71}Ge

In the natural germanium detectors, 140 isotopes of ground state (GS) ^{71}Ge were produced. In the enriched germanium detectors, 275 isotopes of ground state ^{71}Ge were produced. The ground state production rates are then calculated using the simulation exposure. The ground state ^{71}Ge production rate in natural germanium is 0.20 $\pm$ 0.02 c/kg $\cdot$ yr, and the rate in the enriched germanium is 0.19 $\pm$ 0.01 c/kg $\cdot$ yr. Using the Feldman-Cousins method [39],

the 68.7% production rate upper limit is calculated to be 0.22 ± 0.02 c/kg · yr in natural germanium and 0.20 ± 0.01 c/kg · yr in enriched germanium.

From the TALYS simulations of Chapter 12, the estimated amount of ^{71m}Ge isotopes in the MaGe simulation is 0.0 isotopes in the natural germanium and 0.0 isotopes in the enriched germanium. This corresponds to a production rate of 0.0000 ± 0.0014 c/kg · yr in the natural germanium and a production rate of 0.0000 ± 0.0007 c/kg · yr in the enriched germanium. As before, the 68.7% ^{71m}Ge production rate upper limit is calculated to be 0.0018 ± 0.0016 c/kg · yr in the natural germanium and 0.0009 ± 0.0008 c/kg · yr in the enriched germanium.

The ground state isotope count and the excited state estimate can be found in Table 12.4. The excited state production rates and production rate upper limits can be found in Table 13.1 along with the MaGe excited state production rates and upper limits (Chapter 10).

^{75}Ge

In the natural germanium detectors, 109 isotopes of ground state ^{75}Ge were produced. In the enriched germanium detectors, 330 isotopes of ground state ^{75}Ge were produced. The ground state production rates are then calculated using the simulation exposure. The ground state ^{75}Ge production rate in natural germanium is 0.15 ± 0.01 c/kg · yr, and the rate in the enriched germanium is 0.23 ± 0.01 c/kg · yr. Using the Feldman-Cousins method [39], the 68.7% production rate upper limit is calculated to be 0.17 ± 0.02 c/kg · yr in natural germanium and 0.24 ± 0.01 c/kg · yr in enriched germanium.

From the TALYS simulations of Chapter 12, the estimated amount of ^{75m}Ge isotopes in the MaGe simulation is 20.4 isotopes in the natural germanium and 88.2 isotopes in the enriched germanium. This corresponds to a production rate of 0.029 ± 0.006 c/kg · yr in the natural germanium and a production rate of 0.061 ± 0.006 c/kg · yr in the enriched germanium. As before, the 68.7% ^{75m}Ge production rate upper limit is calculated to be 0.035 ± 0.007 c/kg · yr in the natural germanium and 0.067 ± 0.007 c/kg · yr in the enriched germanium.

The ground state isotope count and the excited state estimate can be found in Table 12.4. The excited state production rates and production rate upper limits can be found in Table 13.1 along with the MaGe excited state production rates and upper limits (Chapter 10).

^{77}Ge

In the natural germanium detectors, 3 isotopes of ground state ^{77}Ge were produced. In the enriched germanium detectors, 10 isotopes of ground state ^{77}Ge were produced. The ground state production rates are then calculated using the simulation exposure. The ground state ^{77}Ge production rate in natural germanium is 0.0042 $\pm$ 0.0025 c/kg $\cdot$ yr, and the rate in the enriched germanium is 0.0069 $\pm$ 0.0022 c/kg $\cdot$ yr. Using the Feldman-Cousins method [39], the 68.7% production rate upper limit is calculated to be 0.0075 $\pm$ 0.0033 c/kg $\cdot$ yr in natural germanium and 0.0095 $\pm$ 0.0026 c/kg $\cdot$ yr in enriched germanium.

From the TALYS simulations of Chapter 12, the estimated amount of ^{77m}Ge isotopes in the MaGe simulation is 1.8 isotopes in the natural germanium and 5.9 isotopes in the enriched germanium. This corresponds to a production rate of 0.0026 $\pm$ 0.0019 c/kg $\cdot$ yr in the natural germanium and a production rate of 0.0041 $\pm$ 0.0017 c/kg $\cdot$ yr in the enriched germanium. As before, the 68.7% ^{77m}Ge production rate upper limit is calculated to be 0.0060 $\pm$ 0.0029 c/kg $\cdot$ yr in the natural germanium and 0.0064 $\pm$ 0.0021 c/kg $\cdot$ yr in the enriched germanium.

The ground state isotope count and the excited state estimate can be found in Table 12.4. The excited state production rates and production rate upper limits can be found in Table 13.1 along with the MaGe excited state production rates and upper limits (Chapter 10).

Chapter 12

TALYS Simulation

This chapter discusses the various TALYS simulations performed on isotopes of germanium. These simulations are a necessary in order to directly compare the MaGe and FLUKA muon simulation results, Chapters 10 and 11, with the delayed cosmogenics data analysis results, Chapter 6.

As the MaGe and FLUKA simulations do not produce meta-stable states, only the ground state production rates of ^{71}Ge, ^{75}Ge, and ^{77}Ge can be calculated from the simulation results. In order to compare the simulations with the excited state production rates of ^{71m}Ge, ^{75m}Ge, and ^{77m}Ge measured in Chapter 6, excited state production rate estimates must be extracted from the simulation results.

These simulated excited state production rates will be extracted by utilizing the TALYS software to estimate the isomeric production ratio, which can then be applied to the simulated ground state production rates.

12.1 Ground State Production Processes

The primary production processes of the signature isotopes, ^{71}Ge, ^{75}Ge, and ^{77}Ge, are known from the MaGe and FLUKA simulations.

12.1.1 MaGe particles

The MaGe simulations show that neutrons and gammas are the particles that contribute the most to the production of the signature isotopes.

In natural germanium detectors for the MaGe simulation:

Neutrons and gammas produce 99.81% of all ^{71}Ge

- 23 isotopes (4.43%) produced by gammas.
- 484 isotopes (93.26%) produced by neutron capture.
- 11 isotope (2.12%) produced by neutron inelastic scattering.

Neutrons and gammas produce 100% of all ^{75}Ge

- 3 isotopes (0.73%) produced by gammas.
- 405 isotopes (98.78%) produced by neutron capture.
- 2 isotopes (0.49%) produced by neutron inelastic scattering.

Neutrons produce 100% of all ^{77}Ge

- 41 isotopes (100%) produced by neutron capture.

In enriched germanium detectors for the MaGe simulation:

Neutrons produce 71.43% of all ^{71}Ge

- 28 isotopes (71.43%) produced by neutron inelastic scattering.

Neutrons and gammas produce 99.48% of all ^{75}Ge

- 102 isotopes (26.94%) produced by gammas.
- 254 isotopes (65.80%) produced by neutron capture.
- 26 isotopes (6.74%) produced by neutron inelastic scattering.

Neutrons produce 100% of all ^{77}Ge

- 635 isotopes (100%) produced by neutron capture.

12.1.2 FLUKA particles

The FLUKA simulations show that neutrons and gammas are the particles that contribute the most to the production of the signature isotopes.

FLUKA ShowersFromFile simulation

In natural germanium detectors for the FLUKA ShowersFromFile simulation:

- Neutrons and gammas produce 96.46% of all ^{71}Ge
  - 166 isotopes (22.62%) produced by gammas.
  - 542 isotopes (73.84%) produced by neutrons (capture and inelastic scattering).
    - Using MaGe as a basis, this likely corresponds to 530 produced through neutron capture and 12 produced through neutron inelastic scattering.
- Neutrons and gammas produce 95.91% of all ^{75}Ge
  - 28 isotopes (6.75%) produced by gammas.
  - 370 isotopes (89.16%) produced by neutrons (capture and inelastic scattering).
    - Using MaGe as a basis, this likely corresponds to 368 produced through neutron capture and 2 produced through neutron inelastic scattering.
- Neutrons produce 100% of all ^{77}Ge
  - 18 isotopes (100%) produced by neutrons (capture).

In enriched germanium detectors for the FLUKA ShowersFromFile simulation:

- Neutrons and gammas produce 95.88% of all ^{71}Ge
  - 12 isotopes (0.91%) produced by gammas.
  - 1246 isotopes (94.97%) produced by neutrons (capture and inelastic scattering).
    - Using MaGe as a basis, this likely corresponds to 0 produced through neutron capture and 1246 produced through neutron inelastic scattering.

Neutrons and gammas produce 97.08% of all ^{75}Ge

- 431 isotopes (30.72%) produced by gammas.
- 931 isotopes (66.36%) produced by neutrons (capture and inelastic scattering).
    - Using MaGe as a basis, this likely corresponds to 845 produced through neutron capture and 86 produced through neutron inelastic scattering.

Neutrons produce 98.1% of all ^{77}Ge

- 52 isotopes (98.1%) produced by neutrons (capture).

FLUKA MeiHime Simulation

In natural germanium detectors for the FLUKA MeiHime simulation:

Neutrons and gammas produce 95.71% of all ^{71}Ge

- 15 isotopes (10.71%) produced by gammas.
- 119 isotopes (85.00%) produced by neutrons (capture and inelastic scattering).
    - Using MaGe as a basis, this likely corresponds to 116 produced through neutron capture and 3 produced through neutron inelastic scattering.

Neutrons and gammas produce 97.25% of all ^{75}Ge

- 1 isotope (0.92%) produced by gammas.
- 105 isotopes (96.33%) produced by neutrons (capture and inelastic scattering).
    - Using MaGe as a basis, this likely corresponds to 104 produced through neutron capture and 1 produced through neutron inelastic scattering.

Neutrons produce 100% of all ^{77}Ge

- 3 isotopes (100%) produced by neutrons (capture).

In enriched germanium detectors for the FLUKA MeiHime simulation:

Neutrons and gammas produce 97.45% of all ^{71}Ge

- 1 isotopes (0.36%) produced by gammas.
- 267 isotopes (97.09%) produced by neutrons (capture and inelastic scattering).
    * Using MaGe as a basis, this likely corresponds to 0 produced through neutron capture and 267 produced through neutron inelastic scattering.

Neutrons and gammas produce 97.28% of all ^{75}Ge

- 118 isotopes (35.76%) produced by gammas.
- 203 isotopes (61.52%) produced by neutrons (capture and inelastic scattering).
    * Using MaGe as a basis, this likely corresponds to 184 produced through neutron capture and 19 produced through neutron inelastic scattering.

Neutrons produce 100% of all ^{77}Ge

- 10 isotopes (100%) produced by neutrons (capture).

12.2 Simulated Interactions

Therefore the following interactions are simulated with TALYS to determine the correct isomeric production ratio: neutrons on ^{70}Ge, neutrons on ^{72}Ge, neutrons on ^{74}Ge, neutrons on ^{76}Ge, gammas on ^{72}Ge, gammas on ^{76}Ge.

These interactions will cover $\sim 95\%$ the signature isotope production in the MaGe and FLUKA simulations.

12.3 Kinetic Energy

The kinetic energy of neutrons and gammas that are moving through the germanium detectors, and can therefore create these signature isotopes, can be extracted from the MaGe simulation.

Figures 12.1 and 12.2 shows the simulated kinetic energy spectrum of neutrons and gammas in the germanium detectors.

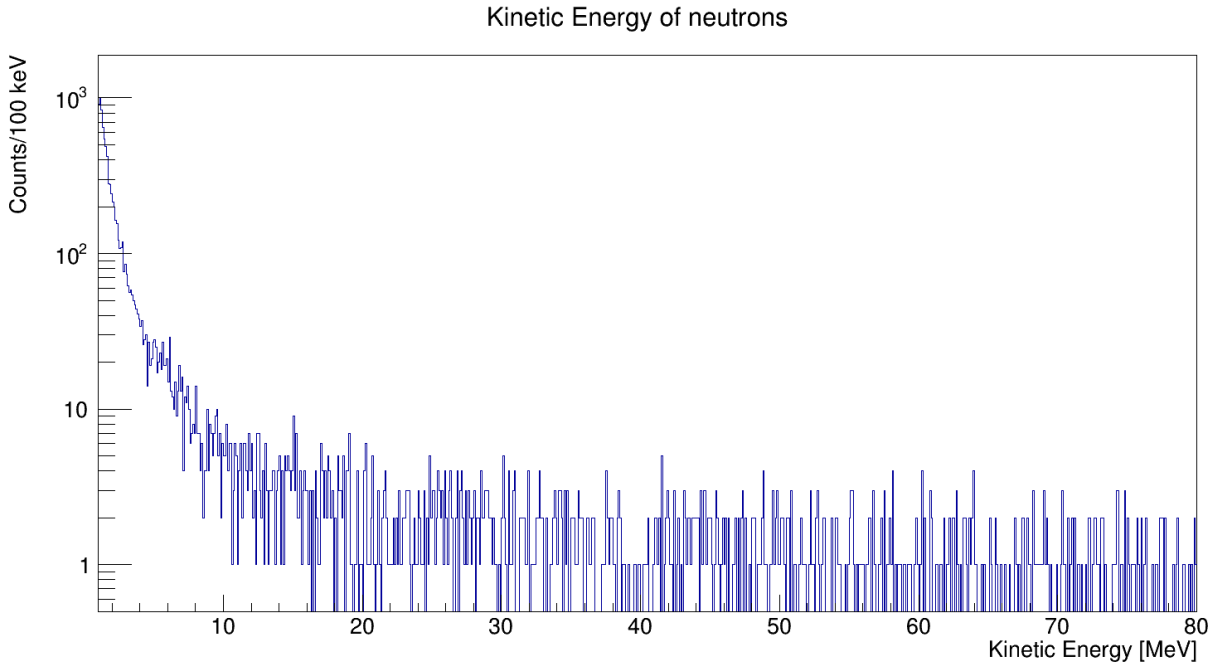

Figure 12.1: Kinetic energy spectrum of neutrons inside germanium detectors. From MaGe muon simulations.

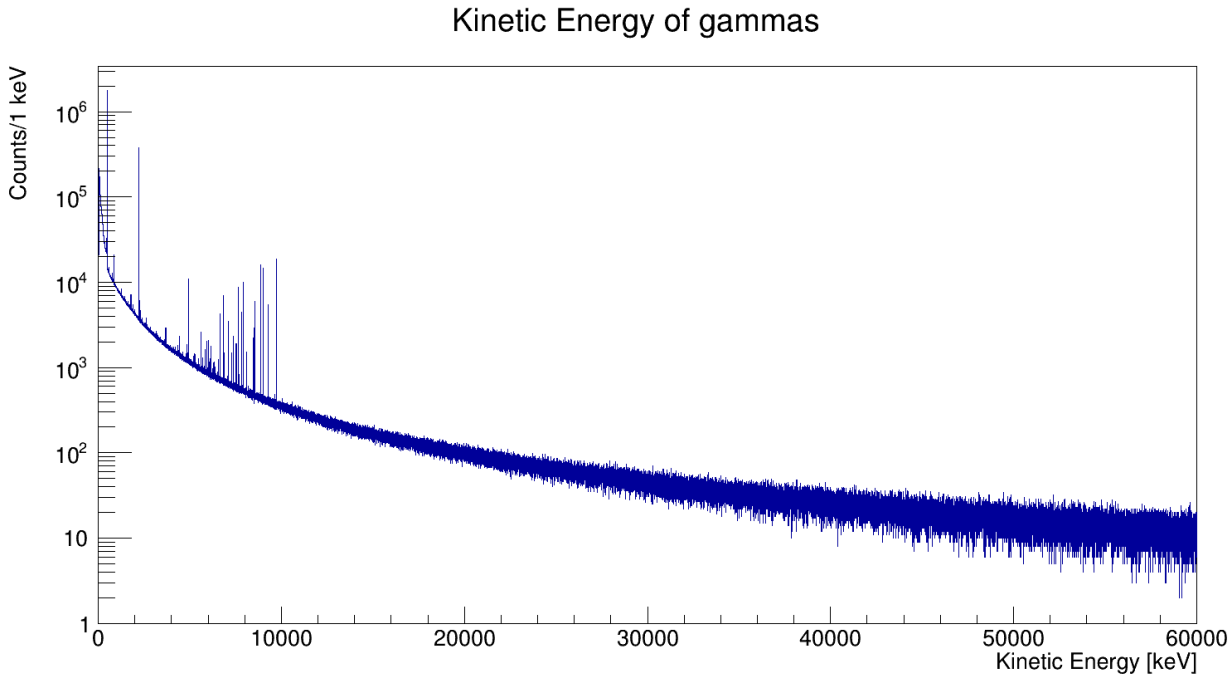

Figure 12.2: Kinetic energy spectrum of gammas inside germanium detectors. From MaGe muon simulations.

Both spectra have a peak at low energies and have long high energy tails. It is not feasible to simulate the entire neutron or gamma energy spectra as TALYS has an upper limit of 1 GeV. Therefore a region of interest is defined for each particle. Approximately 98.8% of gammas have a kinetic energy within the window [10 keV, 60 MeV]. This will be the region of interest for TALYS simulations of gamma interactions. Approximately 98.4% of neutrons have a kinetic energy within the window [10 eV, 80 MeV]. This will be the region of interest for TALYS simulations of neutron interactions.

Figure 12.3 and 12.4 shows the normalized gamma and neutron kinetic energy spectra in the respective regions of interest.

12.4 Isomeric Ratios

The six TALYS simulations were run with an energy range of [1 eV, 1 GeV] in order to visualize the energy dependence of the excited state isotope production.

Only three TALYS simulations produced any excited state signature isotopes: neutrons on ^{76}Ge, neutrons on ^{74}Ge, and gammas on ^{76}Ge.

Figures 12.5, 12.6, 12.7, and 12.8 show the non-zero isomeric ratios for the full energy range [1 eV, 1 GeV] and the gamma and neutron regions of interest.

The only signature excited states produced with TALYS were ^{75m}Ge and ^{77m}Ge. No excited state of ^{71}Ge was produced and no other excited states of ^{75}Ge and ^{77}Ge were produced.

The isomeric ratios all flatten out at higher energies, with the gamma induced isomeric ratio flattening at $\sim$ 45 MeV, and the three neutron induced isomeric ratios flattening at $\sim$ 25 MeV.

12.5 Production Cross Section

In addition to the isomeric ratio, TALYS also provides the production cross section of the ground state and excited state isotopes.

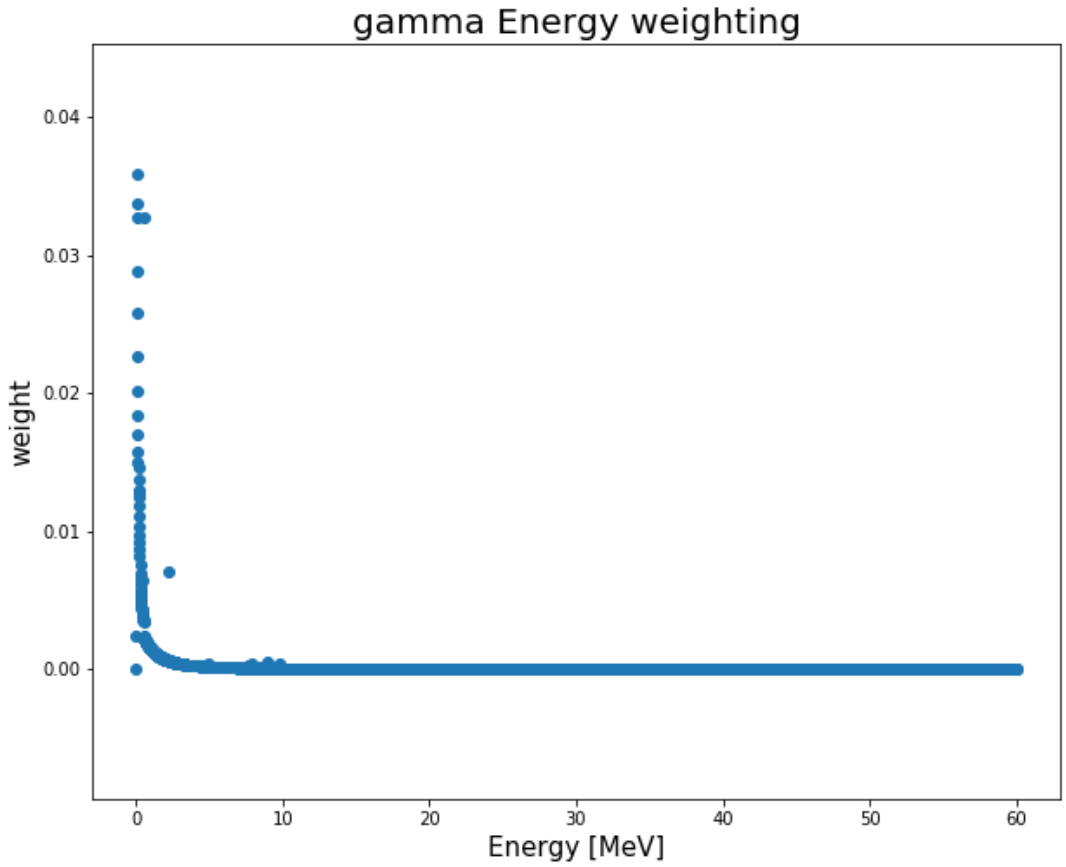

Figure 12.3: Normalized kinetic energy spectrum of gammas inside germanium detectors. From MaGe muon simulation.

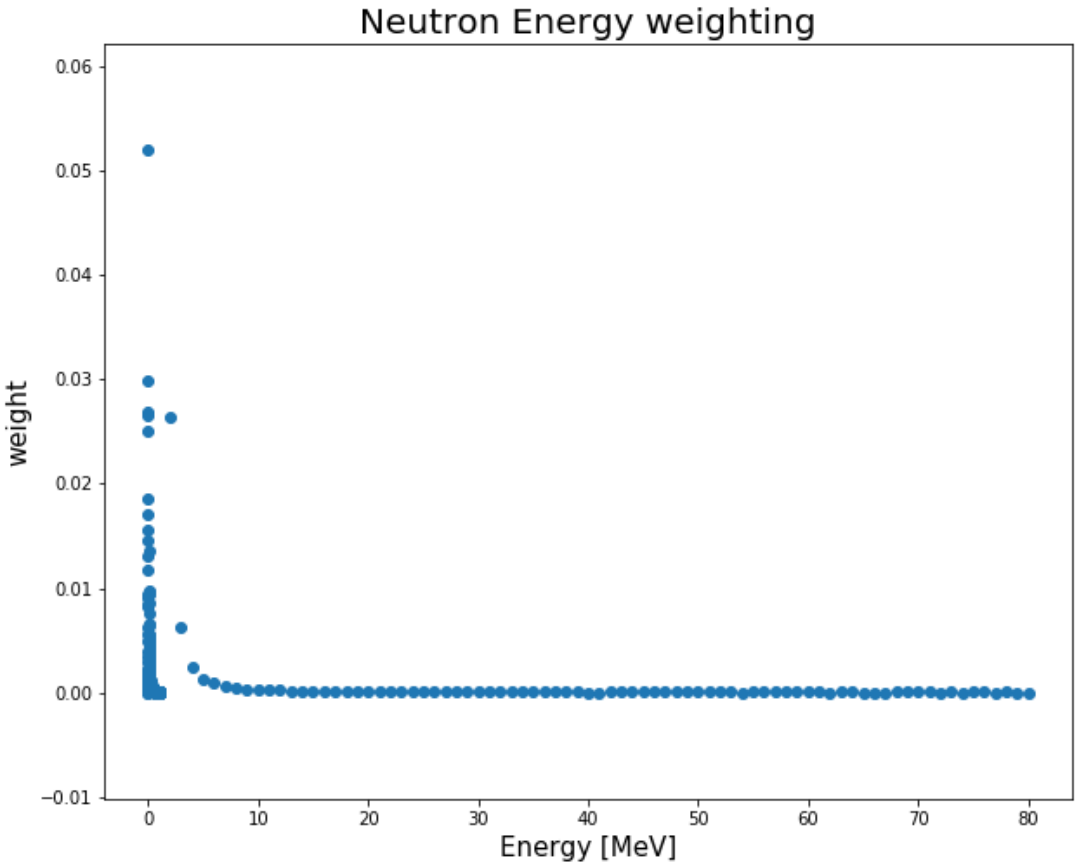

Figure 12.4: Normalized kinetic energy spectrum of neutrons inside germanium detectors. From MaGe muon simulation.

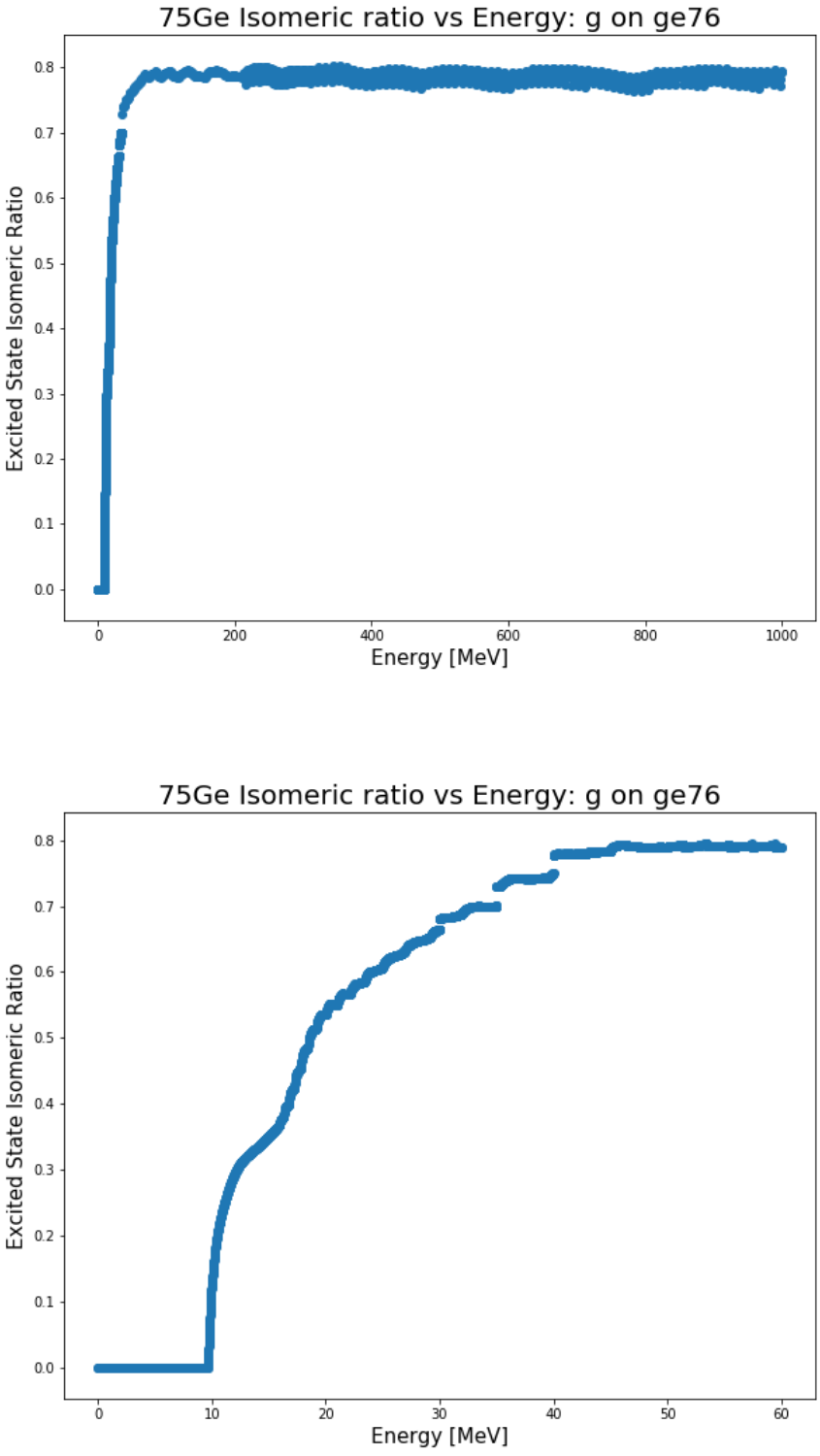

Figure 12.5: Isomeric ratio of ^{75}Ge from TALYS gamma on ^{76}Ge simulation. Full energy range (top) and gamma energy region of interest (bottom).

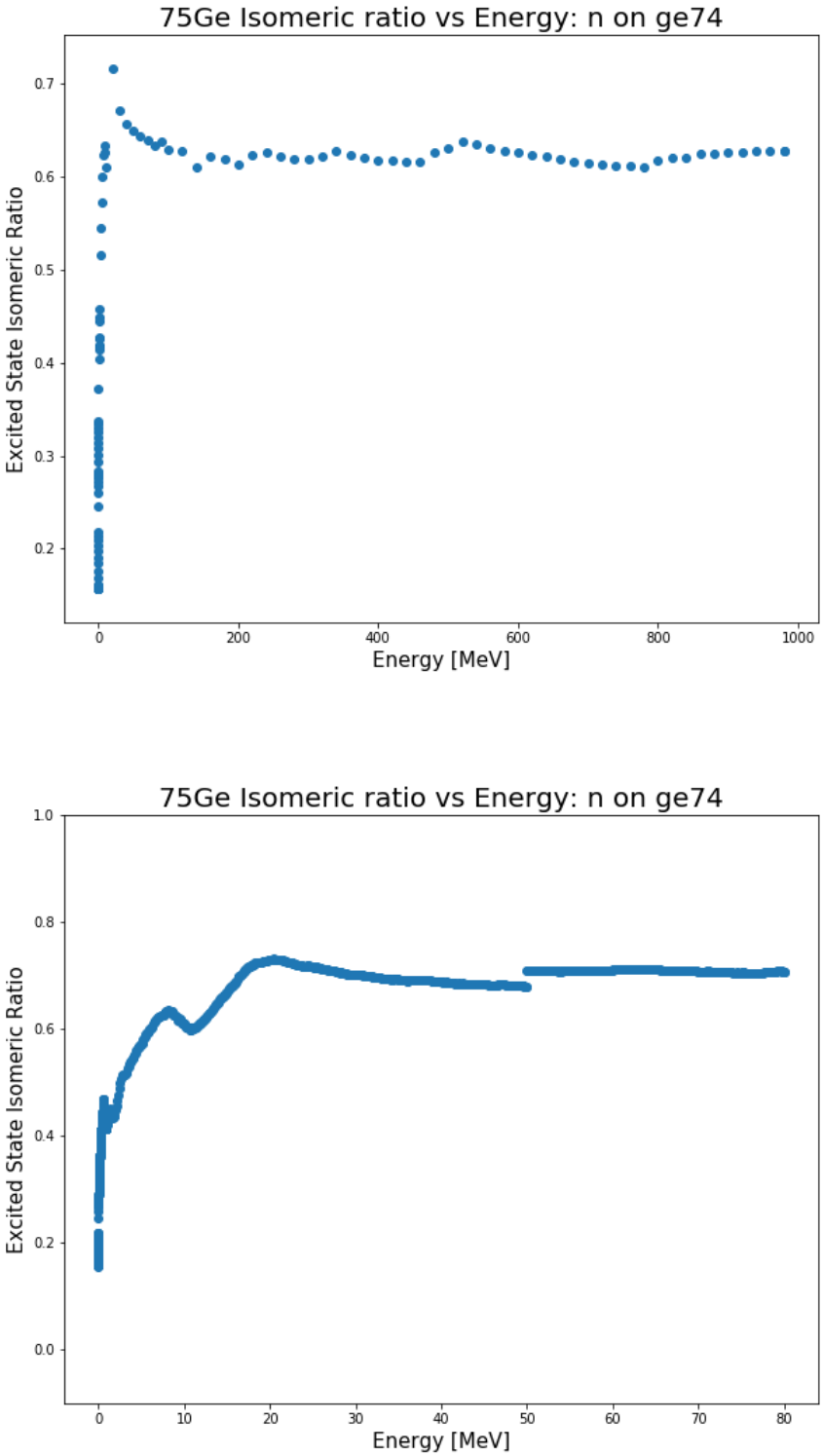

Figure 12.6: Isomeric ratio of ^{75}Ge from TALYS neutron on ^{74}Ge simulation. Full energy range (top) and neutron energy region of interest (bottom).

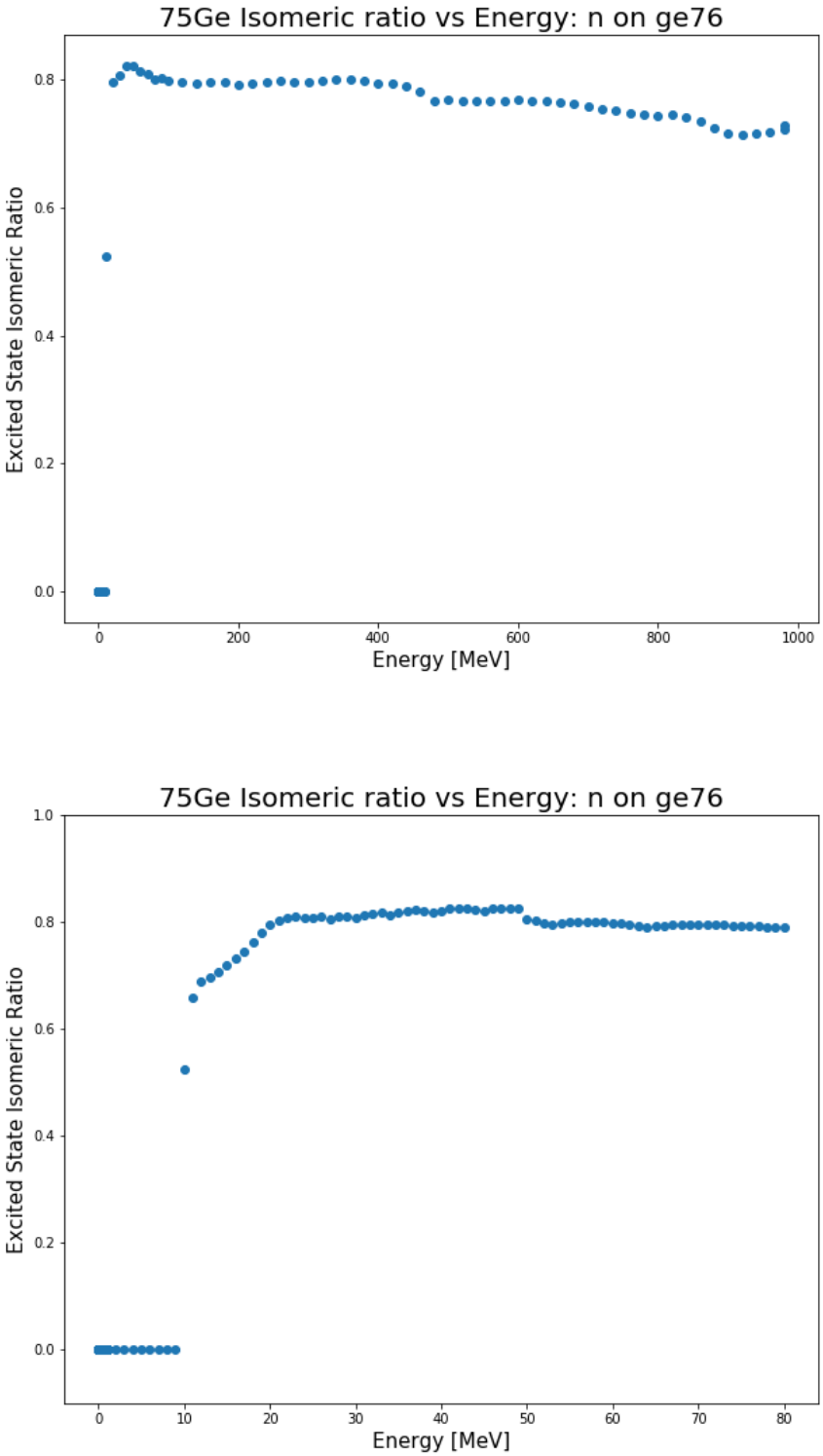

Figure 12.7: Isomeric ratio of ^{75}Ge from TALYS neutron on ^{76}Ge simulation. Full energy range (top) and neutron energy region of interest (bottom).

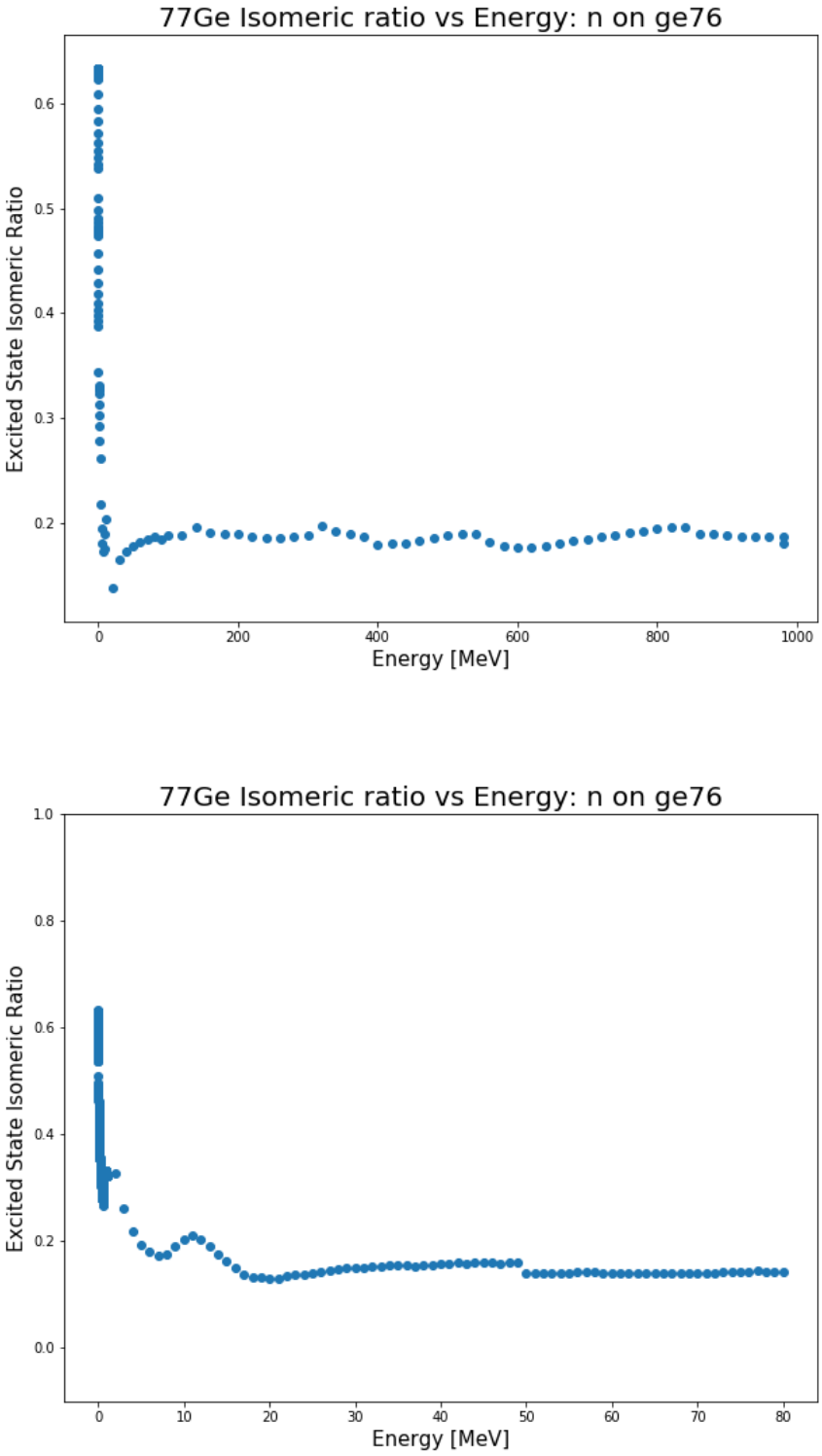

Figure 12.8: Isomeric ratio of ^{77}Ge from TALYS neutron on ^{76}Ge simulation. Full energy range (top) and neutron energy region of interest (bottom).

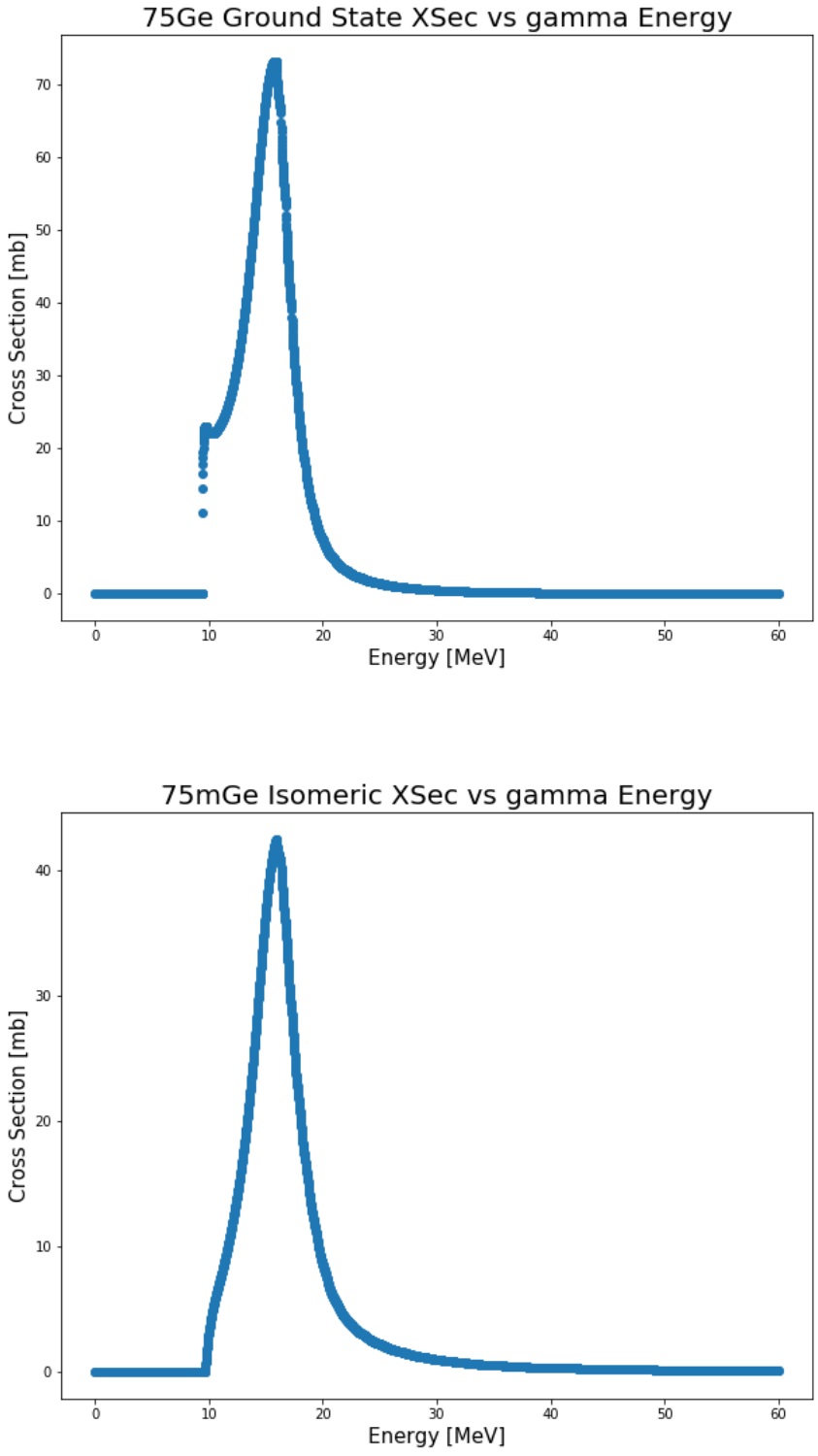

Figure 12.9: Production cross section of ^{75}Ge from TALYS gamma on ^{76}Ge simulation. Ground state (top) and excited state (bottom).

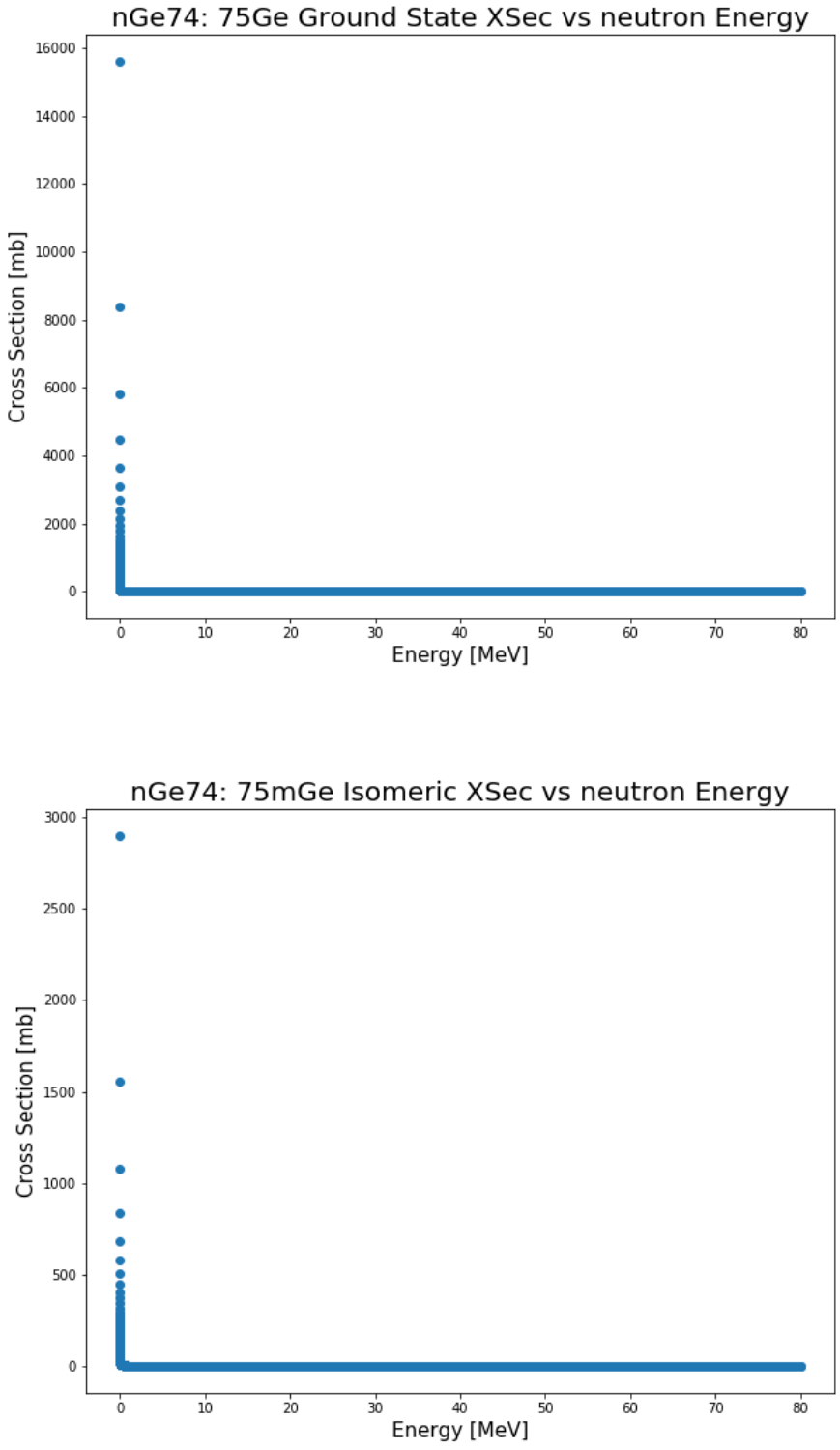

Figure 12.10: Production cross section of ^{75}Ge from TALYS neutron on ^{74}Ge simulation. Ground state (top) and excited state (bottom).

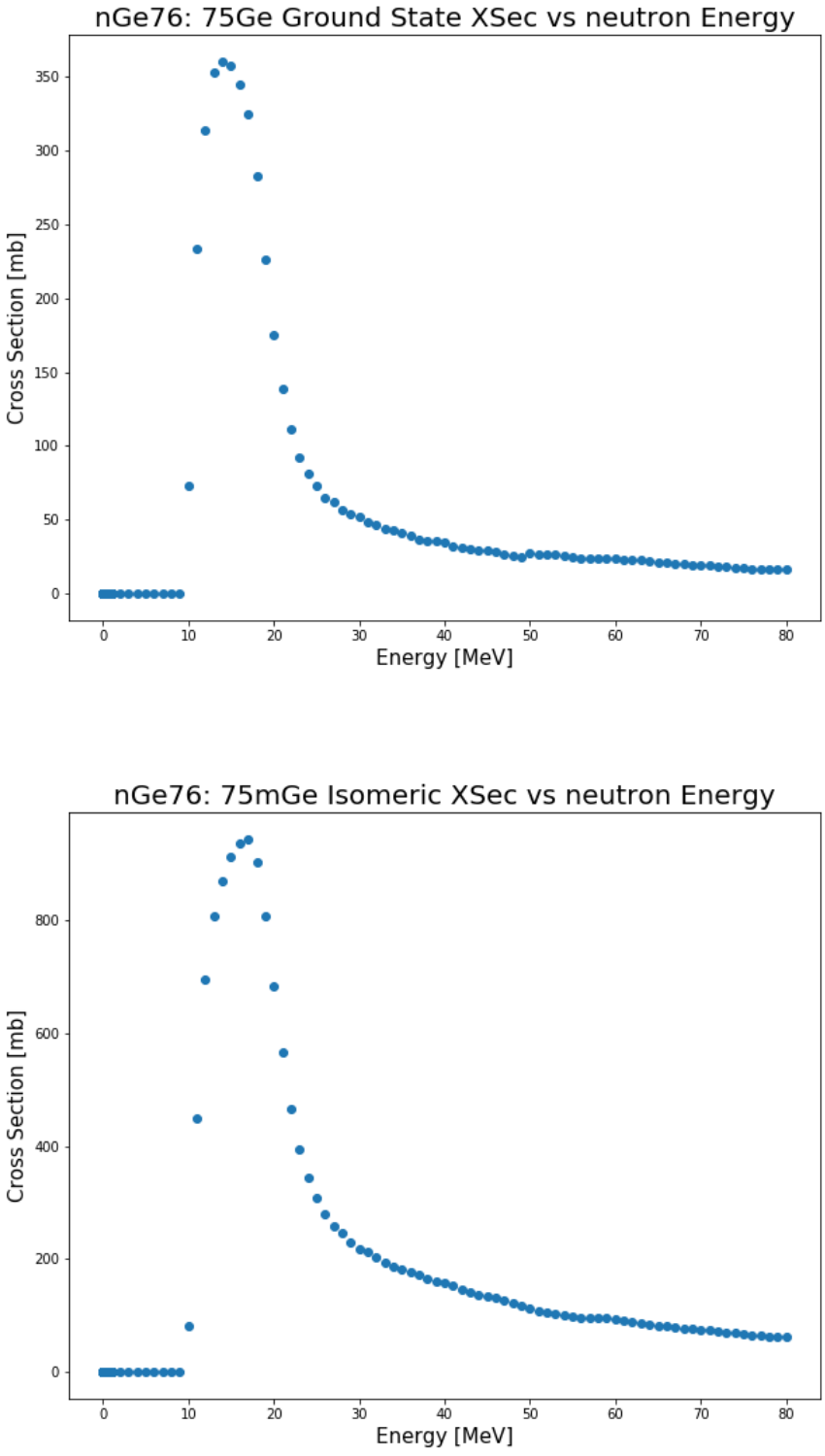

Figure 12.11: Production cross section of ^{75}Ge from TALYS neutron on ^{76}Ge simulation. Ground state (top) and excited state (bottom).

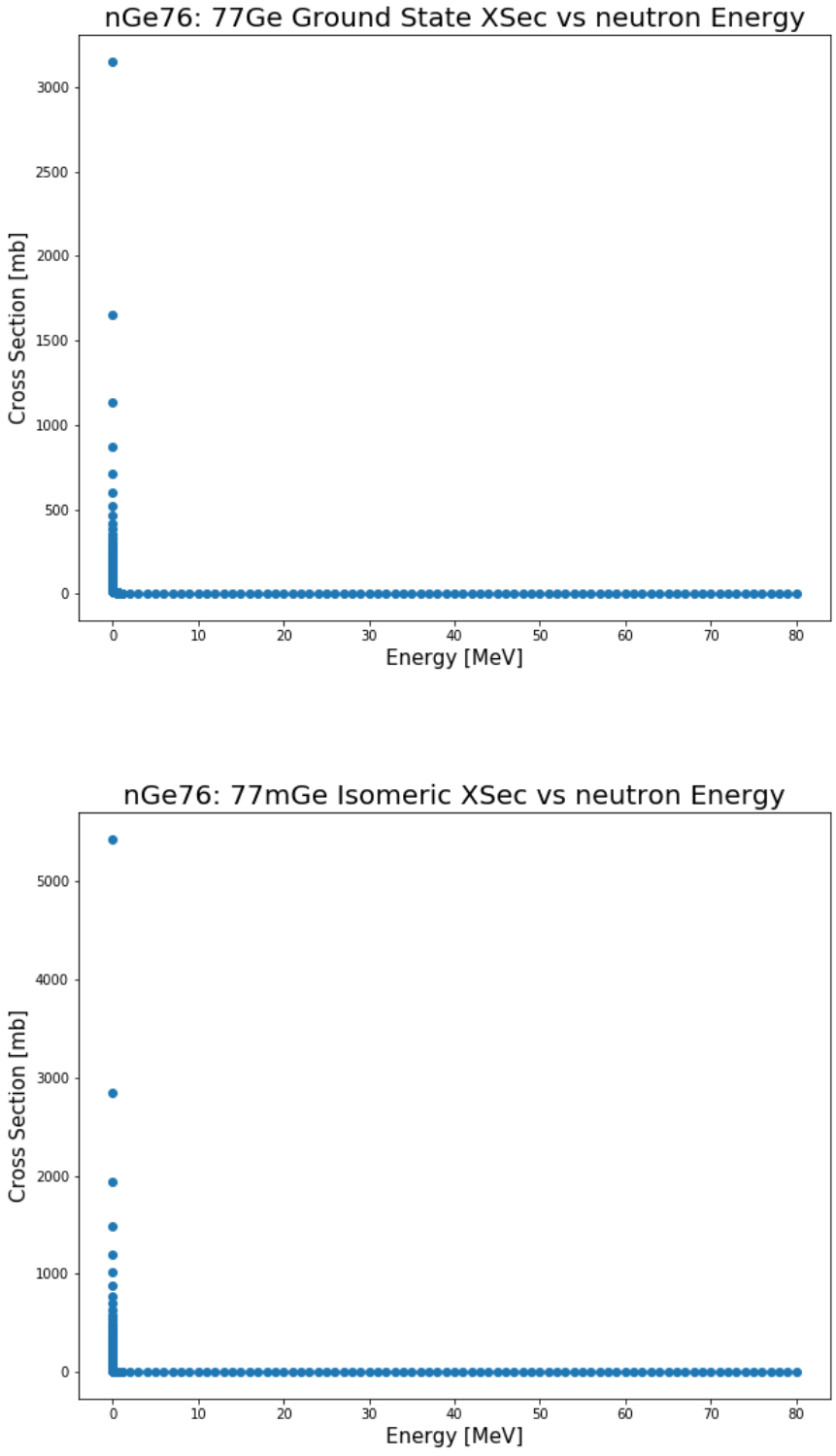

Figure 12.12: Production cross section of ^{77}Ge from TALYS neutron on ^{76}Ge simulation. Ground state (top) and excited state (bottom).

Figures 12.9, 12.10, 12.11, and 12.12 show the production cross sections for the ground state and first excited state of the signature isotopes.

12.6 Realistic MAJORANA Production Cross Section

It is necessary to combine the production cross sections with the kinetic energy spectra from the MAJORANA MAGE simulation. The realistic MAJORANA excited state production ratios can then be determined by calculating the ratio between the excited state isotope production cross section times kinetic energy and the total isotope production cross section times kinetic energy (excited state and ground state).

12.6.1 ^{71}Ge

As no ^{71}Ge excited state isotopes were produced by TALYS the MAJORANA ^{71}Ge excited state production ratio is zero.

12.6.2 ^{75}Ge

Figures 12.13, 12.14, and 12.15 show the production cross section multiplied by the kinetic energy spectrum for the ground state ^{75}Ge and the excited state ^{75m}Ge.

The integral of each (cross section times kinetic energy) spectrum can be found in Table 12.1

12.6.3 ^{77}Ge

Figure 12.16 shows the production cross section multiplied by the kinetic energy spectra for the ground state ^{77}Ge and the excited state ^{77m}Ge.

The integral of the neutron on ^{76}Ge $\rightarrow^{77}$ Ge (cross section times kinetic energy) spectrum can be found in Table 12.1

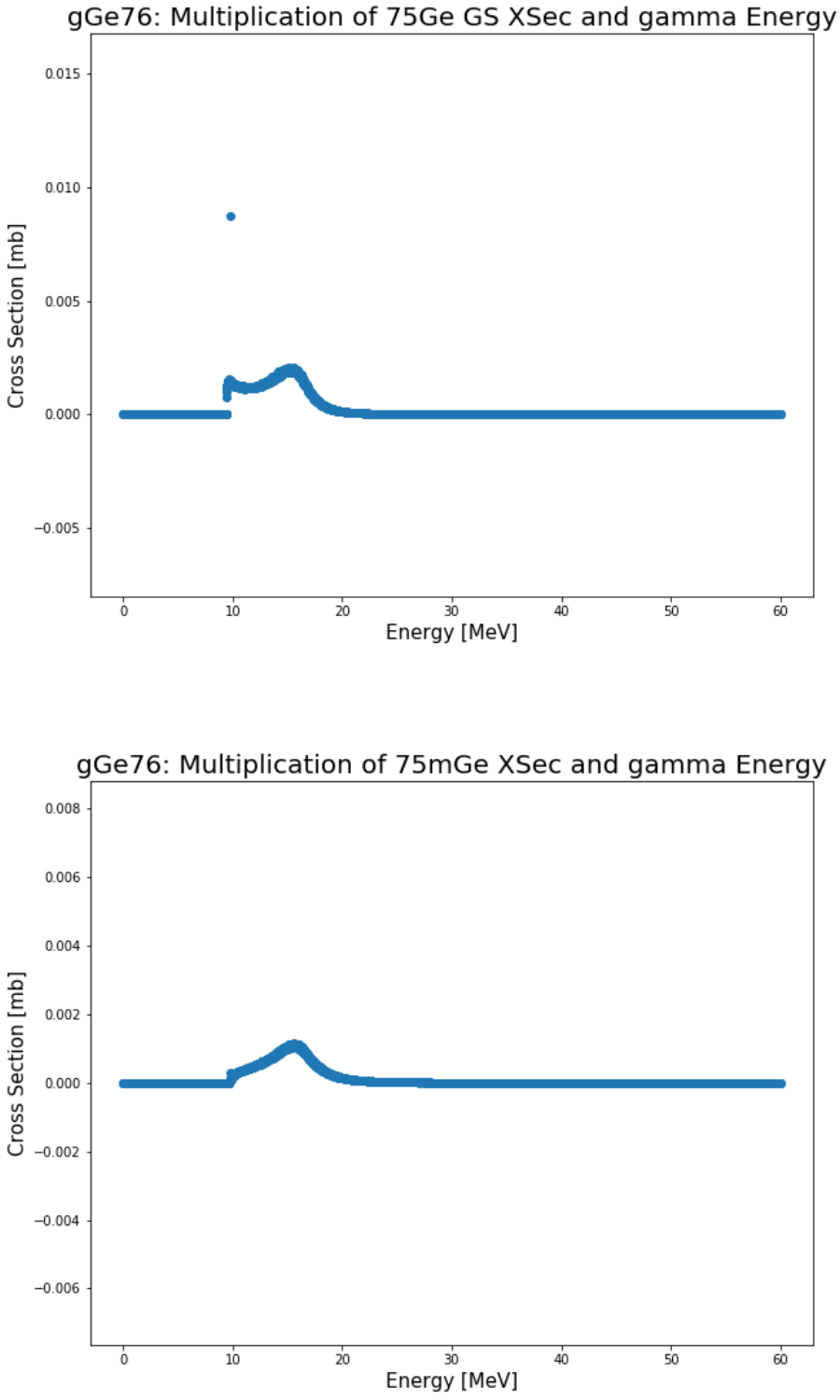

Figure 12.13: Production cross section times kinetic energy of ^{75}Ge from TALYS gamma on ^{76}Ge simulation. Ground state (top) and excited state (bottom).

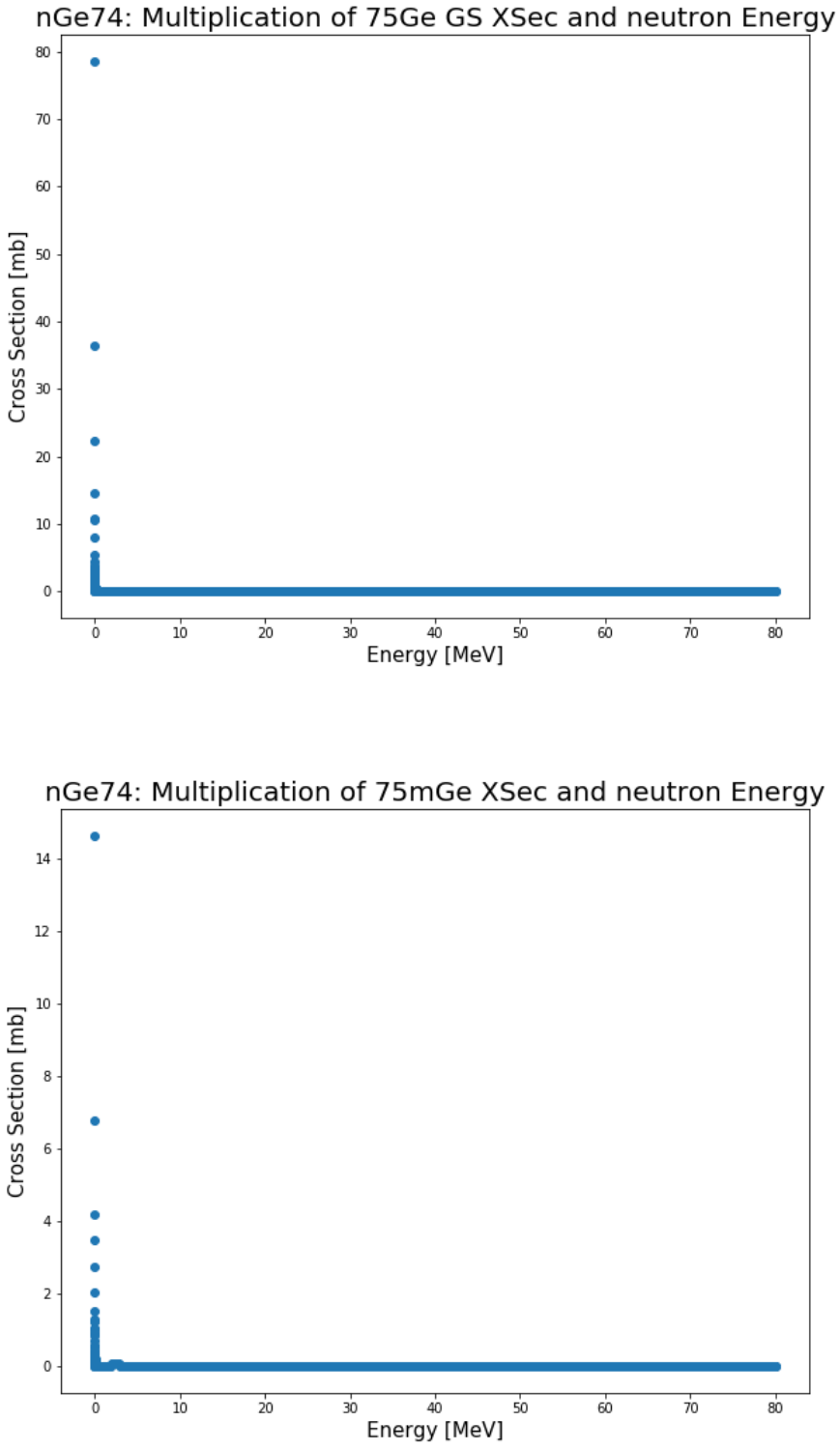

Figure 12.14: Production cross section times kinetic energy of ^{75}Ge from TALYS neutron on ^{74}Ge simulation. Ground state (top) and excited state (bottom).

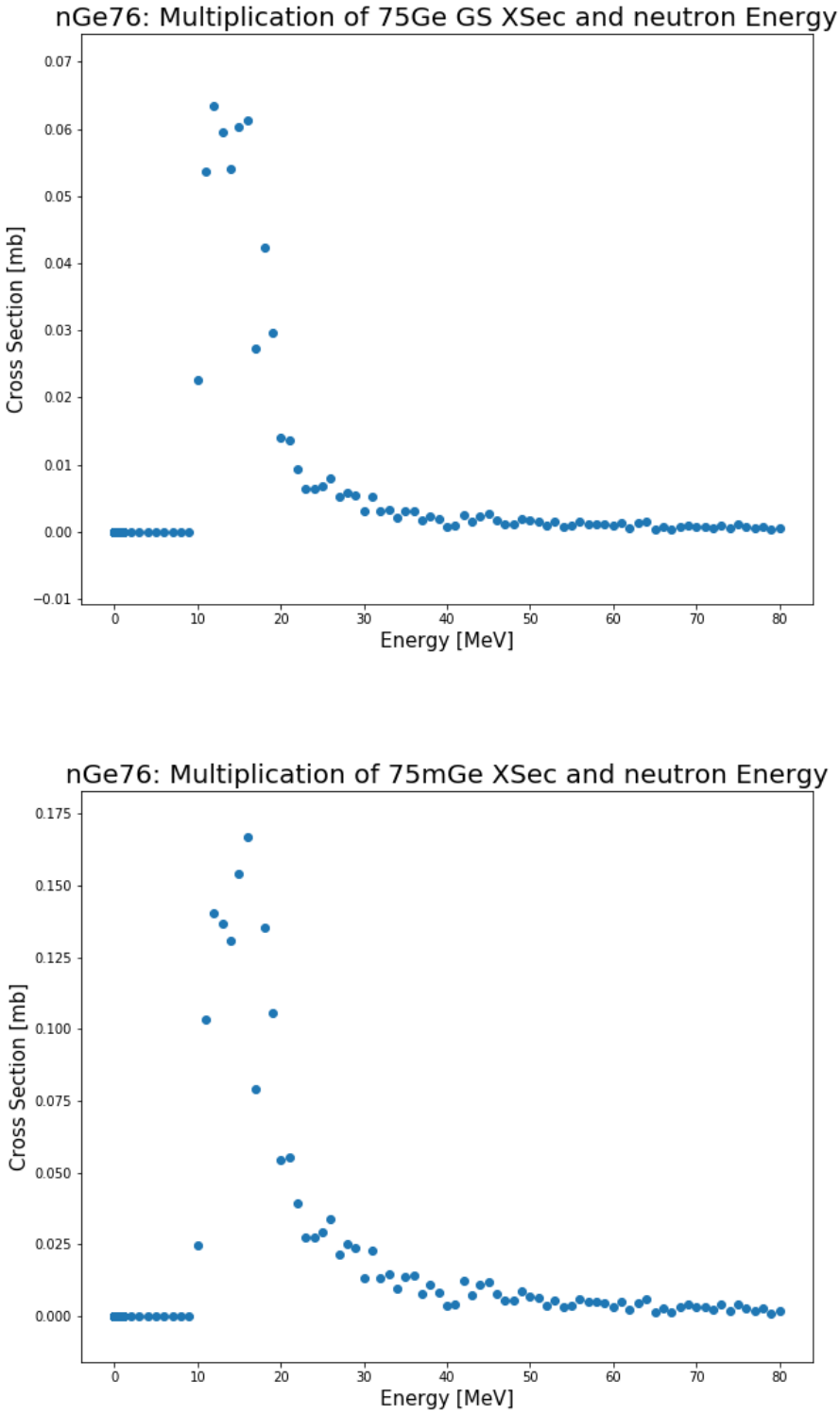

Figure 12.15: Production cross section times kinetic energy of ^{75}Ge from TALYS neutron on ^{76}Ge simulation. Ground state (top) and excited state (bottom).

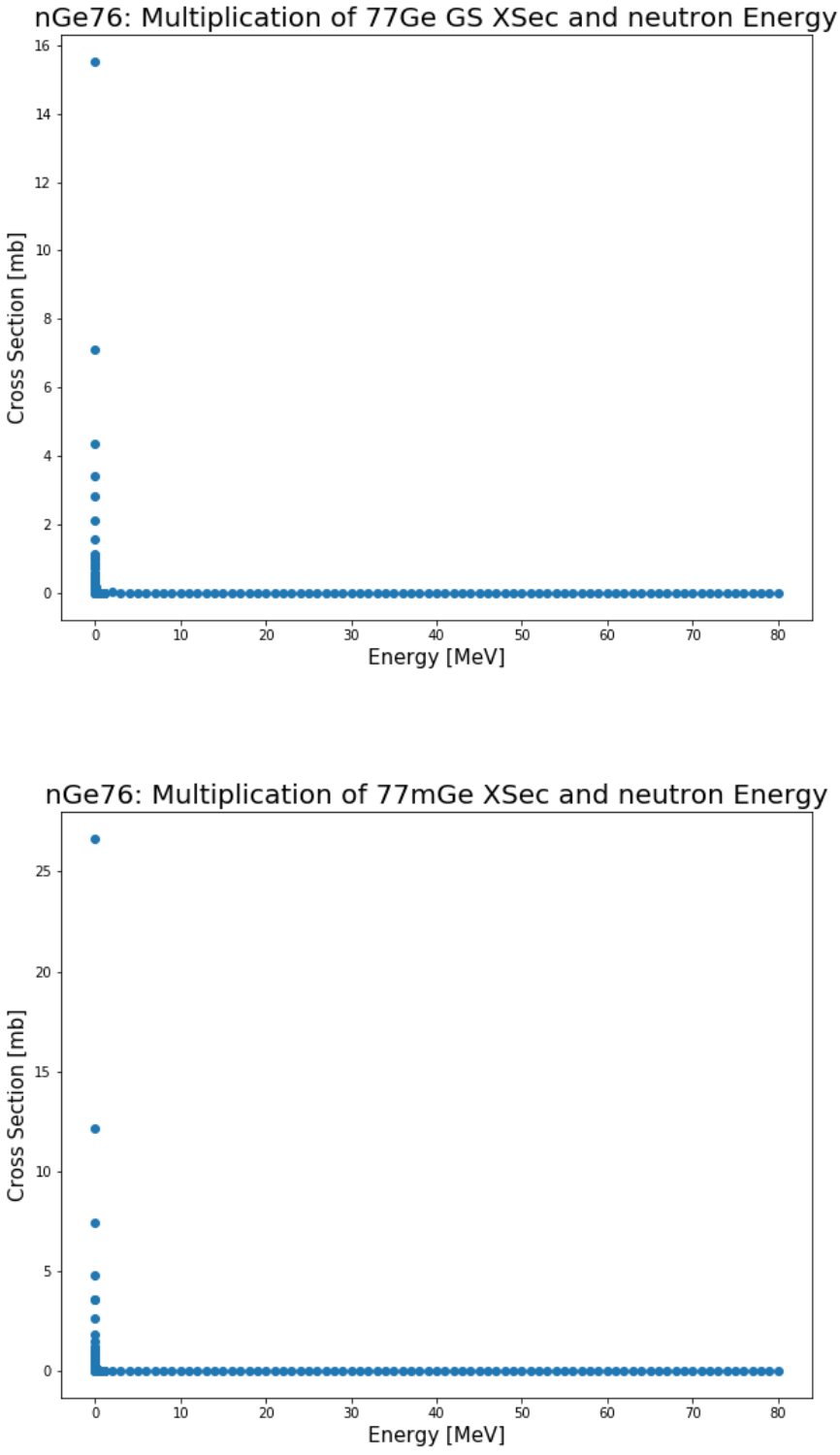

Figure 12.16: Production cross section times kinetic energy of ^{77}Ge from TALYS neutron on ^{76}Ge simulation. Ground state (top) and excited state (bottom).

12.7 Excited State Production Ratio

The integrals of the (production cross section times kinetic energy) are used to calculate the excited state production ratios. For a given excited state ^{Am}X and ground state ^{A}X with the available (cross section times kinetic energy), the excited state and ground state production ratios can be calculated using the following equations:

$$^{Am}\text{X Ratio} = (^{Am}\text{X xsec} \cdot \text{KE})/[(^{Am}\text{X xsec} \cdot \text{KE}) \cdot (^{A}\text{X xsec} \cdot \text{KE})] \quad (12.1)$$

$$^{A}\text{X Ratio} = (^{A}\text{X xsec} \cdot \text{KE})/[(^{Am}\text{X xsec} \cdot \text{KE}) \cdot (^{A}\text{X xsec} \cdot \text{KE})] \quad (12.2)$$

The ratios for the non-zero interactions can be found in Table 12.2.

12.8 Application to Simulations

These interaction ratios (Table 12.2) are the applied to the simulation results using the ground state production processes in Section 12.1 as a weighting.

The photon nuclear processes are described by the (Gamma on ^{76}Ge $\rightarrow^{75}$ Ge) interaction ratio. The neutron capture processes are described by the (Neutron on ^{74}Ge $\rightarrow^{75}$ Ge) and (Neutron on ^{76}Ge $\rightarrow^{77}$ Ge) interaction ratios. The neutron inelastic scattering process are described by the (Neutron on ^{76}Ge $\rightarrow^{75}$ Ge) interaction ratio.

Table 12.3 shows the estimated excited state production for each TALYS interaction. Table 12.4 shows the estimated excited state production for each signature isotope. These excited state estimates are used compare the simulation and data analysis results in Chapter 13.

Table 12.1: (Production cross section times kinetic energy) integrals for each TALYS interaction.

TALYS interaction	Ground State Integral [arb]	Excited State Integral [arb]
Gamma on ^{76}Ge $\rightarrow^{75}$ Ge	6.3566	3.2529
Neutron on ^{74}Ge $\rightarrow^{75}$ Ge	1383.1644	316.3450
Neutron on ^{76}Ge $\rightarrow^{75}$ Ge	3.1518	9.1852
Neutron on ^{76}Ge $\rightarrow^{77}$ Ge	315.3785	456.8387

Table 12.2: Ground state and excited state production ratios for each TALYS interaction.

TALYS interaction	Ground State Production Ratio	Excited State Production Ratio
Gamma on ^{76}Ge $\rightarrow^{75}$ Ge	0.6615	0.3385
Neutron on ^{74}Ge $\rightarrow^{75}$ Ge	0.8139	0.1861
Neutron on ^{76}Ge $\rightarrow^{75}$ Ge	0.2555	0.7445
Neutron on ^{76}Ge $\rightarrow^{77}$ Ge	0.4084	0.5916

Table 12.3: Excited state isotope estimates for each TALYS interaction.

MaGe		
TALYS interaction	Estimated Excited State Isotopes	
	NatGe	EnrGe
Gamma on ^{76}Ge $\rightarrow^{75}$ Ge	1.0	34.5
Neutron on ^{74}Ge $\rightarrow^{75}$ Ge	75.4	47.3
Neutron on ^{76}Ge $\rightarrow^{75}$ Ge	1.5	19.4
Neutron on ^{76}Ge $\rightarrow^{77}$ Ge	24.3	375.7
FLUKA SFF		
TALYS interaction	Estimated Excited State Isotopes	
	NatGe	EnrGe
Gamma on ^{76}Ge $\rightarrow^{75}$ Ge	9.5	145.9
Neutron on ^{74}Ge $\rightarrow^{75}$ Ge	68.5	157.3
Neutron on ^{76}Ge $\rightarrow^{75}$ Ge	1.5	64.0
Neutron on ^{76}Ge $\rightarrow^{77}$ Ge	10.6	30.8
FLUKA MH		
TALYS interaction	Estimated Excited State Isotopes	
	NatGe	EnrGe
Gamma on ^{76}Ge $\rightarrow^{75}$ Ge	0.3	39.9
Neutron on ^{74}Ge $\rightarrow^{75}$ Ge	19.4	34.2
Neutron on ^{76}Ge $\rightarrow^{75}$ Ge	0.7	14.1
Neutron on ^{76}Ge $\rightarrow^{77}$ Ge	1.8	5.9

Table 12.4: Ground state isotopes produced in the MaGe, FLUKA ShowersFromFile (SFF), and FLUKA MeiHime (MH) simulations, alongside the total estimate of excited state isotopes produced.

MaGe				
Isotope	Ground State Produced		Excited State Estimate	
	NatGe	EnrGe	NatGe	EnrGe
^{71}Ge	519	7	0.0	0.0
^{75}Ge	410	386	77.9	101.2
^{77}Ge	41	635	24.3	375.7
FLUKA SFF				
Isotope	Ground State Produced		Excited State Estimate	
	NatGe	EnrGe	NatGe	EnrGe
^{71}Ge	734	1312	0.0	0.0
^{75}Ge	415	1403	79.5	367.2
^{77}Ge	18	53	10.6	30.8
FLUKA MH				
Isotope	Ground State Produced		Excited State Estimate	
	NatGe	EnrGe	NatGe	EnrGe
^{71}Ge	140	275	0.0	0.0
^{75}Ge	109	330	20.4	88.2
^{77}Ge	3	10	1.8	5.9

Chapter 13

Comparison of Simulations and Data Analysis

Scientific experiments which require extremely low background rates also require significant monetary and time investments. These experiments are typically designed based on results from large simulation campaigns. Accurate simulation tools are necessary for low background experiments to be successful. A variety of simulation packages are available to the scientific community and they are constantly being improved. It is vital that these simulation packages be repeatedly benchmarked with data to ensure the community is using the appropriate tools. This chapter is the culmination of significant efforts to bring together data analysis and simulations of in situ cosmogenic backgrounds in the Majorana Demonstrator, with the goal of benchmarking these simulation tools.

In this work, three different simulations of muons onto the Majorana Demonstrator were performed. Two different software packages were used, as well as two different primary muon generators. The three simulations are (1) MaGe using the ShowersFromFile generator, (2) FLUKA using the ShowersFromFile generator (FLUKA SFF), and (3) FLUKA using the MeiHime generator (FLUKA MH). These simulations were used to estimate the irreducible muon-induced background rate in the Demonstrator as well as estimate the production rates of three muon-induced excited state isotopes, with input from TALYS simulations. In addition, a data analysis of the three muon-induced excited state isotopes was performed, and the production rates were measured using Demonstrator data.

13.1 ^{71m}Ge, ^{75m}Ge, and ^{77m}Ge Rate Comparison

Table 13.1 contains the excited state production rates, and 68.7% excite state production rate upper limits for the data analysis, the MaGe simulation, and both FLUKA simulations (ShowersFromFile and MeiHime). The three simulations show different predictions for these three excited state isotope production rates. The MaGe simulation predicts the highest excited state isotope production rates, while FLUKA predicts the lowest. Of the two FLUKA simulations, the MeiHime generator predicts the lowest excited state isotope production rates. Low background germanium experiments should be sensitive to the differences between these simulations, however the Majorana experimental upper limits do not let us distinguish which model most accurately predicts the excited state isotope production. These results give us confidence that there is not excessive in situ cosmogenic activations in the Demonstrator compared to the simulation estimates. Additionally, the 68.7% excited state upper limits measured in the data analysis are small, indicating that there is not much in situ activation in the Demonstrator. This analysis paves the way for similar, more statistically significant analyses in future $\beta\beta(0\nu)$ experiments with much larger sensitive detector mass.

This analysis also shows that MaGe and FLUKA , as they are now, are not sophisticated enough to handle isomer production. TALYS, or the appropriate isomer production measurements are necessary for these excited state analyses. As a future development, MaGe and FLUKA should be modified to properly handle isomer productions.

Table 13.1: Excited state production rates and upper limits for Monte Carlo simulations (MaGe, FLUKA SFF, FLUKA MH) and data analysis.

Production Rate	^{71}Ge		^{75}Ge		^{77}Ge	
c/kg · yr	NatGe	EnrGe	NatGe	EnrGe	NatGe	EnrGe
MaGe						
ES Rate	0.00 ± 0.04	0.00 ± 0.02	2.96 ± 0.34	1.87 ± 0.19	0.93 ± 0.19	6.95 ± 0.36
ES UL 68.7%	0.05 ± 0.04	0.02 ± 0.02	3.30 ± 0.35	2.06 ± 0.20	1.11 ± 0.21	7.31 ± 0.37
FLUKA ShowersFromFile						
ES Rate	0.0000 ± 0.0014	0.0000 ± 0.0007	0.112 ± 0.013	0.253 ± 0.013	0.015 ± 0.005	0.021 ± 0.004
ES UL 68.7%	0.0018 ± 0.0016	0.0009 ± 0.0008	0.125 ± 0.013	0.266 ± 0.014	0.021 ± 0.005	0.025 ± 0.004
FLUKA MeiHime						
ES Rate	0.0000 ± 0.0014	0.0000 ± 0.0007	0.029 ± 0.006	0.061 ± 0.006	0.0026 ± 0.0019	0.0041 ± 0.0017
ES UL 68.7%	0.0018 ± 0.0016	0.0009 ± 0.0008	0.035 ± 0.007	0.067 ± 0.007	0.0060 ± 0.0029	0.0064 ± 0.0021
Data Analysis Open+Blind						
ES Rate	0.622 ± 0.442	0.333 ± 0.201	0.597 ± 2.663	0.998 ± 1.467	-0.454 ± 13.813	2.056 ± 8.523
ES UL 68.7%	1.069 ± 0.086	0.532 ± 0.041	1.886 ± 0.123	1.659 ± 0.104	6.467 ± 0.413	5.837 ± 0.359

13.2 In Situ Cosmogenic Background Rate

As a result of the ^{71m}Ge, ^{75m}Ge, and ^{77m}Ge rate comparison, we verified that there is no abnormality between the models estimates and the data measurements for cosmogenically induced backgrounds. We compare the simulated cosmogenic background rates with the background measurement of the latest MAJORANA result. Table 13.2 shows the simulated muon-induced background rates from all MAGE and FLUKA simulations. In the MAJORANA $\beta\beta(0\nu)$ analysis utilizing 26 kg $\cdot$ yr of enriched germanium exposure, the background index was measured to be $6.1 \pm 0.8 \cdot 10^{-3}$ c/(keV $\cdot$ kg $\cdot$ yr) after all analysis cuts [15]. This measurement used data from MAJORANA Data Sets 0-6a, and an energy window of 360 keV between 1950-2350 keV. This measured background index corresponds to a background rate of 2.196 ± 0.288 c/kg $\cdot$ yr. It is clear that the largest cosmogenic background estimate, 0.34 ± 0.12 c/kg $\cdot$ yr from MAGE, is much smaller than the measured background rate of 2.196 ± 0.288 c/kg $\cdot$ yr. This indicates that the cosmogenic background contribution is much smaller than the experimentally achieved background. As expected by the background model (Figure 3.4), in situ cosmogenic backgrounds are not a major contributor to the overall $\beta\beta(0\nu)$ background. This is confirmation that the Sanford Underground Research Facility is a good location for the MAJORANA DEMONSTRATOR.

Table 13.2: The MAJORANA DEMONSTRATOR muon-induced background rates in the natural and enriched detectors estimated from the MAGE FLUKA SFF, and FLUKA MH simulations. The two cuts used are the muVeto cut and the Granularity cut. Energy All: [0, 14000 keV]. Energy Region ROI: [1950 keV, 2350 keV].

Material	Energy	Cuts	MAGE Rate c/kg · yr	FLUKA SFF Rate c/kg · yr	FLUKA MH Rate c/kg · yr
NatGe	All	None	2696.62 ± 10.13	615.45 ± 0.93	244.38 ± 0.59
NatGe	All	All Cuts	59.17 ± 1.50	12.62 ± 0.13	3.91 ± 0.07
EnrGe	All	None	2116.77 ± 6.26	544.65 ± 0.61	214.93 ± 0.38
EnrGe	All	All Cuts	43.20 ± 0.89	13.91 ± 0.10	4.23 ± 0.05
NatGe	ROI	None	32.08 ± 1.10	2.40 ± 0.06	1.24 ± 0.04
NatGe	ROI	All Cuts	0.08 ± 0.05	0.07 ± 0.01	0.05 ± 0.01
EnrGe	ROI	None	25.76 ± 0.69	2.09 ± 0.04	0.74 ± 0.02
EnrGe	ROI	All Cuts	0.26 ± 0.07	0.04 ± 0.01	0.015 ± 0.003

Chapter 14

Conclusion

The MAJORANA DEMONSTRATOR is a successful low background physics experiment which has produced world leading $\beta\beta(0\nu)$ results, [15], as well as numerous other publications [2] [7] [16] [18] [20] [33]. It has been in stable operation underground for six years. One of the major components of the DEMONSTRATOR is the active muon veto system. I have been a lead collaborator in software support and data analysis of the veto system since 2016. The success of the veto system, with an estimated muon tagging efficiency of 97.17%, and the muVeto analysis cut, with an estimated background rejection efficiency of 97.8% (when used in conjunction with the Granularity cut), have helped the MAJORANA DEMONSTRATOR achieve the an extremely low background index of 11.9 $\pm$ 2.0 $c/(\text{FWHM} \cdot \text{tonne} \cdot \text{y})$ [15], second only to the GERDA collaboration [13].

In addition my work on the veto system, I have been the lead collaborator of an in situ cosmogenic activation analysis. This analysis used a combination of data from both the veto system and the germanium detectors. This resulted in the first cosmogenic activation study performed with a large germanium detector array. Different Monte Carlo models were evaluated relative to this data. The corresponding publication is forthcoming.

Since joining the MAJORANA collaboration I have continually contributed to the operations and analyses of the MAJORANA DEMONSTRATOR. These contributions include (1) participating on-site with installation of DEMONSTRATOR shielding, detectors, and modules, (2) monitoring vital DEMONSTRATOR systems required for everyday operations and data processing, (3) participating in bi-yearly collaboration meetings discussing all

MAJORANA operations, tasks, and analyses, (4) giving presentations to the scientific community as a representative of the MAJORANA collaboration, (5) developing and implementing veto system error checks and optimizing the veto system to reduce error rates, (6) using DEMONSTRATOR data to investigate five prominent muon-induced background signatures visible in the DEMONSTRATOR, (7) using GEANT4/MAGE simulations to estimate the veto system efficiency for all major veto panel configurations, (8) building a version of the DEMONSTRATOR geometry for use with the FLUKA Monte Carlo code, (9) using FLUKA simulations to estimate the effect of environmental neutrons on two different DEMONSTRATOR shield configurations, (10) using FLUKA and GEANT4/MAGE simulations to estimate the DEMONSTRATOR in situ muon-induced background rate for the natural germanium and enriched germanium detectors, (11) comparing the in situ muon-induced background rates measured in the data analysis with the simulated results, with help from additional TALYS simulations.

Performing these tasks greatly improved a number of my skills, including (1) programming with C++, Python, and FORTRAN, (2) utilizing GEANT4, MAGE, FLUKA, and TALYS software packages to perform simulations, (3) handling large amounts of data and performing statistical analyses, (4) presenting physics results and ideas to the scientific community, (5) using computer clusters to perform software tasks, and (6) completing miscellaneous tasks in a professional lab environment.

Bibliography

[1] Aalseth, C. E. et al. (2002). The IGEX Ge-76 neutrinoless double beta decay experiment: Prospects for next generation experiments. *Phys. Rev. D*, 65:092007. 12

[2] Aalseth, C. E., e. a. (2018). Search for neutrinoless double-β decay in ^{76}Ge with the MAJORANA DEMONSTRATOR. *Phys. Rev. Lett.*, 120:132502. 179, 189

[3] Abe, K. et al. (2014). Precise Measurement of the Neutrino Mixing Parameter θ_{23} from Muon Neutrino Disappearance in an Off-Axis Beam. *Phys. Rev. Lett.*, 112(18):181801. 5

[4] Abgrall, N. et al. (2014). The MAJORANA DEMONSTRATOR Neutrinoless Double-Beta Decay Experiment. *Adv. High Energy Phys.*, 2014:365432. 15, 17

[5] Abgrall, N. et al. (2016). The MAJORANA DEMONSTRATOR radioassay program. *Nucl. Instrum. Meth. A*, 828:22–36. 20

[6] Abgrall, N. et al. (2017a). Muon Flux Measurements at the Davis Campus of the Sanford Underground Research Facility with the MAJORANA DEMONSTRATOR Veto System. *Astropart. Phys.*, 93:70–75. 22, 28, 29, 120

[7] Abgrall, N. et al. (2017b). New limits on bosonic dark matter, solar axions, pauli exclusion principle violation, and electron decay from the MAJORANA DEMONSTRATOR. *Phys. Rev. Lett.*, 118:161801. 16, 179

[8] Abgrall, N. et al. (2017c). The Large Enriched Germanium Experiment for Neutrinoless Double Beta Decay (LEGEND). *AIP Conf. Proc.*, 1894(1):020027. 12

[9] Abgrall, N. et al. (2020). ADC Nonlinearity Correction for the MAJORANA DEMONSTRATOR. *IEEE Trans. Nucl. Sci.*, 68(3):359–367. 189

[10] Abusaleem, K. and Singh, B. (2011). Nuclear Data Sheet 112, 133. 63, 65

[11] Adamson, P. et al. (2020). Improved Constraints on Sterile Neutrino Mixing from Disappearance Searches in the MINOS, MINOS+, Daya Bay, and Bugey-3 Experiments. *Phys. Rev. Lett.*, 125(7):071801. 5

[12] Agostinelli, S. et al. (2003). GEANT4: A Simulation toolkit. *Nucl. Instrum. Meth.*, A506:250–303. 103, 104

[13] Agostini, M. et al. (2020). Final results of gerda on the search for neutrinoless double-β decay. *Phys. Rev. Lett.*, 125:252502. 10, 12, 179

[14] Aker, M. et al. (2019). Improved upper limit on the neutrino mass from a direct kinematic method by katrin. *Phys. Rev. Lett.*, 123:221802. 7

[15] Alvis, S. I., e. a. (2019). Search for neutrinoless double-β decay in ^{76}Ge with 26 kg yr of exposure from the MAJORANA DEMONSTRATOR. *Phys. Rev. C*, 100:025501. xi, 10, 12, 16, 19, 24, 25, 56, 60, 62, 177, 179, 189

[16] Alvis, S. I. et al. (2018). First limit on the direct detection of lightly ionizing particles for electric charge as low as $e/1000$ with the MAJORANA DEMONSTRATOR. *Phys. Rev. Lett.*, 120:211804. 16, 179

[17] Alvis, S. I. et al. (2019a). Multisite event discrimination for the MAJORANA DEMONSTRATOR. *Phys. Rev. C*, 99(6):065501. 57, 189

[18] Alvis, S. I. et al. (2019b). Search for trinucleon decay in the MAJORANA DEMONSTRATOR. *Phys. Rev. D*, 99(7):072004. 16, 179, 189

[19] Anton, G. et al. (2019). Search for Neutrinoless Double-β Decay with the Complete EXO-200 Dataset. *Phys. Rev. Lett.*, 123(16):161802. 10

[20] Arnquist, I. J. et al. (2021). Search for double-β decay of ^{76}Ge to excited states of ^{76}Se with the MAJORANA DEMONSTRATOR. *Phys. Rev. C*, 103(1):015501. 179, 189

[21] Barabash, A. S. (2013). Average and recommended half-life values for two neutrino double beta decay: Upgrade-2013. *AIP Conf. Proc.*, 1572(1):11–15. 7

[22] Benato, G. (2015). Effective Majorana Mass and Neutrinoless Double Beta Decay. *Eur. Phys. J. C*, 75(11):563. 7

[23] Best, A., Görres, J., Junker, M., Kratz, K.-L., Laubenstein, M., Long, A., Nisi, S., Smith, K., and Wiescher, M. (2016). Low energy neutron background in deep underground laboratories. *Nucl. Instrum. Meth. A*, 812:1–6. 129

[24] Bettini, A. (2008). *Introduction to Elementary Particle Physics*. Cambridge University Press, Cambridge. 4, 5

[25] Bilenky, S. M. and Giunti, C. (2015). Neutrinoless double-beta decay: A probe of physics beyond the standard model. *Int. J. Mod. Phys. A*, 30(04n05):1530001. xiv, 7, 10

[26] Boswell, M. et al. (2011). MaGe-a Geant4-based Monte Carlo Application Framework for Low-background Germanium Experiments. *IEEE Trans. Nucl. Sci.*, 58:1212–1220. 36, 50, 103, 104

[27] Bugg, W., Efremenko, Y., and Vasilyev, S. (2014). Large plastic scintillator panels with wls fiber readout; optimization of components. *Nucl. Instrum. Meth.* xv, 34, 36, 37, 49, 50, 117

[28] Campani, A. et al. (2020). Status and results from the CUORE experiment. *Int. J. Mod. Phys. A*, 35(36):2044016. 10

[29] Cooper, N. G. (1997). Celebrating the neutrino. *Los Alamos Science*, (25). doi:10.2172/569122. 3

[30] Cuesta, C. (2016a). Run selection and data cleaning of DS0; final. *M-TECHDOCUNIDOC-2017-010*. Internal Document. 67, 79, 90, 94

[31] Cuesta, C. (2016b). Run selection and data cleaning of DS1; final. *M-TECHDOCUNIDOC-2017-011*. Internal Document. 67, 79, 90, 94

[32] Cuesta, C. and Buuck, M. (2017). Run selection and data cleaning of DS3; final. *M-TECHDOCUNIDOC-2017-008*. Internal Document. 67, 79, 90, 94

[33] Cuesta, C. et al. (2017). Background model for the MAJORANA DEMONSTRATOR. *J. Phys. Conf. Ser.*, 888(1):012240. xiv, 27, 179

[34] de Kerret, H. et al. (2020). Double Chooz θ_{13} measurement via total neutron capture detection. *Nature Phys.*, 16(5):558–564. 5

[35] Decowski, M. P. (2016). KamLAND's precision neutrino oscillation measurements. *Nucl. Phys. B*, 908:52–61. 5

[36] Dolinski, M. J., Poon, A. W., and Rodejohann, W. (2019). Neutrinoless double-beta decay: Status and prospects. *Ann. Rev. Nucl. Part. Sci.*, 69(1):219–251. 8, 9

[37] Edwins, D., Guiseppe, V., Tedeschi, D., Wiseman, C., Meijer, S., Reine, A., Caldwell, T., Gilliss, T., Haufe, C., and Radford, D. (2018). Livetime and Exposure for MAJORANA DEMONSTRATOR Data Sets 0-6; draft. *M-TECHDOCUNIDOC-2018-032*. Internal Document. xi, 54, 57, 58

[38] Elliott, S. R., Hahn, A. A., and Moe, M. K. (1987). Direct evidence for two-neutrino double-beta decay in ^{82}Se. *Phys. Rev. Lett.*, 59:2020–2023. 7

[39] Feldman, G. J. and Cousins, R. D. (1998). Unified approach to the classical statistical analysis of small signals. *Phys. Rev. D*, 57:3873–3889. 75, 86, 101, 135, 136, 137, 144, 145, 146, 147, 148

[40] Ferrari, A., Sala, P. R., Fasso, A., and Ranft, J. (2005). FLUKA: A multi-particle transport code (Program version 2005). 109

[41] Gando, Y. (2018). Neutrinoless double beta decay search with KamLAND-Zen. *PoS*, NOW2018:068. 10

[42] Gilliss, T. F. (2019). *Statistical Modeling and Markov Chain Monte Carlo Inference of the MAJORANA DEMONSTRATOR Background Data*. PhD thesis, University of North Carolina. 15

[43] Giuliani, A., Gomez Cadenas, J. J., Pascoli, S., Previtali, E., Saakyan, R., Schaffner, K., and Schonert, S. (2019). Double Beta Decay APPEC Committee Report. xiv, 8, 13

[44] Giuliani, A. and Poves, A. (2012). Neutrinoless double-beta decay. *Adv. High Energy Phys.*, 2012:38. Article ID 857016. xiv, 8, 11

[45] Gray, F., Ruybal, C., Totushek, J., Mei, D., Thomas, K., and Zhang, C. (2010). Cosmic ray muon flux at the sanford underground laboratory at homestake. *Nucl. Instrum. Meth. A*, 638. 22

[46] Guiseppe, V. (2018). New Results from the MAJORANA DEMONSTRATOR Experiment. http://doi.org/10.5281/zenodo.1286900. XXVIII International Conference on Neutrino Physics and Astrophysics (Neutrino 2018). 63, 77, 89, 92

[47] Henning, R. (2016). Current status of neutrinoless double-beta decay searches. *Reviews in Physics*, 1:29–35. xiv, 14

[48] Hu, Q., Ma, H., Zeng, Z., Cheng, J., Chen, Y., He, S., Li, J., Shen, M., Wu, S., Yue, Q., Yue, J., and Zhang, H. (2017). Neutron background measurements at china jinping underground laboratory with a bonner multi-sphere spectrometer. *Nucl. Instrum. Meth. A*, 859:37–40. xvii, 110, 113

[49] International Atomic Energy Agency (2020). IAEA Nuclear Data Service Live Chart of Nuclides. https://www-nds.iaea.org/relnsd/vcharthtml/VChartHTML.html. xv, xvi, 64, 78, 88, 93

[50] Jiang, M. et al. (2019). Atmospheric Neutrino Oscillation Analysis with Improved Event Reconstruction in Super-Kamiokande IV. *PTEP*, 2019(5):053F01. 5

[51] Klapdor-Kleingrothaus, H. V., Dietz, A., Harney, H. L., and Krivosheina, I. V. (2001). Evidence for neutrinoless double beta decay. *Mod. Phys. Lett. A*, 16:2409–2420. 12, 16

[52] Koning, A., Hilaire, S., and Duijvestijn, M. (2007). Talys-1.0. In *Proceedings of the International Conference on Nuclear Data for Science and Technology*, pages 211–214, Nice, France. EDP Sciences. 112

[53] Martin, R. D. et al. (2015). Status of the MAJORANA DEMONSTRATOR experiment. *AIP Conf. Proc.*, 1604(1):413–420. 8, 9

[54] Mei, D. and Hime, A. (2006). Muon-induced background study for underground laboratories. *Phys. Rev.*, D73:053004. 110

[55] Negret, A. and Singh, B. (2013). Nuclear Data Sheet 114, 841. 66, 76, 77

[56] Nesaraja, C. (2014). Nuclear Data Sheet 115, 1. 87

[57] Nicholas Ruof, W. P. (2020). Multi-site event discrimination v2 for the MAJORANA DEMONSTRATOR; draft. Internal Document. 57

[58] Reine, A., Caldwell, T., Cuesta, C., Guinn, I., and Myslik, J. (2017). Run selection and data cleaning of DS5 (M1 and M2); final. *M-TECHDOCUNIDOC-2017-020*. Internal Document. 67, 79, 90, 94

[59] Reine, A., Caldwell, T., Cuesta, C., Guinn, I., and Myslik, J. (2018). Run selection and data cleaning of DS6 (M1 and M2); draft. *M-TECHDOCUNIDOC-2018-034*. Internal Document. 67, 79, 90, 94

[60] Reine, A. and Cuesta, C. (2017). Run selection and data cleaning of DS2; final. *M-TECHDOCUNIDOC-2017-013*. Internal Document. 67, 79, 90, 94

[61] Schubert, A. G. (2012). *Searching for neutrinoless double-beta decay of germanium-76 in the presence of backgrounds*. PhD thesis, University of Washington. 68, 80, 95

[62] Zyla, P. et al. (2020). Review of Particle Physics. *PTEP*, 2020(8):083C01. 5, 6, 7

Vita

Andrew Lopez was born in a U.S. Naval Hospital in Naples, Italy on April 6, 1990. He attended Montgomery County High School in Mount Sterling, Kentucky and graduated in 2008. After high school, Andrew studied at Eastern Kentucky University, where he completed a B.S. in Physics in 2012. Andrew was then accepted into the Ph.D. program of the Department of Physics and Astronomy at the University of Tennessee in the fall of 2012.

During his time in the Ph.D. program he has developed several useful skills. These skills include:

Presenting physics results and ideas at public meetings.

Handling sensitive components, such as germanium detectors.

Performing lab tasks in an ultra clean environment.

Programming in the C++, Python, and FORTRAN languages, as well as using the CERN ROOT data analysis framework.

Using computer clusters for performing software tasks.

Utilizing the GEANT4, MAGE, FLUKA, and TALYS software packages to simulate physics interactions.

Performing data analyses to measure physical quantities, and to identify errors in subsystems using both real and simulated data.

Andrew's work has contributed to many of the MAJORANA collaboration publications. The following are a list of the most recent publications:

ADC Nonlinearity Correction for the MAJORANA DEMONSTRATOR. IEEE Trans. Nucl. Sci. 68 (2020) 3, 359-367 [9].

Search for Double-β Decay of ^{76}Ge to excited states of ^{76}Se with the MAJORANA DEMONSTRATOR. Phys.Rev.C 103 (2021) 1, 015501 [20].

Search for Neutrinoless Double-β decay in ^{76}Ge with 26 kg·yr of exposure from the MAJORANA DEMONSTRATOR. Phys. Rev. C 100, 025501 Published 23 August 2019 [15].

Multisite Event Discrimination for the MAJORANA DEMONSTRATOR. Phys. Rev. C 99, 065501 Published 7 June 2019 [17].

Search for trinucleon decay in the Majorana Demonstrator Phys. Rev. D 99, 072004 Published 12 April 2019 [18].

Search for Neutrinoless Double-β Decay in ^{76}Ge with the MAJORANA DEMONSTRATOR. Phys. Rev. Lett. 120, 132502 Published 26 March 2018 [2]. .

More publications are expected in the near future.

Andrew has presented or participated in the following conferences and workshops:

Presented: American Physics Society April Meeting of 2016 in Salt Lake, Utah.

Presented: American Physics Society Division of Particles and Fields Meeting of 2017 in Aurora, Illinois.

Participated: Amherst Center for Fundamental Interactions School on Double Beta Decay of 2017 in Amherst, Massacusetts.

Presented: American Physics Society April Meeting of 2019 in Denver, Colorado.

Andrew was awarded the Chancellor's Citation for Extraordinary Profession Promise in 2018 by the Universtity of Tennessee. Andrew was also awarded the Office of Science Graduate Student Research (SCGSR) award in 2018 by the Department of Energy Office of Science. The SCGSR award was used to fund six months of research that Andrew performed

at Los Alamos National Laboratory (LANL) with host scientist Dr. Steven Elliott. This research at LANL started on November 5, 2018 and ended May 3, 2019.